HIGH CHI POLYMERS FROM HYDROPHOBIC INITIATORS FOR ULTRA-SMALL MICROPHASE SEPARATION

Hancox, Ellis

A thesis submitted in partial fulfilment of the requirements for the degree of

Monash Warwick Alliance Joint Doctor of Philosophy in Chemistry

University of Warwick,

Department of Chemistry

July 2022

Under the primary supervision of **Prof. David M. Haddleton**

Funded by the Monash-Warwick Alliance

Under the secondary supervision of **Prof. Thomas P. Davis/Dr. Michael Whittaker**

Drug delivery, Disposition & Dynamics, Faculty of Pharmacy,
Monash Institute of Pharmaceutical Sciences, Monash University

Contents

Table of Figures

Table of Tables

Abbreviations

RDRP	Reversible-deactivation radical polymerisation
NMP	Nitroxide-mediated polymerisation
AMRP	Aminoxyl-mediated radical polymerisation
TEMPO	2,2,6,6-tetramethylpiperidin-1-yl)oxyl
RAFT	Reversible addition-fragmentation chain transfer
ATRP	Atom-transfer radical polymerisation
CTA	Chain transfer agent
DP	Degree of polymerisation
PISA	Polymerisation induced self-assembly
bpy	2,2'-bipyridine
SARA	Supplemental activator and reducing agent
SET LRP	Single-electron transfer-living radical polymerisation
DMPA	2,2-dimethoxy-2-phenylacetophenone
TPMA	tris(pyridylmethyl)amine
Me_6TREN	tris[2-(dimethylamino)ethyl]-amine
χ	Flory-Huggins interaction parameter
$Đ$	Dispersity
M_n	Number-average molecular weight
M_w	Weight-average molecular weight
SAXS	Small-angle X-ray scattering
T_{ODT}	Order-disorder transition temperature
T_{OOT}	Order-order transition temperature
EUV	Extreme UV
BCP	Block copolymer
DSA	Directed self-assembly
T_g	Glass transition temperature
LC	Liquid crystal
WAXS	Wide-angle X-ray scattering
$P(q)$	Form factor

$S(q)$	Structure factor
d	Domain spacing
q	Scattering vector
AFM	Atomic force microscopy
N	Total degree of polymerisation
F_A/F_B	Volume fraction
PFO-OH	Perfluorooctanol
BiB	Bromoisobutyryl bromide
COSY	COrrelated SpectroscopY
NMR	Nuclear magnetic resonance
HSQC	Heteronuclear Single Quantum Coherence
F_n-PAA_m	Fluoro-acrylic acid polymers. n = number of fluorine atoms, m = number of acrylic acid units
GPC	Gel permeation chromatography
MALDI-Tof-MS	Matrix-assisted laser desorption-ionisation time-of-flight mass spectroscopy
DSC	Differential scanning calorimetry
T_m	Melting temperature
T_c	Crystallisation temperature
$T_{g,\infty}$	Glass transition temperature at infinite molecular weight
TGA	Thermogravimetric analysis
DMA	Dynamic mechanical analysis
σ	Stress
e	Strain
FT-IR	Fourier-transform infrared spectroscopy
λ	Wavelength
2θ	Scattering angle
LAM	Lamellar
HEX	Hexagonally packed cylinders
DIS	Disordered
F_{13}	Perfluorooctyl bromoisobutyrate initiator

F_{17}	Perfluorodecyl bromoisobutyrate initiator
F_{21}	Perfluorododecyl bromoisobutyrate initiator
d*	Domain size
TEM	Transmission electron microscopy
ODT	Order-disorder transition
OOT	Order-order transition
I_{peak}	Peak intensity
σ/FWHM	Full-width half-maximum
AMBiB	Antracenemethanol bromoisobutyrate initiator
PMDETA	N,N,N′,N′′,N′′-Pentamethyldiethylenetriamine
N-propyl	N-propyl-1-pyridin-2-ylmethanimine
C_{18}	Octadecyl bromoisobutyrate
EEMA	1-ethoxyethyl methacrylate
MBPA	Methyl α-bromophenylacetate
SkMA	Solketal methacrylate
GMMA	Glyceryl monomethacrylate
NtrisBiB	*N*-[3-[tris(trimethylsiloxy)silyl]propyl] 2-bromoisobutyramide
TRIS	3-[tris(trimethylsiloxy)silyl]propyl methacrylate

Acknowledgements

Firstly, I would like to thank Professor Dave Haddleton for the opportunity to work under his supervision and progress towards achieving a PhD. He has provided motivational support, an answer to all questions (science or otherwise), and a relaxed environment to work in. He is one of the most knowledgeable people I'll ever meet and I'm grateful to have learned from him. The skills I've learned from pursuing a PhD, both technical and (inter)personal, have shaped and taught me what I'm capable of achieving. Gaining these life skills and completing this PhD will always be some of my most precious achievements and I have Dave to thank for it.

I would also like to thank Professor Paul Topham and Dr Matt Derry from Aston University and Dr Martin Greenall from Lincoln University. Without these three, my PhD would have looked very different. Paul and Matt have shared constant knowledge and suggestions about microphase separation and Martin provided the modelling which led to the pinnacle of this work.

I'd like to thank Dr Paul Wilson, Professor Stefan Bon and Dr David Fox for general scientific chats and helpful suggestions. Fox also helped me as senior tutor during my undergraduate, it was the beginning years of long discussions over a cup of tea. I'll miss those chats!

I'm grateful to the RTPs at Warwick, particularly to Steve Huband in the X-ray diffraction RTP and Dan Lester & James Town in the Polymer RTP. Steve happily explained the same things to me over and would let me book the SAXS for a week at a time. Dan/James constantly do brilliant work for the RTP and are so light-hearted, it's been a joy.

The Haddleton group has had and has many talented scientists, and I've been fortunate to work with and get to know many of them. Evelina helped me immensely in my early PhD days and stayed a good friend after she left Warwick. Congkai and Spyros and I started together and have been great friends during our time as PhD students. Also thank you to Despina, Samantha, Vincent, Hannes, Arkadios, Lucas, Chris and Katie P and Katie E who have all been supportive friends.

Also thank you to all the people I met in Australia, for being welcoming and supportive during unprecedented times. Thank you to Dr Mikey Whittaker for taking me under his wing and introducing me to Fiona!

Finally, I can't thank Luke enough. He's read my whole thesis, more than once, and helped me improve my writing skills. He's bounced ideas with me, provided so much support and been a constant motivator throughout my PhD.

Declaration

This thesis is my own work except where it contains work based on collaborative research, I have detailed below the contributions of collaborators for each chapter.

I also confirm that this thesis has not been submitted for a degree at another university.

Professor Paul Topham and Dr Matthew Derry, Chapter 2 and 3. Contributed knowledge of block copolymer microphase separation and guidance in creating the phase diagram (section 3.5).

Dr Martin Greenall, Chapter 2. Conducted theoretical modelling and predictions (section 3.3).

Dr Steve Huband, Chapter 2 and 3. Performed SAXS measurements and exported data.

Dr David Fox, Chapter 5. Performed the simulation of the ^{1}H NMR spectrum of NtrisBiB (section 5.3.4).

Abstract

This work focuses on the use of copper-mediated polymerisation as a versatile method to produce low molecular weight polymers with narrow dispersity (< 3000 Da, $Đ$ < 1.20) for the specific aim of studying their self-assembly in the solid state via microphase separation. By exploiting the theory of microphase separation of block copolymers, separated polymer phases have been achieved by maximising the Flory-Huggins interaction parameter (χ) and minimising the total degree of polymerisation (molecular weight, N).

The study of block copolymer behaviour has grown in prominence and academic interest due to applications in the microelectronics industry, which has become a significant driving force for obtaining smaller domains, as it can lead to higher density data storage. This work focusses on the synthesis of highly amphiphilic polymers produced by copper-mediated polymerisations and studying their self-assembly in the solid state.

Initially an F_{13} initiator (perfluorooctyl bromoisobutyrate) was used as a pseudo block to minimise N and maintain high χ. The conditions of the polymerisation of poly(acrylic acid) using this initiator were optimised and polymer morphologies and domain sizes were inferred from Small-angle X-ray scattering (SAXS). The use of both solvent and temperature annealing show different assemblies, and thermal annealing was shown to alter the structures.

The work moved onto the investigation of an F_{17} and F_{21} pseudo block (perfluorodecyl bromoisobutyrate and perfluorododecyl bromoisobutyrate), While domain sizes were found to be larger than those in F_{13}-PAA films, F_{17}/F_{21} polymers exhibited longer range order and more crystallinity. Block copolymer models were used to predict the phase behaviour of these polymers and a phase diagram was developed.

Finally, the scope of hydrophobic initiators and hydrophilic monomers possible for use in the synthesis and microphase separation of high χ, low N polymers was investigated. The polymerisation conditions were optimised for targeting low degree of polymerisation with both acrylates and methacrylates and included incorporation of additional photo-responsive properties via an anthracene end group.

Chapter 1: Introduction

1.1 Basics of polymerisation

Fundamentally, there are two mechanisms for polymer synthesis: step growth and chain growth. Step growth mechanisms involve a stepwise addition of monomer units to a polymer chain, for example in a series of condensation reactions. The joining of monomers to dimers and trimers and subsequent oligomers leads to an exponential increase in molecular weight, hence, high molecular weight polymers require long reaction times. Chain growth polymerisations, in contrast, grow by sequential additions of monomer units to the end of a propagating polymer chain. This process requires an initiating moiety, often an ionic or radical species, and leads to an increasing exponential decay in molecular weight as the monomer feed is consumed.[1] The short-lived nature of radicals means that achieving low molecular weight is difficult, and it is usually impossible to make block copolymers. This concept is shown in Figure 0-1, where molecular weight vs conversion is presented for chain growth, step growth and living polymerisations. Efforts to control polymerisations have provided the ability to predict molecular weight, add functionality and introduce properties previously out of the reach of synthetic polymer chemists.

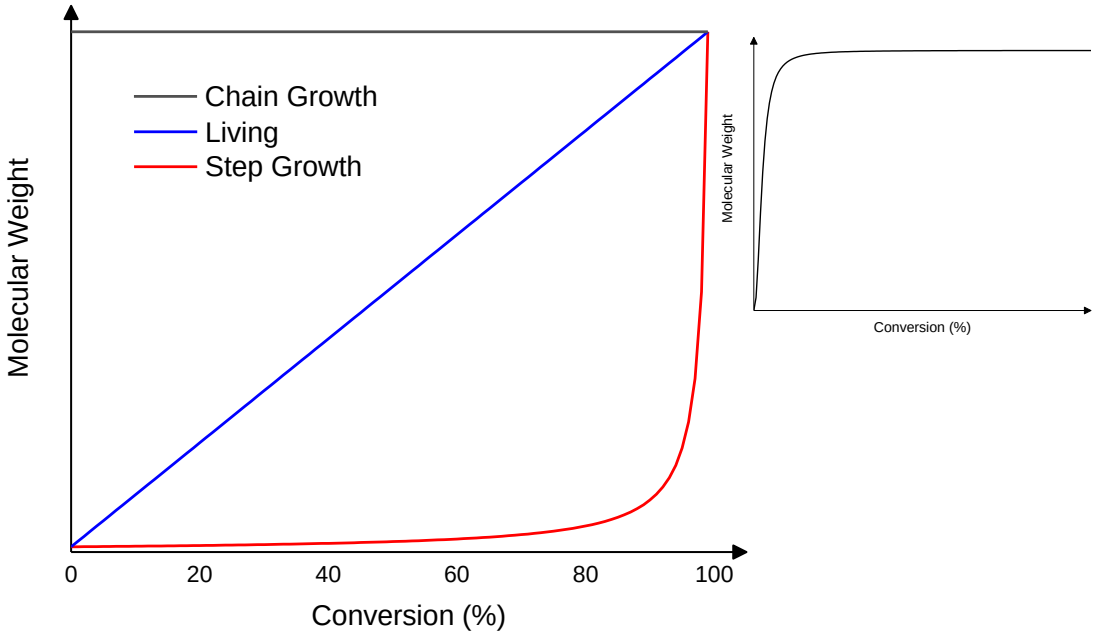

Figure 0-1. Molecular weight with conversion for step growth, chain growth and living polymerisations. Inset shows chain growth polymerisation at very low conversion.

1.2 Controlled polymerisation

Removing the termination step from the mechanism of radical polymerisation can lead to living polymerisation with greater control of polymer molecular weight and dispersity (molecular weight distribution) and has previously been referred to as "living radical" polymerisation. The first efforts in living polymerisation were by Szwarc in 1956 in which a sodium-naphthalene complex was used as the initiator in an anionic polymerisation of styrene.[2,3] The description of the process as "living" was introduced as the addition of another monomer feed continued the polymerisation. The result was the synthesis of "block copolymers", giving proof that the polymer was "alive", and polymerisation could continue with additional monomer addition.

1.2.1 Reversible-deactivation radical polymerisation (RDRP)

In practical terms, the absolute removal of all possible termination pathways is impossible and especially so for an essentially radical based chain growth. Therefore, the IUPAC-suggested term is reversible-deactivation radical polymerisation (RDRP), which is an umbrella term for multiple controlled radical polymerisation types.[4] RDRPs aim to reduce the concentration of radicals present during polymerisation, however the short-lived nature of radicals enables infrequent termination. This can be via abstraction of backbone protons which lead to branching points and increase dispersity. Common examples of RDRPs are atom-transfer radical polymerisation (ATRP), reversible addition-fragmentation chain transfer (RAFT),nitroxide-mediated polymerisation (NMP) and Copper-mediated RDRP (Cu-RDRP).

1.2.1.1 Nitroxide-mediated polymerisation (NMP)

One of the first attempts to carry out stable radical-mediated polymerisation was by Otsu in 1956-1957.[5,6] The concept of "living" radical polymerisation was not introduced until 1982,[7] by work in which disulfide initiators were cleaved photochemically at the C-S bond resulting in a propagating carbon radical and a *mediating* sulfur radical. After propagation, these two radicals can reversibly recombine to deactivate the reaction. Unfortunately the sulfur radical can also initiate polymerisation which led to high dispersities, therefore the need for a stabilised mediating radical became apparent. The observation that the same polymer made by different polymerisation techniques exhibited differences in stability suggested that structural irregularities develop during chain initiation and termination.[8] This prompted the development of a method by which to monitor the initiation of radical polymerisation. Nitroxides were introduced through radical trapping in an attempt to

quantitatively characterise radical reactions,[9] and ultimately led to the term nitroxide-mediated polymerisation (NMP),[10] patented by Solomon *et al.* in 1985.[11] The accepted IUPAC term is now aminoxyl-mediated radical polymerisation (AMRP).[12] Nitroxides have been studied along with their derivatives, alkoxyamines, as mediators in NMP.[13] (2,2,6,6-tetramethylpiperidin-1-yl)oxyl (TEMPO) is a particularly well established alkoxyamine mediator, and was key in the development of unimolecular NMP in which the requirement for a separate initiating molecule is removed, Figure 0-2.[14]

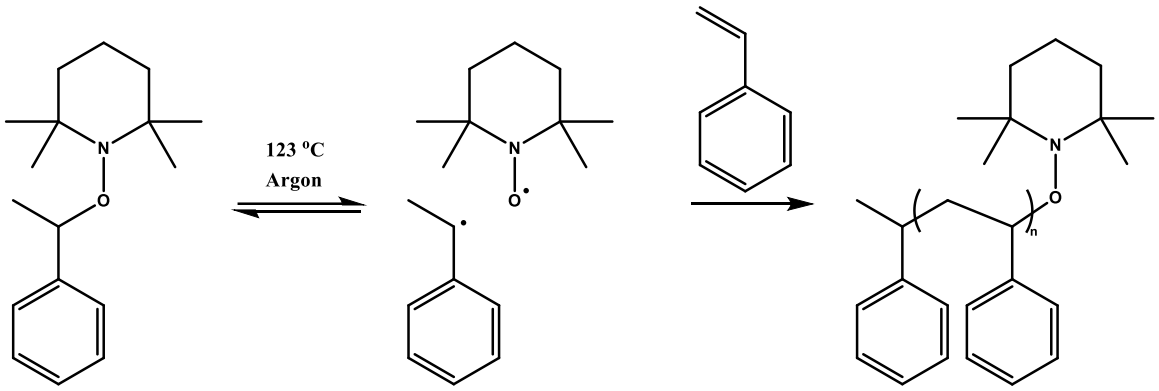

Figure 0-2. Example of a unimolecular initiator used in nitroxide mediated polymerisation.[14]

1.2.1.2 Reversible addition-fragmentation chain transfer (RAFT)

First reported in 1998,[15] reversible addition-fragmentation chain transfer (RAFT) is an RDRP mechanism and relies on an equilibrium between dormant and active chains.[16] Whereas NMP and ATRP rely on the persistent radical effect[17] *i.e.* the radicals do not undergo self-termination which leads to reversibility, RAFT is a degenerative transfer mechanism meaning that the number of radicals in the activation-deactivation process is constant and therefore there is a need for a radical initiation source.[18] The initiating species adds to a chain transfer agent (CTA) or RAFT agent thus creating the equilibrium between dormant and active radical species, Figure 0-3. RAFT agents often contain a thiocarbonylthio group (Z-(C=S)-SR), in which monomer units are added between the R· and the Z-(C=S)-S· group of the RAFT agent. The dispersity can be narrow due to the rate of addition/fragmentation being higher than the rate of propagation, ultimately resulting in a similar degree of polymerization (DP) for all polymer chains at any point in time. A perceived advantage of RAFT over NMP or ATRP is the range of monomers which are

compatible, although custom RAFT agents must be synthesised, and polymers are produced with dithioester end groups which cause red-yellow colouring unless the end group is removed.

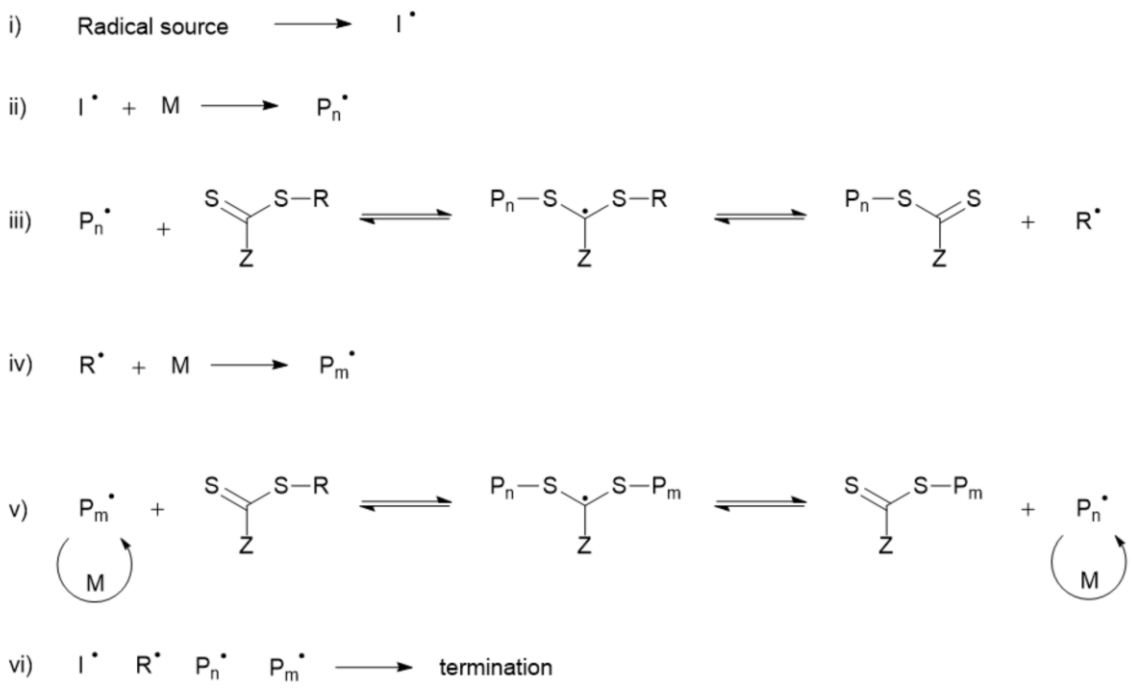

Figure 0-3. Mechanism of reversible addition-fragmentation chain transfer polymerisation (RAFT).[19]

1.2.1.3 ATRP

Atom-transfer radical polymerisation (ATRP, coined by Matyjaszewski) was first reported independently by Sawamoto[20] and Matyjaszewski[21] in 1994 and 1995, who demonstrated "living" polymerisation of methyl methacrylate (MMA) and styrene (S), respectively.

A linear plot of $\ln[M]_0/[M]$ versus time suggested that the mechanism could be considered "living", owing to a constant concentration of growing radicals throughout the polymerisation, and the rate of termination was negligible due to the equilibrium between proposed active and dormant radical species. Matyjaszewski's group used 1-phenylethyl chloride (1-PECl) as the alkyl halide initiator and Cu(I)Cl complexed with 2,2'-bipyridine (bpy) formed the mediating species. Removal of these reagents produced an uncontrolled polymerisation[13] and the necessity of these reagents led to the proposal of the mechanism (Figure 0-4) which is widely accepted today.

In general terms, an alkyl halide (R-X) is activated by a redox-active transition metal complex (M^m-L), to form an active species. The metal, often copper (0) (although ruthenium,[23] iron,[24], nickel,[25] palladium[26] and molybdenum[27] are also effective) will undergo single electron transfer oxidation (X-M^{m+1}-L) and generate the active species ($R^{\bullet}$) which is free to polymerise ($P^{\bullet}$) or recombine with the metal complex to form the dormant species (P-X).[28,29] The rate constant of activation (k_{act}) is much smaller than deactivation (k_{deact}) therefore propagation occurs intermittently. The complex X-M^{m+1}-L deactivates the radical and returns the polymer to its dormant state (P-X) and the metal to its active state M^m-L.[28] This equilibrium is strongly shifted to the left, favouring dormant species and thus there are a minimal number of radicals present at any time leading to a reduced probability for termination events and very low dispersities can be achieved with this system. Termination reactions can occur in ATRP, which are often via disproportionation or radical coupling, but a successfully controlled ATRP reaction will have less than a few percent of terminated polymer chains.[29]

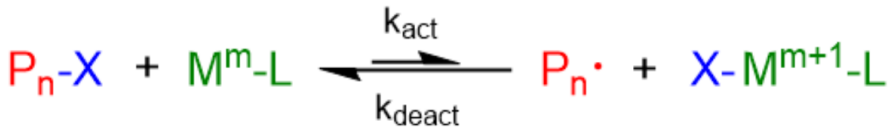

Figure 0-4. The widely accepted mechanism for atom transfer radical polymerisation (ATRP) by Cu(I) complexes.

Ultimately, it is the choice and properties of the metal catalyst and the relative stabilities of the M^m and M^{m+1} oxidation states which determines the position of equilibrium position, K_{eq}, where $K_{eq} = k_{act}/k_{deact}$. The complex needs to have readily available n and n+1 oxidation states (to facilitate a single electron redox process), an affinity to form bonds to halogens and space in the coordination complex to accommodate the halogen. However, the initiator also has some influence on equilibrium position due to the relative strength on the R-X bond, and various alkyl halides have been studied as polymerisation initiators.[29,30] Halogenated alkanes,[20,21] benzylic α-haloesters,[31,32] α-haloketones, α-halonitriles,[33] and sulfonyl halides[34] have shown good initiating properties because they help facilitate the homolytic dissociation of the R-X bond, and inform the types of monomers that are polymerisable.[35] Many monomer types are compatible with this type of polymerisation, particularly those which stabilise the propagating radical with an

electron withdrawing group conjugated to the sp^2 carbon orbital containing the unpaired electron.[29,36] These include styrene,[37] acrylates,[38] methacrylates and acryonitrile[39]; each monomer has its own equilibrium constant for atom transfer and radical propagation which can alter the equilibrium constant.

The role of the ligand is to improve the solubility of the complex in addition to controlling the equilibrium between oxidation states of the metal: different ligands may be more suitable for a given monomer as the stability of the radical will be monomer dependant and not amenable to be changed. For copper complexes, nitrogen containing ligands usually give optimal results as when compared to oxygen, sulfur and phosphorus donor ligands, which have less suitable electronic properties and binding constants.[40] Other important factors include lability, number of binding sites and the electronic withdrawing/donating ability of substituents on the ligand. A labile ligand allows for easier reorganisation of the complex, activity increases with the number of binding sites and is reduced with strongly electron withdrawing substituents. Inappropriate ligand choice can lead to unwanted chain transfer of the terminal halogen to the ligand which deactivates the macromolecule by leading to a high concentration of radicals or a dormant reaction with a stable alkyl halide.

1.2.1.4 Importance of the initiator

Features of an appropriate ATRP initiator include: presence of multiple halogens at the carbon where the radical is formed, presence of carbonyl, ester or phenyl groups which stabilise the radical and help facilitate homolytic dissociation of the halogen and finally steric congestion around the radical carbon to reduce side reactions.[41] Therefore α-haloesters and α-haloketones with tertiary α-carbons are the most commonly used initiators. Other useful chemical functionality can be incorporated into these initiators, providing a facile route to α-functional telechelic polymer chains. The choice of halogen leaving group is also important, due to the difference in strength of the carbon-halogen bond. Initiators with Bromine or Chlorine are often the most suitable, as the C-F bond is too strong to undergo cleavage and C-I is too weak.

The role of the initiator is the starting point of polymer chain growth. In a living polymerisation the degree of polymerisation (DP) is determined by the monomer to initiator ratio (Equation 1), where a *higher* concentration of initiator leads to a polymer of *shorter* chain length. The R group on the α-carbon strongly affects $k_{initiation}$ and influences how controlled polymer growth is considered to be as it controls the stability of the ensuing radical. The R group at the Ω-end of the initiator can be chosen

to be hydrophilic, hydrophobic and/or incorporate specific functional groups. The importance of choice of initiator is more significant at lower DP, as the volume/weight fraction of the initiator becomes larger with respect to the whole polymer. Careful consideration must be given to this when designing polymers for self-assembly (or to avoid self-assembly), as the polymer may be undesirably amphiphilic and lead to undesirable polymerisation-induced self-assembly (PISA).

$$\mathrm{DP} = \frac{[\mathrm{M}]}{[\mathrm{I}]} \text{ x conversion} \qquad (1)$$

1.2.1.5 Cu(0)-RDRP

Cu(0)-mediated RDRP is a versatile technique allowing polymerisations of various activated monomers in both organic and aqueous media.[42] Universal conditions have been developed for the polymerisation of acrylates, methacrylates and styrene. The importance and role of ligand and initiator have been widely investigated.[35,43,44]

The accuracy of two alternative models for the mechanism of Cu(0)-RDRP have been debated: supplemental activator and reducing agent (SARA ATRP) and single-electron transfer (SET LRP), Figure 0-5.[45] In SARA ATRP, activation (of the initiator in the first step and the propagating chain from then on) by Cu(I) is the major contribution to the mechanism. Cu(0) is a supplemental activator of alkyl halides and deactivates excess Cu(II) via comproportionation.[46] In SET LRP, Cu(0) is the primary activator of alkyl halides and Cu(I) does not contribute, instead instantaneously disproportionating to Cu(0) and Cu(II). In both mechanisms, Cu(II) is the major deactivating species.

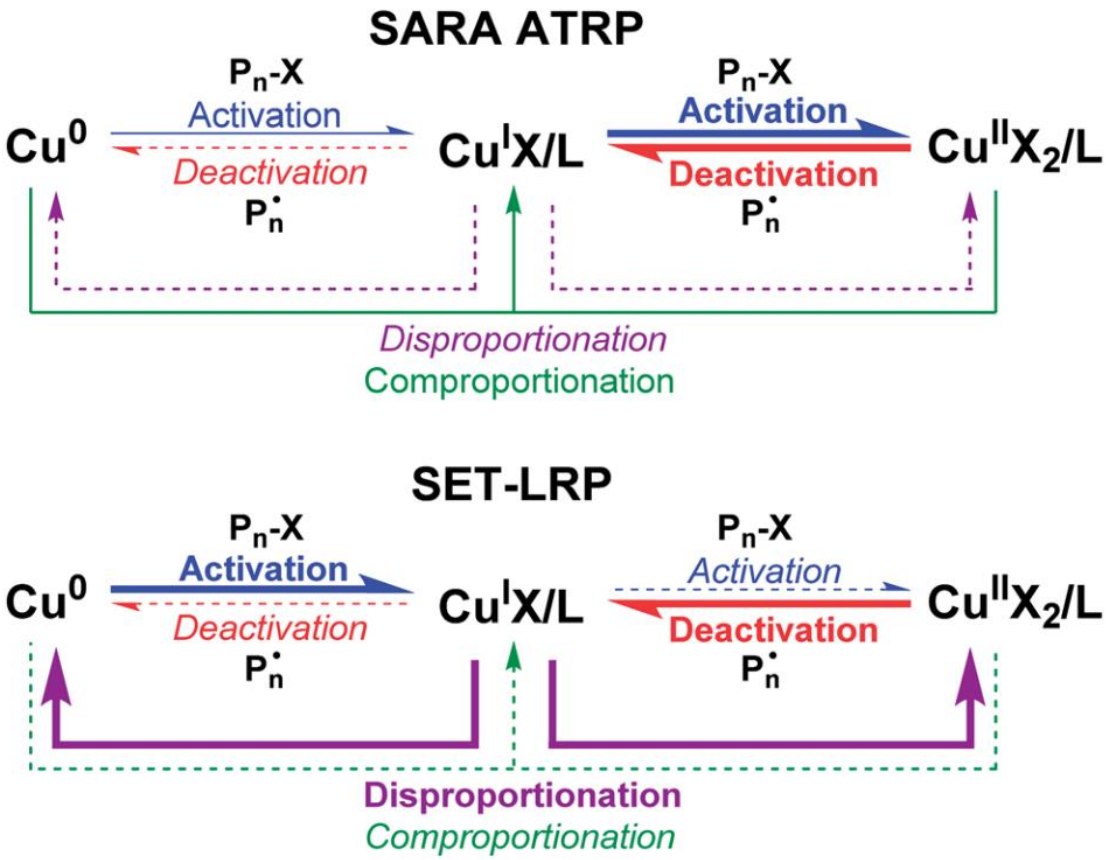

Figure 0-5. SARA ATRP and SET LRP mechanisms. Bold arrows indicate major reactions, solid lines indicate supplemental/contributing reactions and dashed lines indicate minor/neglected reactions. Image taken from literature.[45]

In 1997, Matyjasewski proposed that Cu(0) can reduce Cu(II) to Cu(I), which removes deactivating species and generates activating species, maintaining a controlled polymerisation.[47]

Later, in 2006, Percec proposed that Cu(0) species donate an electron to the alkyl halide, generating Cu(I) which can rapidly disproportionate into Cu(0) and Cu(II) which mediate the initiation and reversible termination.[48] Percec labelled this mechanism as a single-electron transfer living radical polymerisation (SET-LRP) that occurs via an outer-sphere mechanism. The disproportionation of Cu(I) has since been utilised to polymerise monomers in aqueous systems.[49,50] Kinetic studies of Cu(0) in organic solvent (such as DMSO) with amine ligands by both Matyjaszewski[51] and Haddleton[52] disagree with the proposed SET LRP mechanism, however it is supported in aqueous systems.[53]

1.2.1.6 Photo-induced copper-mediated RDRP

Photo-induced[54,55] (and electrochemically induced[56,57]) polymerisation can beneficially add spatial and temporal control by providing or removing stimuli.[58,59] Particularly with light stimulus, faster rates of reaction and lower activation energy pathways are observed without the need for additional chemical components.[49,60] In 2000, ATRP was found to have higher conversion in visible light than in dark conditions.[22] This observation led directly to the use of UV light for initiation, initially tested with methyl methacrylate (MMA)[16] and styrene (S)[61] using 2,2-dimethoxy-2-phenylacetophenone (DMPA) as a photoinitiator, Figure 0-6. In this system either of the radicals R· could initiate polymerisation which lead to poor initiation efficiency and broad molecular weight distributions.

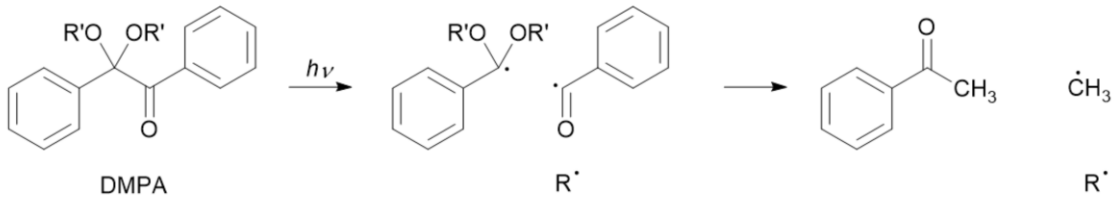

Figure 0-6. DMPA as a photoinitiator.

More recently, work has focused on utilising light stimuli to directly influence the ATRP equilibrium.[62] Tertiary amine containing ligands/substrates such as tris(pyridylmethyl)amine (TPMA)[63] or tris[2-(dimethylamino)ethyl]-amine (Me_6TREN)[64] readily absorb high energy light. In copper systems, this results in a photo mediated reduction of Cu(II) to Cu(I) via an excited state complex, thereby driving the equilibrium to be favourable for polymerisation without the presence of Cu(0) or a photoinitiator.

Me_6TREN and Cu(II) are a particularly effective combination that require low concentrations copper/ligand, with the ability to polymerise many acrylate monomers using UV light (λ = 360 nm), with near quantitative conversions and low dispersities across a variety of targeted molecular weights. This system also tolerates multifunctional alkyl halide initiators which, combined with excellent end group fidelity, produces α,ω-telechelic polymers and allows for the synthesis of block copolymers via chain extension.[65]

Low dispersities in final polymer materials are ideal for microphase separation (section 0), as this positively influences morphology and/or prevents complex ordering.[66] This is especially important at low molecular weights where dispersity is harder to control, as dispersities are higher in early stages of polymerisation.[65] Photo-induced copper-mediated RDRP has been frequently used in this thesis, due to the ability to target low molecular weight polymers with low dispersity and use functional initiators.

The system developed at Warwick using 365 nm irradiation of excess free primary amine ligand followed by energy transfer to complexed ligand results in efficient photoreduction of Cu(II) to Cu(I). This polymerisation process has been shown to give unprecedented narrow dispersities especially at very low DP, these are normally difficult to access via RDRP. In addition, there is no evidence of termination by any method from MALDI-TOF making this ideal, and probably the only way, to access the low DP required and to be able to realistically differentiate between DP = 5, 10, 14, etc due to this narrow dispersity at such low DP.

1.3 Microphase separation

1.3.1 Block copolymers

A homopolymer is a polymer comprised of only one monomer. The concept of copolymers (more than one monomer), has been discussed since the 1950s,[67] and these are synthesisable in the form of alternating (ABABAB), random/statistical (AABABABB) or block copolymers (A_nB_m). Block copolymers (BCPs), which can be easily synthesised via RDRP techniques by sequential monomer addition,[68] are of commercial interest as adhesives, foams, thermoplastic elastomers and, particularly, surfactants.[69] Other areas of interest for BCPs include: drug delivery,[70–72] superhydrophobic materials,[73–75] nanolithography,[76–78] photonics,[79] actuators,[80–83] water filtration,[84] and thermoplastic elastomers.[85–87]

These molecules consist of a hydrophilic and a hydrophobic block, which often results in their self-assembly into nanostructures. For example, PMAA-*b*-PS cannot macrophase separate (oil and water) as blocks are bound by a covalent bond. Therefore, the polymer chains assemble into structures that maximise and minimise the contact between similar and dissimilar blocks, respectively.[88] Large differences in polarity or electrostatics can also drive microphase separation due to thermodynamic incompatibility. One theoretical study suggests that a blend of oppositely charged polymer electrolytes (immiscible) allows microphase separation, in which the microstructures are stabilised (and do not macrophase separate) by excess Coulomb energy and follow the strong segregation limit, Figure 0-7.[89]

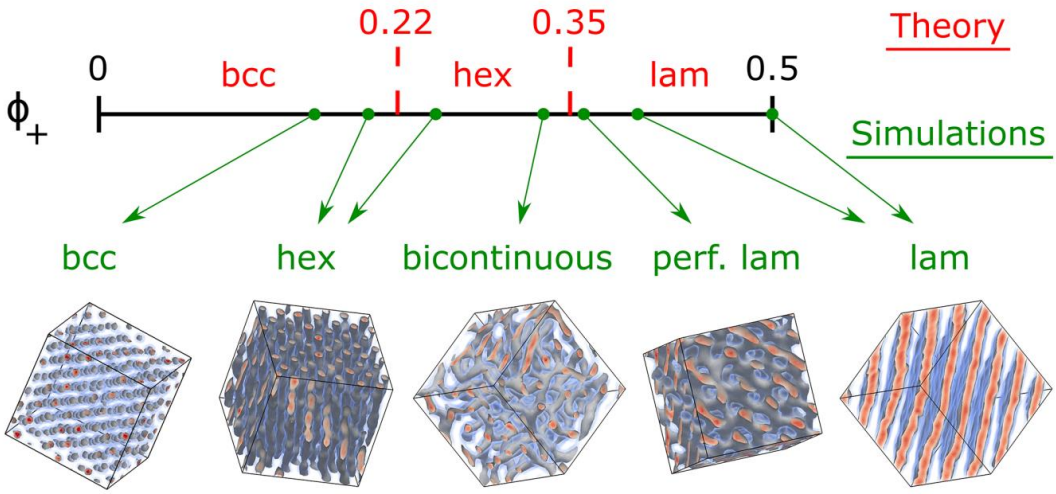

Figure 0-7. Diagram of blend morphologies in the strong segregation limit, when the boundary ϕ+ values are found to be independent of χ; ϕ+ is the polycation volume fraction in the blend. Top and bottom parts of the scheme show theoretical predictions for the binodals of the conventional morphologies and dissipative particle dynamics simulations data. The snapshots were obtained for the following incompatibilities: χ = 15.18 for ϕ+ =

0.166; χ = 7.59 for ϕ+ = 0.25; χ = 7.084 for ϕ+ = 0.33; χ = 5.06 for ϕ+ = 0.36; χ = 3.1625 for ϕ+ = 0.5. The box size for the bcc phase was changed to L = 38.4 to fit an integer number of periods. Figure has been reproduced from ref. 89.

The Flory-Huggins interaction parameter (χ) describes the cost of free energy between contact of dissimilar blocks.[90] There are competing forces between the enthalpic contribution of mixing and the entropic penalty associated with elongation of polymer chains, and the structures formed are a result of balancing these forces.[80] The reorganisation of block copolymer chains is known as microphase separation. High χ polymers are those with highly incompatible segments and have attracted significant attention owing to their potential to form sub-10 nm (Amylose-*b*-poly(styrene)),[91] sub-5 nm (poly(cyclohexylethylene)-*b*-poly(methyl methacrylate)),[92] and sub-3 nm domain sizes when using low molecular weight species. This is of significant interest in the field of microelectronics due to the potential for using these materials for lithography.[93] Hillmyer and co-workers[93] suggested that domain sizes as small as 2 nm could be achieved, with well-defined features, using a low molecular weight BCP with fluorinated and ionic blocks. Fluorinated BCPs have been used to achieve microdomains smaller than 40 nm[94] and fluorinated ATRP initiators have also been synthesised for use in microphase separation, however, the molecular mass of these polymers ranged from 7000-30,000 Da.[95]

Alongside χ, factors that most directly influence the microphase separation are total degree of polymerisation (N) and volume fraction of the blocks (f_A).[96] Extensive theory has been developed to understand the behaviour of block copolymer assembly,[97] the theoretical phase diagram and possible structures for a symmetrical block copolymer in the solid phase is shown in Figure 0-8. A minimum segregation limit is given by χN >10.5, values lower that this only produced disordered states and materials.

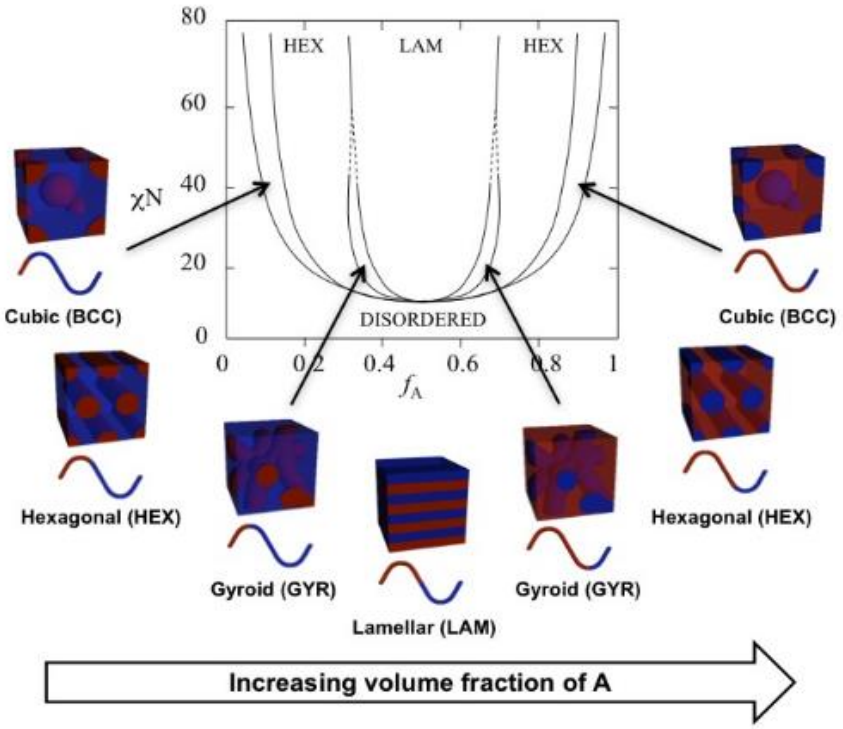

Figure 0-8. Phase diagram of possible block copolymer phases in the solid state. Image taken from literature.[80]

Microphase separation of block copolymers has also been widely investigated in solution but is often just referred to as "block copolymer self-assembly", particularly as controlled RDRP techniques allow the use of a wider range of monomers than was previously possible with anionic polymerisation.[98]. It is now possible to target different morphologies including micelles, cylindrical micelles and bilayers/vesicles[98] (and complicated structures in-between)[99] according the packing parameter, p, given in equation (2).

$$p = \frac{v}{al} \tag{2}$$

Where v and l are the volume and length of the hydrophobic chain, and a is the area of the head group. This equation is derived from the competing forces that result in self-assembly of molecules. Hydrophobic attraction of like-chains brings molecules together, and hydrophilic repulsion of ionic/steric head groups forces contact with water.[100] These interactions occur mainly around the interfacial regions, changing the interfacial area (a) per molecule in contact with the aqueous phase. Calculations show that spherical micelles are favoured when $p < 1/3$, cylindrical micelles when $1/3 < p < ½$ and vesicles when $½ < p < 1$.[101]

1.3.2 Dispersity

Dispersity (*Đ*), by definition, is the ratio of the weight- and number-average molecular weight (M_w/M_n) and is used as the standard measure of the range of molecular weights in a polymer sample (the molecular weight distribution), and it is noted that to be a polymer there inherently must be such a mass distribution. Generally, low dispersities are ideal for microphase separation, and increasing dispersity can alter morphology or prevent complex ordering.[66] The dispersity of BCPs has a significant effect on microphase structure, generally, increasing *Đ* increases domain size which is predicted by self-consistent field theory.[102] It has been shown that what is normally considered a low dispersity for controlled radical polymerisation actually has a significant standard deviation e.g *Đ* = 1.25 has a relative standard deviation of 50% of the polymer M_n.[103] This is especially Important at low molecular weights where dispersity is harder to control and particularly with ATRP, dispersities are higher in early stages of polymerisation.[65]

Considering a BCP with a minor block with *Đ* = 1, and a major block where *Đ* is varied, the composition and morphology changes dramatically. As *Đ* is increased in the major block, the microphase structure changes from cylinders to gyroid to lamellar, which is reversed when *Đ* is increased in the minor block.[104] Also, high dispersity decreases the order-disorder temperature (T_{ODT}) due the disordered phase becoming favoured *i.e.* when heating the BCP, it will enter the disordered phase at a lower temperature. This is reflective of the degree of polymer crystallinity. T_{ODT} can be determined from small angle x-ray scattering (SAXS) measurements (See section 1.4.1), wherein rapid broadening of the principal peak with temperature indicates the T_{ODT}. Discrete polymers show higher order peaks while disperse samples do not, suggesting dispersity reduces attainability of long-range order.[105]

1.3.3 Inducing microphase separation

Following Moore's Law, the number of components in integrated circuits have, more or less, doubled every 2 years.[106] The microelectronics industry has developed around lithographic techniques and been dominated by photolithography,[107] however, the resolution of feature sizes is limited by the wavelength of the beam used (KrF = 248 nm and ArF = 193 nm excimer lasers)[108]. Shorter wavelength lithography lasers have been developed (F_2 = 157 nm) and extreme UV lithography (EUV) use wavelengths at 13.5 nm, although thermal instability then becomes an important factor.[109]

The microphase separation of BCPs has become an area of interest that addresses the issue of minimum obtainable feature size and has lower production costs. Usually, a BCP will require an external stimulus to induce microphase separation. These include solvent vapour,[110–112] thermal (including microwave),[113–115] combination of both,[116,117] laser,[118,119] shear flow,[118,120] and electric field annealing.[121]

There is a demonstrable need to reducing the defect density of unguided BCP self-assembly. Defects are a particular challenge with small molecular weight BCPs with high Flory Huggins interaction parameters which produce sub-20 nm periodicities.[122–126]

1.3.3.1 Directed self-assembly (DSA)

Directed self-assembly (DSA) requires a substrate which is often pre-patterned to guide the formation of nanoscale features. Two methods of implementing DSA are most widely used; graphoepitaxial/physical epitaxy which relies on the selective wetting of the substrate by one of the blocks. (contains elements of chemical interaction to produce topographic structures/patterns) and chemoepitaxy (substrate is chemically patterned to define affinity with a particular block of the BCP).[127] In both cases a "top-down" method, used to define a chemical or topographic pattern of differences, is combined with a bottom-up self-assembly process where synthetically designed molecules assemble through controlled interactions.[128,129]

The microphase separation of BCPs can be controlled purely by molecular design and solvent choice on flat and untemplated surfaces, but the limits of ordering are defined by the grain boundaries of crystalline structures and the density of defects. This often prevents the use of purely bottom-up approaches in situations where response to individual stimuli is required"[128] Outside of continuum self-assembly (when any solid surface is used to drive assembly) the feature density (including roughness) and the strength of physical or chemical interactions between surface and molecule are of great importance.[130]

1.3.3.2 Thermal annealing

When annealing a block copolymer, the temperature must be raised above the glass transition temperature (T_g) of both polymer blocks to allow efficient reorganisation of an ensemble of polymer chains.[131,132]

Annealing tends to move a collection of polymer chains away from kinetically or thermodynamically trapped states and closer to thermodynamic equilibrium. This is

typically achieved by thermal or solvent annealing, and less frequently solvent vapour annealing is used to access kinetically-trapped morphologies.[133] Despite this distinction, careful tuning of parameters and combinations of types of annealing can allow access to a broad selection of kinetically or thermodynamically unfavourable morphologies. Microwave annealing is used infrequently in the field, partly due to the inextricable link between heating and the application of microwave radiation to solutions.[134] Microwave annealing, for the reason mentioned previously, tends to be realised on faster timescales than purely thermal methods.[135]

1.3.3.3 Solvent annealing

In solvent annealing, polymer films are submerged or exposed to quantities of solvent vapour,[136] the rate of solvent evaporation can be used to affect changes to polymer which, even if induced at the surface, can propagate through the entire film. The literature suggests that solvent presence imparts mobility to the polymer chains, which in turn enables a rapid removal of defects.[137] Extended periods of solvent annealing leads to higher intensity second order structural peaks in SAXS, which implies higher crystallinity and longer range order being introduced.[138]

1.3.4 Photo-switchable molecules

Molecules that exhibit photochromic reactions are of interest due to the repeatable control over material properties (self-assembly, conductivity, solubility, wettability, polarity, fluorescence, viscosity)[139–142]. The photo-alignment of liquid crystal (LC) polymers has been investigated for the last 2.5 decades and becomes important in liquid crystal displays.[143] Ikeda[144] and Seki groups[145] reported photo-controlled alignment using visible light to align LC nanocylinders, which led to the observation of photo-induced microphase separation in block copolymers.[146] Linear polarised light is an effective light source which aligns polymers depending on irradiation angle and can induce morphology changes if polarisation is removed.[145,147] Photo-induced microphase separation is a clean and reliable method to obtaining long range order in BCP systems.

Photoswitching can occur by different reactions, some reversible examples include: isomeric change in conformation (stilbenes,[148] azobenzenes,[148–150] cinnamtes[149]), ring closure (chromenes, diarylethenes,[150] fulgides,[149,150] dimerization (anthracene,[148,151] cinnamates,[151] coumarin,[149] thymine,[150] stilbenes) and donor-acceptor Stenhouse adducts (DASA), which cyclise to form a compact, hydrophilic, zwitterionic species

from an extended, hydrophobic, neutral species.[152–154] Irreversible photoswitches also exist; sulfonium triflate based PAG and *o*-Nitro-benzyl derivatives.[149]

If a photoresponsive molecule was synthesised as an alkyl halide initiator (and was also hydrophobic), it could be used to polymerise a low molecular weight (amphiphilic) polymer. This would either allow microphase separation by polarity difference, photo-induced microphase separation, or a change in morphology with light irradiation.

Azobenzene is a photo-switchable molecule that has been used numerous times, due to a simple switch between cis and trans isomers with different wavelengths of light.[146,147,155–157] This reaction allows a change in molecular volume, and can allow a reversible change between physical states.[158] Coumarin is a dye[159] which undergoes a [2+2] cycloaddition dimerization when irradiated with UV light. Coumarin derivatives show numerous biological benefits[160] and find use as fluorescent probes.[161] It has also been used as an ATRP initiator to synthesise an end-capped photosensitive polymer, however, the dimerization reaction was incomplete.[162] Similarly to coumarin, anthracene and its derivatives undergo a [4+4] cycloaddition with UV light, which has shown use as a photocrosslinker,[163,164] a coupling agent,[165] and light-erasable systems.[166] Anthracene (non-dimerised) has a conjugated electron system and is, therefore, highly hydrophobic and exhibits pi-pi stacking,[167] which can contribute to anthracene self-assembly.

1.3.5 Industrial uses and wider literature

Large scale industrial lithography processes have not implemented block copolymer self-assembly to produce consumer related products, however research groups active in the area mention the advantages this technology would bring. The most promising areas for industrial use of BCP self-assembly include biomedical applications, nanocomposites, nanoporous membranes and lithography.[168]

Nanoparticles and nanostructures in solution are beneficial for use in biological applications. Vesicles or hydrogels made by BCP self-assembly can be used for drug release, in which complex mesophase structures are ideal for encapsulating therapeutic agents.[169]

Nanocomposites can be combined with nanoparticles that would not normally form nanostructures, allowing control of catalytic activity, optoelectric and magnetic properties. Alternatively, they can be used as strengthening agents when they

assemble in thermosets which exhibit improved mechanical properties due to toughening, which is dependent of the morphology adopted by the BCP.[170]

Nanoporous membranes have been employed in fuel cells that require membranes with selective permeability, which can be modified by BCP composition. Membranes have also been used for water filtration to remove microplastics (5-100 nm), desalination and as artificial kidneys. This diverse range of property control is obtained by tuning pore size, morphology, stimuli-response, size distribution etc which is only achievable with BCPs.[171]

BCP self-assembly is particularly prominent for use in lithography, as BCPs can obtain smaller feature sizes than current techniques used in industry. For example, Hawker. *et al.* showed that the self-assembly of a cyclic polystyrene-*b*-polyethylene oxide polymer reduces domain size by ~30% compared to its linear analogue due to a reduced hydrodynamic radii.[172] Furthermore, bottom-up BCP lithographic processes are fully compatible with industry standard technologies.[168]

1.4 Characterisation

1.4.1 Small-angle X-ray scattering SAXS

Small-angle X-ray scattering (SAXS) is an accurate and non-destructive analytical technique in which many structural properties of materials can be determined, including; molecular weight, particle structure, microphase structure, domain spacing and dispersity of particles. This presents a wide field of applications, SAXS is particularly useful in polymer and colloid research but also used in biological materials, nanocomposites, food, pharmaceuticals and in quality control. In a typical SAXS set-up, structural information can be resolved in the range of 0.1-5 nm although this can be extended to 100 nm, known as wide-angle x-ray scattering (WAXS).[173]

A SAXS pattern is obtained by recording the X-rays that have been scattered by electrons in a sample, relative to the incident wave. X-rays that are scattered and lose energy become out of phase with the incident wave and as a result are not detected. Occasionally, the oscillation frequency of the electrons matches that of the incident wave, known as Thomson scattering. Consequently, there is no loss of energy during the collision and these constructive waves carry the structural information which are detected in SAXS.[174] All substances will scatter X-rays, therefore, solid or liquid phase materials with solid, liquid or gaseous domains can be examined. However, air also contributes to scattering meaning measurements must be performed in vacuum or a background measurement is subtracted from data, depending on sample stability.[175]

Microscopy and scattering techniques both require the interaction of matter with radiation and a degree of contrast (a difference in electron density between the particles and the continuous medium) to study an object. Despite these similarities, they are complementary techniques due to the method in which data is reconstructed. Microscopy uses lenses to magnify an image, which results in loss of wave phases, whereas scattering investigates the whole illuminated sample volume. X-rays are measured relative to the wavelength of incident radiation. To become independent from wavelength, scattering patterns are often presented as a function of q, where q is the displacement from the incident wave or "scattering vector". Equation 3 illustrates how scattering patterns are often considered in reciprocal space and particles have structure in real space. Hence, why scattering and microscopy techniques are complementary, and both should be used for a more complete characterisation.

$$q = \frac{4\pi}{\lambda}\sin(\theta) \quad (3)$$

Scattering patterns are comprised of two components, the form factor and structure factor. The form factor, *P(q)*, is considered per particle where the distance between particles is larger than the wavelength. The detected waves for each particle can be summed if the sample is dilute and monodisperse (same size and shape particles). This scenario would produce data with sharp minima which represent the particle radius, however, in practical terms, samples size often exhibits a degree of dispersity. The result of this is a broadening of the minima from which the dispersity can be calculated.[176] The structure factor, *S(q)*, is considered when intra- and inter-molecular distances are of the same order of magnitude (i.e. concentrated samples), this additional interference multiplies with the form factor and provides information about particle position with respect to one another. Attractive and repulsive interactions are indicated by an increase or decrease in intensity, respectively. Finally, pronounced peaks form due to highly ordered and crystalline structures. Incorporation of Bragg's law of diffraction into the previous equation presents:

$$q = \frac{2\pi}{d} \quad (4)$$

where *d* is the particle separation or domain size. These peaks in the structure factor occur at well-defined angles, indicative of crystal symmetry and long-range order. Bragg's law can therefore be used to calculate domain spacing, lattice parameters and miller indices and ultimately, morphology.[177]

The ratio of *q*-values of typical structures are:

Lamellar – 1, 2, 3, 4, 5…

Hexagonally packed cylinders[178] – 1, √3, √4, √7, √9…

Cubic – 1, √2, √3, 2, √5…

1.4.2 Atomic Force Microscopy (AFM)

Microscopy techniques give data that is complementary to scattering data, Table 0-1.[175] In both (optical) microscopy and scattering, waves are scattered from an object but the processing step differentiates the information which is extracted. Scattering data records the intensity of scattered waves, whereas microscopy uses a lens to reconstruct the waves as an image (this is the optical method of reconstruction,

scattering data can be processed mathematically to reconstruct an image as well, however, 3D information is lost as phase data is lost when recording data).

Table 0-1. Comparison of information obtained from microscopy and scattering data.

Feature	Microscopy	Scattering
Small details	Visible	Not visible
Results	Unique, not representative	Representative, integrated
Local structure	Extractable	Not extractable
Average structure	Hard to obtain	Always obtained
Preparation artifacts	Inherent	Scarce (in vitro)

Atomic force microscopy (AFM) is a scanning probe technique primarily used to determine topology but is also capable of calculating adhesion, indentation, stiffness, and dissipation etc. In AFM a sample is imaged in either contact mode (which risks tip collision with tall structures), non-contact or tapping mode, (which was used in this thesis), and nanometre resolution is obtainable. During measurements a sharp tip oscillates in the z direction while scanning in the x and y directions, which is monitored by a feedback loop that detects changes in oscillation frequency as the tip interacts with the surface and maintains the distance between tip and sample (set-point). A laser beam is directed at the top of the cantilever and reflected onto a position-sensitive four-segment photo-detector which tracks the position of the laser spot.[179] Compared to electron microscopy techniques, AFM provides 3D information, equipment is much less costly and soft/sensitive samples are measurable as AFM can be used in various environments.

1.5 Objectives

The purpose of this thesis was to synthesise highly amphiphilic (high χ) low molecular weight polymers using controlled copper-RDRP for use in microphase separation. With the specific aim of obtaining small domain sizes, polymers must have low molecular weight, but also have a high Flory-Huggins interaction parameter to compensate for degree of polymerisation. Therefore, a sufficiently hydrophobic alkyl halide initiator was used to synthesise a sufficiently hydrophilic polymer chain, allowing low dispersity and low molecular weight to be obtained. Polymer films were prepared (and annealed) then Small-angle X-ray scattering measurements determined morphology and domain size.

Beyond this, an investigation into the phase behaviour of these low molecular weight polymers was undertaken and an experimental phase diagram was created, which allows specific morphology/domain size targeting. Additional hydrophilic monomers and hydrophobic initiators were investigated for this specific approach to microphase separation, which include the incorporation of photo-responsive behaviour to add functionality to the phase-separated films.

Overall, this work shows a novel approach - by which the initiator has a significant role and should be considered in all polymerisations - to obtaining the smallest domain sizes possible in block copolymer microphase separation.

Chapter 2: Fluorinated initiator for microphase separation

Contents

In this chapter, the concept of using an initiator to influence microphase separation has been investigated. To achieve microphase separation, three factors need to be considered: the Flory-Huggins interaction parameter, χ, the molecular weight, N, and the volume fraction of each block, f_A/f_B. Modifying these allows the tuning of morphology and domain spacing. The minimisation of domain spacing has been pushed by the microelectronics industry, which is achieved by maximising χ, and minimising N. High χ is obtained by combining highly incompatible polymer blocks and low N is obtained by incorporation of an initiator that consists of the first block in an amphiphilic polymer. Small-angle X-ray scattering (SAXS) was used to characterise morphology and domain spacing in polymer films, corroborated by atomic force microscopy (AFM) images.

2.1 Fluorinated initiator

2.1.1 Synthesis

The self-assembly of block copolymer materials has often been exploited to decrease the lower size limit of microphase separation and obtain the smallest separations between similar domains. Here a so-called "*pseudo-block*" polymerisation strategy was used in which a novel, highly fluorinated, hydrophobic initiator was used as one segment (Figure 2-1). Fluorocarbons are incredibly hydrophobic and have been used extensively due to this attractive property.[180] Therefore, a fluorinated segment combined with a highly hydrophilic repeating unit should generate a highly amphiphilic polymer. It was hoped that the χ parameter is high enough to allow microphase separation to be observed with polymers of very low molecular weight. It has been predicted in the literature that the combination of a fluorinated block with a highly polar block could allow domain spacings as small as 2 nm.[93]

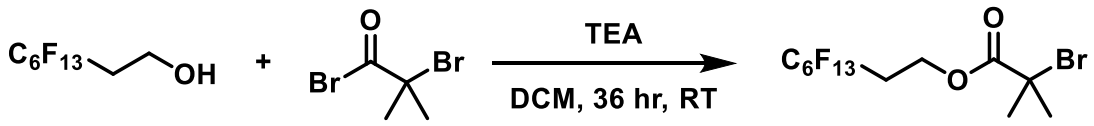

Figure 2-1. Synthesis of a fluorinated initiator, perfluorooctyl bromoisobutyrate (F_{13}).

Perfluorooctanol (PFO-OH) was chosen as a suitable starting material for the synthesis of a fluorinated initiator due to its' ready availability and low price, especially when compared with longer-chain fluorinated relatives. The two methylene units decouple the electronic effects of the electron withdrawing CF_2 groups from the oxygen atom, leading to reactivity resembling an alkyl alcohol, such as ethanol. PFO-OH was reacted with bromoisobutyryl bromide (BiB) to give the desired product in good yield (78%), from a simple esterification reaction adapted for hydrophobic initiators.[181] ^{1}H NMR characterisation data are given in Figure A 2-1 and Figure A 2-2 for both starting materials (BiB and PFO-OH). The fluorinated initiator, perfluorooctyl bromosiobutyrate (F_{13}), was characterised by nuclear magnetic resonance (NMR) spectroscopy, including ^{1}H, ^{13}C & ^{19}F NMR which are discussed herein.

2.1.2 NMR Characterisation

2.1.2.1 ^{1}H NMR

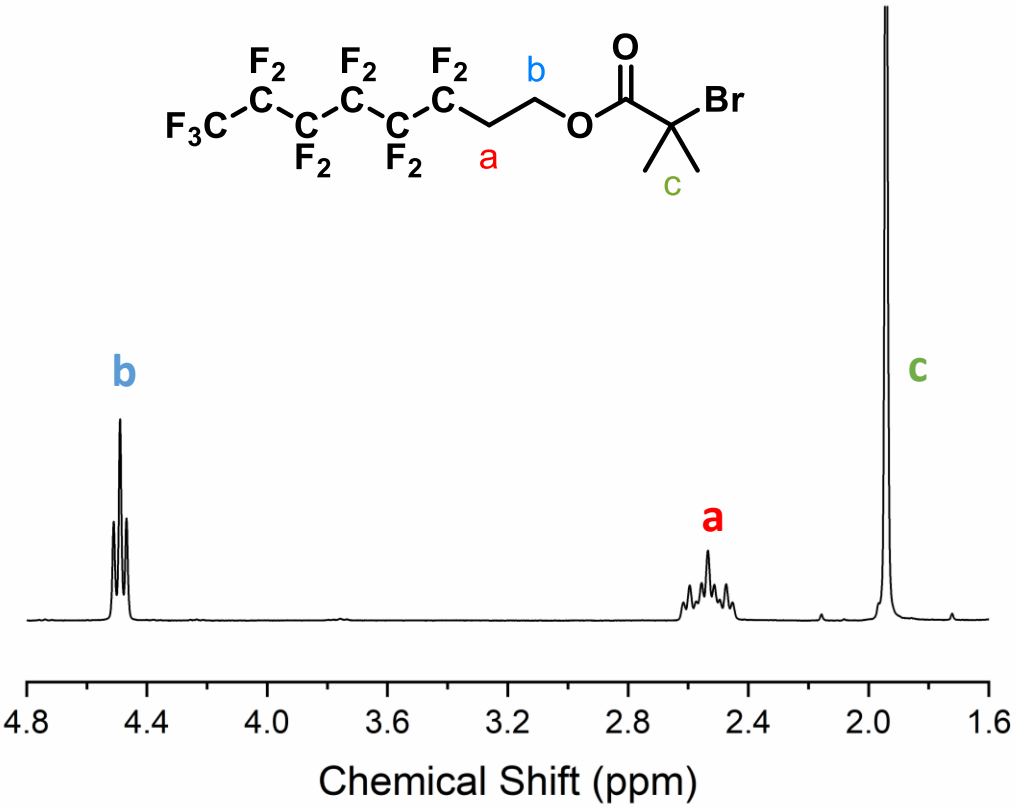

Figure 2-2. ^{1}H NMR spectrum of F_{13} in $CDCl_3$.

The assignment for the proton NMR spectrum of F_{13} is straightforward as there are only 3 different proton environments, labelled as (a), (b) and (c) (Figure 2-2). Environment (a) shows an interesting splitting pattern of a tt, exhibiting $^{3}J_{HH}$ and $^{3}J_{FH}$ coupling constants, calculated to be 6.3 Hz and 18.2 Hz respectively. The coupling constant for triplet (b) is 6.4 Hz, very close to the $^{3}J_{HH}$ coupling in (a). A full expansion of the spectrum including peak positions and relative integrals is given in Figure A 2-3. The proton spectrum shows the product is highly pure as no peaks related to impurities are evident. Although supplementary, further confirmation of these assignments is given in COSY NMR (Figure A 2-4) which shows the coupling between the two CH_2 groups.

2.1.2.2 ^{13}C NMR

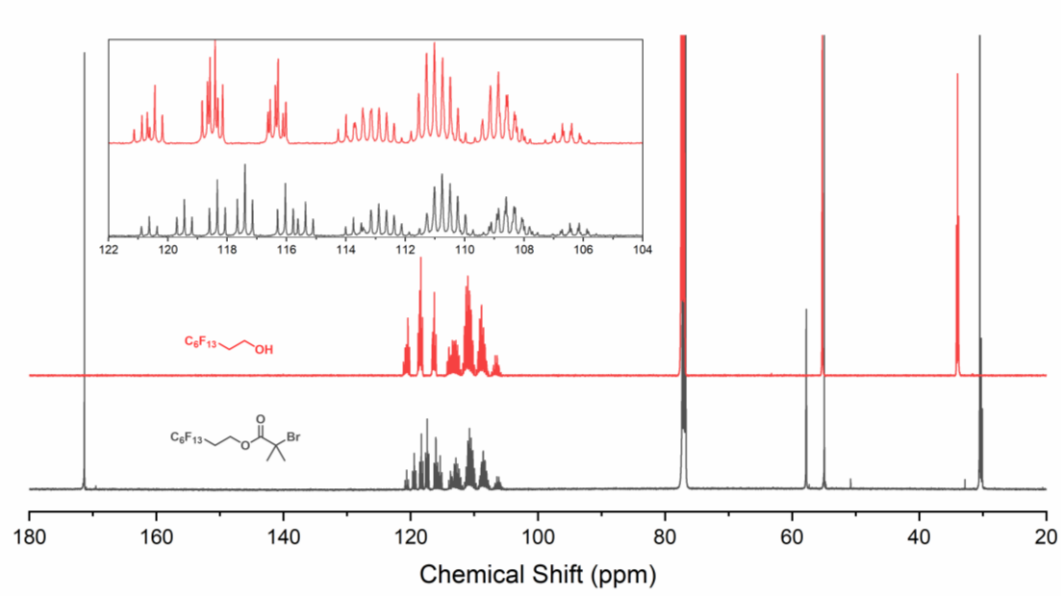

Figure 2-3. ^{13}C NMR (inverse-gated) spectra of PFO-OH and F_{13} in $CDCl_3$. Inset shows expansion of chemical shift values 122 to 104 ppm.

^{13}C NMR was necessary to provide an indication of the length of the fluorinated carbon chain. An inverse-gated-decoupled spectrum gives more quantitative integration values[182] and therefore the chain length can be estimated. Figure 2-3 shows the ^{13}C spectra for both PFO-OH and F_{13} as their comparison makes assignment much simpler, Figure A 2-5. The expected peak multiplicity for the CH_2-O environment is a singlet due to decoupling of $^2J_{CH}$, which initially makes the singlet at 55.0 ppm a likely assignment. However, when compared to the ^{13}C spectrum for PFO-OH, this singlet is not present. As a result, the CH_2-O peak can be assigned to the weak triplet at 57.8 ppm, which is also present in the PFO-OH spectrum. This assignment was corroborated in the HSQC spectrum, Figure A 2-6. This splitting pattern is associated with an exhibited $^3J_{CF}$ coupling of 4.5 Hz. The remaining simple assignments include the singlet C=O at 171.3 ppm, singlet C-Br at 55.0 ppm and the triplet CH_2CF_2 at 30.3 ppm with a $^2J_{CF}$ coupling of 21.1 Hz, also seen in the PFO-OH spectrum. Integration also helped assign the singlet at 30.5 ppm to $(CH_3)_2$ which is the only environment to contain more than one carbon.

The remaining, unassigned, peaks in the region of 122 to 104 ppm include more than 60 individual peaks. This complexity is a result of numerous carbon-fluorine couplings, consequently efforts have been made to predict the spectra and coupling constants.[183] It is integration of this region that gives an indication of the fluoro-alkyl chain length.

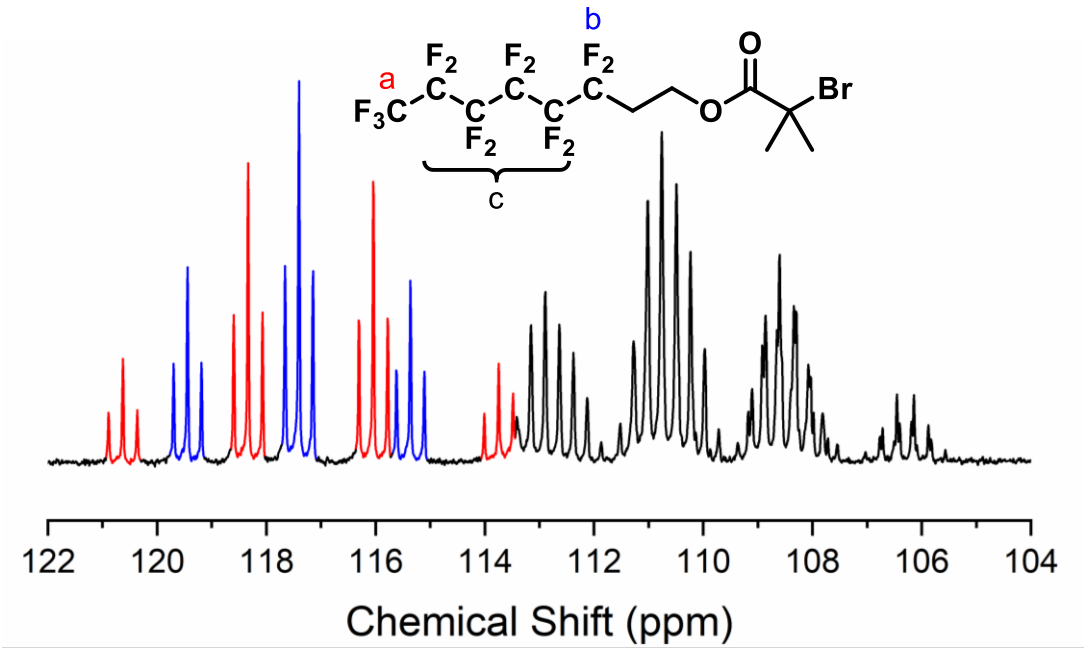

Figure 2-4. ^{13}C NMR of F_{13} from 122 to 104 ppm, showing splitting from carbon-fluorine coupling.

Decoupling from fluorine and hydrogen could not be carried out simultaneously, meaning that $^{2}J_{CF}$ coupling to CF_2 groups materialises as many overlapping triplets. Despite this, some assignments can be made and Figure 2-4 shows a higher magnification section of the spectrum. Highlighted in blue and red are two distinct splitting patterns that are distinguishable from the remaining carbon environments, regardless of overlapping splitting. Firstly, environment (a)/(red) is a quartet of triplets. The quartet nature signifies that this peak must be caused by either the 7th or 8th carbon (counting from the ester group), because it must be either adjacent or directly bonded to three fluorine atoms. By examining the coupling constants, the correct environment can be determined. The most common carbon-fluorine coupling constants are in the ranges of: $^{1}J_{CF}$ = 250 – 300 Hz, $^{2}J_{CF}$ = 20 – 40 Hz, $^{3}J_{CF}$ = 1 – 10 Hz, $^{4}J_{CF}$ = 0 – 2 Hz, however, there are many cases outside these ranges and where 4-bond coupling is larger than the 3-bond, which also has a strong dependence on the CCCF dihedral angle.[184,185] The coupling constants for the quartet of triplets were calculated at J_{CF} = 288 Hz for the quartet and 33 Hz for the triplet. This makes it clear the 288 Hz is a 1-bond C-F coupling, and due to the quartet splitting, the 8th carbon must be responsible. This same logic suggests a triplet of triplets multiplicity for environment (b)/(blue), of which the coupling constants are $^{1}J_{CF}$ = 257 and $^{2}J_{CF}$ = 32 Hz. In addition, the only notable differences in the peaks between F_{13} and PFO-OH for the CF_2 carbons occur in the triplet of triplets (inset Figure 2-3), this is sensible as (b) is the closest fluorocarbon to the alcohol which changes its electronic structure

when converted to the ester. The 4 CF_2 groups lie in between an overlapping mixture of multiplets ((c)/(black)) and are therefore unassignable, due to numerous $^1J_{CF}$ and $^2J_{CF}$ couplings.

2.1.2.3 ^{19}F NMR

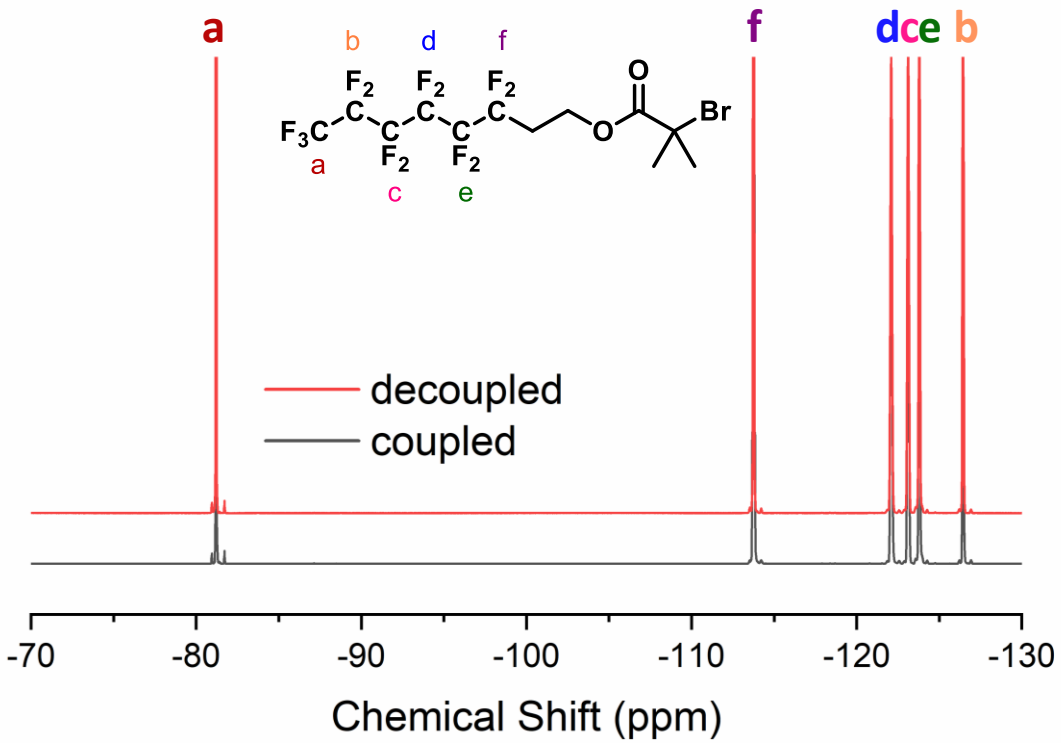

Figure 2-5. ^{19} F NMR spectra of F_{13} with both coupling and decoupling from $^3J_{FH}$.

^{19}F NMR also provided useful information for characterising F_{13}, these spectra are decoupled from $^2J_{FF}$ couplings with the additional option of decoupling from $^3J_{FH}$, both of which are shown in Figure 2-5. The most obvious feature is the presence of 6 individual peaks, which implies 6 separate fluorine environments. This agrees with the desired structure shown schematically in the inset. Although ^{19}F NMR is highly sensitive and spectra can be integrated, it should be treated with caution. CF_2 units tend to integrate well but CF_3 units often integrate to a relative 2.3 (rather than 3), due to the wide spectral range of fluorine NMR. ^{1}H NMR is inherently quantitative, however, ^{19}F requires careful control of many parameters e.g. equal excitation for all signals, optimisation of data processing and use of a suitable standard reference.[186,187] All (relative) integrals are 2, other than the peak at -81.2 which is 2.3 and signifies the CF_3, fully integrated spectra are given in Figure A 2-7.

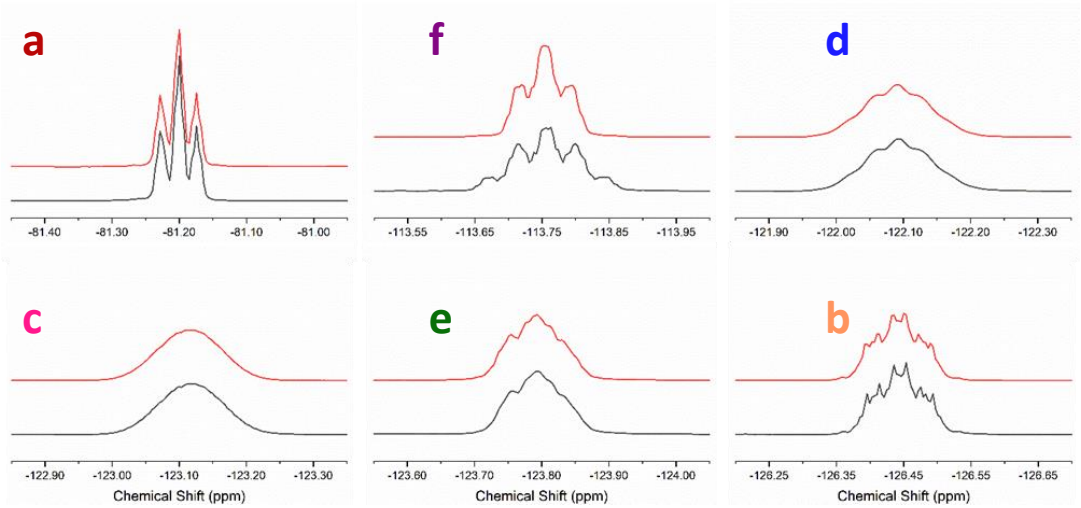

Figure 2-6. Expansion of each peak in the ^{19}F NMR spectra shown in Figure 2-5. Letter labels indicate the fluorine environments depicted in Figure 2-5. Red shows decoupled and black shows the coupled spectrum to hydrogen.

Expanded views of the peak fine structure are shown in Figure 2-6. The ppm range for peak (a) is consistent with that expected for the CF_3 group,[188] and the prominent triplet structure is caused by the single neighbouring CF_2 group. Peak (f) is the only peak which shows differences when coupled or decoupled from $^3J_{FH}$; therefore, the responsible carbon is the one adjacent the CH_2. Peaks (d), (c) and (e) are much broader as a result of many $^3J_{FF}$ couplings, and probably $^4J_{FF}$ as well. The exact assignments of these three peaks were made with help from the full characterisation of PFO-OH, which uses 2D correlations to inform peak assignment.[189] Finally, peak (b) differs from the triplet-like multiplicity seen in the fine structure of the other peaks. This is because the environment responsible for this peak is the CF_2 adjacent the CF_3, so $^3J_{FF}$ induces quartet fine structure as well as triplet structure from the other adjacent CF_2.

2.2 Polymer synthesis

2.2.1 Polymerisation of *tert*-butyl acrylate (F_{13}-P*t*BA$_m$)

2.2.1.1 Synthesis and NMR

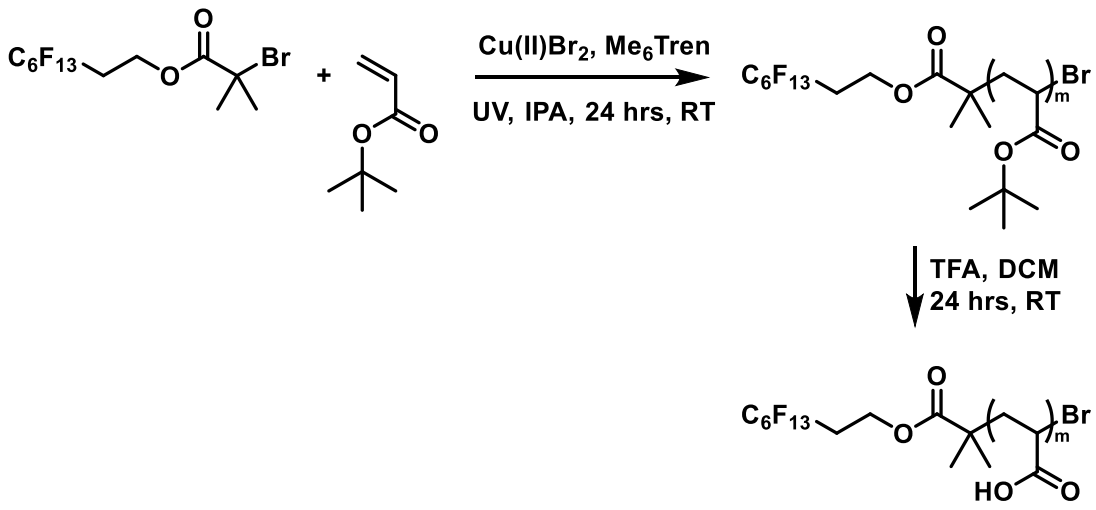

Figure 2-7. Synthesis of F_{13}-P*t*BA$_m$ polymers.

F_{13} was tested for its efficacy by polymerising methyl acrylate (MA) using a photo-induced Cu(II)-RDRP system in DMSO. High conversions, good end-group fidelity, predictable molecular weights and low dispersities for a range of molecular weights (Figure A 2-8) were observed. This proved that the presence of fluorine does not hinder polymerisation hence a series of low molecular weight poly(*tert*-butyl acrylate) (P*t*BA) polymers were polymerised from F_{13} (F_{13}-P*t*BA$_m$) followed by deprotection to poly(acrylic acid) (F_{13}-PAA$_m$). Poly(acrylic acid) was used as the highly polar repeat unit for the second block as it is hydrophilic (in contrast to a fluorocarbon chain), can be easily deprotected from *t*BA,[190] has been used widely in polymer self-assembly and is suitable for microphase separation in bulk.[191–193] Directly polymerising acrylic acid was not possible due to the complications associated with an amine based catalytic complex.[194] A set of EBiB-initiated polymers were synthesised for comparison to a polymers with no fluorinated segment, referred to as F_0-PAA$_m$.

Table 2-1. Molecular weight characteristics of F_{13}-PAA_m polymers. GPC was conducted on the precursor F_{13}-P*t*BA_m polymers.

Sample[a]	N[b]	$M_{n,\,GPC}$ (g mol^{-1})[c]	$Đ_{GPC}$[d]	$M_{n,\,NMR.}$ (g mol^{-1})[e]	$M_{n,\,MALDI}$ (g mol^{-1})
F_{13}-PAA_4	9	1400	1.08	801	741
F_{13}-PAA_5	10	1450	1.06	873	N/A
F_{13}-PAA_6	11	1400	1.09	945	848
F_{13}-PAA_9	14	1900	1.11	1162	978
F_{13}-PAA_{11}	16	1950	1.10	1306	1317
F_{13}-PAA_{15}	20	2650	1.08	1594	N/A
F_{13}-PAA_{18}	23	3400	1.10	1810	1744
F_{13}-PAA_{25}	30	4300	1.13	2515	2097

[a] Degree of polymerization calculated from F_{13}-P*t*BA_m (^{1}H NMR). [b] N = total degree of polymerisation (see section 5.3.1 in Experimental, Methods & Calculations). [c] THF GPC of F_{13}-P*t*BA_m against poly(methyl methacrylate) standards. [d] Dispersity calculated from GPC of F_{13}-P*t*BAm in THF. [e] $M_{n,\,NMR}$ calculated from N_{NMR} values.

DMSO is a popular solvent for Cu(II)-RDRP, as short reaction times are possible and a wide variety of monomers and Cu(II)Br_2 are soluble therein. The Cu(II)-RDRP photoinduced synthesis of F_{13}-P*t*BA_m was carried out in isopropanol (IPA) rather than DMSO, to prevent problems associated with the biphasic system formed upon polymerisation of *t*BA.[195] These polymerisations required 24 hours in IPA at room temperature and proceeded with high monomer conversions (all >99 %) yielding products with low dispersities (1.06-1.13) (Table 2-1). The low dispersities are inherent to this process, as there is no need for sequential monomer addition. A range of molecular weights were synthesised, aiming for the lowest possible degree of polymerisation (DP) to aim for the smallest achievable domain spacing. As the fluorine block length is constant, the acrylic acid volume fraction (f_{AA}) increases with molecular weight and an accompanying change in morphology is expected. DP was calculated by integrating the peak for *tert*-butyl in the repeat unit and comparing to the peak of the dimethyl group in the initiator. Conversion was calculated by comparing the integral of the *tert*-butyl peak to the unreacted monomer vinyl peaks (NMR spectra of F_{13}-P*t*BA_mwere obtained in $CDCl_3$, Figure A 2-9).

2.2.1.2 Gel Permeation Chromatography (GPC)

GPC was performed in THF (rather than $CHCl_3$) due to issues with the similarity of the refractive indices of solvent and analyte. Fluorocarbons have low refractive indices[196] e.g. poly(tetrafluoroethene) = 1.35, perfluorohexane = 1.25, perfluorooctane = 1.28 and $CHCl_3$[197] has an RI of 1.45. This manifests as the unusual

situation where lower molecular weight F_{13}-P*t*BA$_m$ polymers (which have higher fluorocarbon content) exhibit a negative RI trace (Figure 2-8). Polymers with a smaller fluorocarbon content (higher P*t*BA content) give positive RI traces, molecular weights in the mid-range show regions of positive and negative RI in the same trace, which precludes dispersity and molecular weight calculations. For these reasons, THF was used as a GPC solvent as it allowed consistent measurement of dispersity and molecular weight. GPC traces in THF showed positive monomodal distributions with no shouldering or tailing, the presence of which would indicate initiator inefficiency (Figure A 2-10).

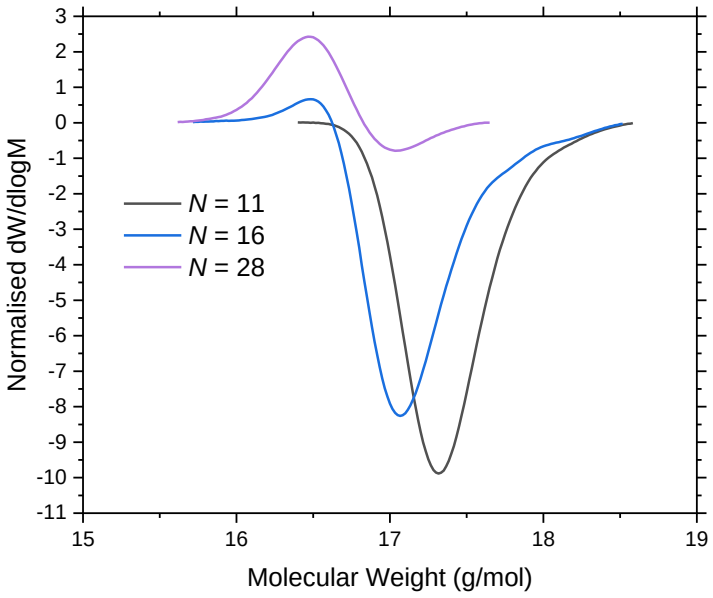

Figure 2-8. Refractive index traces in GPC for F_{13}-P*t*BA$_m$ polymers in $CHCl_3$.

2.2.2 Synthesis and characterisation of poly(acrylic acid) (F_{13}-PAA$_m$)

2.2.2.1 Synthesis and NMR

F_{13}-P*t*BA$_m$ polymers were "deprotected" using trifluoroacetic acid (TFA) in DCM to give poly(acrylic acid) (F_{13}-PAA$_m$) (Figure 2-7). Precipitation was not viable for purification as these polymers are highly amphiphilic after deprotection, therefore solvents in which both blocks are immiscible are rare. The reduction in molecular weight (due to the loss to the *tert*-butyl group in the deprotection step), further improves their solubility to the detriment of precipitation. Most of the TFA was removed by rotary evaporation, then portions of acetone were repeatedly added to

remove residual TFA as an azeotrope. The polymers began to precipitate as TFA was removed/replaced but became swollen in the presence of acetone. Portions of acetone were used to rinse out any impurities and the polymer was finally dried in a vacuum oven, resulting in a white solid. ^{1}H NMR spectra of the product lacked a *tert*-butyl peak confirming the deprotection was complete (Figure 2-9). For clarity, the DP was calculated before the deprotection step due to no appropriate protons being present after deprotection. Further ^{1}H NMR spectra were only used to confirm the attachment of the fluorinated segment (presence of methylene units) to the deprotected poly(acrylic acid).

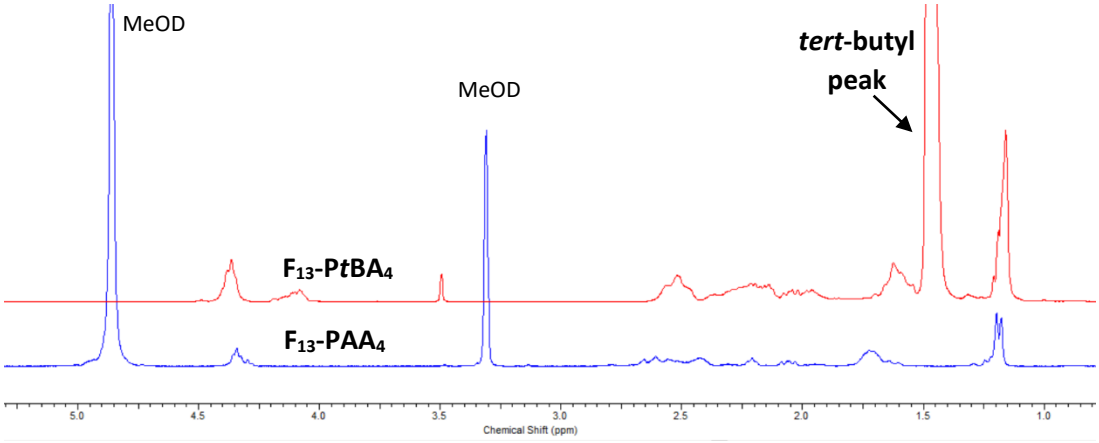

Figure 2-9. ^{1}H NMR comparison of F_{13}-P*t*BA_4 (in $CDCl_3$) and F_{13}-PAA_4 (in MeOD).

GPC analysis was not successfully performed for the F_{13}-PAA_m polymers, as these samples failed to elute correctly in both THF and DMF solvents. This was attributed to high amphiphilicity and low molecular weight, which could easily result in unwanted self-assembly or poor dissolution. The use of a column with unsuitable pore size (column size C) would produce less accurate data for objects of this size.

2.2.2.2 MALDI-ToF-MS

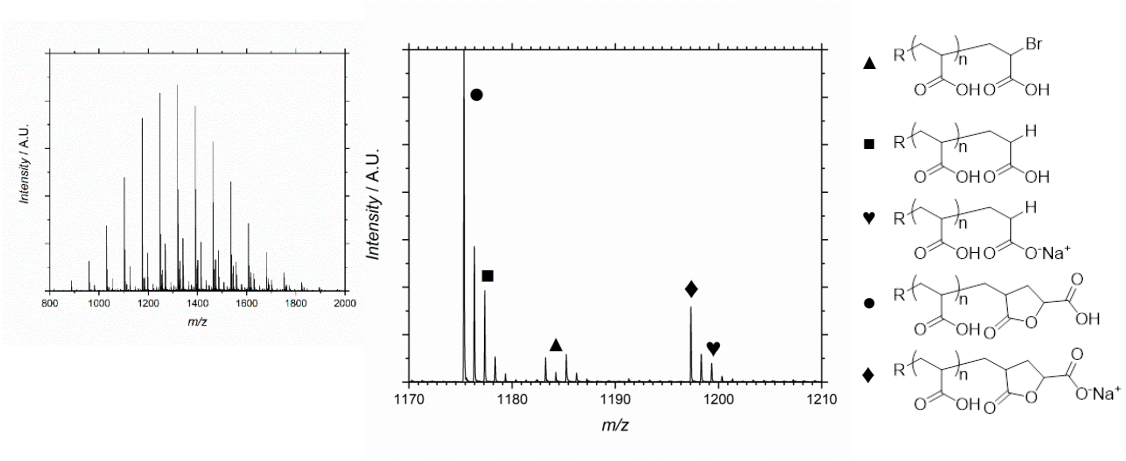

Figure 2-10. MALDI-ToF-MS spectrum of F_{13}-PAA_{11}. Left = full spectrum, centre = expanded region, right = end group key.

Matrix-assisted laser desorption/ionisation time of flight mass spectrometry (MALDI-ToF-MS) is a soft ionisation mass spectrometry technique which was used to reinforce structural characterisation. All spectra show a repeat unit mass of 72 g mol^{-1}, consistent with an acrylic acid repeat unit. Multiple distributions of end group masses were present in the data (example Figure 2-10, other polymer spectra given in Figure A2-12 - Figure A2-17) and are consistent with the loss of bromine as might be expected with the conditions used in the deprotection chemistry. Bromine must be lost after polymerisation, but during the deprotection step, because these polymers have narrow weight distributions and no tailing, meaning that end group exchange must occur after polymerisation. The most abundant distribution cluster shows loss of HBr which usually leads to a vinyl end group. In the current understanding of this polymerisation route, there are no plausible reaction pathways to achieve this. Alternatively, cyclisation may occur during the deprotection step (Figure 2-11).[194] Residual TFA could, indeed, continue to deprotonate acrylic acid units and promote this cyclisation and lead to elimination of HBr. Rigidity of polymer chains would be expected to increase, which is more important at lower molecular weights. In this case we can consider hydrogen bonding between lactone rings; it is thought that microphase separation phenomena are minimally affected by chain rigidity.[198] The remaining distributions most likely result from impurities induced during sample preparation; addition of NaI enables carboxylic acid proton exchange (adding 1 or more sodium acrylate units) and is not representative of the synthesised sample. M_n and $Đ$ were also calculated from MALDI spectra (using the highest intensity peaks (Table 2-1)) but were used only to confirm the success of the synthesis. Both GPC and

^{1}H NMR were found to be unreliable for pAA quantification, and MALDI is known to underestimate molecular weight due to varying ionisation efficiencies. With these caveats, MALDI-ToF-MS has been shown to give reliable values for polymers of low dispersity and low *N*.[199]

Figure 2-11. Suggested end group cyclisation route results in loss of 'HBr'.

2.2.2.3 Differential Scanning Colorimetry (DSC)

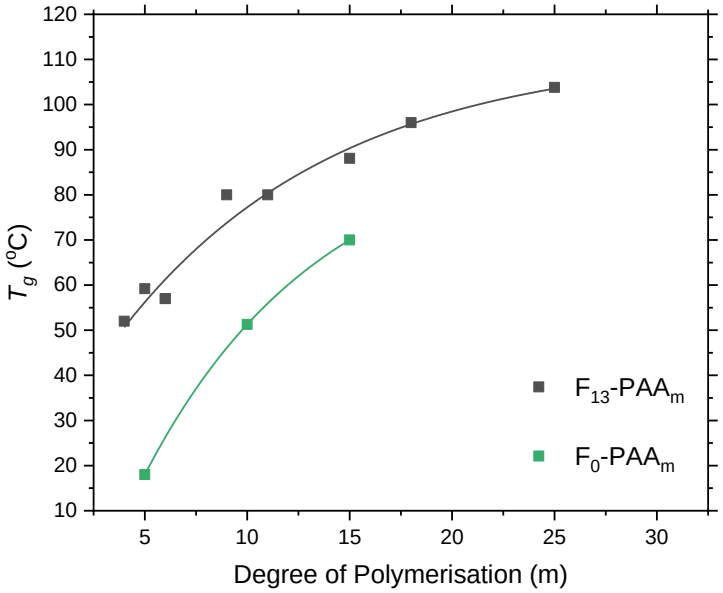

Figure 2-12. T_g for F_n-PAA_m determined by DSC.

Differential scanning calorimetry (DSC) is a thermal analysis technique used to determine thermal transitions (T_g and T_m) of polymers. The difference in energy required to maintain constant temperature (of an empty pan and one with sample) is measured, revealing T_g's as slopes and T_m/T_c as peaks or troughs. All traces (Figure A) showed no T_m or T_c and 1 T_g for each polymer which is unusual. Block copolymers are expected to exhibit a T_g for each block and although the formal synthetic route of these polymers is the same for producing homopolymers, they are expected to behave

as low molecular weight block copolymers. The trend in T_g with N (Figure 2-12) shows logarithmic growth, which agrees with the Flory-Fox equation,[200] below:

$$T_g = T_{g,\infty} - \frac{K}{M_n} \quad (1)$$

Here, $T_{g,\infty}$ is the theoretical glass transition temperature at infinite molecular weight and K is an empirical parameter related to the free volume in the polymer sample. Chain ends hold greater free volume than backbone units therefore a higher molecular weight polymer (higher backbone unit to chain end ratio) exhibits a smaller free volume and a higher T_g.

2.2.2.4 Thermogravimetric Analysis (TGA)

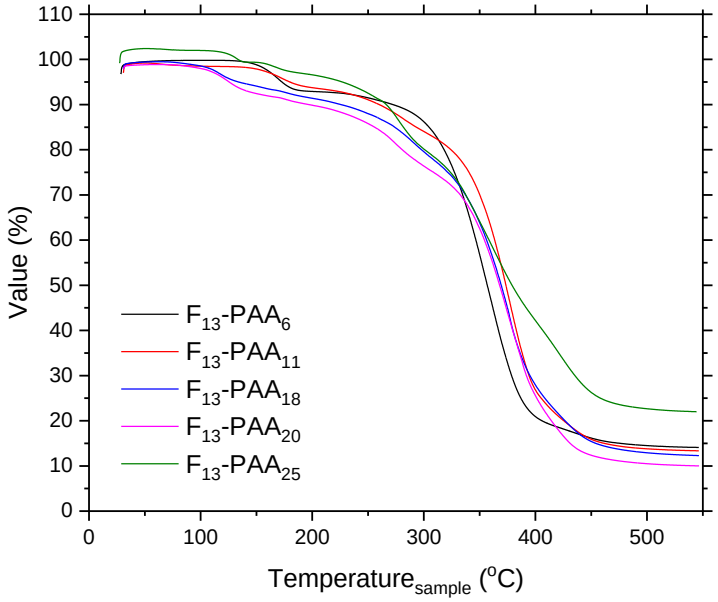

Figure 2-13. TGA traces for F_{13}-PAA_m.

Thermogravimetric analysis (TGA) is an analytical technique which records mass as a function of temperature and provides information about purity, composition, thermal stability, and degradation temperature. TGA data for F_{13}-PAA_m polymers are shown in Figure 2-13, all give a similar profile with a large mass loss at ~320 °C. There are multiple, smaller, mass losses at lower temperatures suggesting that alternative degradation pathways produce other small molecules (as these polymers were

purified well). The F_{13}-PAA_m isotherms show similar features to those in literature, in which the degradation pathways were corroborated by FTIR.[201] In this study the behaviour is divided into three stages, the first (70-142 °C) is accompanied by a 2.5% mass loss which is mostly attributed to the loss of water but also anhydride formation and release of residual acrylic acid monomer (however no acrylic acid monomer peaks were present in ^{1}H NMR spectra for F_{13}-PAA_m polymers). The second stage (142-335 °C) is accompanied by a mass loss of 27.4% and likely due to loss of acrylic acid, CH_4 and CO_2, which is reflective of the anhydride formation and intermediate species which lead to ketones, ketenes and unsaturated compounds.[202] In another study, Mg^{2+}/Ca^{2+} poly(acrylic acid) salts were shown to produce CO_2 and acetone as major thermal degradation products.[203] The third stage (335 °C and above) is accompanied by a mass loss of 55.2% which represents depolymerisation, leaving a residual carbon residue of 14.9%. These features are all present in Figure 2-13, implying that the small mass losses are due to degradation of poly(acrylic acid) rather than presence of impurities. Also, poly(tetrafluoroethene) thermally degrades above 400 °C which suggests that the fluorinated moiety in F_{13}-PAA_m remains stable.

2.2.2.5 Dynamic Mechanical Analysis (DMA)

Dynamic mechanical analysis (DMA) is a further thermal analysis technique in which T_g can be observed. Here, the viscoelastic properties of polymers are examined by applying a sinusoidal stress and measuring the resulting strain. In viscoelastic materials, stress (σ) can lag behind strain (e) by a varying amount. Purely elastic materials, for example, have an immediately measurable response as both stress and strain are in phase. Purely viscous materials, in contrast, have a 90° out-of-phase lag of stress. Stress can be considered to be comprised of two components, an elastic component, $\sigma\cos\delta$ (storage modulus) and a viscous component, $\sigma\sin\delta$ (loss modulus).[204] These two components can be combined to give $\tan\delta$, which gives the degree of phase lag in a viscoelastic material i.e. $\tan\delta > 1$ has dominating viscous properties. When recording a temperature sweep, T_g causes a large increase in viscosity and is observed by a peak in loss modulus, which reflects an increase in $\tan\delta$.

DMA can also exploit the frequency dependence of stress and strain, by measuring a frequency sweep. Here, the change in storage modulus results in a change in tanδ. The storage modulus is high at higher frequencies as there is less time for uncoiling/rotation of the main chain and the material exhibits glassy behaviour. At lower frequencies the storage modulus is low as chains have more time to rearrange, showing rubbery behaviour. When the test frequency matches the natural frequency

of the main chain rotations in the material, the phase lag is strongest and indicates T_g. Not only do polymers display main chain rotations, but side chains and end groups also produce their own frequency, known as secondary transitions. These transitions often occur at lower temperatures and lower intensity than the glass transition.[205] The ability to distinguish these frequencies makes DMA a powerful method for polymer characterisation and has the potential to show the change from an ordered microphase-separated phase to a homogeneous state.[206]

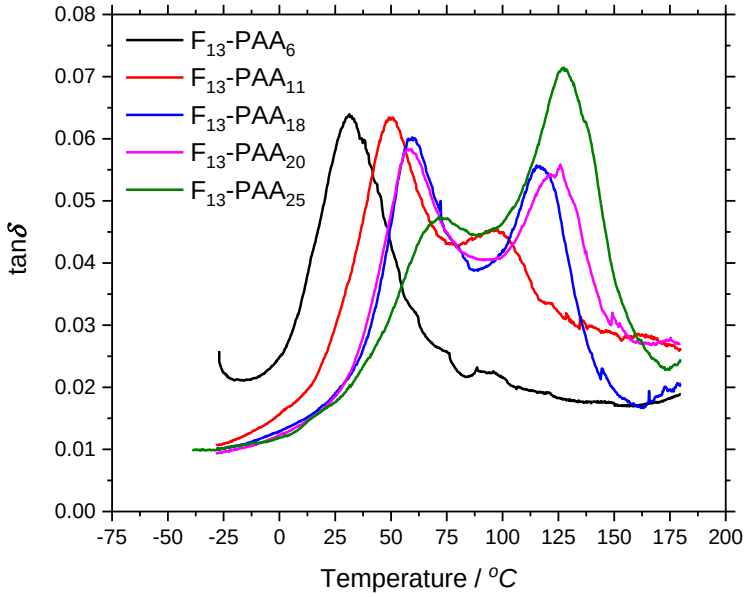

Figure 2-14. tanδ data from DMA for F_{13}-PAA_m.

F_{13}-PAA_m polymers were heated from -30 to 180 °C (Figure 2-14) and DMA data shows two peaks in tanδ (storage modulus and loss modulus shown in Figure A - Figure A2-20). Due to the block-like structure of these polymers, the two peaks are assigned to the T_g of each block. The first peak (lower temperature) is assigned to the discrete fluorocarbon block because the initiator is a liquid at room temperature and has a melting point lower than the T_g of poly(acrylic acid).[207] Also, the relative intensity of this peak to the second decreases with increasing molecular weight/block length, a direct result of increasing viscosity in the second (acrylic acid) block. This further supports assignment of the first peak to the fluorinated block. Following this notion, a homopolymer (e.g. F_{13}-PAA_{100}) should not show this first peak unless it could be considered a secondary interaction. If this were true, the free volume of the lower DP polymers must be more dominant than the frequency of main chain rotation. This may explain why DSC data showed only 1 peak per polymer, as they

were treated as homopolymers. The first peak gradually shifts to higher temperatures with DP which suggests mixing of phases; peak position should not change if the block does not change or was fully segregated from the other.

2.2.3 Poly(sodium acrylate) (F_{13}-$PNaA_{25}$)

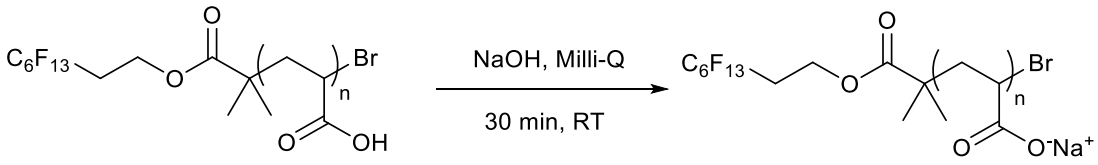

Sinturel *et al.* investigated the requirements for theoretically achieving the smallest possible domain size, concluding that the combination of a fluorinated block and a highly ionic block could achieve this.[93] Inspired by this proposition, poly(acrylic acid) was neutralised to the ionic poly(sodium acrylate) with the prospect of increasing χ. F_{13}-PAA_{25} was dissolved in Milli-Q water, followed by dropwise addition of $NaOH_{(aq)}$ for 30 mins at room temperature. The resulting solution was dialysed and freeze dried to produce a white solid. Poly(sodium acrylate) was not polymerised directly due to increased reaction time, low conversion and poor dispersity.[208,209]

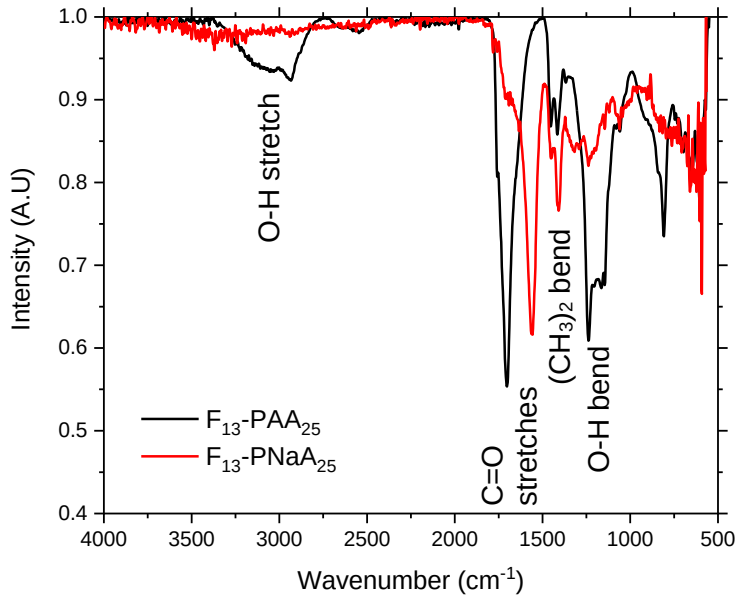

Figure 2-15. FT-IR spectra of F_{13}-PAA_{25} and F_{13}-$PNaA_{25}$.

Figure 2-15 shows the FT-IR spectra of both F_{13}-PAA_{25} and F_{13}-$PNaA_{25}$. The broad peak at 3056 cm^{-1} shows the O-H stretch in F_{13}-PAA_{25}, which is not present in F_{13}-

$PNaA_{25}$ (nor O-H bend) and indicates full conversion. The change in wavenumber of the carbonyl stretch from 1703 cm^{-1} to 1560 cm^{-1} with neutralisation indicates a change of vibration in that bond. Carboxylate ions have a negative charge which is delocalised across the double bond and forms a resonance structure, which decreases the double bond character and agrees with a decrease in wavenumber.[210]

SAXS measurements were performed on F_{13}-PAA_{25} and F_{13}-$PNaA_{25}$ after both solvent and thermal annealing (Figure 2-16). F_{13}-$PNaA_{25}$ showed a smaller domain size than F_{13}-PAA_{25} for both annealing types which indicate stronger segregation between domains and is corroborated by the higher intensity principal peaks. For both polymers, there was an increase in domain spacing when thermal annealing compared to solvent annealing, these data are shown in Table 2-2. There was no presence of higher order peaks, suggesting no change (or formation) in morphology (full SAXS profile (q = 0 – 1.8) shown in Figure A2-21). Poly(sodium acrylate) was not studied further as the differences in data were not thought to be of importance for this study.

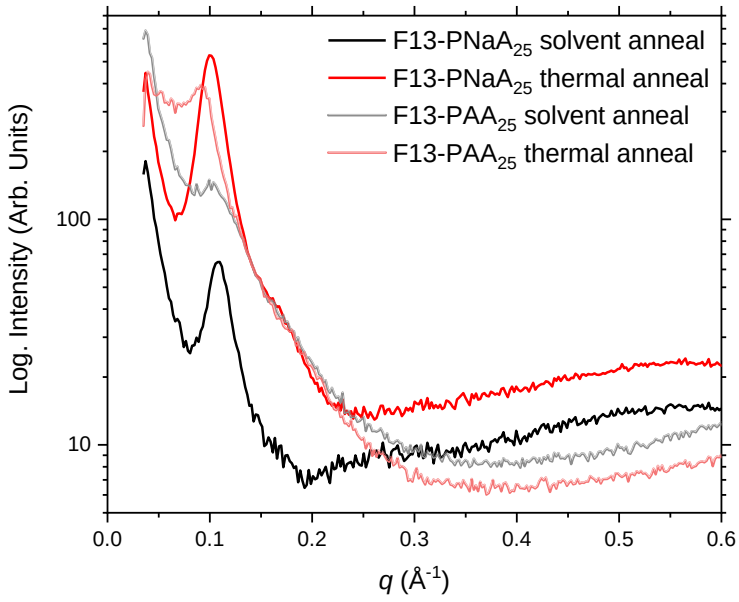

Figure 2-16. SAXS profiles for F_{13}-PAA_{25} and F_{13}-$PNaA_{25}$, prepared by solvent and thermal annealing.

Table 2-2. Scattering vector and domain spacing of solvent and thermal anneal samples for F_{13}-PAA_{25} and F_{13}-$PNaA_{25}$.

Polymer	Scattering vector (solvent) ($Å^{-1}$)	Domain spacing (solvent) (nm)	Scattering vector (thermal) ($Å^{-1}$)	Domain spacing (thermal) (nm)
F_{13}-PAA_{25}	0.099	6.4	0.091	6.9
F_{13}-$PNaA_{25}$	0.110	5.7	0.099	6.4

2.3 Polymer self-assembly

2.3.1 Annealing

Bulk polymer samples may exist in an unwanted amorphous or crystalline state, so annealing may be required to induce microphase separation. This can be achieved either by thermal annealing (to reach thermodynamic equilibrium), or the same samples may be annealed under alternative conditions to obtain alternative kinetically trapped morphologies.[133] One example of this is solvent vapour annealing in which solvent type, concentration and evaporation rate are important factors which all influence the microphase separation process. The ultimate goal is to obtain a defect-free, single grain morphology (long range order), highlighting the importance of the annealing process and understanding the factors that influence microphase separation. long range order is obtained by removed grain boundaries, formed by slow coarsening kinetics that can prevail over a thermodynamic driving force. A block copolymer's ability to produce a defect-free structure is given by the coarseness of the template and the degree of coupling between the template and block copolymer.[130]

2.3.1.1 Solvent vapour annealing

F_{13}-PAA_m polymers were dissolved in a solvent in which both segments are soluble, (methanol and THF are suitable) to prevent self-assembly before the solvent evaporation process, and to prevent preferential swelling of one of the blocks which can lead to morphologies away from thermal equilibrium. 3 ml of saturated polymer solution was left in a PTFE boat inside a sealed solvent vapour environment (same solvent type as the polymer solution) to slow the evaporation rate. This allowed the polymer to reorganise into a low energy conformation (microphase separated) and produces a thick film of polymer (ca. 250 microns).

2.3.1.2 Thermal annealing

Thermal annealing involved heating the polymer films in a controlled manner and allowing it to cool. Heating above the polymers T_g provides energy and mobility for polymer chains to reorganise in its rubbery state.[211] F_{13}-PAA_m solvent vapour annealed

films were heated to 120 °C for 24 hours then cooled to room temperature, trapping the polymer in a low energy conformation. Generally, thermal annealing is preferred to solvent annealing as variables such as evaporation rate, solvent concentration, solvent type/selectivity are mitigated.

2.4 Small-angle X-ray scattering (SAXS)

There are many modes of operation in SAXS experiments as many sample geometries and morphologies can be probed with a SAXS instrument. This data was recorded in transmission mode, which involves transmitting the entire x-ray beam through the sample and measuring the scattering pattern. A 2D image of scattering intensity is recorded (Figure 2-17) and the scattering vector (the difference between the scattered wave vector and the incident wave vector) is determined, of which, a cross section is used to determine morphology and domain spacing after fitting with idealised models. These measurements were performed on both solvent vapour annealed films and thermal annealed films.

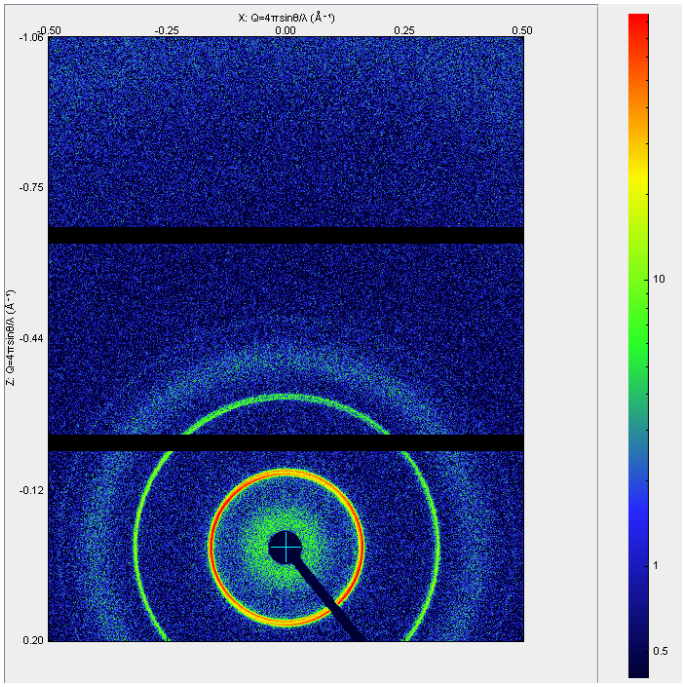

Figure 2-17. 2D image of scattering data of F_{21}-PAA_5 measured in transmission mode at 34 °C. Black bars indicates gaps between detectors.

SAXS profiles of annealed F_{13}-PAA_m polymers show a strong principal peak (q^*, indicated by red arrow, Figure 2-18), which is not present in EBIB-initiated polymers (F_0-PAA_m) (Figure A2-22 - Figure A 2-23) or in the F_{13}/F_0 initiators alone (Figure A 2-24). This can be translated to an interplane distance between similar domains

(which is smaller than the chain length of polymers) and suggests that F_{13}-PAA_m polymers have a χ value large enough for microphase separation. Intensity is given as a function of scattering vector (q) which results from a photon of wavelength (λ) scattering off a sample at angle of 2θ ($q = \frac{2\pi sin\theta}{\lambda}$). When incorporated into Bragg's law, this equation allows for the direct calculation of domain spacing from principal peak values ($d = \frac{2\pi}{q}$ for lamellar, $d = \frac{2\pi sin60}{q}$ for hexagonally packed cylinders (see calculation in Experimental, Methods & Calculations)). Peaks at higher q (second order) occur at well-defined values due to long-range crystalline symmetry and give therefore indicate specific morphologies. Peaks occurring at q/q^* = 1, 2, 3, 4 etc. are representative of lamellar (LAM) and q/q^* = 1, √3, 2, √7 etc. are representative of hexagonally packed cylinders (HEX).

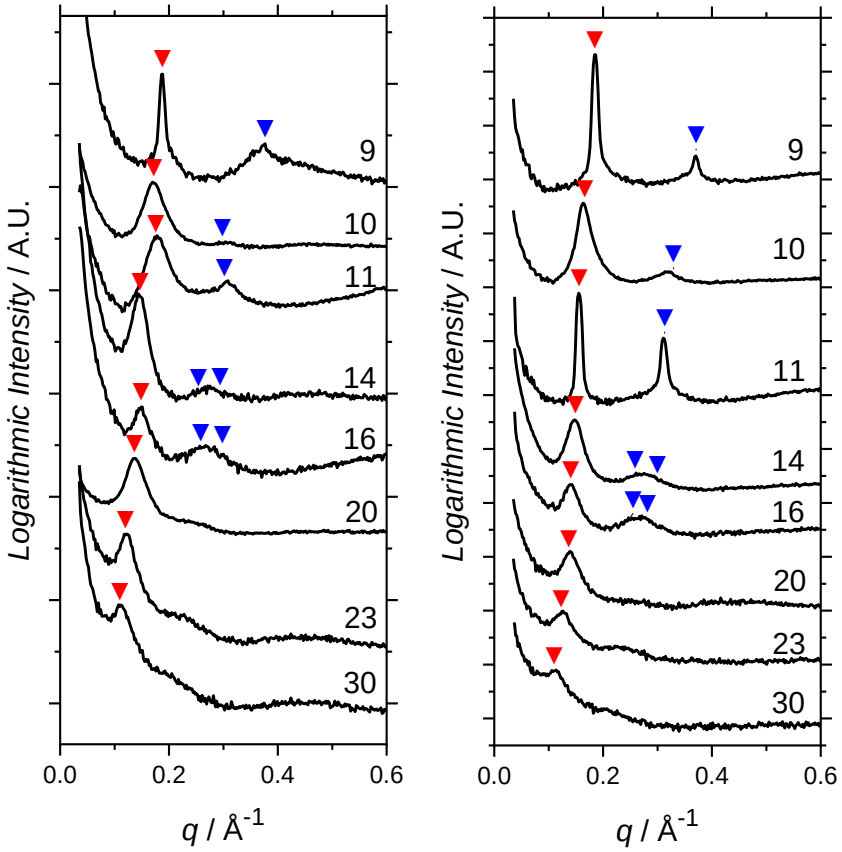

Figure 2-18. Left: SAXS profiles of solvent vapour annealed (in MeOH) and Right: thermal annealed F_{13}-PAA_m polymers. Numbers above traces are N = total degree of polymerisation. Red arrow = principal peak (q^*), blue arrow = theoretical positions of higher order peaks ($2q$ and/or $\sqrt{3}q$ based on q^*).

Polymer morphology was determined from fitting the higher order peak positions to those predicted from theoretical models. The theoretical position of LAM/HEX peaks

based on the principal peak position (labelled by blue arrows in Figure 2-18) were compared to experimental peak positions from SAXS profiles. Depending on the percentage error between these, the morphologies were assigned LAM, HEX or DIS (disordered) if no higher order peaks are present (Table 2-3).

Table 2-3. Assembly properties of annealing F_{13}-PAA_m polymers.

Polymer	Solvent Anneal morphology	Interplane spacing (nm)	Thermal anneal morphology	Interplane spacing (nm)
F_{13}-PAA_4	LAM	3.34	LAM	3.38
F_{13}-PAA_5	HEX	3.66	LAM	3.81
F_{13}-PAA_6	HEX	3.59	LAM	4.02
F_{13}-PAA_9	HEX	4.27	HEX	4.16
F_{13}-PAA_{11}	HEX	4.22	HEX	4.46
F_{13}-PAA_{15}	DIS	(4.59)	DIS	(4.60)
F_{13}-PAA_{18}	DIS	(5.28)	DIS	(5.10)
F_{13}-PAA_{25}	DIS	(5.71)	DIS	(5.80)

As DP increased, morphology changed from LAM to HEX to DIS which is the expected trend as molar fraction (f_{AA}) increases based on theoretical phase diagrams. As f_{AA} increases further (and molecular weight, concomitantly), morphology becomes disordered (hence bracketed interplane distances in Table 2-3) as χ is no longer large enough to realise microphase separation. As the poly(acrylic acid) DP increases, the interplane spacing increases, ranging from 3.3 nm to 5.8 nm. If the F_{13} group were the only consideration for domain size, it should remain fixed as it is a discrete moiety in all polymers, so the increase in interplane distance is a result of PAA chains forcing the F_{13} domains apart. This is apparent in both thermal and solvent vapour annealed SAXS data and interplane spacing is similar for both types of annealing (Figure 2-19).

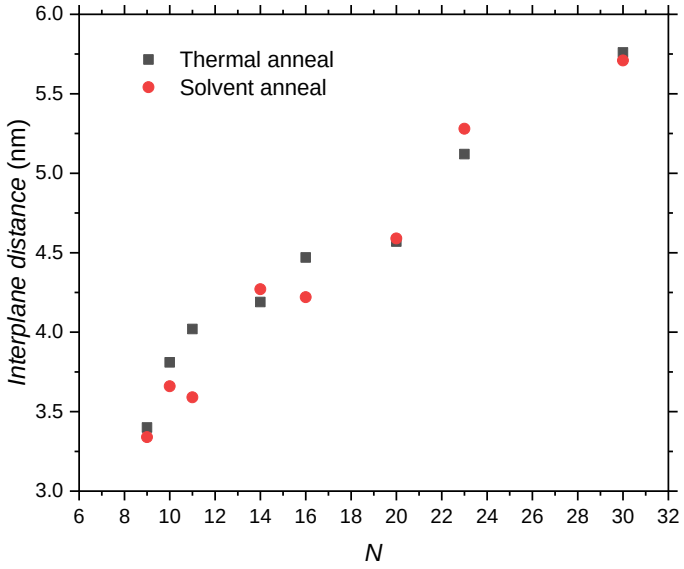

Figure 2-19. Interplane spacing (nm) vs. *N* (total degree of polymerisation).

2.5 Atomic force microscopy (AFM)

Microscopy gives complementary results to scattering methods and both must be used to fully analyse a sample. For example, microscopy can provide details of specific regions of small detail and methods of preparation largely affect topology. However, scattering provides data that is representative of the whole sample and local structure cannot be determined, but sample preparation is straightforward.

AFM images of F_{13}-PAA_{11} on Mica were prepared by spin coating a 5 wt% solution of polymer in MeOH prior to solvent vapour annealing with various solvents for 24 hours, Figure 2-20. The solvents chosen for annealing were a) no annealing, b) H_2O, c) 1:1 v/v H_2O:MeOH and d) MeOH, as block copolymer thin films may form different morphologies with different annealing solvents when different blocks have increased mobility.[133] H_2O and MeOH were chosen because H_2O is a good solvent for PAA and a poor one for the fluorocarbon, and MeOH is a good solvent for both segments. F_{13}-PAA_{13} with no annealing shows an amorphous topology, and acts as a control for other solvent annealed samples. Annealing in pure H_2O shows a fine hair-like structure, which is typically reported as lamellae.[212,213] Similarly when annealed in 1:1 v/v H_2O:MeOH, these fine structures are present but appear more fibrous and rod-like, which can also be considered lamellae. These fine features are present only when water is in the solvent vapour, it can be reasoned that the fluorocarbon chains are forced together by the water which is a poor solvent for the fluorocarbon segment.

Annealing in pure MeOH, (a good solvent for both segments) shows aggregates/loss of structure or could be argued that the hexagonally packed cylinders align end-end to the substrate, which would agree with morphology determined from SAXS measurements for F_{13}-PAA_{11}.

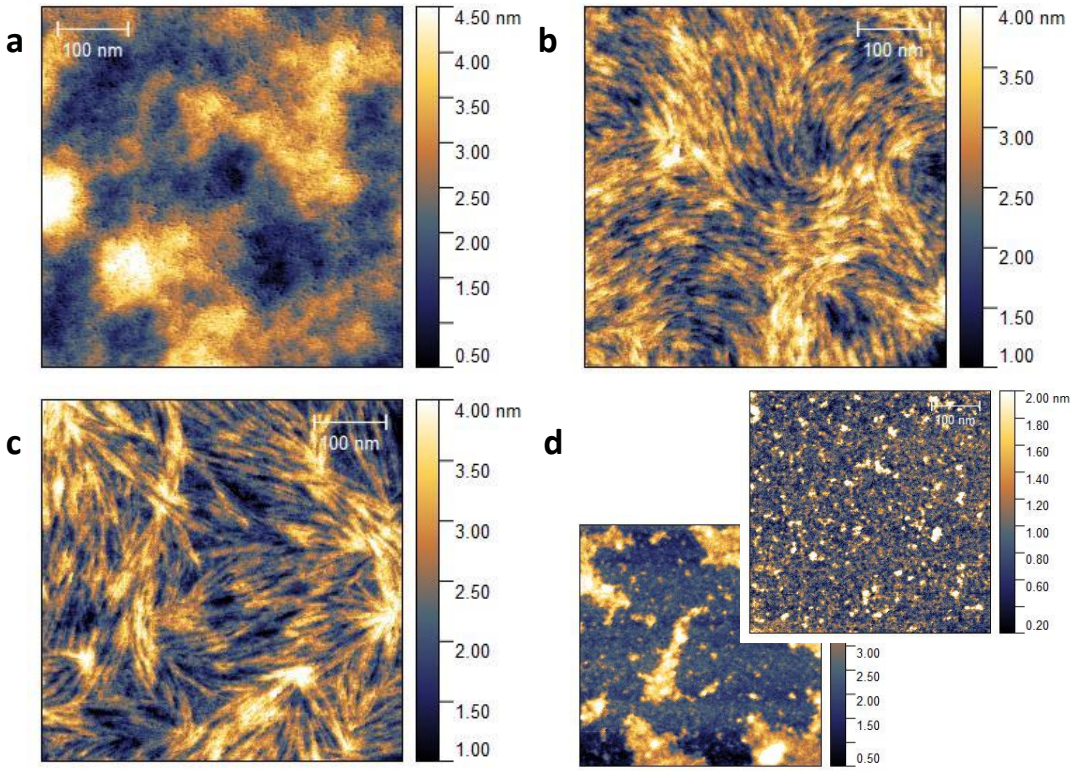

Figure 2-20. Atomic force microscopy (AFM) topography (Bruker Icon) of F_{13}-PAA_{11} annealed for 1 day by a) no anneal b) H_2O c) 1:1 vol. H_2O:MeOH d) MeOH. Solution conditions: 20 µl of 5 wt% polymer in MeOH on Mica.

The same F_{13}-PAA_{11} solutions were spin-coated on Mica but annealed for a longer period of 4 days, Figure 2-21. The purpose of this experiment was to determine the effect of longer exposure to solvent vapour. Overall, all samples showed much larger features, whether these are larger aggregated structures or dust particles is unknown. Again when water is in the solvent vapour (Figure 2-21a & b), fibre-like features are present. When annealed in MeOH, polymer aggregation formed large pillars perpendicular to the substrate, which also supports the HEX morphology from SAXS.

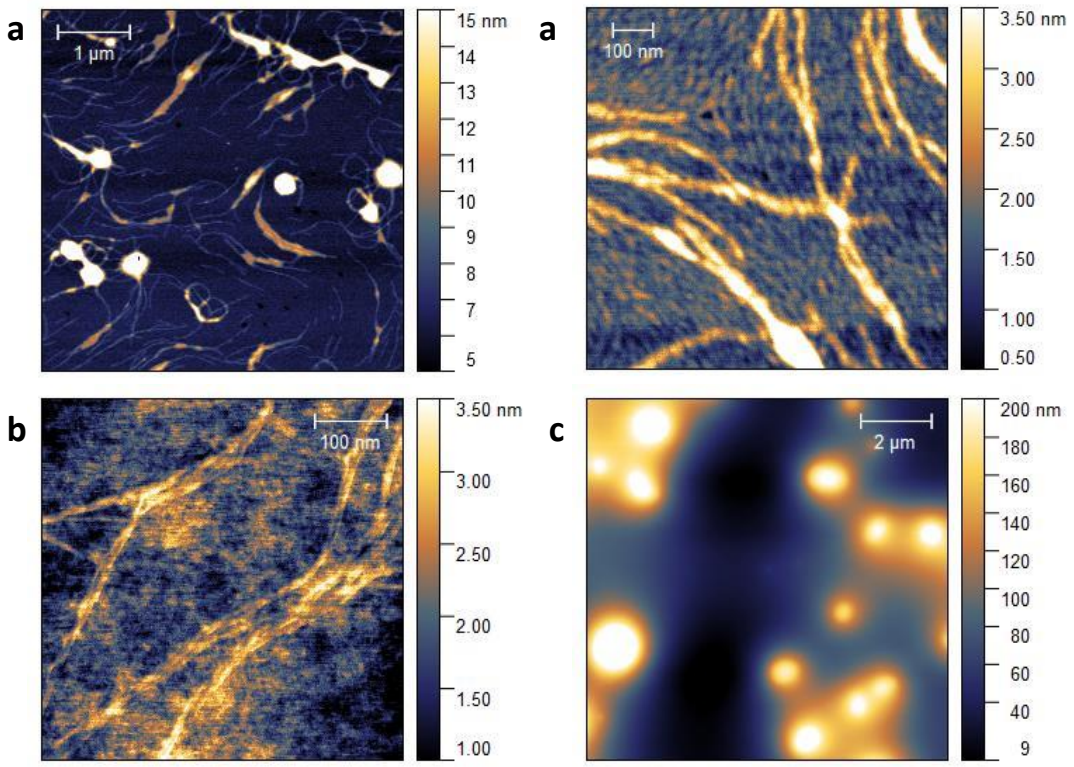

Figure 2-21. Atomic force microscopy (AFM) topography (Bruker Icon) of F_{13}-PAA_{11} annealed for 4 days by a) H_2O b) 1:1 vol. H_2O:MeOH c) MeOH. Solution conditions: 20 µl of 5 wt% polymer in MeOH on Mica.

2.6 Conclusions

An alkyl halide initiator was synthesised with a fluorinated tail due to the hydrophobicity of fluorinated compounds. This, in conjunction with a hydrophilic block (poly(acrylic acid)), provides an amphiphilic polymer with inherently low dispersity and lower molecular weights can be targeted, which is beneficial for microphase separation. A series of poly(acrylic acid) polymers were synthesised using the fluorinated initiator with low molecular weight (M_n 1400 – 4300 g mol^{-1}) and low dispersity (1.06 - 1.13). Polymer films were prepared by different annealing methods, and their morphology and domain spacing studied using small-angle X-ray scattering. With increasing polymer chain length, morphology changed from lamellar to hexagonally packed cylinders and domain spacing increased from 3.38 – 5.80 nm. This work shows that typical block copolymers are not the only route to microphase separation, and that more consideration should be given to the initiator in polymer assembly, particularly with polymers of low molecular weight.

2.7 Appendix

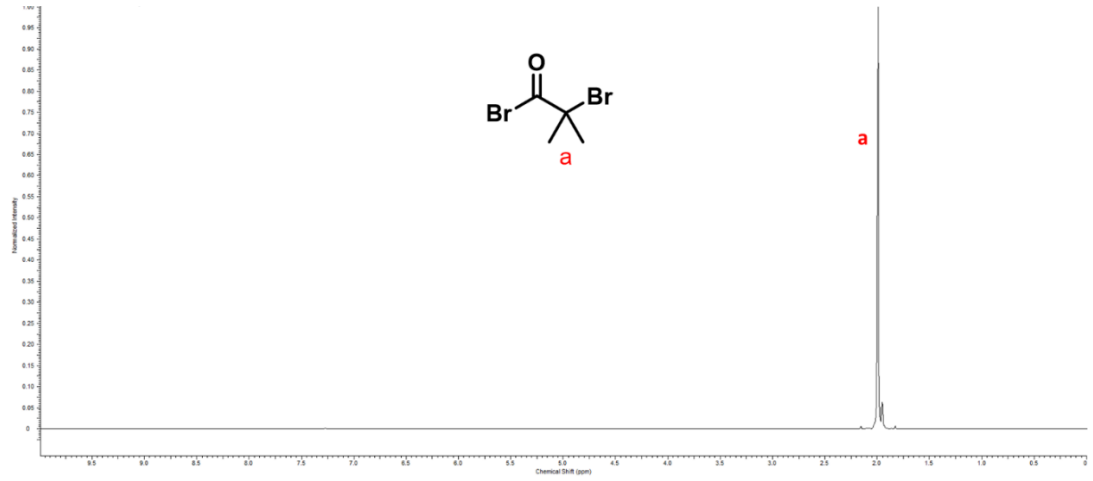

Figure A 2-1. ^{1}H NMR spectrum of bromoisobutyryl bromide in $CDCl_3$.

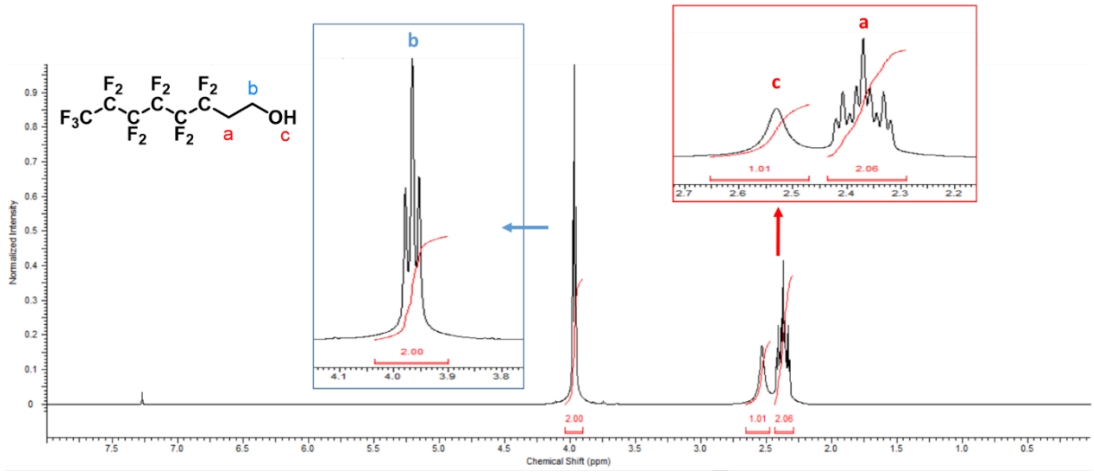

Figure A 2-2. ^{1}H NMR spectrum of perfluorooctanol in $CDCl_3$, including integrals.

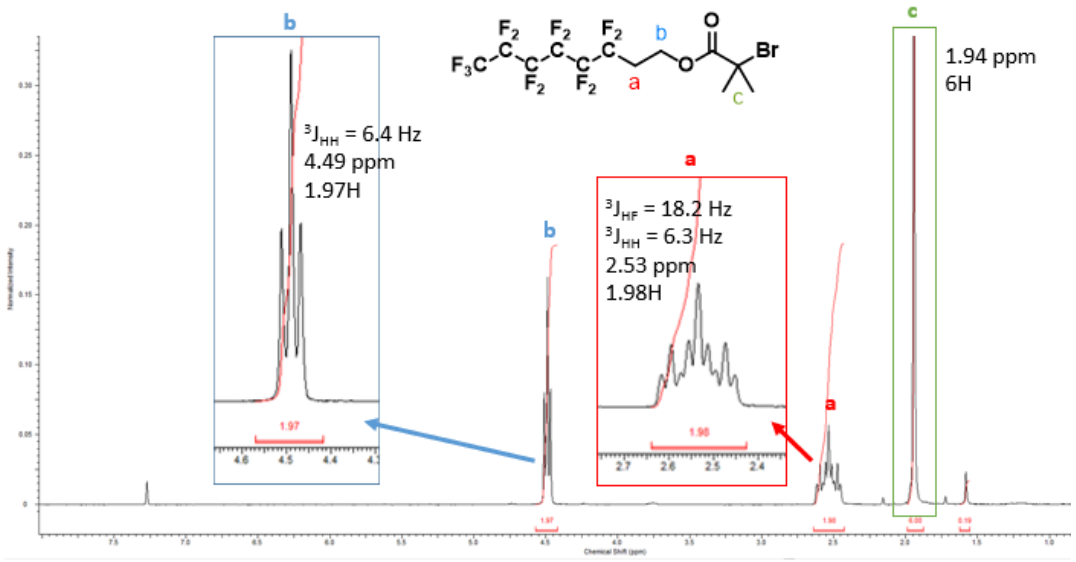

Figure A 2-3. Full expansion of ^{1}H NMR spectrum of F_{13} in $CDCl_3$, including coupling constants, peak positions, and relative integrals.

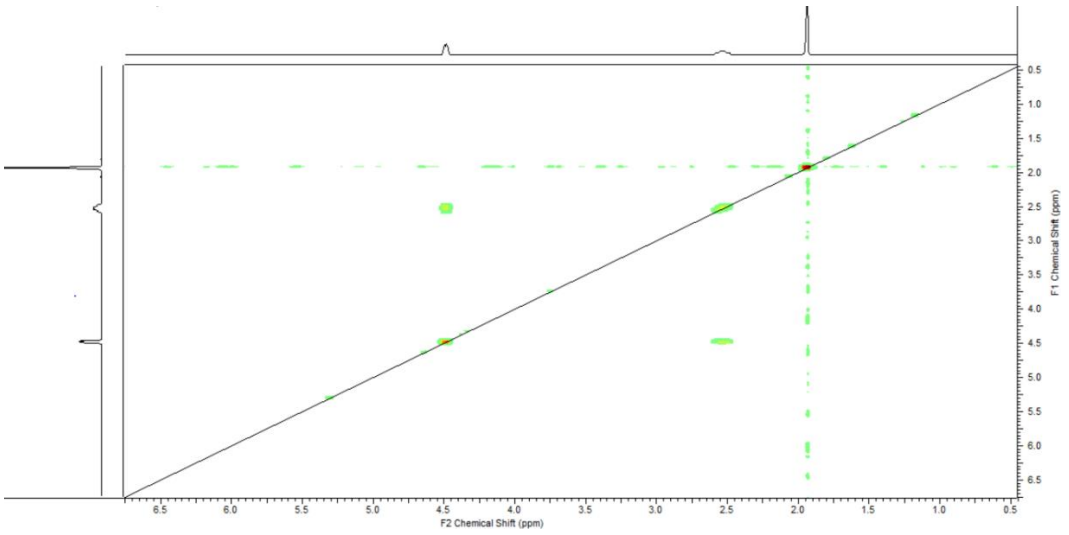

Figure A 2-4. COSY spectrum of perfluorooctyl bromoisobutyrate (F_{13}) in $CDCl_3$.

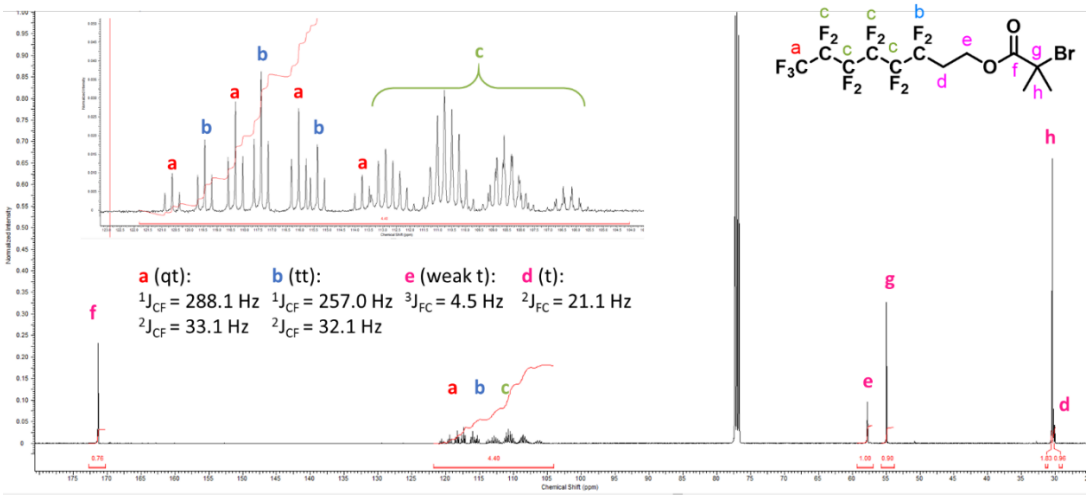

Figure A 2-5. Full ^{13}C NMR spectrum of F_{13} in $CDCl_3$ including integrals and coupling constants.

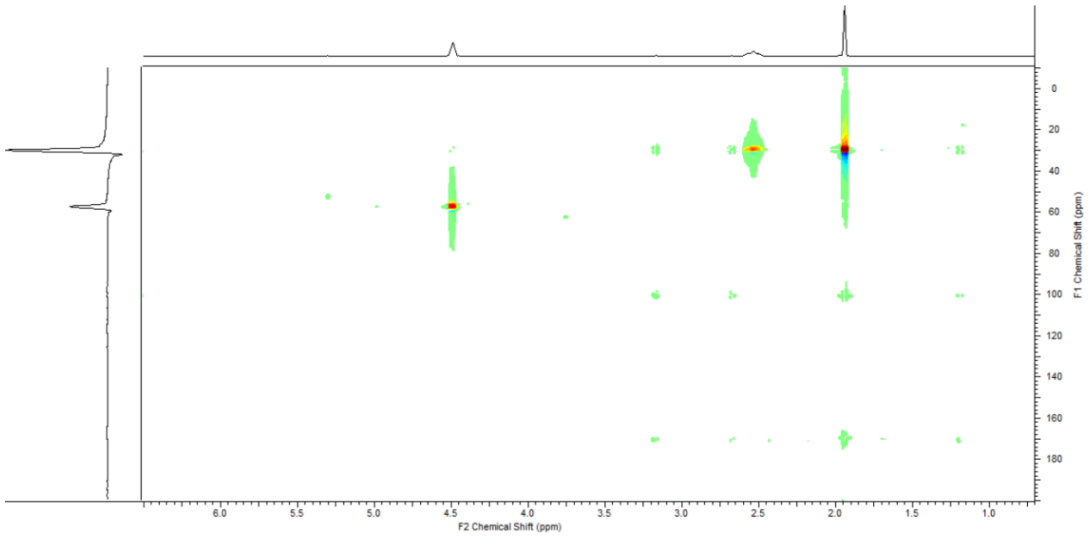

Figure A 2-6. HSQC spectrum of perfluorooctyl bromisobutyrate (F_{13}) in $CDCl_3$.

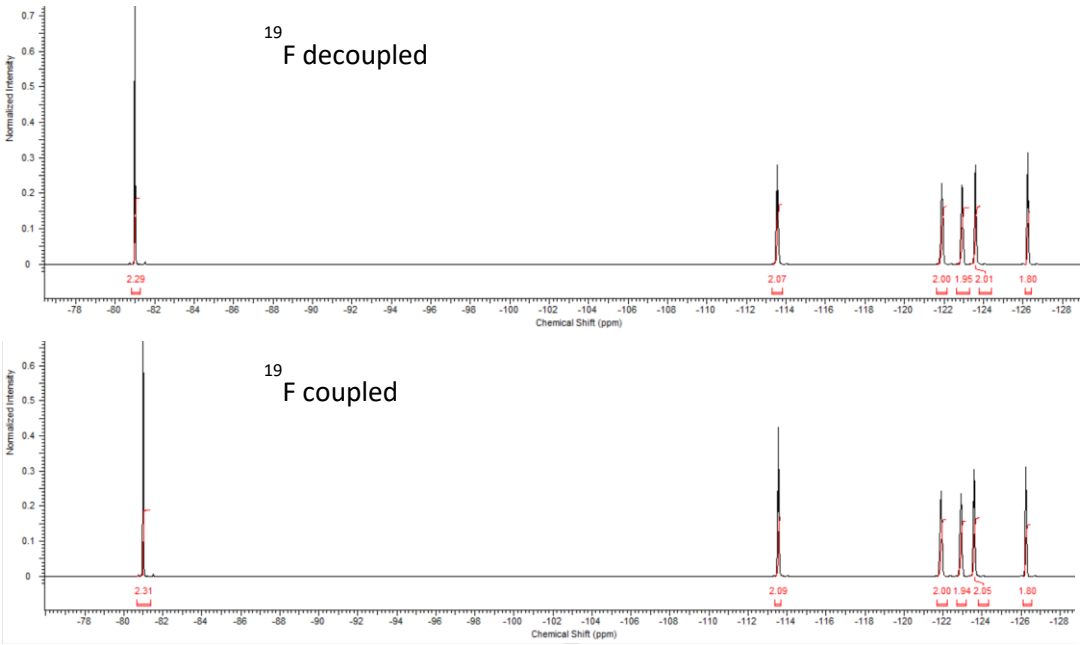

Figure A 2-7. Full ^{19}F NMR spectra of both coupled and decoupled (from $^{3}J_{FH}$), including integrals.

Figure A 2-8. Initiator efficacy characteristics for F_{13}.

Reaction	$M_{n,NMR}$ (g mol^{-1})	Conversion (%)	End Group Fidelity (%)	Dispersity
F_{13}, DMSO, methyl acrylate	5400	99	94	1.19
F_{13}, DMSO, methyl acrylate	27400	>99	58*	1.15
F_{13}, DMSO, methyl acrylate	54100	99	15*	1.32

*note – intensity of single terminal backbone proton is lost to noise with increasing molecular weight.

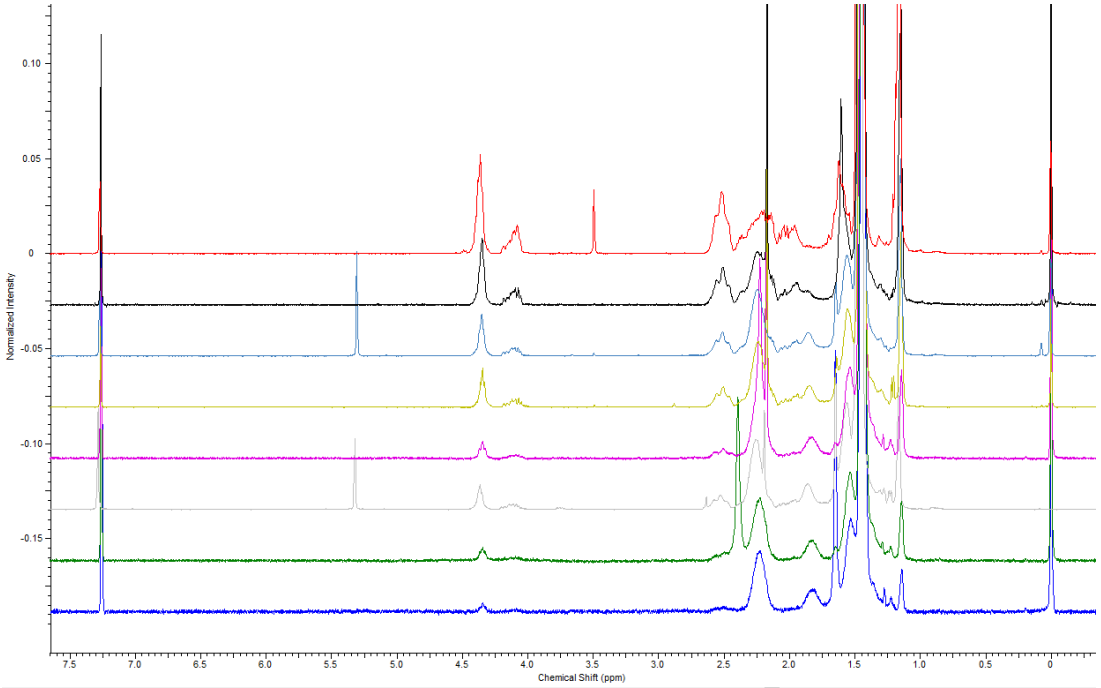

Figure A 2-9. ^{1}H NMR spectrum (400 MHz, $CDCl_3$) of F_{13}-P*t*BA$_m$ in MeOD. m = 4, 5, 6, 9, 11, 15, 18 & 25 from top to bottom.

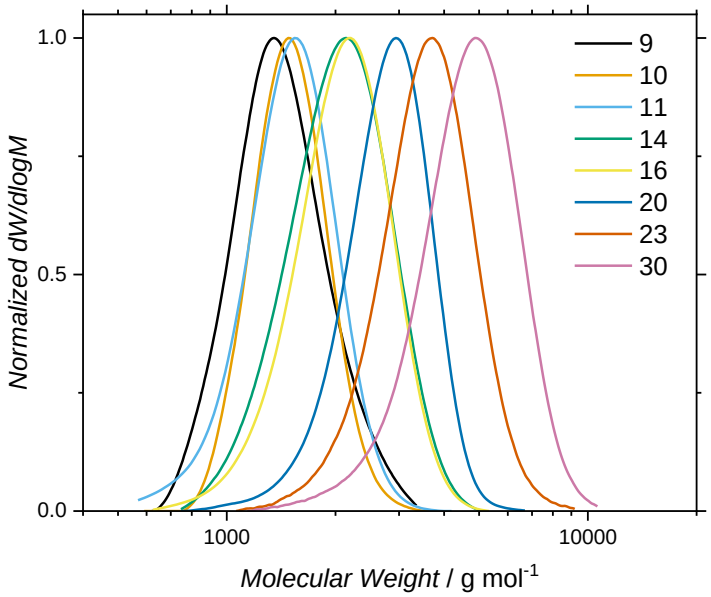

Figure A 2-10. GPC traces of F_{13}-P*t*BA$_m$ polymers in THF. Legend numbers show total DP (*N*).

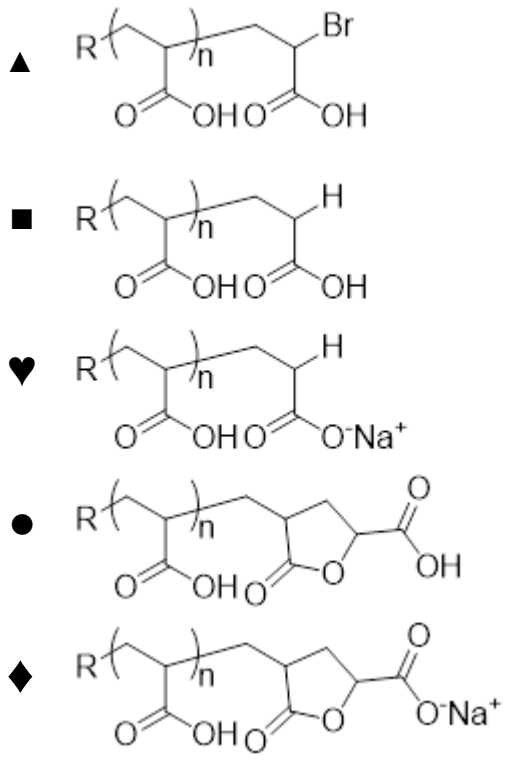

Figure A2-11. Key of end groups found in MALDI spectra for F_{13}-PAA_m polymers.

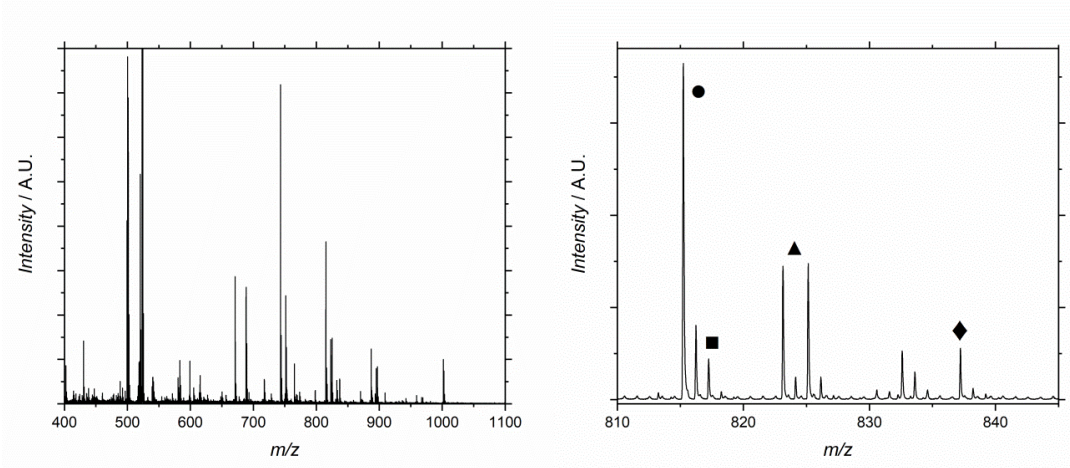

Figure A2-12. MALDI spectrum of F_{13}-PAA_4. Key of end groups in Figure A2-11.

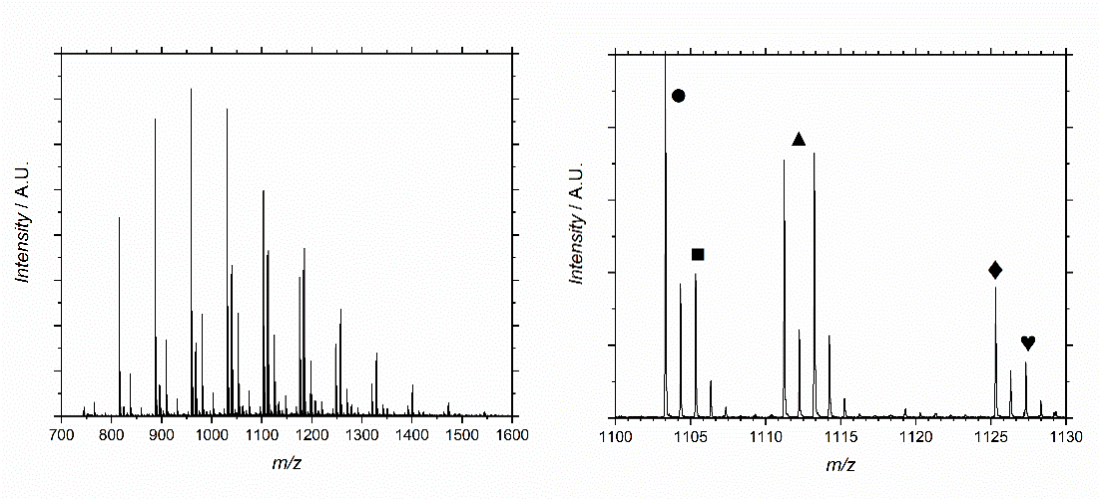

Figure A2-13. MALDI spectrum of F_{13}-PAA_6. Key of end groups in Figure A2-11.

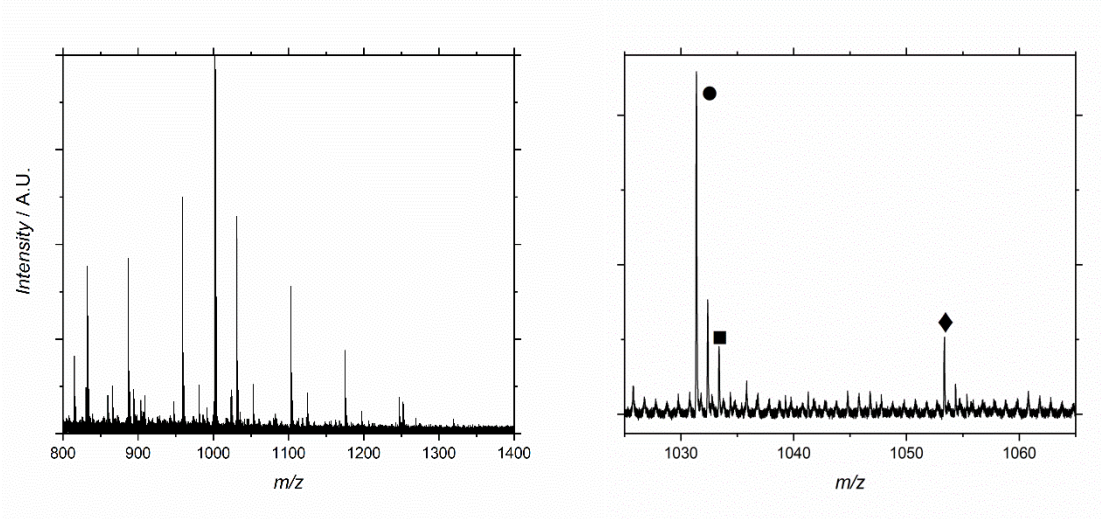

Figure A2-14. MALDI spectrum of F_{13}-PAA_9. Key of end groups in Figure A2-11.

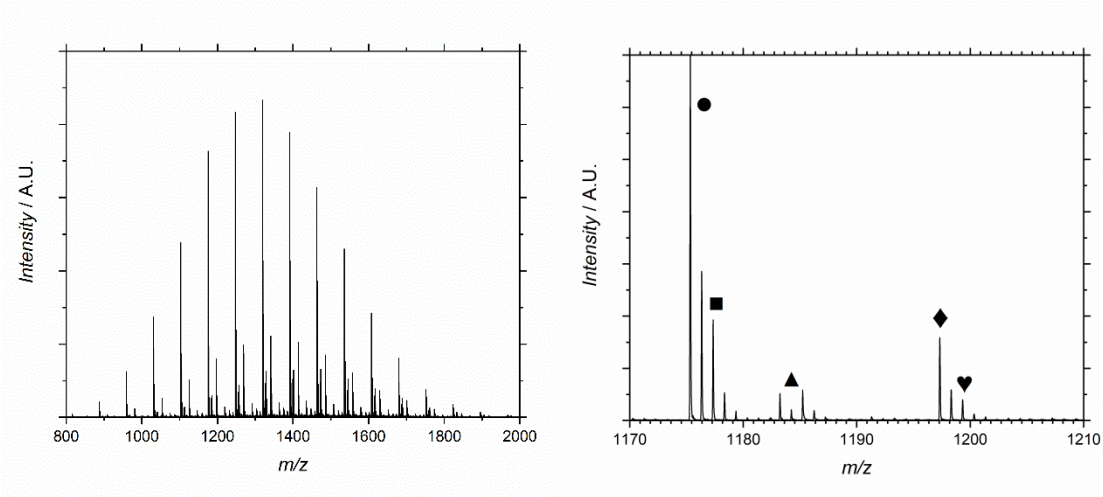

Figure A2-15. MALDI spectrum of F_{13}-PAA_{11}. Key of end groups in Figure A2-11.

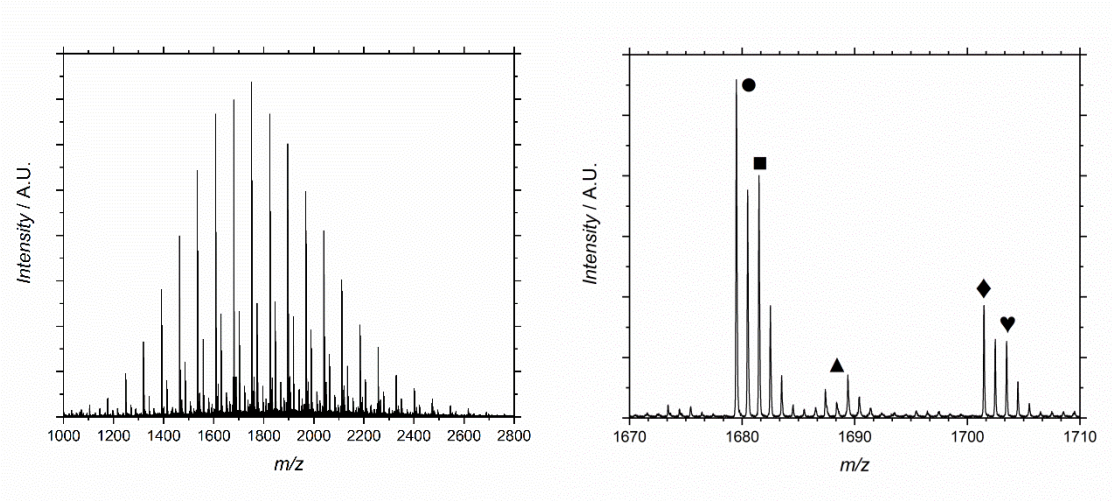

Figure A2-16. MALDI spectrum of F_{13}-PAA_{18}. Key of end groups in Figure A2-11.

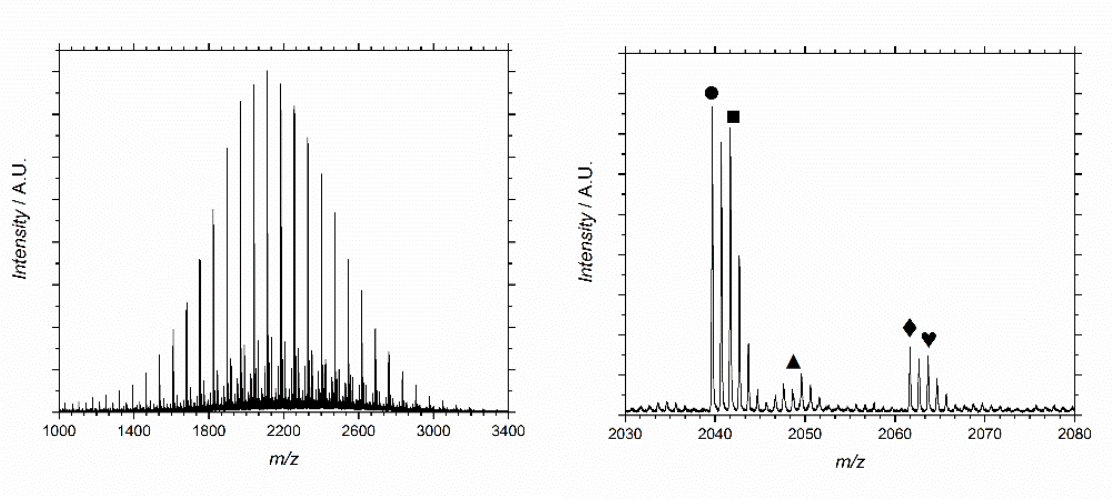

Figure A2-17. MALDI spectrum of F_{13}-PAA_{25}. Key of end groups in Figure A2-11.

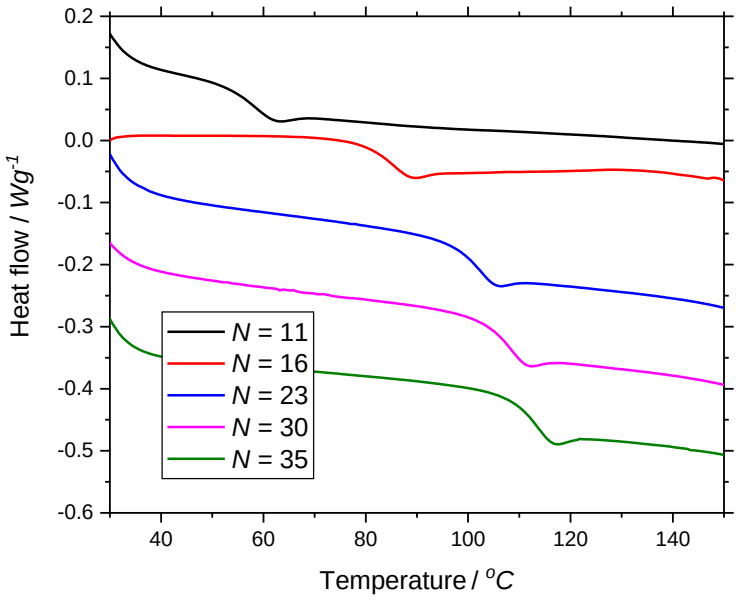

Figure A2-18. DSC traces for F_{13}-PAA_m.

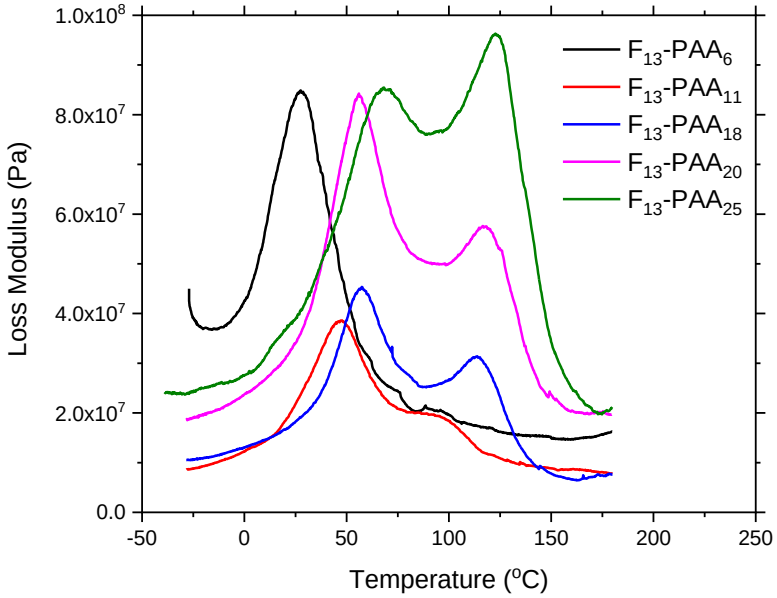

Figure A2-19. Loss modulus data from DMA for F_{13}-PAA_m.

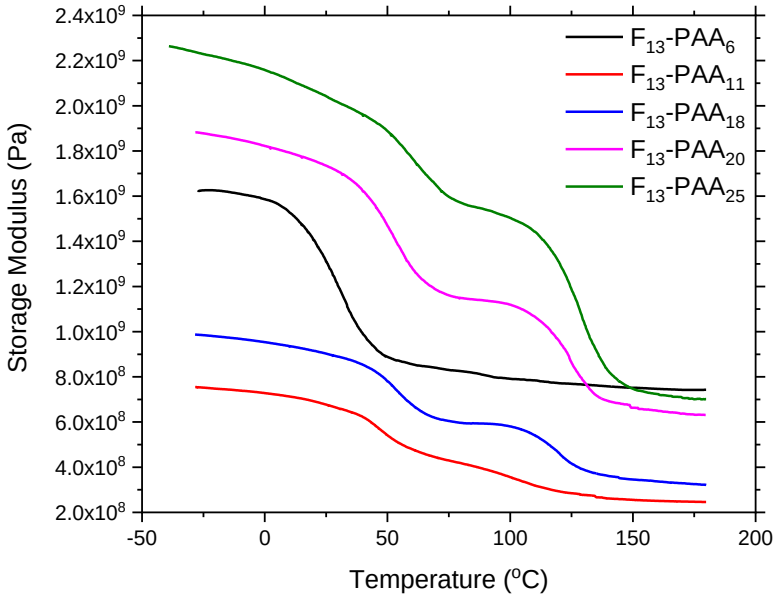

Figure A2-20. Storage modulus data from DMA for F_{13}-PAA_m.

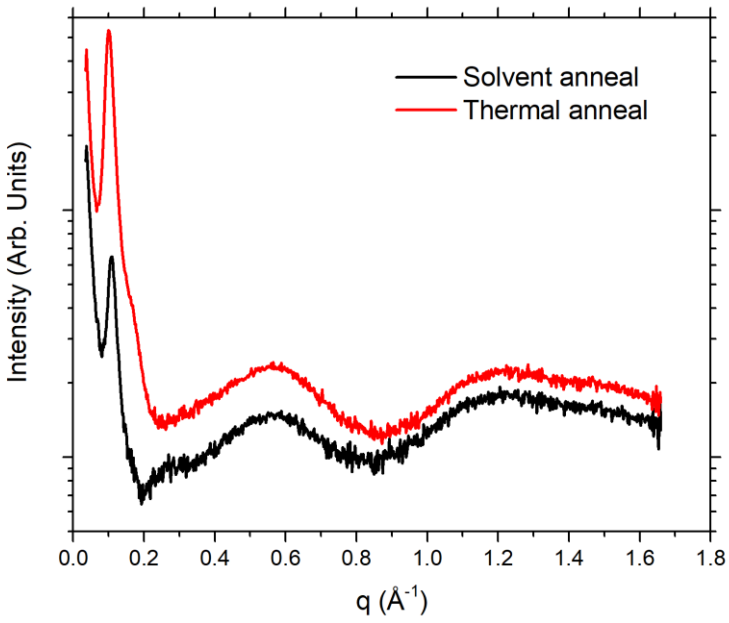

Figure A2-21. Full SAXS profiles for F_{13}-$PNaA_{25}$ prepared by solvent anneal (methanol) and thermal anneal.

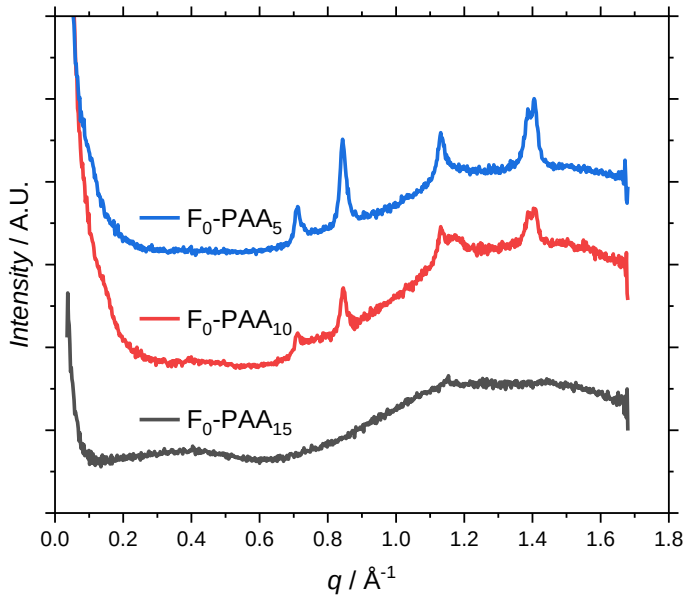

Figure A2-22. SAXS profiles for EBiB-initiated poly(acrylic acid) (F_0-PAA_m) prepared by solvent annealing in methanol.

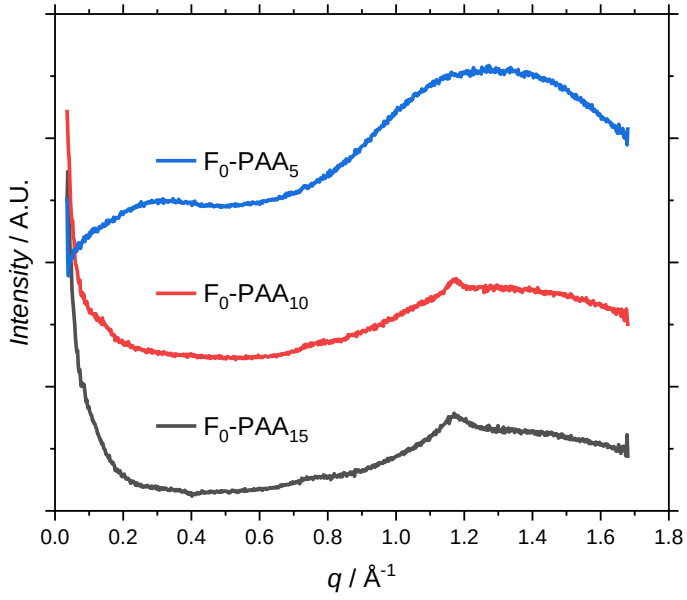

Figure A 2-23. SAXS profiles for EBiB-initiated poly(acrylic acid) (F_0-PAA_m) prepared by thermal annealing.

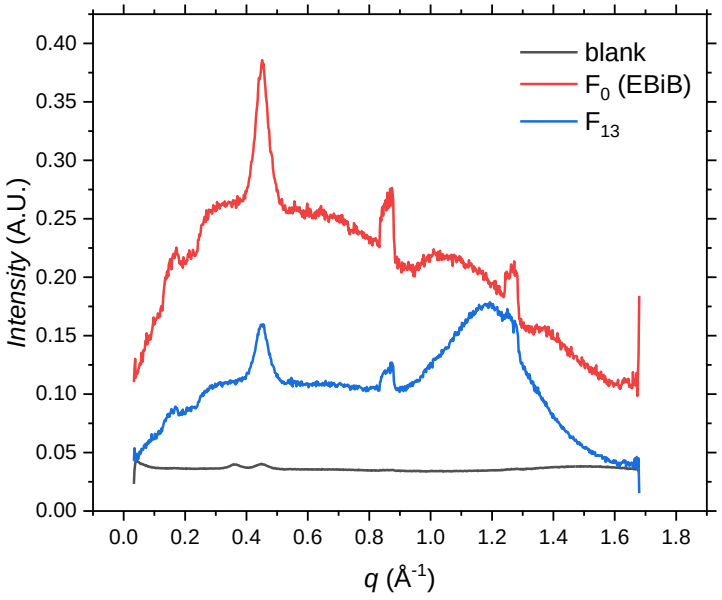

Figure A 2-24. SAXS profiles of liquid initiators (EBiB/F_0 and perfluorooctyl bromoisobutyrate/F_{13}).

Chapter 3: Phase behaviour of short-chain fluorinated polymers

Contents

Following the success of utilising the perfluorooctyl bromoisobutyrate (F_{13}) initiator (introduced in chapter 1) in the synthesis of polymers which undergo microphase separation, this chapter introduces fluoro-acrylic acid polymers with larger fluorine content designed to modify the Flory-Huggins interaction parameter, χ, and to investigate their bulk phase behaviour. By increasing the length of the fluorinated tail in the initiator, the volume fraction of the hydrophobic "block" increases, in turn changing the value of χ and with it, morphology and domain spacing. This allows the comparison of an increasing fluorinated segment (with constant PAA chain length) on SAXS data and corroborating the effect of increasing PAA chain length (with constant but higher fluorine content than F_{13}) with observations made in Chapter 1. With this and theoretical modelling, an experimental phase diagram was created which allows the reproducible targeted of specific morphologies with desired domain sizes.

3.1 F_{17} & F_{21} initiator

Initiators with 17 and 21 fluorine atoms, perfluorodecyl bromoisobutyrate (F_{17}) and perfluorododecyl bromoisobutyrate (F_{21}), were synthesised via the same protocol as F_{13} using 1H,1H,2H,2H-perfluoro-1-decanol and 1H,1H,2H,2H-perfluoro-1-dodecanol as starting material (Figure 3-1, Figure A3-1), respectively (yield = 75.7% (F_{17}) and 50.5% (F_{21})). Chloroform was required for the synthesis of F_{21} as the increase in halogen affinity increased solubility of 1H,1H,2H,2H-perfluoro-1-dodecanol. ^{1}H, ^{13}C and ^{19}F NMR spectra (Figure A3-2 - Figure A3-4) were used to determine molecular mass and allowed an approximate comparison of fluorine content (relative sensitivity of ^{19}F is ~88% of ^{1}H).[214] The difference in number of fluorine atoms between these 3 initiators provides a variety of polymer volume fractions and hydrophobicity, allowing experimental access to a significant portion of a phase diagram.

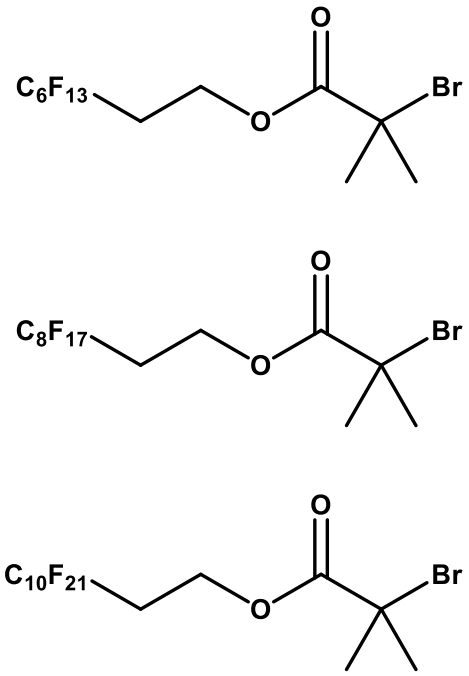

Figure 3-1. Structure of perfluoroalkyl bromide initiators, F_{13} (top), F_{17} (middle), F_{21} (bottom).

3.1.1 F_n-PAA_m synthesis and characterisation

Synthesis of F_{17}-PAA_m and F_{21}-PAA_m followed the same procedure as was used for F_{13}-PAA_n polymers. All polymer syntheses (F_n-PAA_m) involved the polymerisation of F_n-P*t*BA_m, as characterised by GPC (THF eluent) (Figure A3-5 - Figure A3-7) and NMR (Figure A3-8 - Figure A3-13), followed by the same deprotection conditions used for

F_{13}-PAA_n to give the acid. Table 3-1 shows the molecular mass data for all F_n-PAA_m polymers including molecular mass calculated from GPC and ^{1}H NMR, dispersity, volume fraction, total degree of polymerisation and glass transition temperature. MALDI-ToF-MS (Figure A3-14 - Figure A3-17) also showed the same end groups were present, a cyclised lactone distribution being the most abundant. These sets of polymers allow the independent comparison of increasing PAA length and increasing fluorocarbon length to probe their individual effects on microphase separation.

Table 3-1. Molecular characteristic of F_n-PAA_m polymer sets.

Polymer[a] F_n-PAA_m	Molecular mass[a] (M_n, g/mol) (NMR)	Molecular mass[b] (M_n, g/mol) (GPC)	$Đ$ [b]	Volume fraction (f_F)	N[c]	T_g[d] (°C)
F_{13}-PAA_4	801	1400	1.08	0.42	9	52.0
F_{13}-PAA_5	873	1450	1.06	0.37	10	59.2
F_{13}-PAA_6	945	1500	1.11	0.34	11	57.0
F_{13}-PAA_9	1160	1900	1.11	0.26	14	80.0
F_{13}-PAA_{11}	1310	1950	1.10	0.23	16	80.0
F_{13}-PAA_{12}	1380	2000	1.17	0.21	17	83.3
F_{13}-PAA_{15}	1590	2650	1.08	0.18	20	88.1
F_{13}-PAA_{17}	1740	2700	1.14	0.17	22	100.7
F_{13}-PAA_{18}	1810	3400	1.10	0.16	23	96.0
F_{13}-PAA_{22}	2100	3300	1.14	0.13	27	107.1
F_{13}-PAA_{25}	2520	4300	1.13	0.12	30	103.8
F_{13}-PAA_{27}	2460	3900	1.17	0.11	32	112.4
F_{17}-PAA_6	1050	1600	1.13	0.39	12	52.1
F_{17}-PAA_{11}	1410	2400	1.11	0.27	17	78.8
F_{17}-PAA_{17}	1840	2600	1.24	0.20	23	100.0
F_{17}-PAA_{23}	2270	4000	1.15	0.16	29	108.4
F_{17}-PAA_{30}	2780	4600	1.21	0.13	36	111.6
F_{21}-PAA_5	1070	2000	1.04	0.47	12	77.9
F_{21}-PAA_{10}	1430	2200	1.13	0.33	17	86.9
F_{21}-PAA_{16}	1870	2800	1.14	0.24	23	99.5
F_{21}-PAA_{20}	2150	3900	1.16	0.20	27	109.6
F_{21}-PAA_{24}	2440	4100	1.15	0.18	31	110.0

a) Degree of polymerisation and number-average molecular mass determined by ^{1}H NMR of F_n-P*t*BA_m polymers in $CDCl_3$. b) THF GPC data against poly(methyl methacrylate) standards. c) Total polymer degree of polymerisation. d) Taken from DSC data.

3.1.2 Methanol transesterification

3.1.2.1 MALDI-ToF-MS study

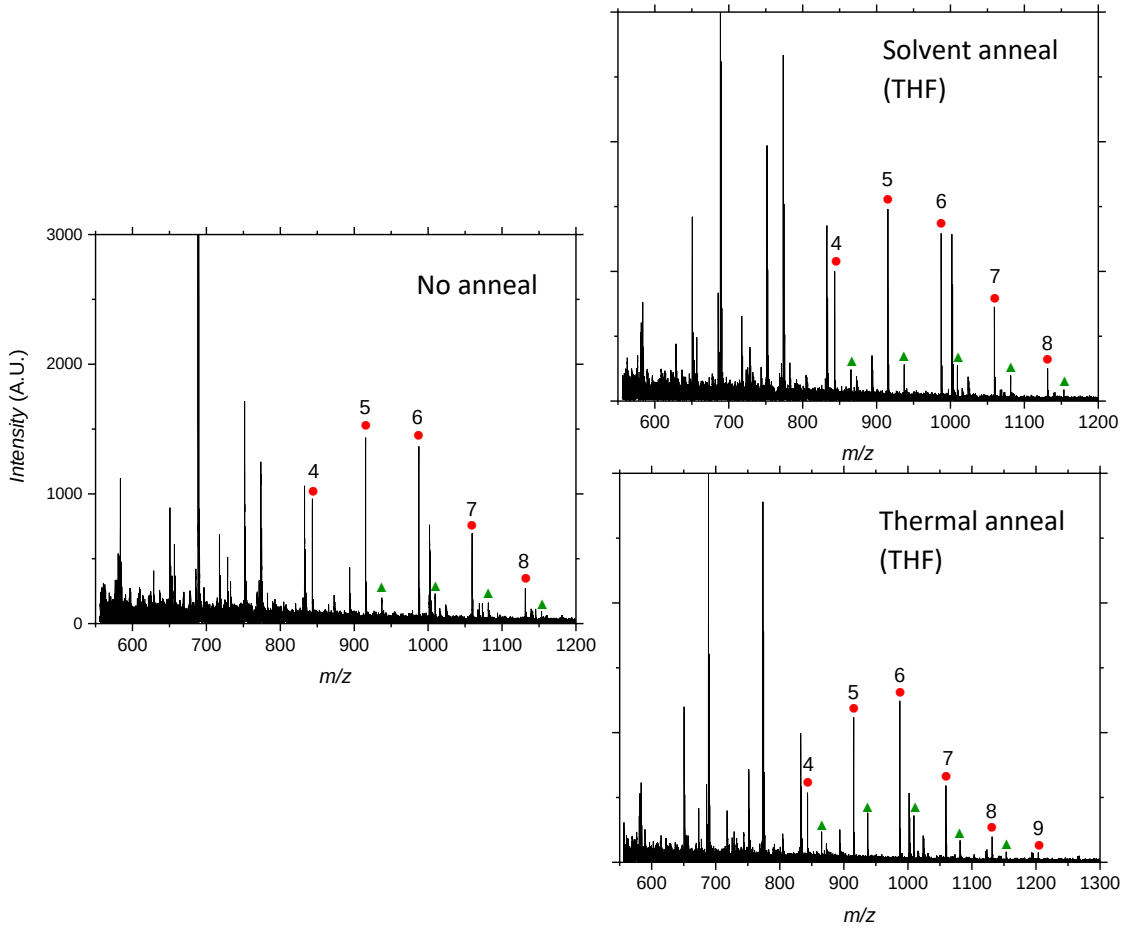

Figure 3-2. MALDI-ToF-MS spectra of F_{17}-PAA_{11} samples after different THF annealing conditions.

The F_n-PAA_m polymers were annealed by various means prior to SAXS measurements. Transesterification of methanol, during the solvent annealing process, was highlighted as a possible adverse effect of annealing. MALDI-ToF-MS was used to investigate the effect of annealing in methanol as compared to THF by direct comparison of data. Figure 3-2 shows the MALDI spectra of F_{17}-PAA_{11} with no annealing (powder), after solvent annealing (film) in THF and after thermal annealing (whereby the solvent-annealed film is heated). Red circles show the most abundant distribution, corresponding to the cyclised end group which is present in all polymers. Green triangles show the distribution relating to a singly substituted sodium acrylate unit and can be disregarded as this occurs during MALDI sample

preparation. No other end group distributions are present indicating no detectable transesterification occurs when PAA is exposed to THF.

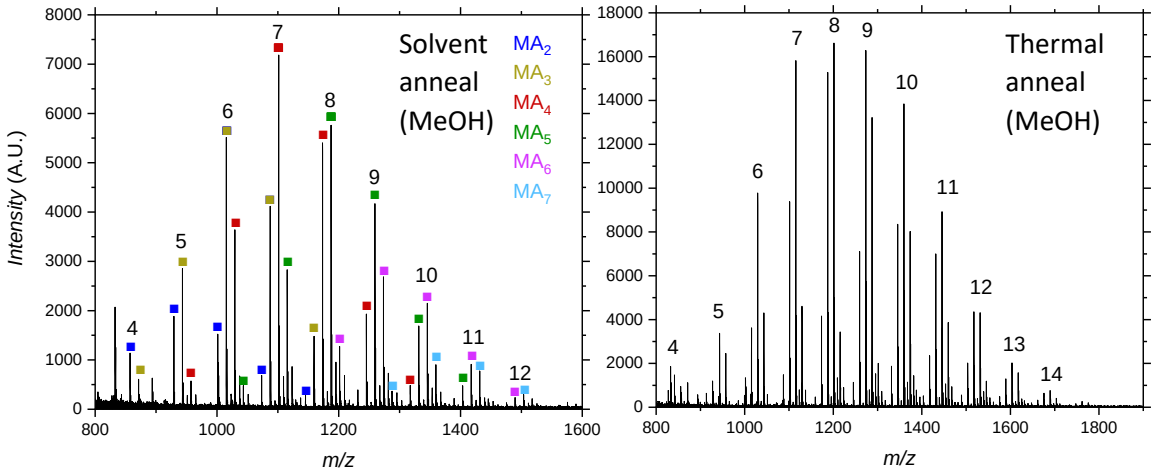

Figure 3-3. MALDI-ToF-MS spectra of F_{17}-PAA_{11} samples after different MeOH annealing conditions.

Figure 3-3 shows MALDI spectra from F_{17}-PAA_{11} after solvent annealing in MeOH and after thermal annealing. The most obvious difference between these spectra and those in Figure 3-2 is the additional mass distributions, which are evidence of a poly(acrylic acid)-*statistical*-poly(methyl acrylate) copolymer, indicating a certain amount of transesterification does occur in methanol. The spectrum of the solvent annealed film has been coloured to show the number of methyl acrylate units present, which range from 2 to 7 units (18 – 63% of polymer transesterified). The fact that poly(methyl acrylate) enters the gaseous state more easily when irradiated by the laser within the MALDI and shows a higher degree of detection (due to higher ester group affinity with sodium salts compared to poly(acrylic acid) must also be borne in mind. This could give the misconception that a greater number of acrylic acid units have transesterified than have actually been. This assertion is corroborated by the larger peak intensity recorded for the methanol-annealed samples than the THF equivalent.

3.1.2.2 ^{1}H NMR study

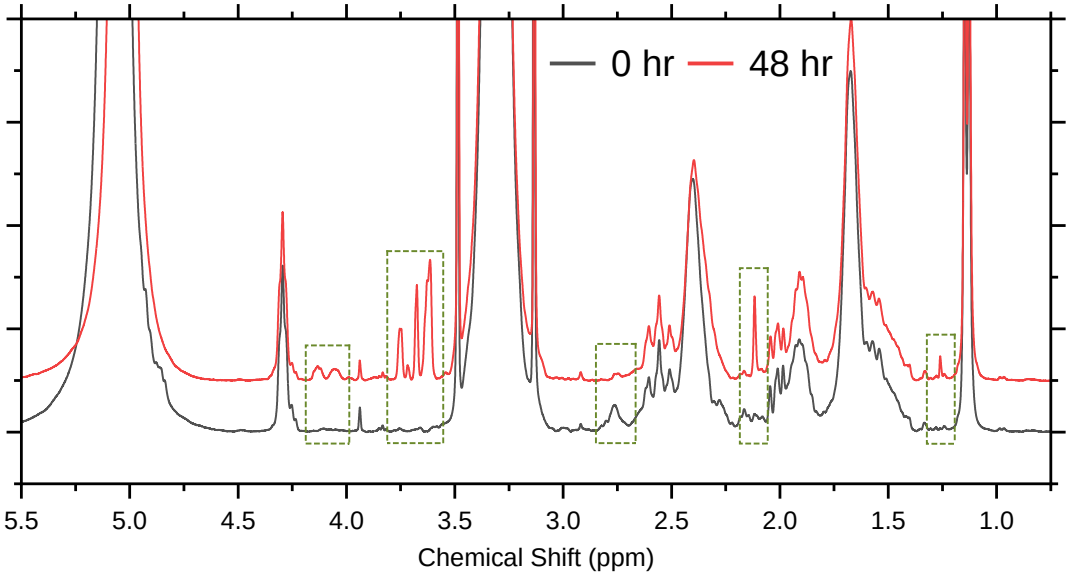

Figure 3-4. ^{1}H NMR spectra (400 MHz) of F_{13}-PAA_{11} in MeOH/MeOD at 0 hrs and after 48 hrs. Highlighted areas indicate changes in peak intensity.

A ^{1}H NMR experiment was also conducted, where F_{13}-PAA_{11} was dissolved in a 1:1 MeOH/MeOD mix to saturation to best reproduce the conditions for film preparation. ^{1}H NMR was performed every 1 hour for 48 hours, as this was the longest period of solvent annealing, after which a solid film would remain, rendering further transesterification unlikely. Figure 3-4 show the ^{1}H NMR spectra of F_{13}-PAA_{11} at 0 hours and 48 hours after dissolution and the highlighted areas show peaks that changed in intensity. The most relevant change is the formation of peaks in the region of 3.6 – 3.8 ppm, which indicate the presence of methyl acrylate units due to transesterification. Other regions of the spectra also showed peak changes at 4.0 – 4.2 ppm (also possibly methyl acrylate), 2.7 – 2.8 ppm, 2.1 – 2.2 ppm and 1.2 – 1.3 ppm with unknown origins.

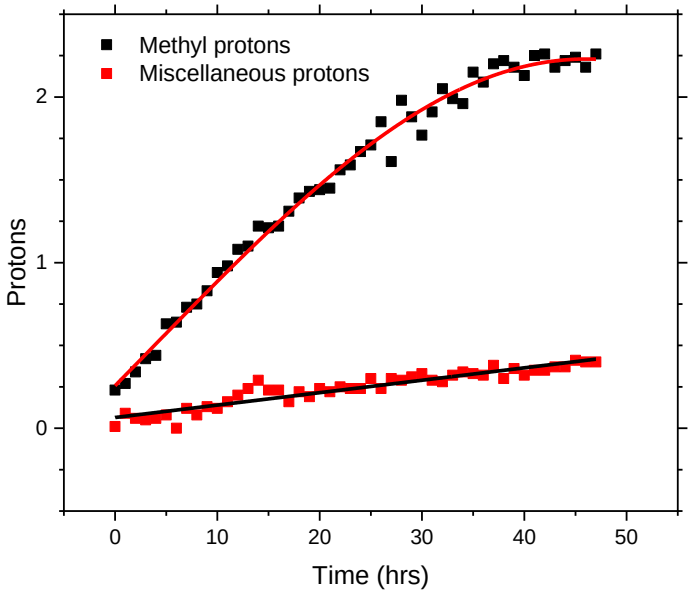

Figure 3-5. ^{1}H NMR (400 MHz) of F_{13}-PAA_{11} in methanol over 48 hours. Number of protons were calculated from NMR spectra integration (Figure 3-4). Methyl protons = 3.6-3.8 ppm, miscellaneous protons = 4.0–4.2 ppm.

Figure 3-5 shows the change in proton number (peak integration) with time for peaks in the spectra (Figure 3-4) corresponding to methyl protons (3.6 – 3.8 ppm) and miscellaneous peaks (4.0 – 4.2 ppm). The spectra were integrated in the same ppm range, however, a degree of human error is associated with the baseline treatment which could not be batch-processed. Peak integrals were referenced to 6H from the $(CH_3)_2$ group which should remain unaffected. During the first 30 hours, there is a linear increase in the number of methyl protons, which eventually plateaus at an approximate average of 2.25 protons *i.e.* 5.8% of AA units were transesterified with MeOH, less than a single methyl acrylate unit per polymer. These experiments were not done to quantify the exact percentage of esterified units and this calculation is purely statistical on existing data. This observation agrees with the conclusion made from MALDI spectra, that transesterification is not significant enough to cause concern when moving forward with this project.

3.2 Small-Angle X-ray Scattering (SAXS)

Two methods of SAXS measurement were performed on F_n-PAA_m polymers; single acquisition after thermal annealing, and time-resolved measurements during thermal annealing. The former provided morphology and domain spacing while the latter provided information allowing investigation into thermal transitions between morphologies and elucidation of an experimental phase diagram

3.2.1 Single acquisition after thermal annealing

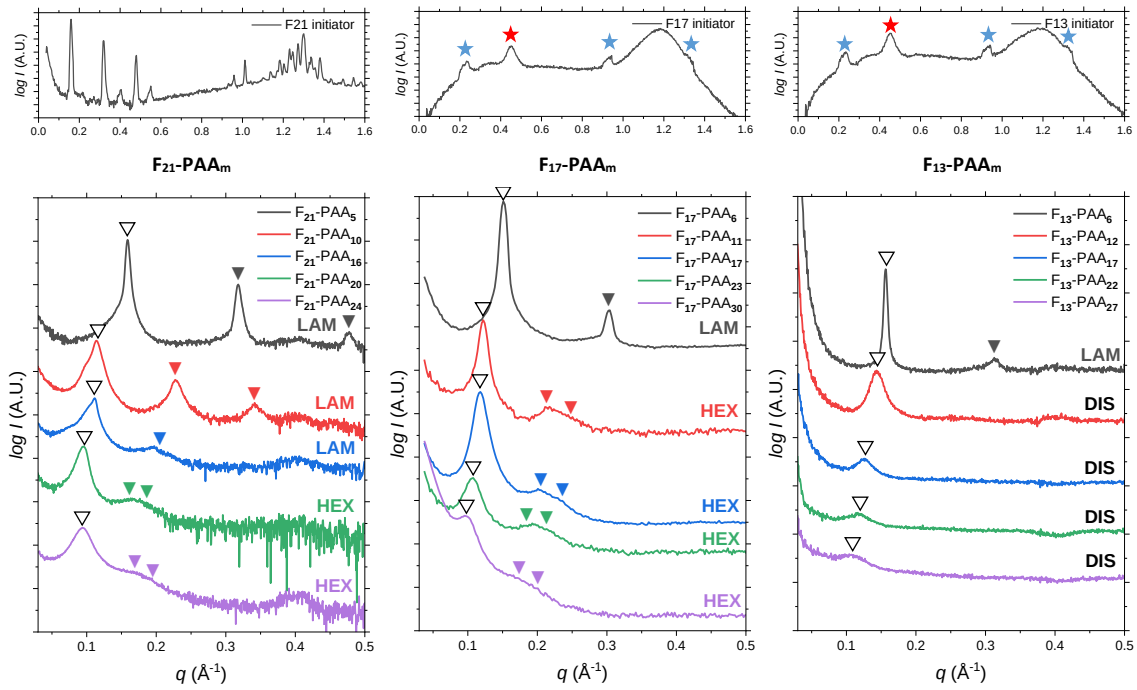

Figure 3-6. Single data SAXS measurements for thermally annealed F_n-PAA_m telechelic homopolymers using F21, F17 and F13 initiators (left to right). Open arrows show principal peak (q^*) position. Shaded arrows indicate theoretical peak positions of the labelled morphology (LAM = lamellar, HEX = hexagonal cylinders, DIS = disordered). SAXS profiles of F21, F17 and F13 initiators (DP = 0) given above. Blue stars indicate artefacts from between detectors, red stars indicate Kapton.

Samples were prepared for single data acquisition by solvent annealing (5.1.15) to initially prepare the polymer as a film, this was followed by thermal annealing at 120 ^oC for 24 hours. These samples were removed from the heat source and allowed to cool to room temperature and SAXS measurements were performed on the resulting films, Figure 3-6. SAXS measurements for the three fluorinated initiators (F_{21}, F_{17}, F_{13}) are shown above their respective data sets. F_{21} is a solid at room temperature and LAM peaks are observed in the scattering pattern, indicating crystallinity. Other peaks (of

lower intensity) are visible but have no clear correlation to an alternative morphology. A larger image of this is given in Figure A3-18. F_{13} and F_{17} are liquids are room temperature and were measured in capillary tubes using Kapton which shows a peak at ~0.45 $Å^{-1}$, indicated by red star. Artefacts are also present (indicated by blue stars) that result from integrating from 1D to 2D due to gaps in detector ranges. These two initiators have no other indication of order other than a slight difference in intensity of the amorphous peak at ~1.2 $Å^{-1}$, a profile for the blank capillary is shown in Figure A3-19. The initiators were not thermally annealed (or solvent annealed) and used as a control for comparison to the polymers.

As mentioned in 1.4, the principal peak position allows the direct calculation of domain spacing (d), which are calculated differently for lamellar and hexagonally packed cylinders. This can also be given as domain size (d^*) (where $d^* = d/2$), which gives the upper limit for the minimum single domain size assuming both domains are equal. Disordered morphologies are treated as LAM domain spacings (d) before conversion to domain size (d^*), therefore, domain sizes show a 'step' in the F_{13}-PAA_m polymers (Figure 3-7).

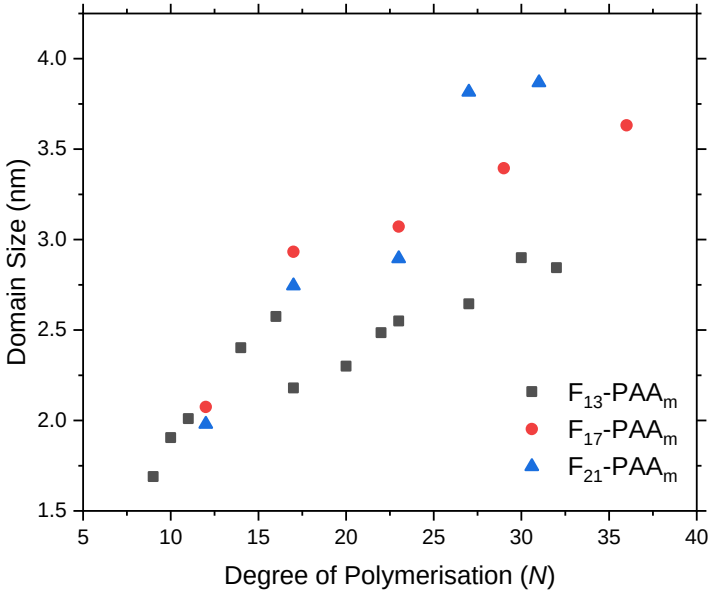

Figure 3-7. Domain size (d^*) versus total degree of polymerisation (N) for all F_n-PAA_m sets.

The domain size increases with increasing PAA chain length for all F_n-PAA_m polymers. The influence of increasing fluorinated segment length is also considered, there is an

increase in domain size with increasing fluorocarbon length, Figure 3-7. This implies a larger fluorinated segment behaves similarly to shorter segments, allowing a correlated increase in fluorinated domain size with increasing the chain length.

Table 3-2. Characteristics of F_n-PAA_m polymers from SAXS measurements.

Polymer F_n-PAA_m	Nano-morphology single data[a]	d^*[a] (single data) (nm)	Nano-morphology <u>before</u> thermal annealing[b]	Nano-morphology <u>after</u> thermal annealing[b]
F_{13}-PAA_4	LAM	1.7	-	-
F_{13}-PAA_5	LAM	1.9	-	-
F_{13}-PAA_6	LAM	2.0	-	-
F_{13}-PAA_9	HEX	2.4	-	-
F_{13}-PAA_{11}	HEX	2.6	-	-
F_{13}-PAA_{12}	DIS	(2.2)	-	-
F_{13}-PAA_{15}	DIS	(2.3)	-	-
F_{13}-PAA_{17}	DIS	(2.5)	-	-
F_{13}-PAA_{18}	DIS	(2.6)	-	-
F_{13}-PAA_{22}	DIS	(2.7)	-	-
F_{13}-PAA_{25}	DIS	(2.9)	-	-
F_{13}-PAA_{27}	DIS	(2.9)	-	-
F_{17}-PAA_6	LAM	2.1	LAM[c]	LAM[c]
F_{17}-PAA_{11}	HEX	3.0	HEX[c]	DIS/HEX[c]
F_{17}-PAA_{17}	HEX	3.1	HEX[c]	HEX[c]
F_{17}-PAA_{23}	HEX	3.4	HEX[c]	HEX[c]
F_{17}-PAA_{30}	HEX	3.7	DIS[c]	DIS[c]
F_{21}-PAA_5	LAM	2.0	LAM	LAM
F_{21}-PAA_{10}	LAM	2.8	LAM	HEX
F_{21}-PAA_{16}	LAM	2.9	LAM	HEX
F_{21}-PAA_{20}	HEX	3.8	HEX	HEX
F_{21}-PAA_{24}	HEX	3.9	HEX	HEX

DIS = disordered, LAM = lamellar, HEX = hexagonally packed cylinders, calculation for HEX given in Experimental, Methods & Calculations. a) Determined by SAXS measurements of single data acquisition samples. d^* = domain size (half-pitch). Domain sizes, bracketed, for disordered morphologies are calculated from the principal peak for completeness, but long-range order is not observed in these samples due to the lack of higher order peaks. b) Morphology observed before and after time-resolved measurements. c) Temperature measurements were recorded with heating/cooling rates of 5 °C/min.

The domain sizes range from 1.7 nm to 3.9 nm across all F_n-PAA_m polymers (Table 3-2) and the morphology changes through LAM, HEX and DIS are shown, typical for block copolymers due to an increase in volume fraction of one block, in this case the fluorinated segment.

3.3 Theoretical modelling

To gain insight into these materials, specifically the dependence of the d on N, a mathematical investigation into the phase behaviour of F_n-PAA_m polymers was conducted using theoretical models.

The very short length of the molecules means that the theoretical treatment for standard block copolymer,[215] which rely on N being large, are unlikely to be appropriate in the present case. To take the shortness of the molecules into account, and the crystalline nature of the F_{21} initiator, it is supposed that the fluorinated segment can be treated as a rod and the PAA segment as a coil. This assumption is supported by simulations of PTFE,[216] which find that these polymers have a Kuhn length of 2.3 nm, which is longer than the molecular length of the fluorinated segment itself and 4-5 times longer than the Kuhn length found for PAA in simulations[217] and experiments.[218] Muller and Schick developed a simple model for block copolymers which includes the limit where incompatibility is high between the two blocks (as proposed for these polymers) based purely on competition between the interfacial free energy and the stretching cost of the coil block,[219] that provides formulae which have been used to fit the domain spacing data for the different F_n-PAA_m morphologies. The formulae have one adjustable parameter which is common to all morphologies (c). The domain spacings of F_{21}-PAA_m polymers in LAM phase were fitted to obtain this parameter, where the justification for the rod-coil model is strongest, this value was then used to predict the domain spacings of all other samples.

The domain spacing in the LAM phase is given by Equation 1:

$$d_L = c\frac{N^{2/3}}{(1-f_F)^{1/3}}, \qquad (1)$$

Here, c is the adjustable parameter. The repeat unit volumes of PAA and PTFE are similar therefore, values of N were used as listed in Table 3-1 and there was no need to normalise it to the repeat unit of one of the segments (as is often used in fits to domain spacing data)[220]. The result of fitting the F_{21}-PAA_m LAM phase is shown with a red line in Figure 3-8.

The calculated value of c was then used to predict the domain spacings for all other F_n-PAA_m polymers. This is suitable as c does not depend on N nor f_F. Polymers with LAM morphologies were predicted using Equation 1, shown as a solid black line

through square data points in Figure 3-8. The prediction for LAM agrees well with the experimental domain spacing for both F_{17}-PAA_m and F_{13}-PAA_m polymers.

The prediction of the rod-coil model for domain spacing in the HEX phase given by equation 2:

$$d_H = 4^{1/3} c \frac{f_F^{1/6}(1-f_F)^{2/3}N^{2/3}}{(1-\sqrt{f_F})(3+\sqrt{f_F})^{1/3}}, \qquad (2)$$

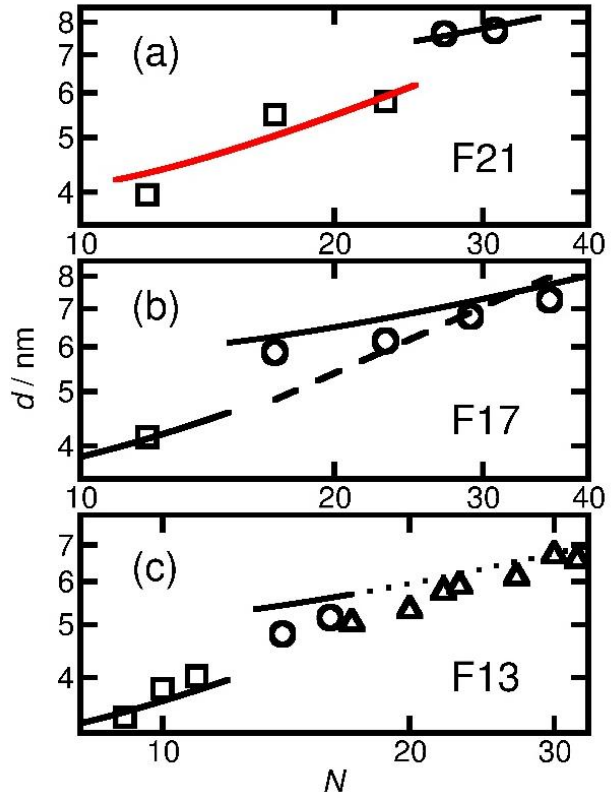

Figure 3-8. Domain spacing (*d*) versus *N* for the thermally annealed (a) F_{21}-, (b) F_{17}- and (c) F_{13}-PAA_m samples. The experimental values are shown by squares for LAM, circles for HEX and triangles when the morphology is uncertain/disordered. For the purposes of comparison with the prediction of the model for the domain spacing in the HEX phase, the inter-plane spacings for the uncertain morphologies have been converted to centre-to-centre distances by multiplication by $2/\sqrt{3}$. The solid red line in (a) shows a fit found using a model of strongly segregated rod-coil polymers. The black solid lines show the predictions of this model, using the value of the fitting parameter from the first fit, for the domain spacing in the other samples. The dashed line in (b) shows a fit assuming the domain spacing is given by $d \propto N^{2/3}$. The prediction for the spacings in (c) whose morphology is uncertain is shown with a dotted line.

The prediction of domain spacing for all HEX F_n-PAA_m polymers, using Equation 2, are shown in Figure 3-8 as a solid black line through circular data points, and is accurate for F_{21}-PAA_m polymers in the HEX phase. Although the numerical values of the prediction for F_{17}-PAA_m are slightly too high, the gradient is reproduced well on a

log-log plot, this is also seen for F_{13}-PAA_m. For comparison, the same HEX data (F_{17}-PAA_m) were fitted to a standard block copolymer coil-coil model which is applicable to all morphologies and under a strong segregation regime using Equation 3[221]:

$$d_{coil,strong} \propto N^{2/3}, \qquad (3)$$

The result of this fit is shown in Figure 3-8 as a black dashed line and has a larger gradient than the experimental data and the rod-coil model prediction. The rod-coil model also gives a better result for the gradient than in the coil-coil weak segregation regime (e.g. due to lower *N*),[222] Equation 4:

$$d_{coil,weak} \propto N^{1/2}, \qquad (4)$$

Figure 3-9 shows the two coil-coil model fits to the F_{17}-PAA_m data (dashed lines) and the rod-coil model prediction using the fitting parameter *c*, obtained from fitting the F_{21}-PAA_m LAM data. The vertical misalignment of the prediction (solid line) is a result of using *c*, whereas the dashed lines are a result of fitting directly to the F_{17}-PAA_m data. However, the rod-coil model (where approximately $d \propto N^{0.3}$) has a shallower slope than either the strong or weak segregation models. The rod-coil model has a better agreement with the experimental data than either (coil-coil) fit despite a linear offset in *d*.

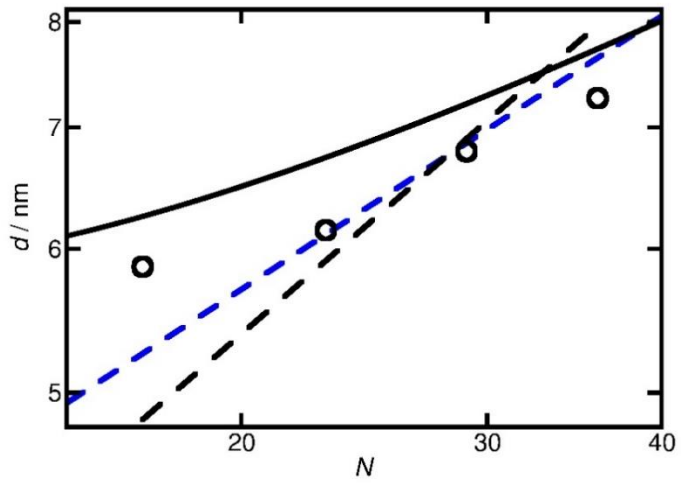

Figure 3-9. Domain spacing (*d*) versus *N* for the thermally annealed HEX F_{17}-PAA_m samples. The solid black line shows the prediction of domain spacing using a model of strongly segregated rod-coil copolymers in the HEX phase, using the value of the fitting parameter (*c*) from the fit to LAM F_{21}-PAA_m polymers. The dashed black line shows the fit using the strong segregation regime for coil-coil copolymers and the dashed blue line the fit using the weak segregation regime for coil-coil copolymers.

The low intensity higher order peaks of the seven F_{13}-PAA_m polymers where N ≥ 17 makes morphology assignment ambiguous. There is evidence from TEM that F_{13}-PAA_{18} (N = 23) forms weakly ordered hexagonally packed cylinders (Figure A3-20), therefore, it is reasonable to compare the domain spacing of these samples with the prediction of the HEX model (Equation 2). These inter-plane distances have therefore been converted into HEX centre-to-centre distances by multiplication by $2/\sqrt{3}$ before plotting, which show good agreement with the HEX model (black dotted line in Figure 3-8). The HEX model prediction agreed well with the nine data points ($N \geq 14$) and shows a shallow slope ($d \propto N^{0.4}$).

Considering only one fitting parameter is used, and the simplicity of the model, the agreement found between experimental data and modelling for all morphologies is very good. The model does not account for the location of the LAM-HEX transition in the current data and predicts it to lie at a much higher value of f_F than seen here, possibly because anisotropic interactions[219] and "shortness" of molecules[223] are not taken into account. Nevertheless, these fits have suggested that all F_n-PAA_m polymers show phase behaviour more like a rod-coil block copolymer than a coil-coil block copolymer in the strong or weak segregation regime.

3.4 Thermal transition investigations

Investigations into order-disorder transitions (ODT) and order-order transitions (OOT) were carried out, as these give insight into the phase behaviour of polymers with a fluorinated segment and a poly(acrylic acid) segment. The transitions are most obvious when the temperature is changed, hence the temperature at which these occur are considered order-disorder and order-order temperatures (T_{ODT} and T_{OOT}). Time-resolved SAXS measurements were performed on bulk polymer samples (as prepared for single acquisition data with no subsequent heating) during thermal annealing. Samples were heated (and then cooled) at 0.5 °C/min from 30 °C to 150 °C to 30 °C and data were collected every 1 minute (i.e. every 0.5 degrees). 0.5 °C/min was the slowest possible ramp rate for the experimental setup, chosen to provide the best chance for the system to attain thermal equilibrium during this thermal anneal process.

3.4.1 F_{21}-PAA_m Time-resolved SAXS measurements

Figure 3-10 shows the heating and cooling cycles for F_{21}-PAA_{10} (other F_{21}-PAA_m data shown in Figure A3-21 - Figure A3-24) measurement progression is given by a colour change from green to red (video representations were created to assist visualising the time-resolved SAXS data[224]). At 30 °C (effectively t = 0 mins), relative peak positions indicate LAM morphology and peak intensity of all peaks is lost as temperature increases. This suggests a loss of ordered morphology, occurring at the T_{ODT}. As χ has an inverse relationship with temperature ($\chi = A + B/T$, where A and B are the enthalpic and entropic contributions for a pair of given entities, respectively), the loss of morphology is expected. Peak intensity returns during the cooling cycle, higher order peaks also reappear which suggests good thermoreversibility (see 3.4.1.1 for a thermoreversibility investigation). All F_{21}-PAA_m samples return to their original morphology (before the thermal anneal process), except F_{21}-PAA_{10} and F_{21}-PAA_{16}. The higher order peaks of these samples change from the relative positions $q = q^*$, $2q^*$, $3q^*$ to $q = q^*$, $\sqrt{3}q^*$, $2q^*$, demonstrating a change in morphology from lamellar (LAM) to hexagonally packed cylinders (HEX). This indicates that HEX is the more thermodynamically stable morphology, and that these samples were kinetically trapped in LAM before the annealing process.

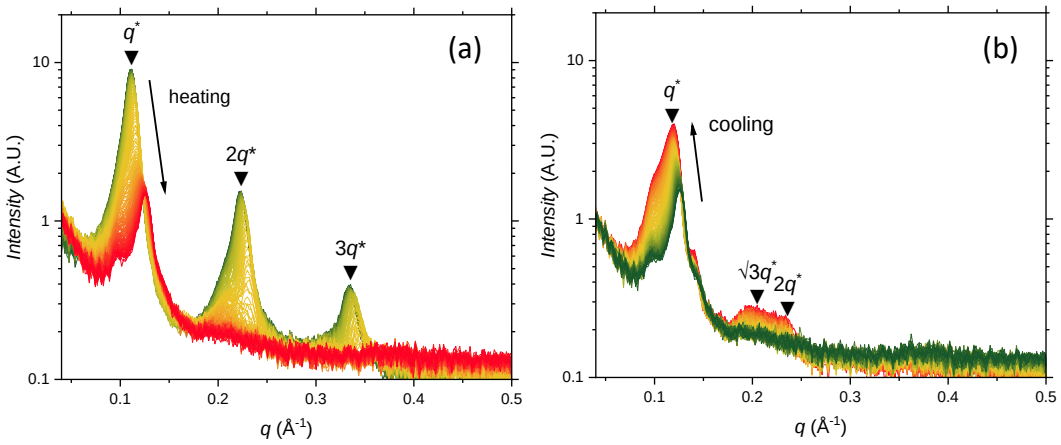

Figure 3-10. Time-resolved SAXS measurements for F_{21}-PAA_{10}. Colour scale from green to red shows the (a) heating cycle (30 °C to 150 °C at 0.5 °C/min) and (b) cooling cycle (150 °C to 30 °C at 0.5 °C/min).

The position of the principal peak (q^*) shifts to higher q values with increasing temperature. This translates to a decrease in domain spacing during heating, which returns to its original position on cooling (F_{21}-PAA_{10} shown in Figure 3-11, other F_n-PAA_m data shown in Figure A3-25). During the heating cycle, there is an interruption to the steady decrease in domain spacing in the form of a small peak at ~ 90 °C, which is unexpected. This is likely due to an OOT which was calculated to occur at 83.5 °C (see section 3.4.2). An explanation for this could be the peak broadening at the OOT has a detrimental effect on the fitting and causes peak position to be altered, which determines domain spacing. There is also evidence of hysteresis, as the domain spacing and principal peak intensity don't fully return to previous values. This evidence, along with the morphology changes stated in the data (Table 3-2) suggests that the polymers are in a kinetically trapped state before thermal annealing and attain (or become closer to) thermal equilibrium when heated.

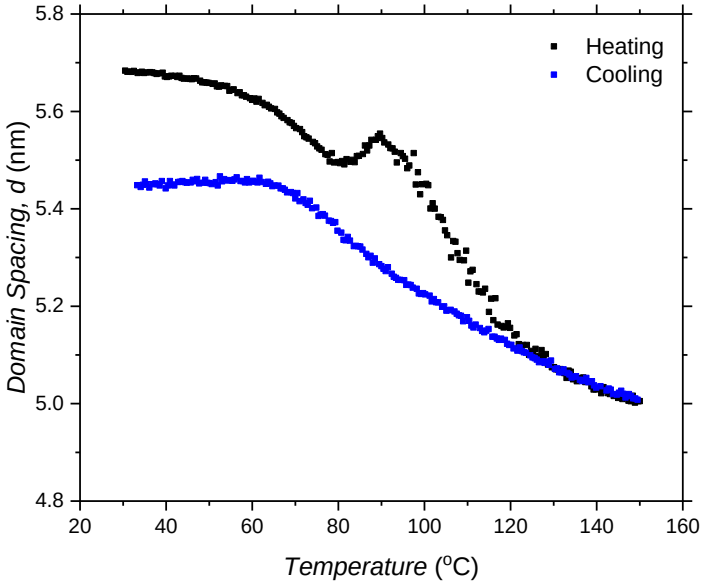

Figure 3-11. Data from time-resolved SAXS measurements of F_{21}-PAA_{10} showing Domain Spacing (*d*) (calculated from fitting of principal peak) against Temperature.

3.4.1.1 F_{17}-PAA_m thermal anneal SAXS measurements

Like the time-resolved SAXS measurements of F_{21}-PAA_m polymers, a preliminary set of thermal anneal experiments were performed using F_{17}-PAA_m. Unlike the F_{21}-PAA_m experiment, samples were heated/cooled at 5 °C/min and measurements were taken every 30 °C. For these reasons, imposed by equipment time constraints, these will be referred to as 'thermal anneal' measurements, not 'time-resolved' measurements. Table 3-3 shows the morphology data obtained from SAXS measurements for all F_{17}-PAA_m polymers.

Table 3-3. Characteristics of F_{17}-PAA_m polymers from SAXS measurements

Polymer F_n-PAA_m	Nano-morphology single data[a]	*d**[a] (single data) (nm)	Nano-morphology <u>before</u> thermal annealing[b]	Nano-morphology <u>after</u> thermal annealing[b]
F_{17}-PAA_6	LAM	2.1	LAM[c]	LAM[c]
F_{17}-PAA_{11}	HEX	3.0	HEX[c]	DIS/HEX[c]
F_{17}-PAA_{17}	HEX	3.1	HEX[c]	HEX[c]
F_{17}-PAA_{23}	HEX	3.4	HEX[c]	HEX[c]
F_{17}-PAA_{30}	HEX	3.7	DIS[c]	DIS[c]

DIS = disordered, LAM = lamellar, HEX = hexagonally packed cylinders, calculation for HEX given in Experimental, Methods & Calculations. a) Determined by SAXS measurements of single data acquisition samples. *d** = domain size (half-pitch). b) Morphology observed before and after time-resolved measurements. c) Temperature measurements were recorded with heating/cooling rates of 5 °C/min.

In order to study the thermoreversibility of these polymers' morphology, F_{17}-PAA_6 was subjected to two heating and cooling cycles (Figure 3-12). Principal peak intensity was found to decrease/increase and peak position moved to higher/lower q values during both heating/cooling cycles, as expected. The higher order $2q$ peak also disappeared and reappeared for F_{17}-PAA_6, indicating an ODT. Principal peaks for other F_{17}-PAA_m polymers (Figure A3-26 - Figure A3-30) show low intensity, due to inherently lower N (lower molecular weight initiator than F_{21} initiator). The lower affinity for microphase separation renders morphology assignment and T_{ODT} calculation troublesome. For this reason, these measurements were not performed on F_{13}-PAA_m polymers.

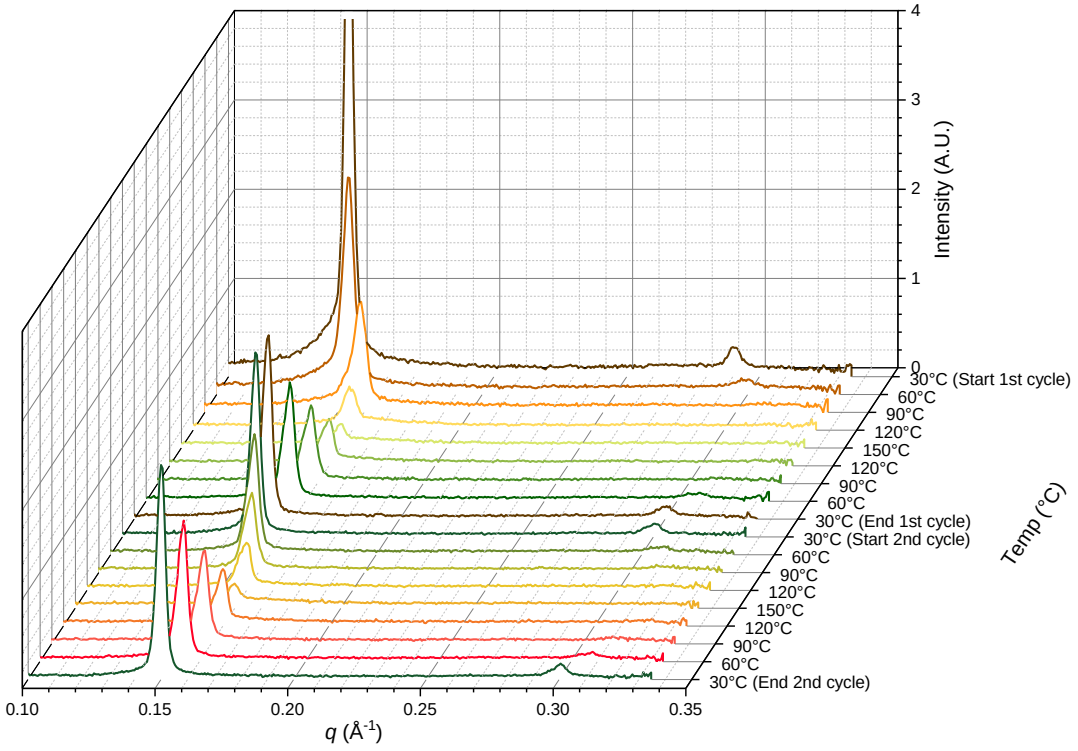

Figure 3-12. Thermal anneal SAXS measurements for F_{17}-PAA_6. Samples were heated (30 °C to 150 °C) and cooled (150 °C to 30 °C) at 5 °C/min, twice.

As F_{17}-PAA_6 was the polymer with the highest expected value of χ, it was anticipated it would have the best chance of microphase separation. For this reason, a second thermal cycle was performed, but only on this polymer. Principal peak intensity and peak position (converted to domain spacing) were determined, Figure 3-13. After the first heating/cooling cycle, both peak intensity and position did not completely revert to starting values, however, full recovery was observed after the second cycle. This implies that the polymer begins in a kinetically trapped state and finds partial thermal

equilibrium after the first heating cycle and completely recovers after the second. This also suggests this process is fully reversible after equilibrium is reached and adjusting heating or cooling parameters could remove the observed hysteresis.

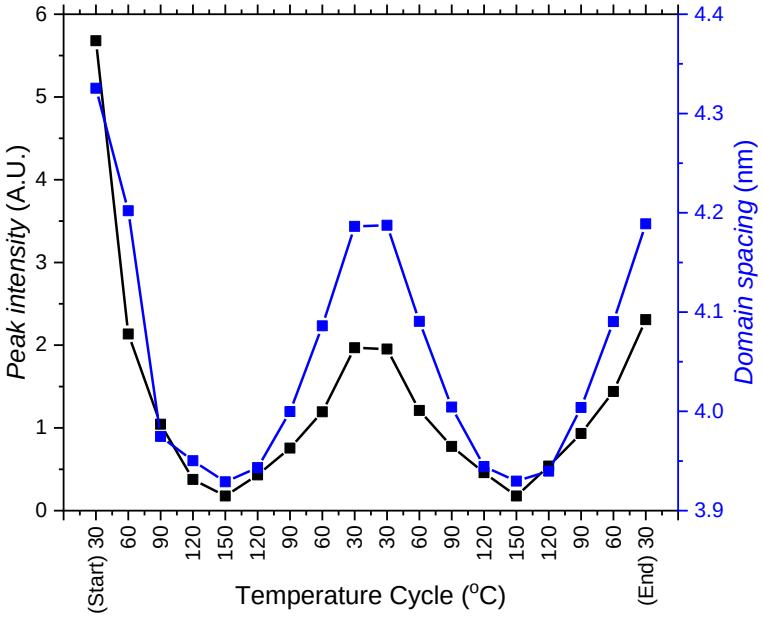

Figure 3-13. Domain spacing and peak intensity calculated from fits (to principal peak) of thermal anneal SAXS measurements of F_{17}-PAA_6, across two heating and cooling cycles (30 °C to 150 °C to 30 °C at 5 °C/min).

3.4.2 T_{OOT}/T_{ODT} calculation

The temperatures at which order-order and order-disorder transitions (T_{OOT}/T_{ODT}) occur were calculated from plots of peak intensity (I_{peak}) and full-width half maximum (FWHM, σ) of the principal peak from thermal anneal SAXS measurements (heating cycle only) against 1/temperature. This plot for F_{21}-PAA_5 is shown in Figure 3-14 (other F_{21}-PAA_m plots in Figure A3-31). The sharp decrease in I_{peak} signifies the temperature in which a transition occurs, corroborated by a sharp increase in $1/\sigma^2$ at the same temperature.

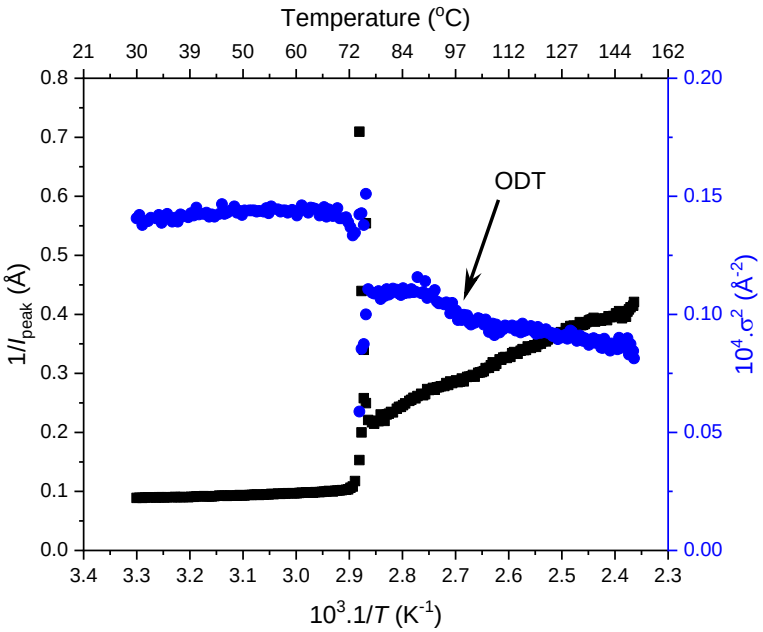

Figure 3-14. Peak intensity (I_{peak}) and full-width half maximum (σ) of the principal peak from thermal SAXS heating cycle vs 1/temperature for F_{21}-PAA_5. Transition temperatures = 73.6 °C and 94.0 °C (T_{ODT}).

In order to determine a value for the transition temperatures, linear trendlines were fitted before, during and after the sharp change in intensity (Figure A3-32 - Figure A3-35). The two intersections were calculated and in addition to a midpoint between them, this was converted to Celsius and stated as the transition temperature value in Table 3-4. Transitions were only calculated for 4 samples (those with highest f_F and lowest N) as polymers with higher PAA content are less ordered. The change in q^* intensity is insufficient to fit three distinguishable straight lines, due to the lack of discernible phase transition.

Table 3-4. F_n-PAA_m polymer thermal characteristics.

Polymer F_n-PAA_m	$T_{OOT,\ midpoint}$ (°C)	$T_{ODT,\ midpoint}$ (°C)	T_g[a] (°C)
F_{17}-PAA_6	-	-	52.1
F_{17}-PAA_{11}	-	-	78.8
F_{17}-PAA_{17}	-	-	100.0
F_{17}-PAA_{23}	-	-	108.4
F_{17}-PAA_{30}	-	-	111.6
F_{21}-PAA_5	73.6	94.0[b]	77.9
F_{21}-PAA_{10}	83.5[c]	87.4	86.9
F_{21}-PAA_{16}	-	102.9	99.5
F_{21}-PAA_{20}	-	105.8	109.6
F_{21}-PAA_{24}	-	-	110.0

a) Taken from DSC data. b) Calculated from FWHM of fitted principal peak in time-resolved SAXS measurements. c) Calculated from FWHM of fitted second (first higher order) peak in time-resolved SAXS measurements.

As F_{21}-PAA_{10} is a special case in which an OOT and ODT can be seen by eye when examining the first higher order peak, the OOT was calculated from this peak. Figure 3-15 shows an expansion of the second peak from Figure 3-10a (at ~0.22 $Å^{-1}$). Before the heating process, the peak has a relative position at $2q^*$ indicating LAM morphology. During heating, a peak at $\sqrt{3}q^*$ appears at approximately 79 °C while the $2q^*$ peak is still present, suggesting a gradual change in morphology to HEX, an OOT and gives a degree of confidence in the phase boundaries presented in the phase diagram (see section 3.5). Such thermally induced transitions can be understood using the phase diagram, since an increase in temperature corresponds to a downwards move in the phase diagram (as $\chi = A + B/T$). At temperature >84.4 °C, the $2q^*$ peak disappears with the $\sqrt{3}q^*$ still present (still HEX), the $\sqrt{3}q^*$ peak then disappears at between 84.4-100 °C, this is the ODT.

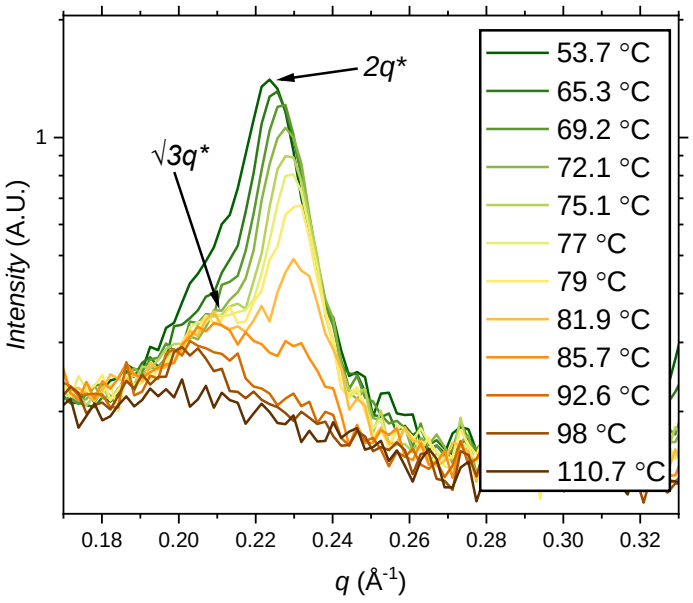

Figure 3-15. Expansion of the second peak in Figure 3-10, showing the order-order transition.

Peak fits were obtained for all traces in the heating cycle of the time-resolved SAXS experiment. This makes the FWHM particularly useful, which is largest when two peaks are present but are fit as one. Figure 3-16 shows the FWHM and intensity with increasing temperature, during the heating cycle. As the fitted peak decreases in intensity until it disappears, all data points above approximately 100 °C can be ignored (these fits either have a very large error or are fitting noise).

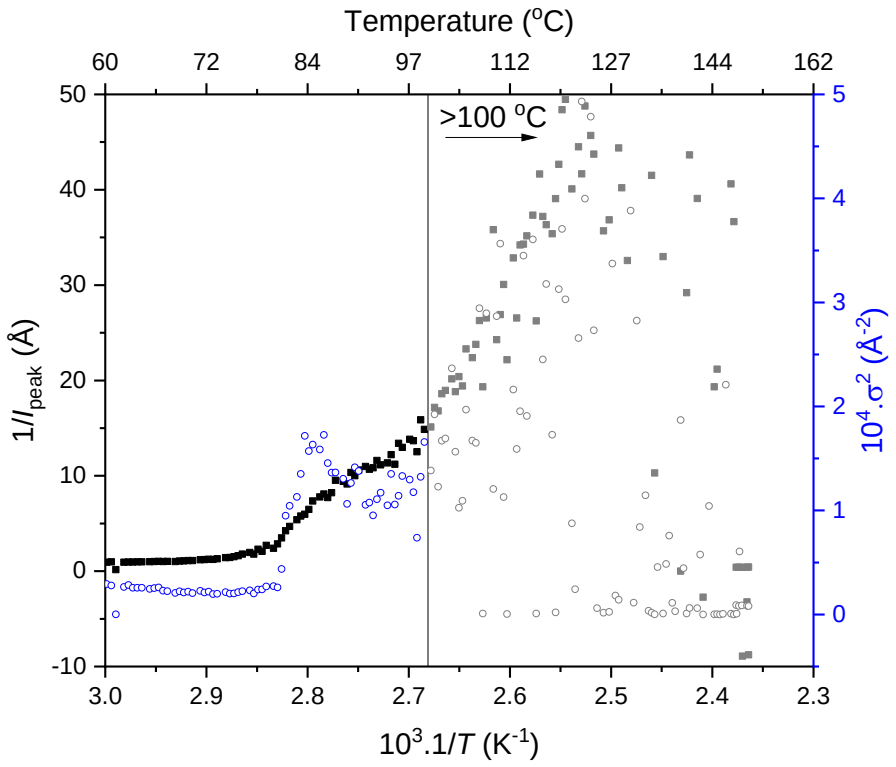

Figure 3-16. Peak intensity (I_{peak}) and full width half maximum (σ) of the second peak (first higher order peak) from thermal SAXS heating cycle vs 1/temperature for F_{21}-PAA_{10}. Transition temperatures = 83.5 °C (T_{OOT}) and 87.4 °C (T_{ODT}). Data points >100 degrees can be ignored due to peak loss.

The OOT occurs as 1 peak ($2q^*$) becomes 2 peaks ($2q^*$ and $\sqrt{3}q^*$) in the SAXS profile, during the morphology change from LAM to HEX, followed by an ODT occurring as 2 peaks ($2q^*$ and $\sqrt{3}q^*$) become 1 ($\sqrt{3}q^*$) then disappear altogether during the change from HEX to DIS. The peak intensity is invariant up to ~79 °C, after which it decreases sharply up to ~88 °C, the midpoint of these two changes is the T_{OOT} (83.5 °C). The intensity then begins to plateau before another sharp decrease at ~97.4 °C, corresponding to the loss of the $2q^*$ peak and the T_{ODT} (which cannot be determined from this plot due to the error associated with data >100 °C). The FWHM also remains constant up to ~79 °C, then increases as the $\sqrt{3}q^*$ peak appears. As the $2q^*$ decreases in intensity until it disappears, the FWHM decreases to reflect the presence of the $\sqrt{3}q^*$ peak only. Above this temperature (~84.4 °C), the ODT occurs and the $\sqrt{3}q^*$ peak fully disappears. Again, no value can be calculated for the T_{ODT} from this plot as data becomes unreliable >100 °C; the T_{ODT} value reported in Table 3-4 was obtained from fits to the principal peak. The linear fit used to obtain the T_{OOT} are shown in Figure A3-36 – Figure A3-37.

3.5 Experimental phase diagram

An experimental phase diagram was constructed using the morphology data obtained from single-acquisition SAXS measurements (Table 3-2), including the data for F_{13}-PAA_m polymers mentioned in Chapter 1 (Figure 3-17). Typical phase diagrams use χN as the y-axis, on the basis that χ is a constant value, at a given temperature, for a set of polymers with the same type of block interaction i.e., PAA and PTFE. Therefore, the shape of this phase diagram (plotted N versus F_f) can be directly compared to those in the literature. The colour bar indicates domain size (d^*) for samples that phase separated into ordered morphologies, disordered samples are shown as open data points. Domain sizes typically decrease on decreasing N and increasing F_f across the range of polymers in this study, attributed to the shorter molecular lengths associated with low N and tighter packing of rod segments.

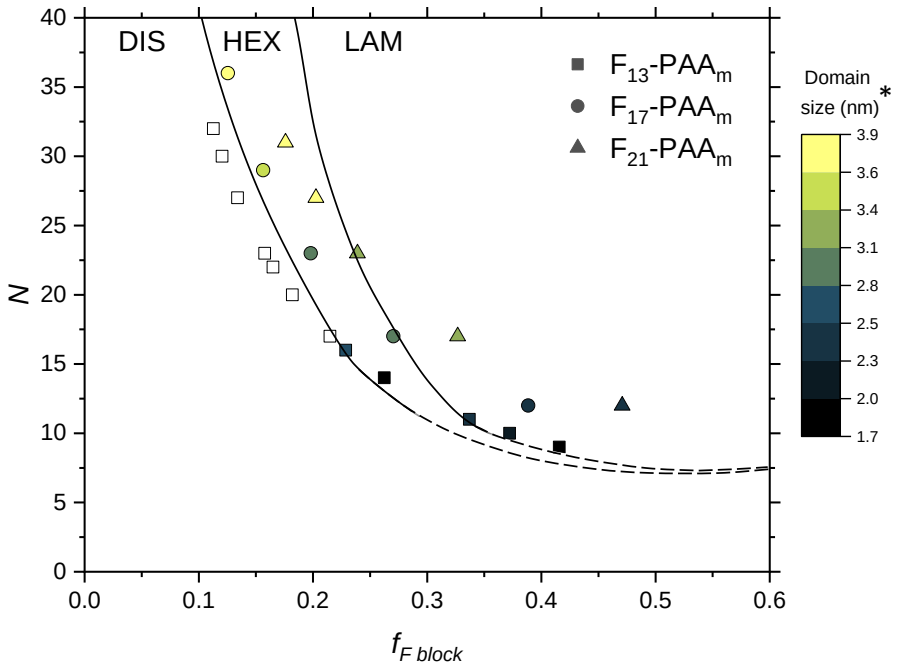

Figure 3-17. Phase diagram for the F_n-PAA_m polymers. Morphologies taken from single data SAXS acquisition after thermal annealing. DIS = disordered, HEX = hexagonally packed cylinders, LAM = lamellae. Note that the phase boundaries are not absolute and are only a guide to the eye. *The domain size (d^*) is estimated as the half-pitch, which provides the upper limit for the minimum single domain size assuming that both domains are equal.

Three regions of morphology were identified, and lines were placed as phase boundaries between these regions as a guide to the eye but it is noted that these are

not absolute. A solid line was used to discern more certain areas (where data points either side show different morphologies), and dashed lines for uncertain areas. F_{13}-PAA_m polymers where N = 14 & 16 are weakly ordered HEX according to SAXS data, suggesting these points are close to the HEX-DIS phase boundary. The morphology changes observed during the slow ramp rate give an approximate indication of the phase boundaries. F_{21}-PAA_{10} shows an OOT, which is represented by a shift downwards on the phase diagram due to a decrease in χ on heating (Figure A3-38 and section 3.4.2). The phase diagram shows a strong resemblance to the theoretical phase diagram of a rod-coil block copolymer with no liquid crystal alignment,[225] highlighting the similarity in phase behaviour between these amphiphilic homopolymers and rod-coil block copolymers. Constructing this phase diagram enables reproducible targeting of specific nanomorphologies with desired domain sizes, a particularly powerful tool in material design and synthesis.

3.6 Atomic force microscopy (AFM)

AFM is a complementary technique which can be used in combination with scattering methods when investigating new and unknown samples/morphology. The F_{21}-PAA_m series were investigated by AFM on different substrates and under different annealing conditions. F_{21}-PAA_{10} was chosen as a standard for investigating differences in annealing and comparisons to F_{13}-PAA_{11} topography (section 2.5) due to the similar length PAA.

Figure 3-18 shows AFM topography images of F_{21}-PAA_{10} prepared on Mica using different solvent vapour annealing conditions. These images are comparable to F_{13}-PAA_{11} (Figure 19, Chapter 1) which were prepared in a similar manner, the difference being the fluorinated tail length (f_F = 0.23 *vs* 0.33) and the volume of solution spin-coated (20 μl *vs* 50 μl). There is little difference observed between the samples prepared with no annealing and annealing in H_2O, which was not apparent for F_{13}-PAA_{11}. Fibrous alignment is visible in the 1:1 vol. H_2O:MeOH anneal, and no long-range structure can be discerned within the methanol annealed sample, which is similar to images obtained for F_{13}-PAA_{11}. Overall, smaller features are visible for F_{13}-PAA_{11}, suggesting that either polymers with lower f_F allow better microphase separation on spin-coated substrates, the AFM tip was of poorer quality or damaged (possibly due to different hydrophobicity levels on the surface), f_F alters the structure in solution prior to spin-coating, or a combination of these points.

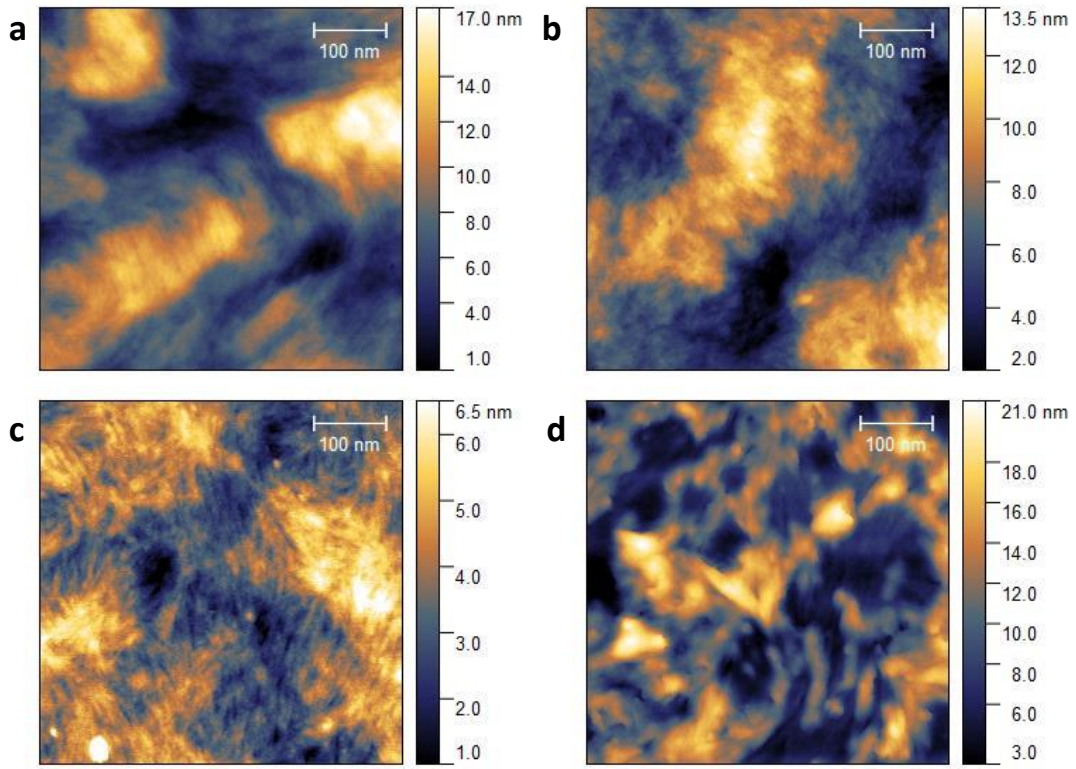

Figure 3-18. Atomic force microscopy (AFM) topography (Bruker Icon) of F_{21}-PAA_{10} annealed by a) no anneal b) H_2O c) 1:1 vol. H_2O:MeOH d) MeOH. Solution conditions: 50 µl of 5 wt% polymer in MeOH on Mica.

The influence of the type of supporting substrate was also investigated using AFM. The same polymer (F_{21}-PAA_{10}) was spin-coated using the same conditions but on a glass slide with both 2.5 wt% and 5 wt% solutions (Figure A3-39 - Figure A3-40), showing minimal differences. Despite the evidence of fibrous structure for the H_2O and 1:1 vol. H_2O:MeOH annealed samples, all images show the same underlying topography seen in the non-annealed sample. This implies the no anneal shows a convolution of the topography of the glass slide itself and is present in all images. Therefore, Mica as the substrate (due to a lower RMS roughness) and 2.5 wt% solutions were used as standard conditions for the remainder of the work.

After considering the results of AFM measurements above, the annealing solvent mix chosen to investigate the effect of increasing PAA chain length was 1:1 vol. H_2O:MeOH as it consistently showed visible fine structure in both F_{21}-PAA_m and F_{13}-PAA_m polymers. Figure 3-19 shows AFM topography images of all F_{21}-PAA_m polymers annealed using this mixture. F_{21}-PAA_5 shows large, flat terraces which are not present

in other images and a height distribution was calculated, showing an average layer height of 2.8 nm (Figure A3-41). In SAXS, this polymer showed lamellar morphology with a domain size of 2.0 nm, in reasonable agreement with step heights in the topography. F_{21}-PAA_{10} showed markedly different topology depending on the area of the substrate being examined, the right image of Figure 3-19b shows a fairly flat surface but with a random array of holes. The height profile (across the holes) consistently shows a layer height of ~ 1 nm (Figure A3-42). The left image of Figure 3-19b shows fibre-like features. The presence of different local topologies (and morphologies) is possible if this polymer is close to a phase boundary (for this sample preparation), so evidence of both structures could be present in one sample. There is little change to the topology when DP ≥ 16, only less overall preferential orientation of the rod-like structures. However, F_{21}-PAA_{20} shows a higher degree of long-range ordered features than other samples F_{21}-PAA_{16} & F_{21}-PAA_{24}, this may also be a result of its location in the phase diagram.

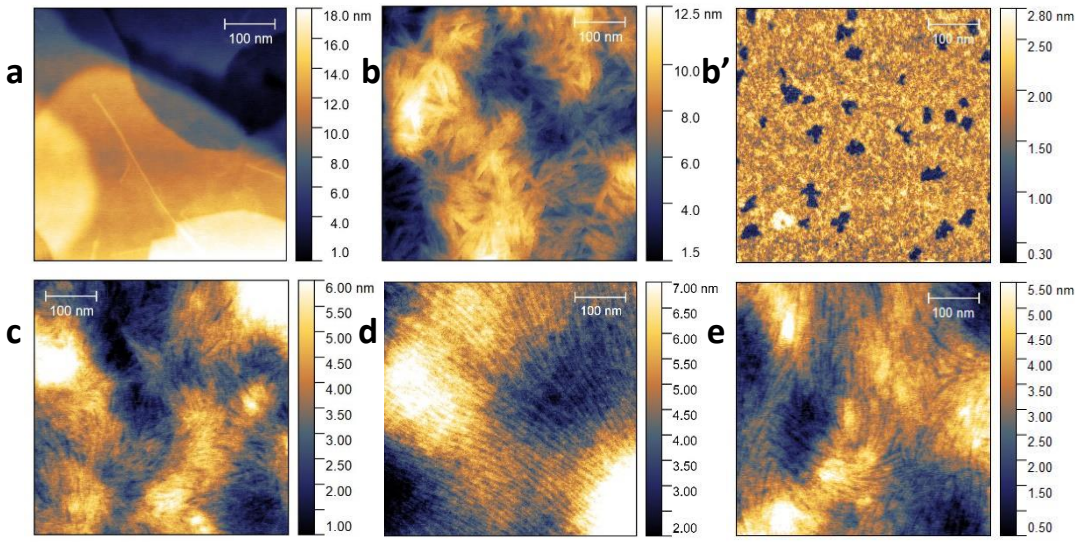

Figure 3-19. Atomic force microscopy topography (Bruker Icon) of a) F_{21}-PAA_5 b/b') F_{21}-PAA_{10} c) F_{21}-PAA_{16} d) F_{21}-PAA_{20} e) F_{21}-PAA_{24}, all annealed 1:1 vol. H_2O:MeOH. Solution conditions: 40 µl of 2.5 wt% polymer on Mica.

The long-range order present in F_{21}-PAA_{20} samples was further investigated. Figure 3-20a shows F_{21}-PAA_{20} prepared in the same manner as Figure 3-19d, revealing the same structures and long-range order over a larger scan area (1 µm). The same sample analysed on an alternative microscope (Figure 3-20b) and using a different tip, shows the same features and proves definitively that these hair-like features are real.

Mechanical properties were also tested on this sample (Figure A3-43) to determine if different phases are discernible by their different physical properties. Adhesion and energy dissipation images show areas of high and low pN and eV which directly correlate; different phases are distinguishable by the methods used here (unless peaks/troughs in topography have direct influence on these measurements).

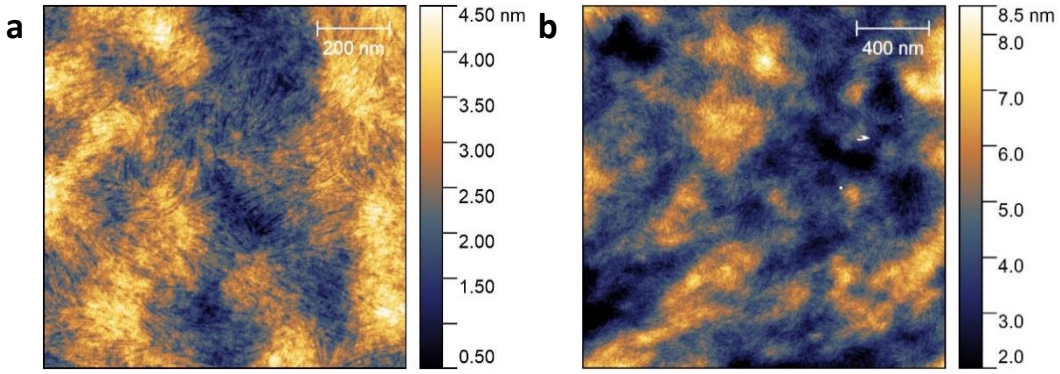

Figure 3-20. Atomic force microscopy topography of F_{21}-PAA_{20} annealed 1:1 vol. H_2O:MeOH. Solution conditions: 40 µl of 2.5 wt% polymer on Mica. Images were recorded on a) Bruker Icon and b) Bruker Innova.

A EBiB-initiated poly(acrylic acid) (F_0-PAA_{15}) was also measured to study the influence of the fluorinated tail on any morphology and phase transition. A sample was prepared and annealed in 1:1 vol. H_2O:MeOH and then compared to F_{13}-PAA_{11} and F_{21}-PAA_{10} which were prepared concomitantly. The topography (Figure A3-44) is similar for all samples and shows fibre-like rods and is mostly likely produced (this topographic feature) by this annealing method. These fibres appear, without quantitative analysis, to be thicker in the F_{21}-PAA_{10} sample, likely due to the longer fluorinated tail.

3.6.1 F_{21}-PAA_m (with NaOH) in water

The stability (and morphology) of the fluoro-acrylic acid polymers in water was investigated via AFM imaging. NaOH was added to THF polymer solutions and solvent exchanged for water to increase the ionic nature of the polymers. Five samples were prepared using F_{21}-PAA_{10}, where different volumes of NaOH were added to neutralise different ratios of acrylic acid units. These ratios were R=0, 0.2, 0.4, 0.6, 1, 3, where R=3 represents a 3-fold excess of NaOH molecules to acrylic acid units and R=0 included no addition of NaOH.

Unfortunately, changing the molar ratio of neutralised acrylic acid units shows no clear trend in the AFM images, Figure 3-21. All images show a holey membrane of consistent height with some aggregates/crystallites depending on the location of the imaging area. It's possible that the holey membrane structures are an artifact of water drying on the Mica, leaving a patterned residue. Though all images are shown with the same dimensions (scale bar = 5 μm), there is no consistency or trend in the size of the holes or their uniformity. AFM samples were also measured 24 hours after the solutions were prepared, as it was thought that given time the polymers may reassemble into more thermodynamically stable structures. This only resulted in a higher concentration of aggregates and a more clustered arrangement of holes, seen across all samples, Figure 3-22.

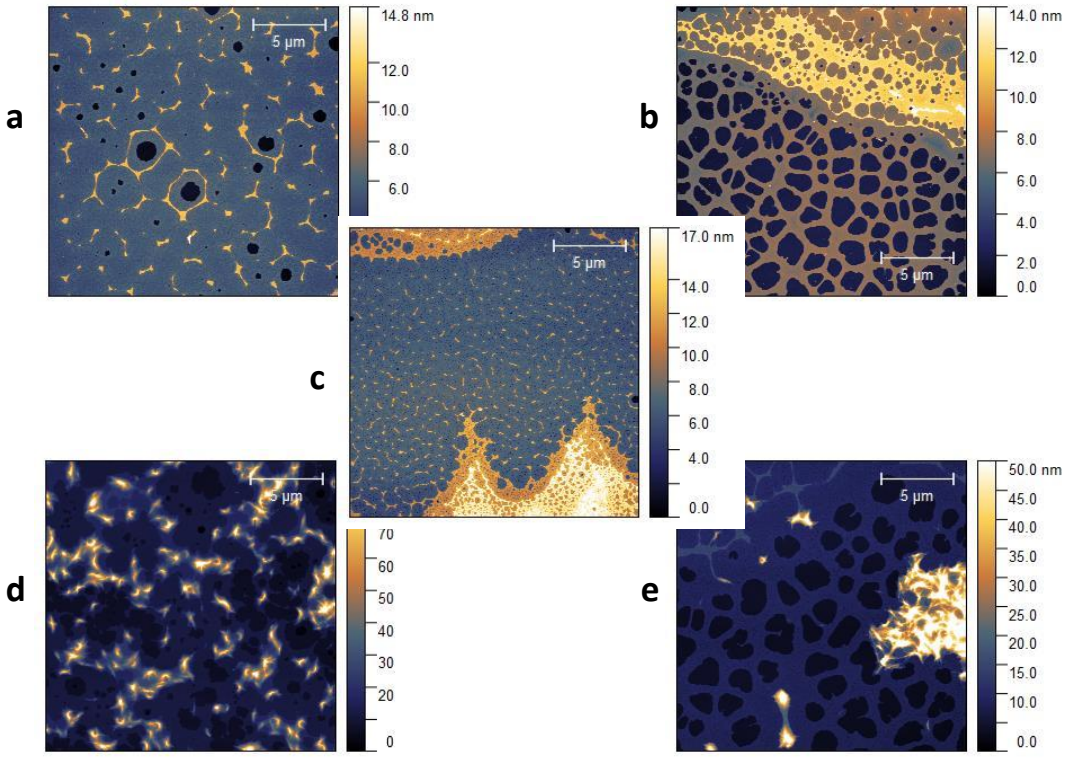

Figure 3-21. Atomic force microscopy topography of F_{21}-PAA_{10} in water with different molar ratios of NaOH to acrylic acid units. a) R=0. b) R=0.2. c) R=0.6. d) R=1. e) R=3. AFM images were measured within 1 hour of solution preparation.

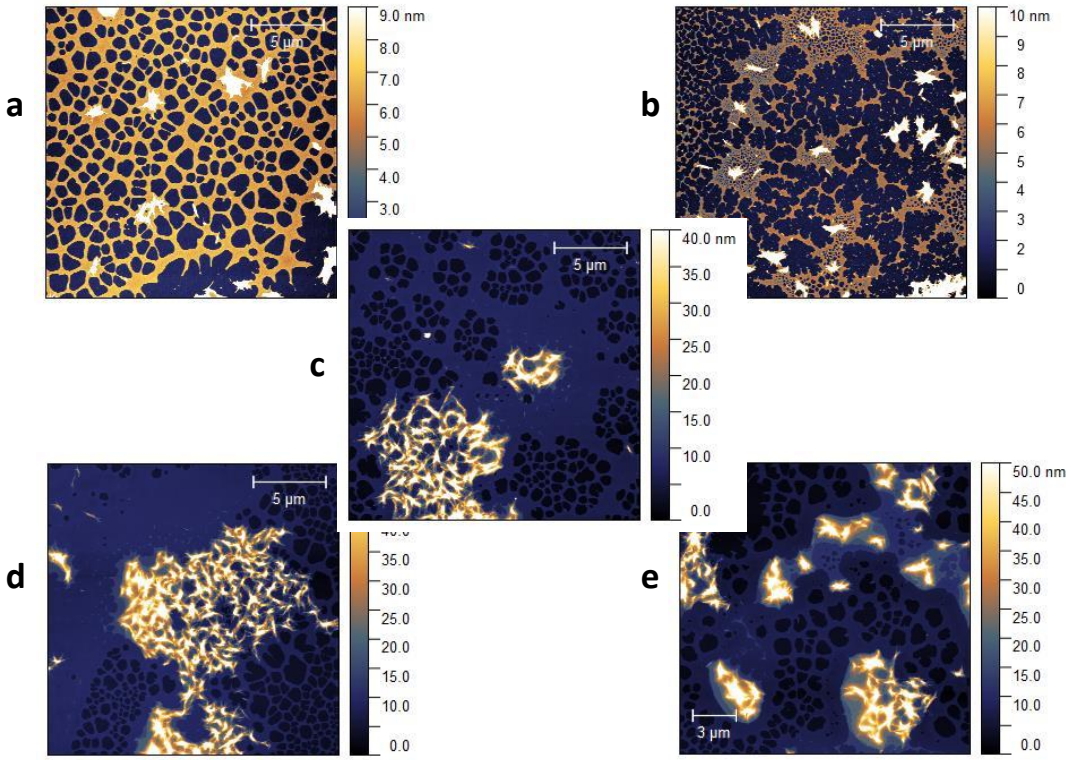

Figure 3-22. Atomic force microscopy topography of F_{21}-PAA_{10} in water with different molar ratios of NaOH to acrylic acid units. a) R=0. b) R=0.2. c) R=0.6. d) R=1. e) R=3. AFM images were measured after 24 hours of solution preparation.

3.7 Conclusions

In this chapter, fluorinated alkyl halide initiators with higher fluorine content were synthesised and used to polymerise a library of fluoro-acrylic acid polymers of differing segment volume fractions, which ranged from f_F = 0.47 – 0.11, obtained with low dispersity ($Đ$ =1.06 – 1.24), low molecular weight (M_n = 1400 – 4100 g mol^{-1}) and achieved high conversion (>99%) All were annealed into thick films and measured using SAXS, showing lamellae, hexagonally packed cylinders and disordered phases and polymers with larger fluorine content showed the strongest microphase separation with lower domain spacings (1.7 – 3.9 nm accounting for morphology), indicative of a high χ value. Theoretical modelling was applied to single acquisition SAXS measurements, which supported the rod-coil phase behaviour rather than the coil-coil model, in both the strong and weak segregation regime. Time-resolved SAXS measurements were performed on F_{21}-PAA_m polymers (those with highest f_F), which revealed order-disorder transition temperatures which increased with increasing polymer chain length, and order-order transition temperature for F_{21}-PAA_5 and F_{21}-PAA_{10}. Also, two polymers changed morphology during the time-resolved measurements, suggesting that the heating process (essentially a thermal anneal) allowed the polymer to approach/attain thermal equilibrium. Finally, a phase diagram was constructed from known morphology, f_F, and N, which can be used as a tool for targeting specific morphologies and domain sizes.

3.8 Appendix

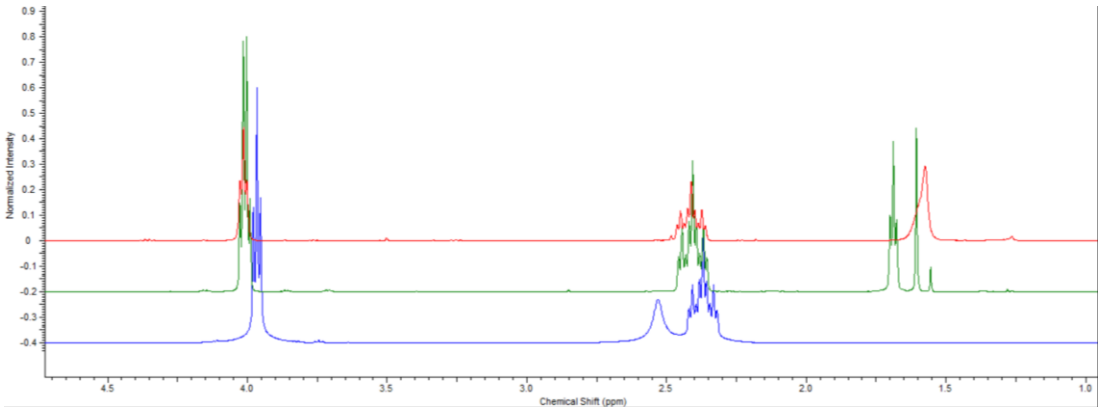

Figure A3-1. ^{1}H NMR spectrum (500 MHz, $CDCl_3$) of fluorinated alcohols (1H,1H,2H,2H-perfluoro-1-octanol, 1H,1H,2H,2H-perfluoro-1-decanol, 1H,1H,2H,2H-perfluoro-1-dodecanol) in $CDCl_3$.

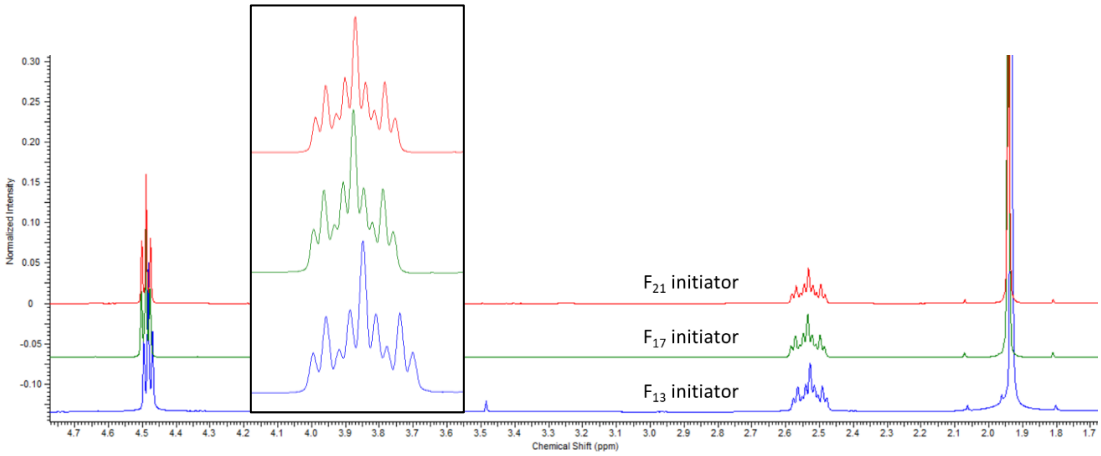

Figure A3-2. ^{1}H NMR spectrum (500 MHz, $CDCl_3$) of F_{13}, F_{17} & F_{21} initiators in $CDCl_3$. Inset shows expansion of 2.7 – 2.4 ppm region.

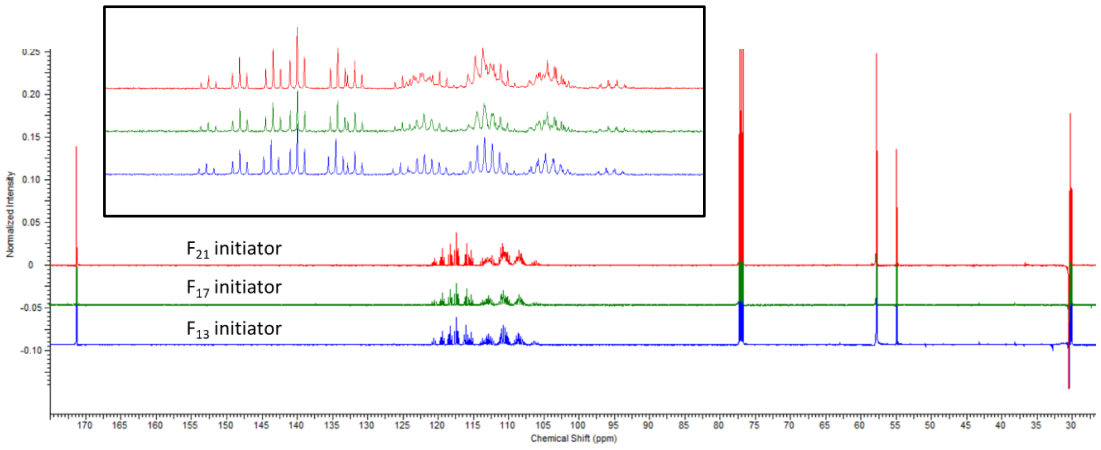

Figure A3-3. ^{13}C (APT) NMR spectrum (500 MHz, $CDCl_3$) of F_{13}, F_{17} & F_{21} initiators in $CDCl_3$. Inset shows expansion of 124 – 104 ppm region.

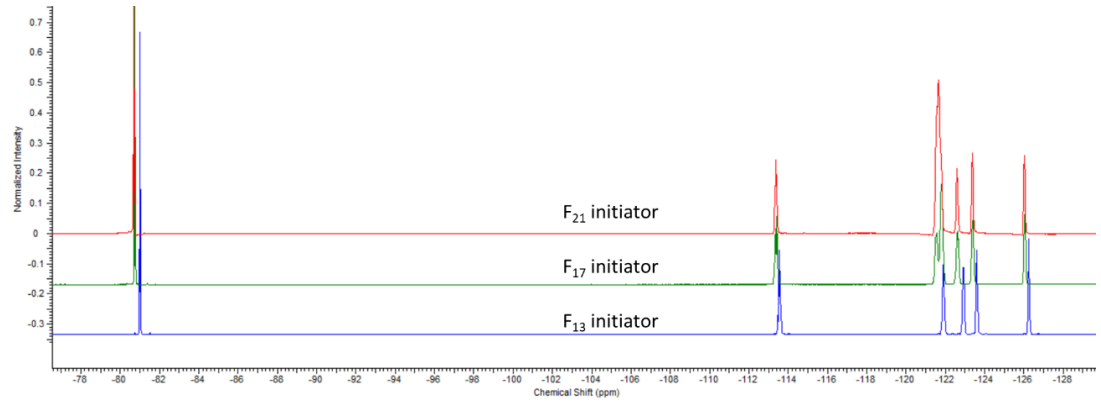

Figure A3-4. ^{19}F NMR (coupled) spectrum (400 MHz, $CDCl_3$) of F_{13}, F_{17} & F_{21} initiators in $CDCl_3$.

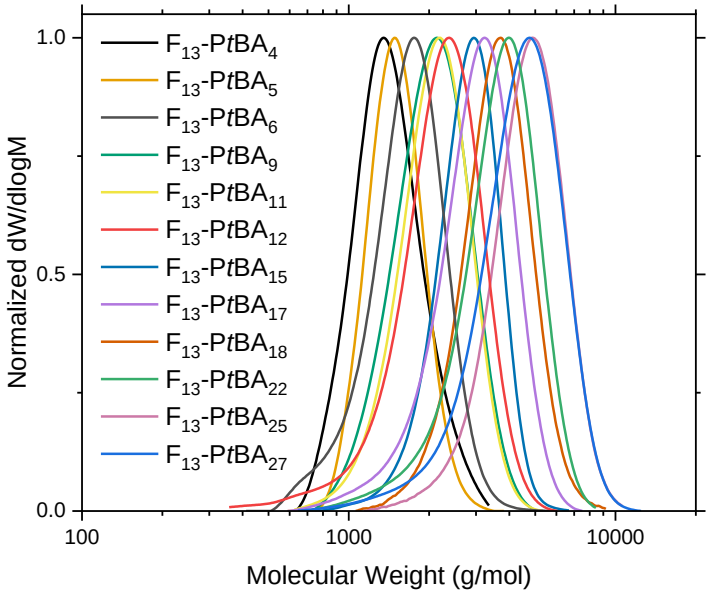

Figure A3-5. GPC traces of F_{13}-P*t*BA$_m$ recorded in THF eluent.

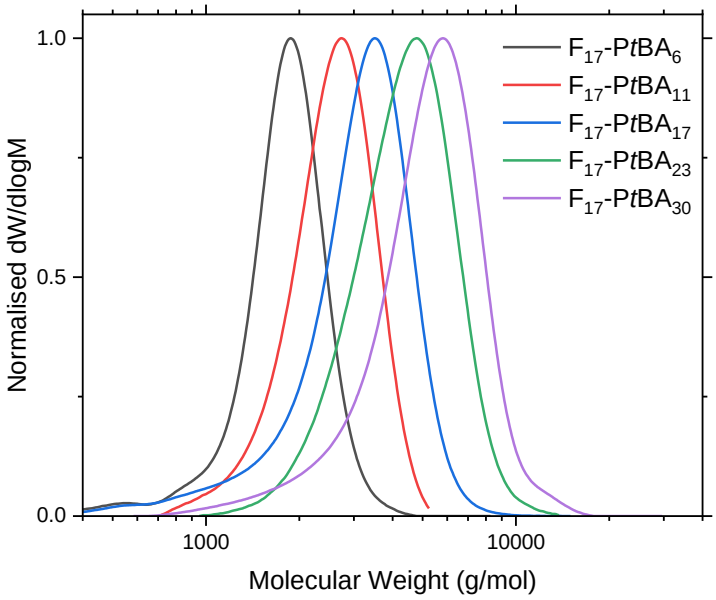

Figure A3-6. GPC traces of F_{17}-P*t*BA$_m$ recorded in THF eluent.

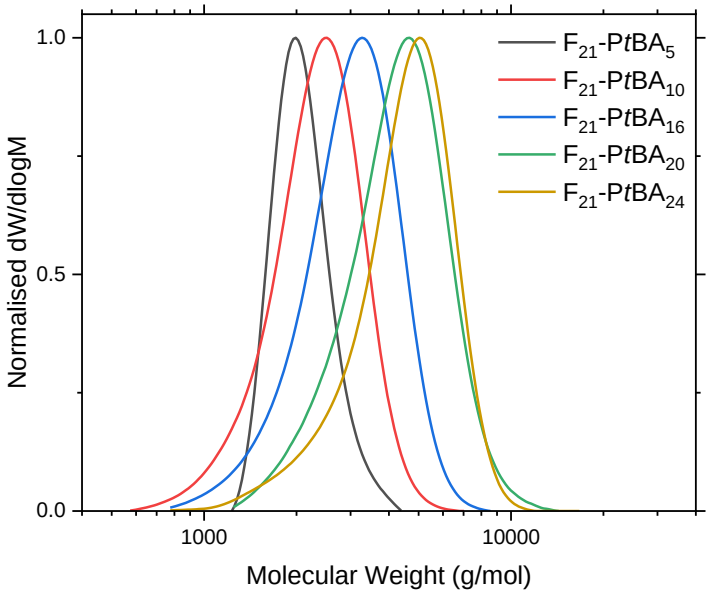

Figure A3-7. GPC traces of F_{21}-P*t*BA$_m$ recorded in THF eluent.

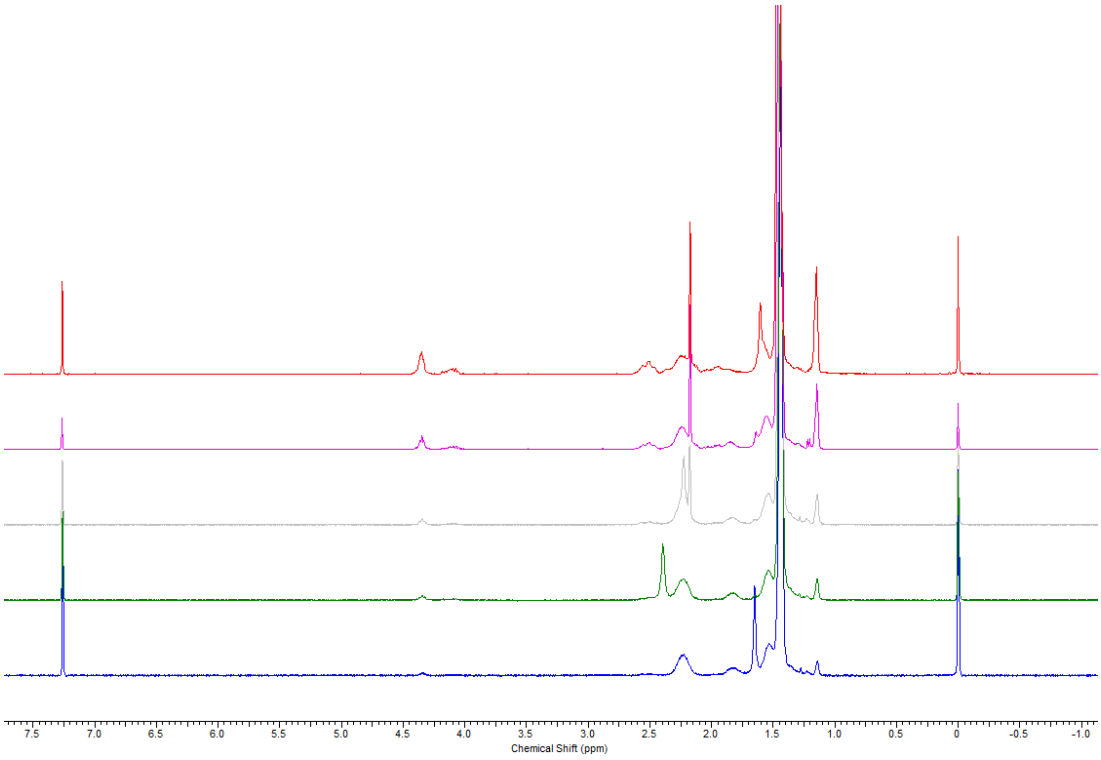

Figure A3-8. ^{1}H NMR spectrum (400 MHz, $CDCl_3$) of F_{13}-P*t*BA$_m$ in $CDCl_3$. m = 6, 12, 17, 22, 27 from top to bottom.

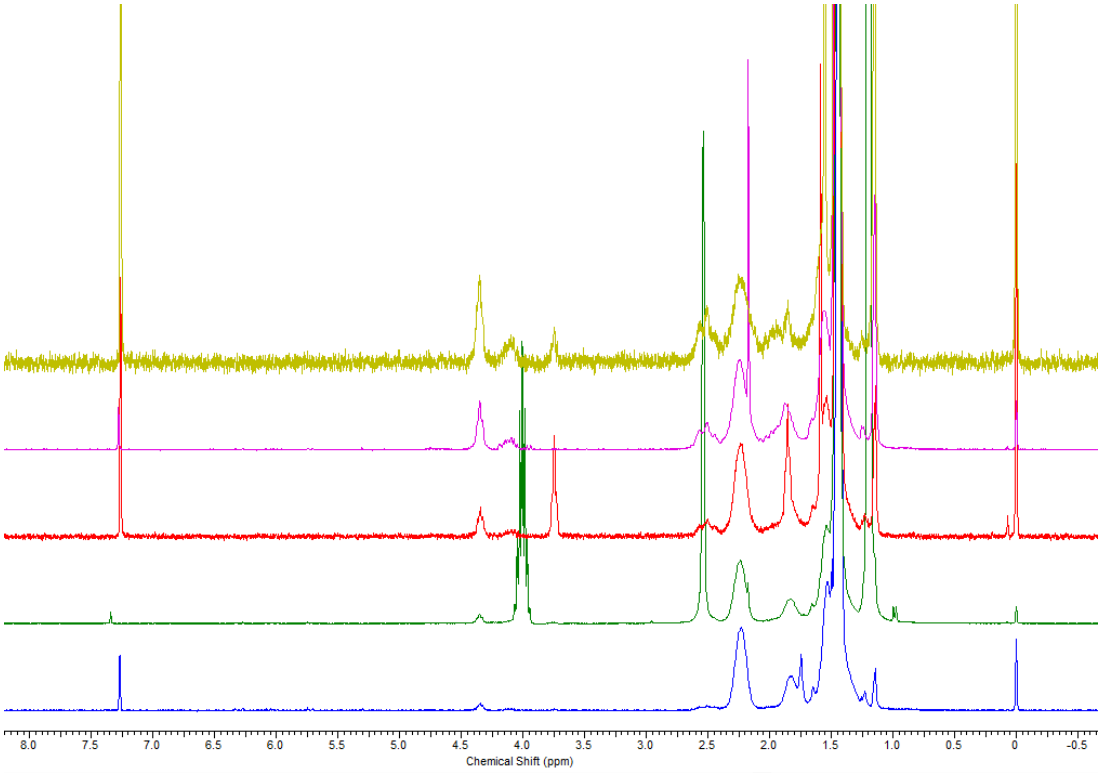

Figure A3-9. ^{1}H NMR spectrum (400 MHz, $CDCl_3$) of F_{17}-P*t*BA$_m$ in $CDCl_3$. m = 6, 11, 17, 23, 30 from top to bottom.

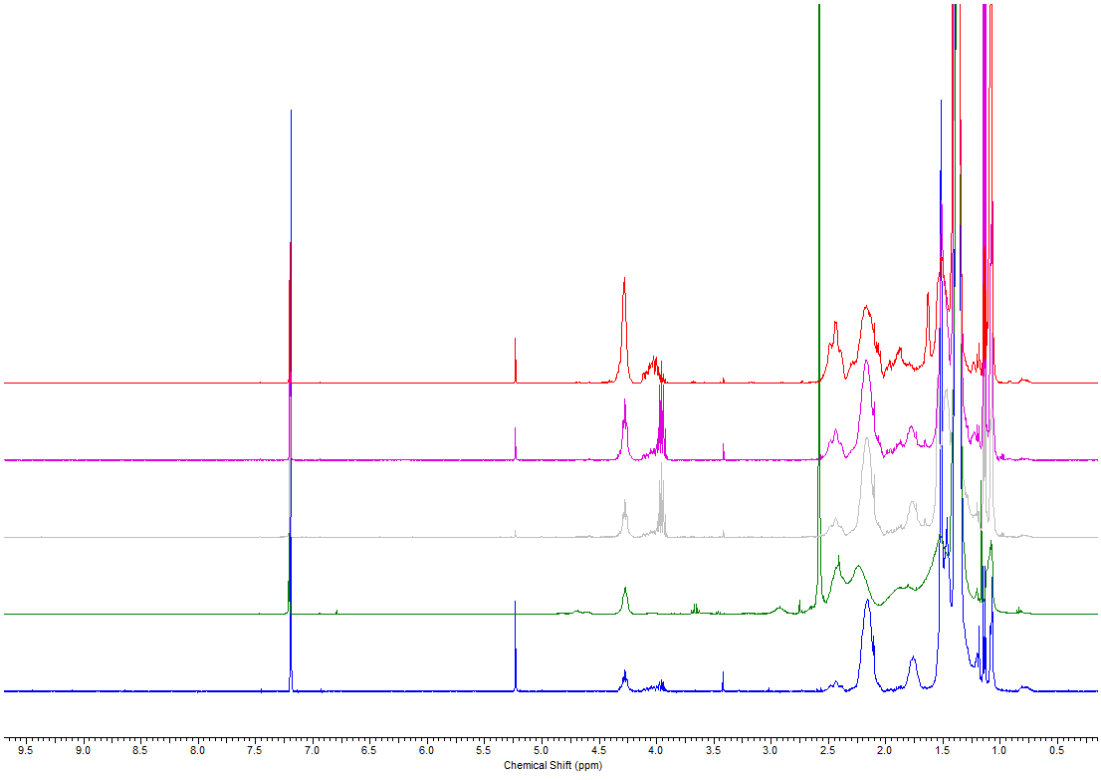

Figure A3-10. ^{1}H NMR spectrum (400 MHz, $CDCl_3$) of F_{21}-P*t*BA$_m$ in $CDCl_3$. m = 5, 10, 16, 20, 24 from top to bottom.

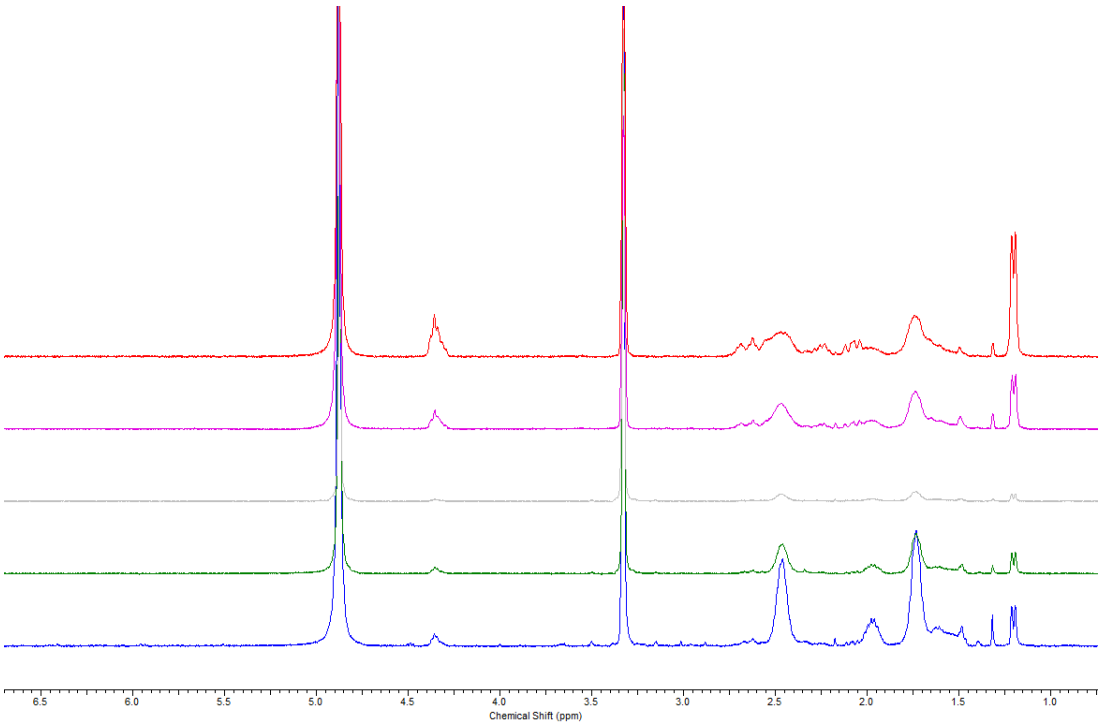

Figure A3-11. ^{1}H NMR spectrum (400 MHz, $CDCl_3$) of F_{13}-PAA_m in MeOD. m = 6, 12, 17, 22, 27 from top to bottom.

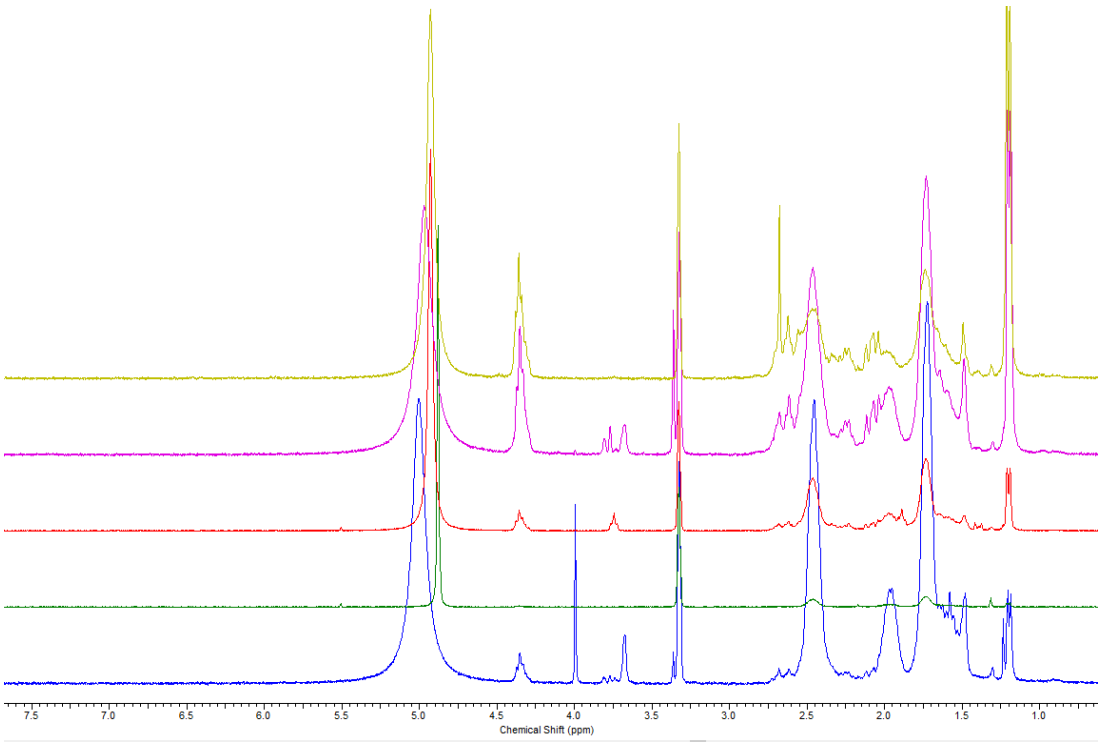

Figure A3-12. ^{1}H NMR spectrum (400 MHz, $CDCl_3$) of F_{17}-PAA_m in MeOD. m = 6, 11, 17, 23, 30 from top to bottom.

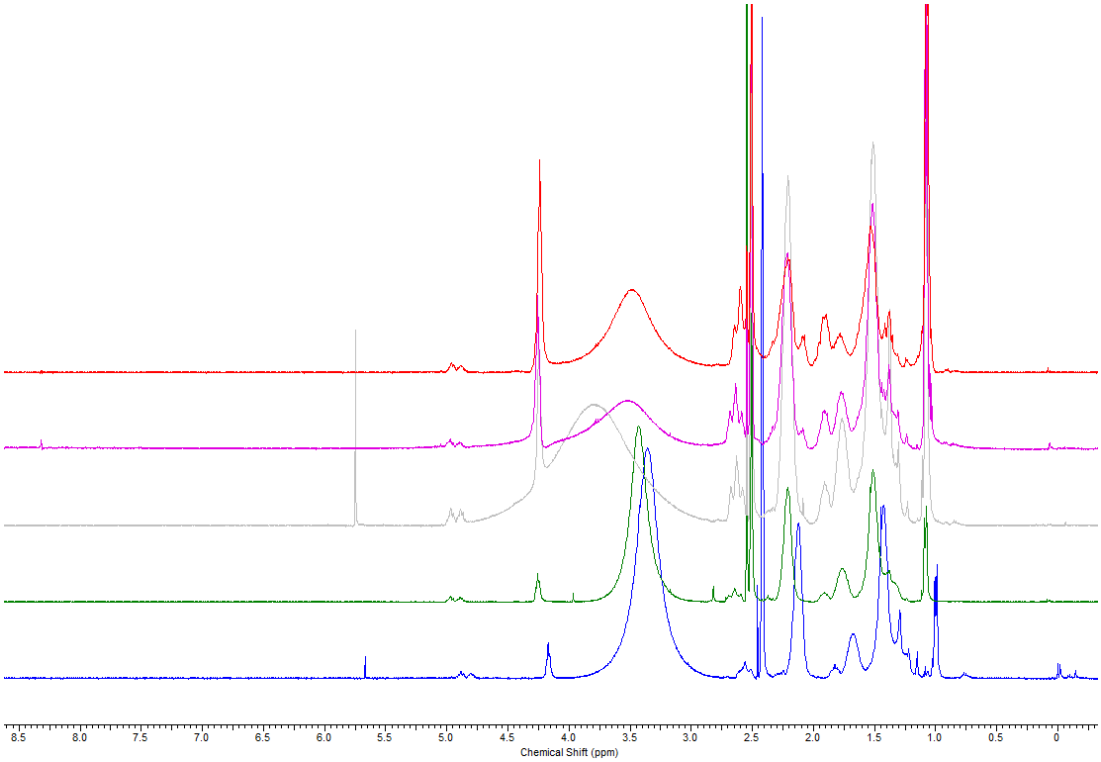

Figure A3-13. ^{1}H NMR spectrum (400 MHz, $CDCl_3$) of F_{21}-PAA_m in d^6-DMSO. m = 5, 10, 16, 20, 24 from top to bottom.

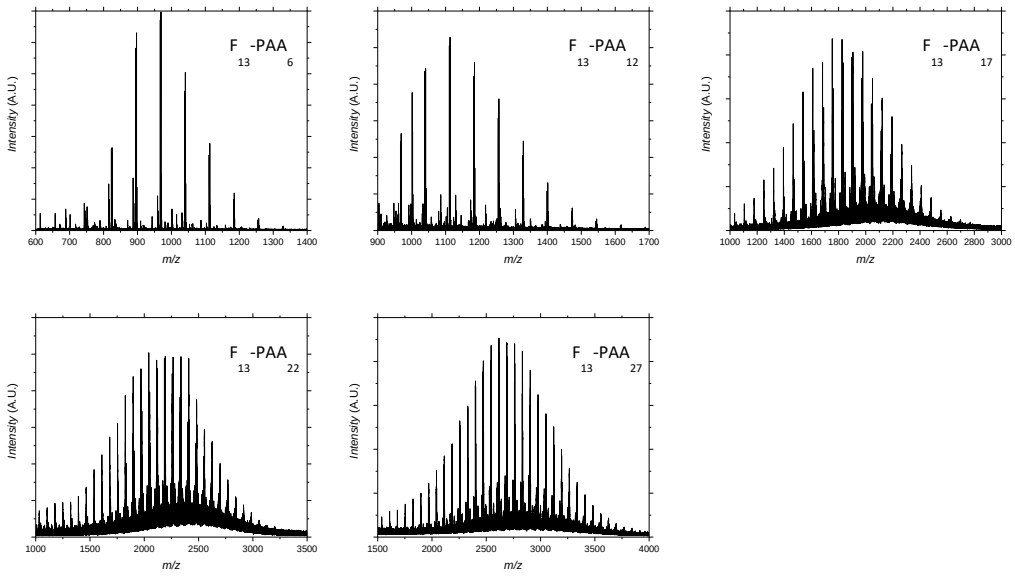

Figure A3-14. MALDI-ToF-MS spectra for F_{13}-PAA_m polymers.

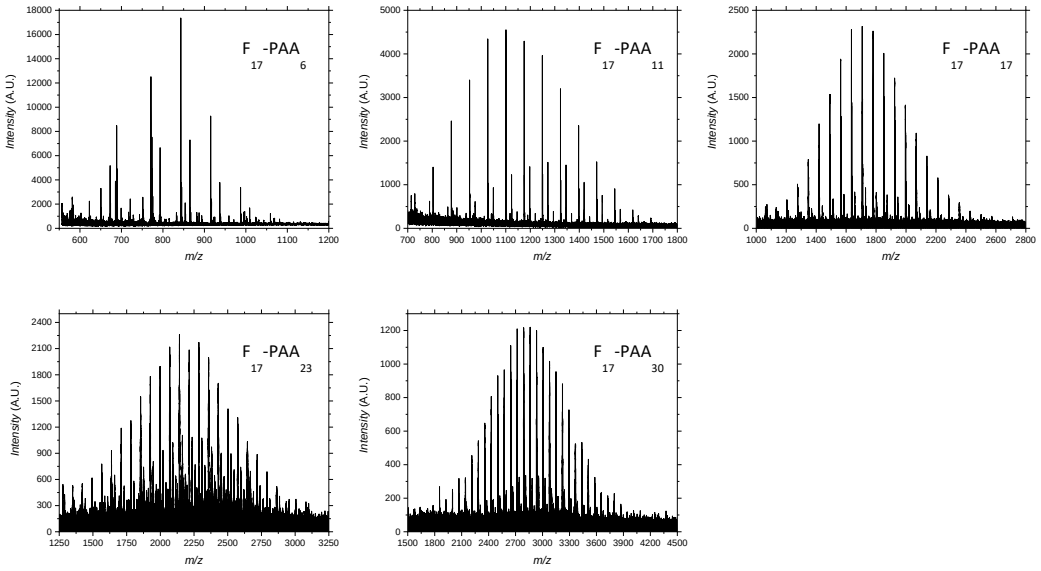

Figure A3-15. MALDI-ToF-MS spectra for F_{17}-PAA_m polymers.

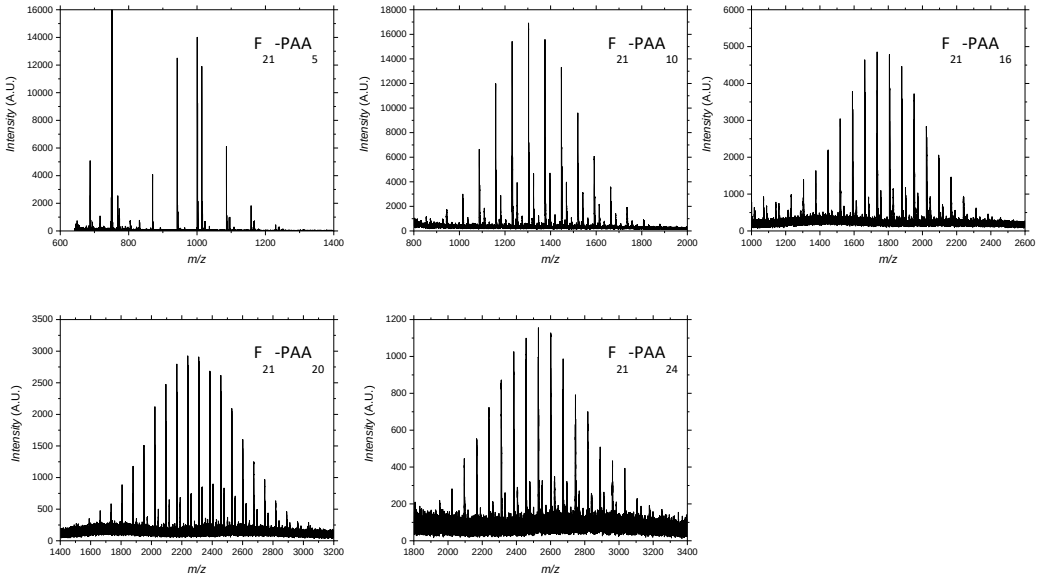

Figure A3-16. MALDI-ToF-MS spectra for F_{21}-PAA_m polymers.

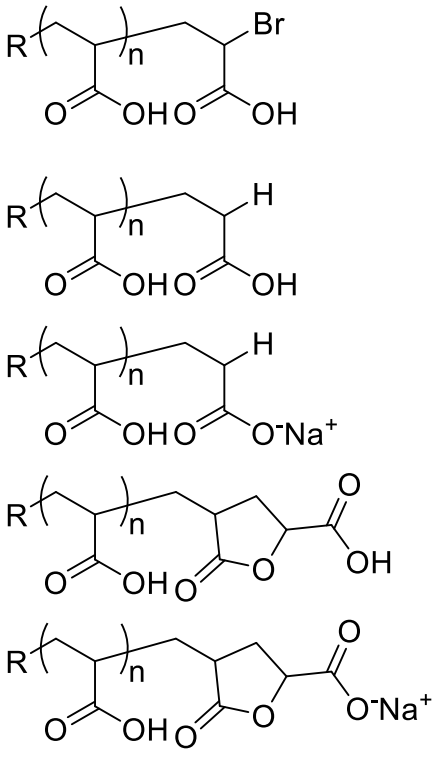

Figure A3-17. End group structures determined from MALDI spectra for all F_n-PAA_m polymers.

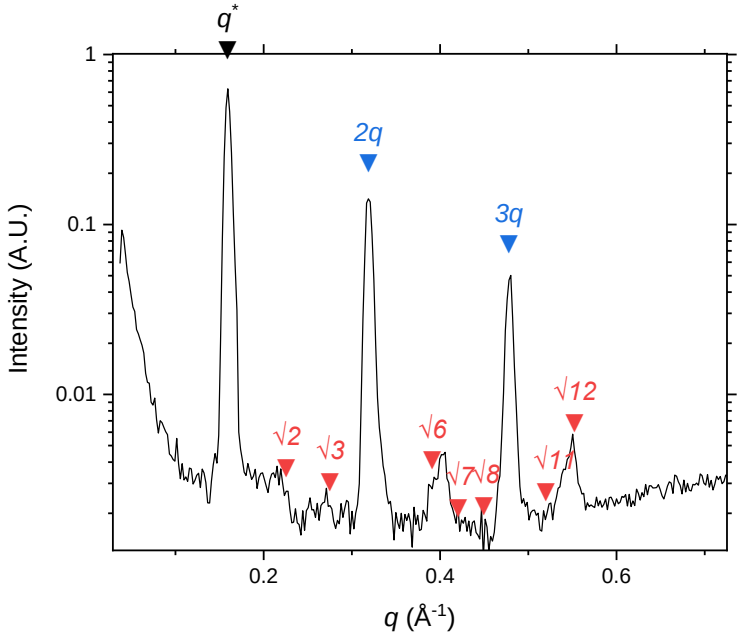

Figure A3-18. SAXS profile for F_{21} initiator. Peaks indicated by blue arrows are present at positions in agreement with a lamellar structure. Red arrows show no agreement with theoretical peak positions. *q peak position translates to a domain spacing of 3.94 nm.**

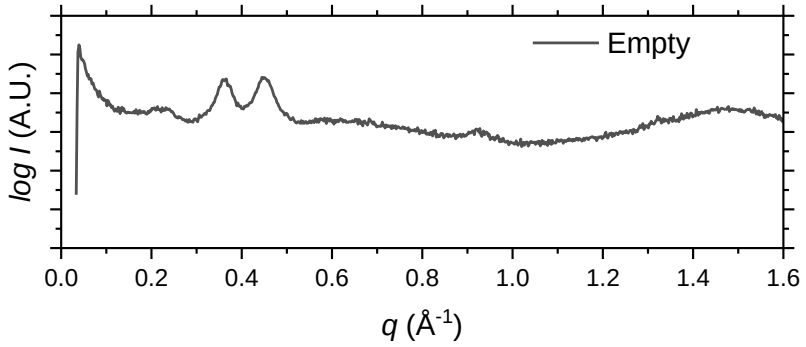

Figure A3-19. SAXS profile for a blank (empty capillary) in liquid capillary measurements. *N.B.* The Kapton peaks are present due to the Kapton windows used in the main SAXS chamber. These windows are necessary to allow air into the chamber for liquid samples.

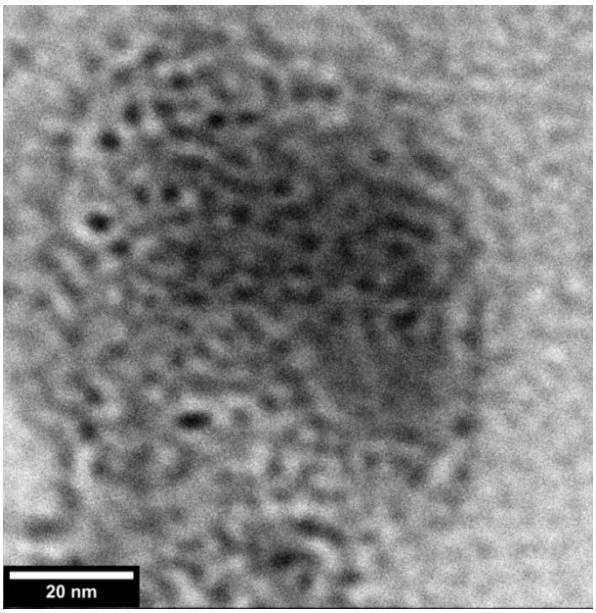

Figure A3-20. TEM images of thermally annealed F_{13}-PAA_{18}.

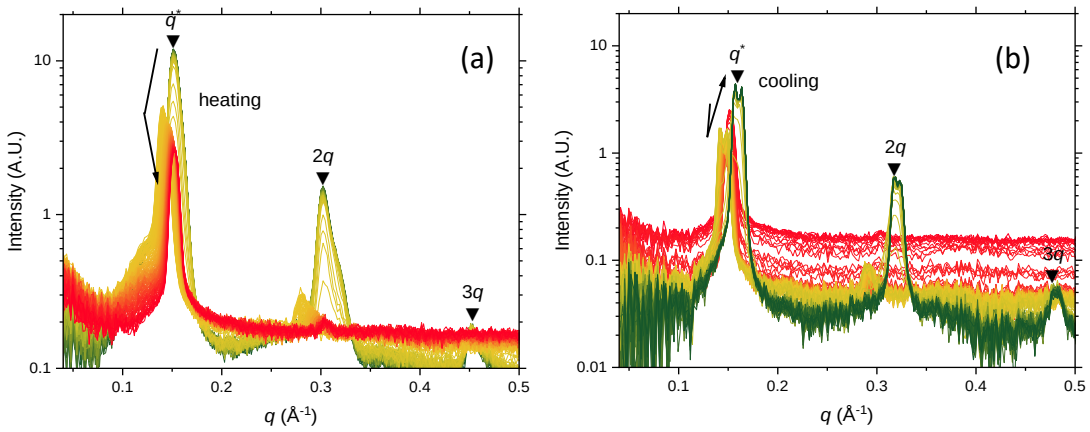

Figure A3-21. Time-resolved SAXS measurements for F_{21}-PAA_5. Colour scale from green to red shows the (a) heating cycle (30 °C to 150 °C at 0.5 °C/min) and (b) cooling cycle (150 °C to 30 °C at 0.5 °C/min).

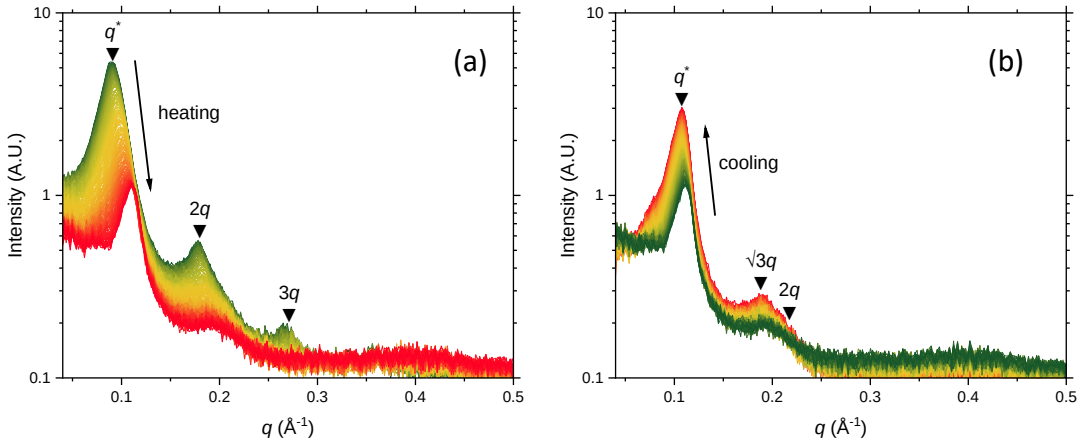

Figure A3-22. Time-resolved SAXS measurements for F_{21}-PAA_{16}. Colour scale from green to red shows the (a) heating cycle (30 °C to 150 °C at 0.5 °C/min) and (b) cooling cycle (150 °C to 30 °C at 0.5 °C/min).

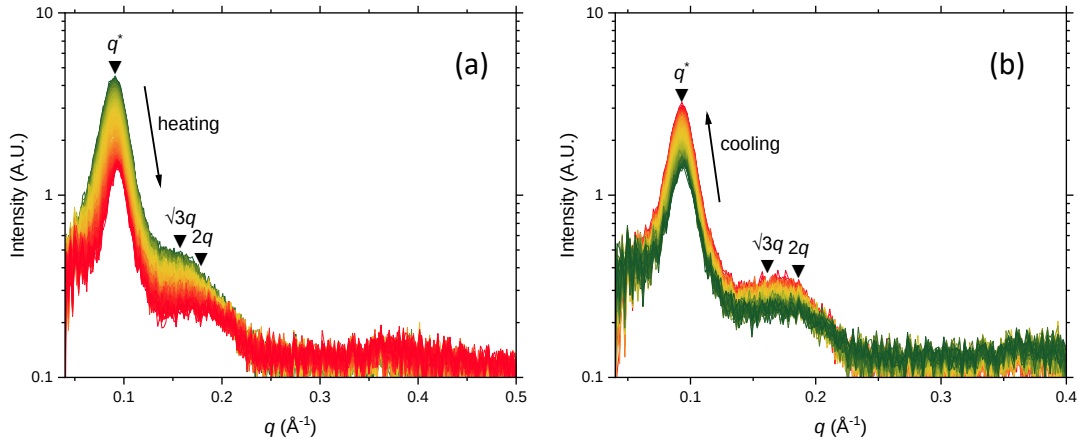

Figure A3-23. Time-resolved SAXS measurements for F_{21}-PAA_{20}. Colour scale from green to red shows the (a) heating cycle (30 °C to 150 °C at 0.5 °C/min) and (b) cooling cycle (150 °C to 30 °C at 0.5 °C/min).

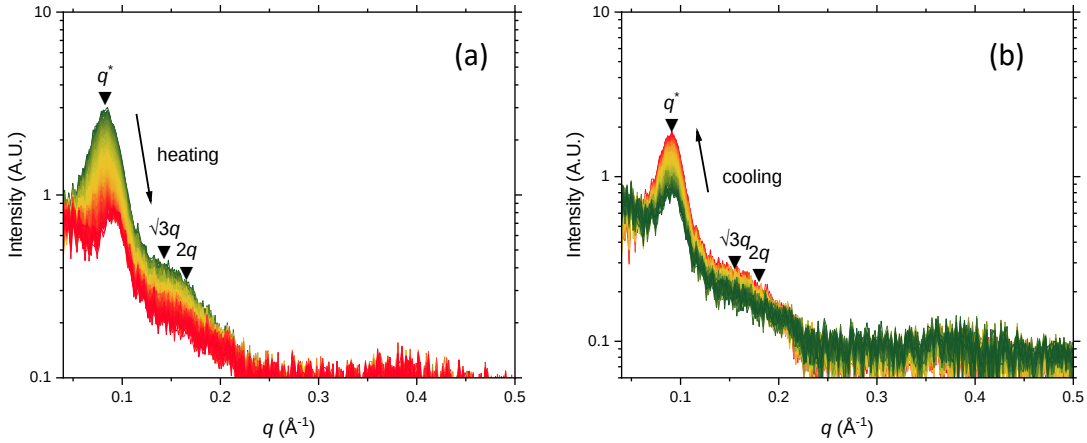

Figure A3-24. Time-resolved SAXS measurements for F_{21}-PAA_{24}. Colour scale from green to red shows the (a) heating cycle (30 °C to 150 °C at 0.5 °C/min) and (b) cooling cycle (150 °C to 30 °C at 0.5 °C/min).

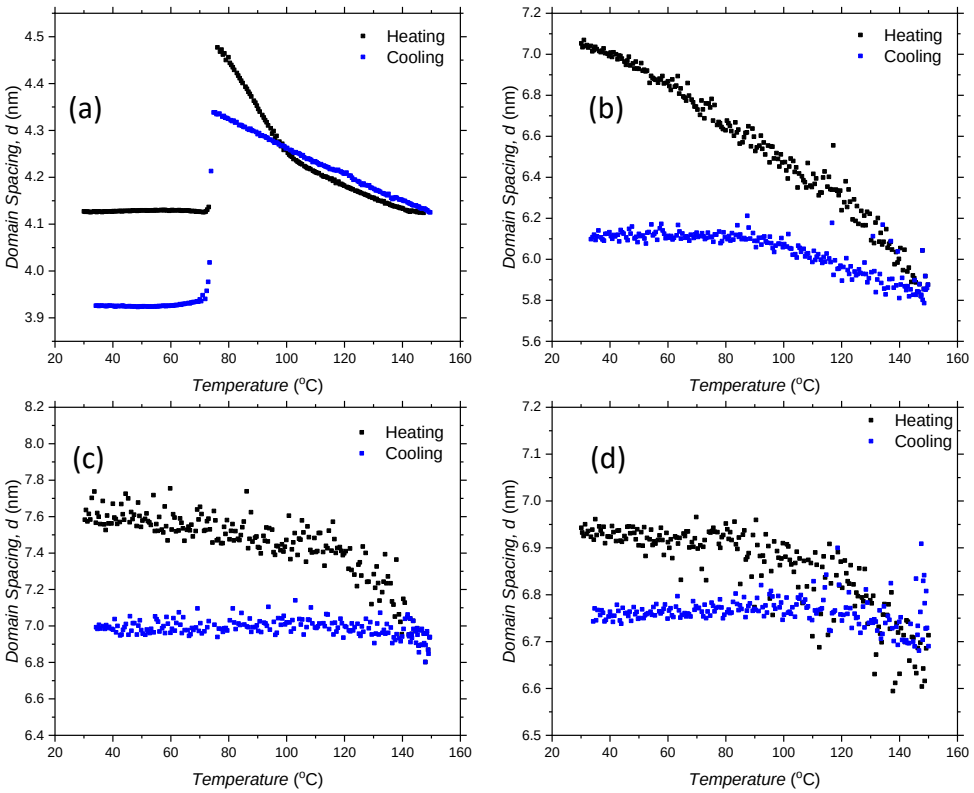

Figure A3-25. Data from time-resolved SAXS measurements showing Domain Spacing (*d*) (calculated from fitting of principal peak) against Temperature for a) F_{21}-PAA_5, b) F_{21}-PAA_{16}, c) F_{21}-PAA_{20}, d) F_{21}-PAA_{24},

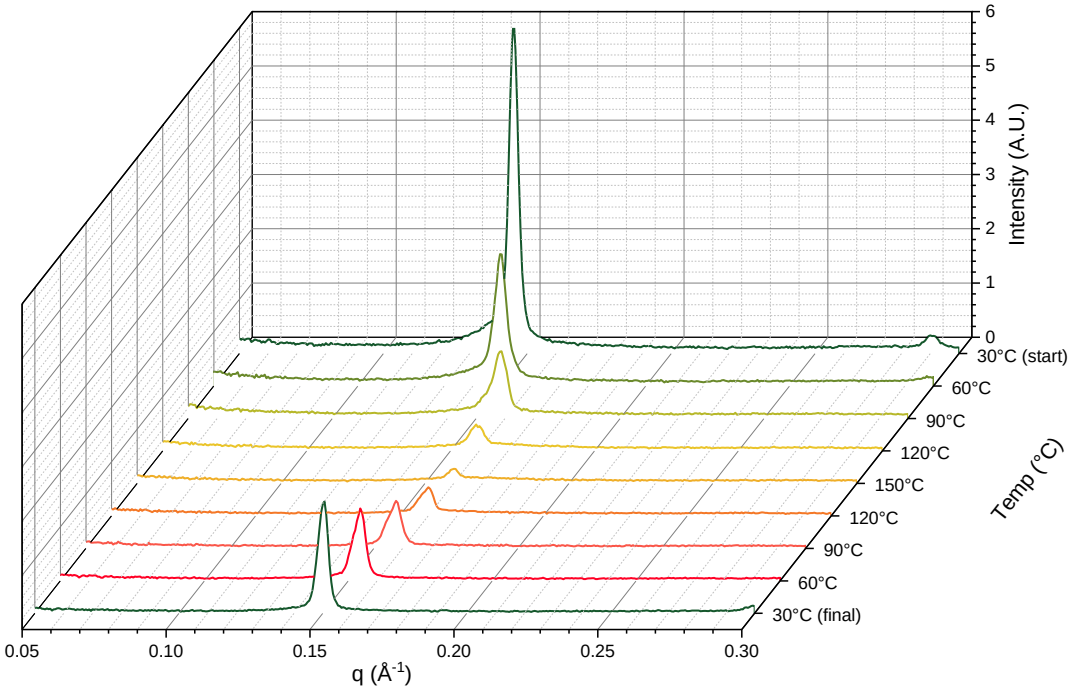

Figure A3-26. Thermal anneal SAXS measurements for F_{17}-PAA_6. Sample was heated (30 °C to 150 °C) and cooled (150 °C to 30 °C) at 5 °C/min.

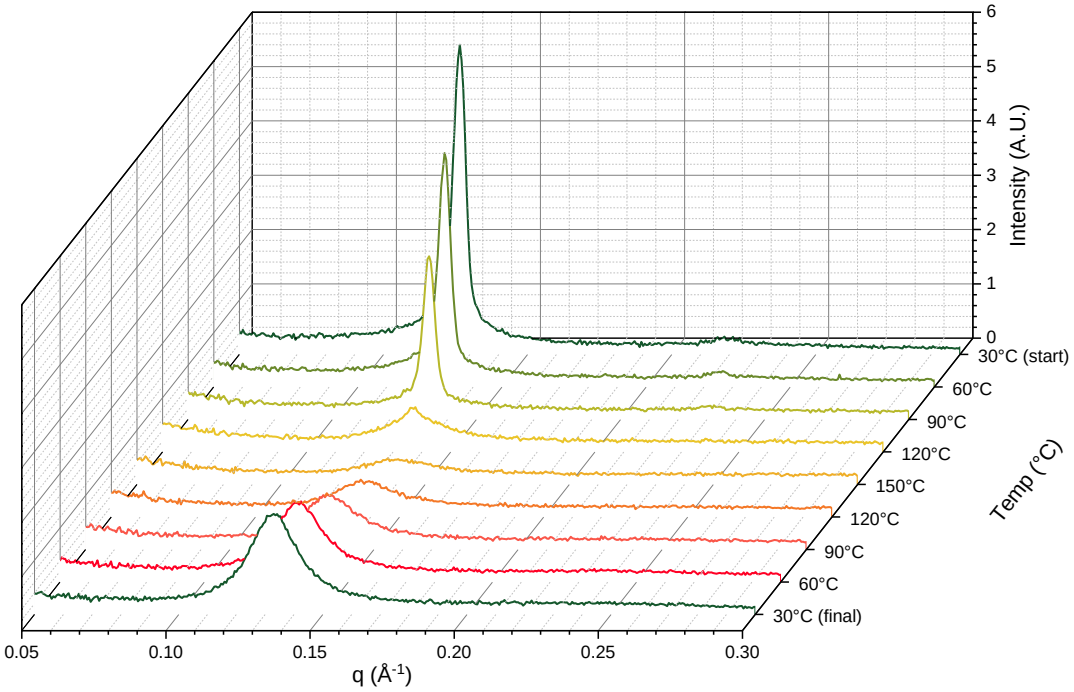

Figure A3-27. Thermal anneal SAXS measurements for F_{17}-PAA_{11}. Sample was heated (30 °C to 150 °C) and cooled (150 °C to 30 °C) at 5 °C/min.

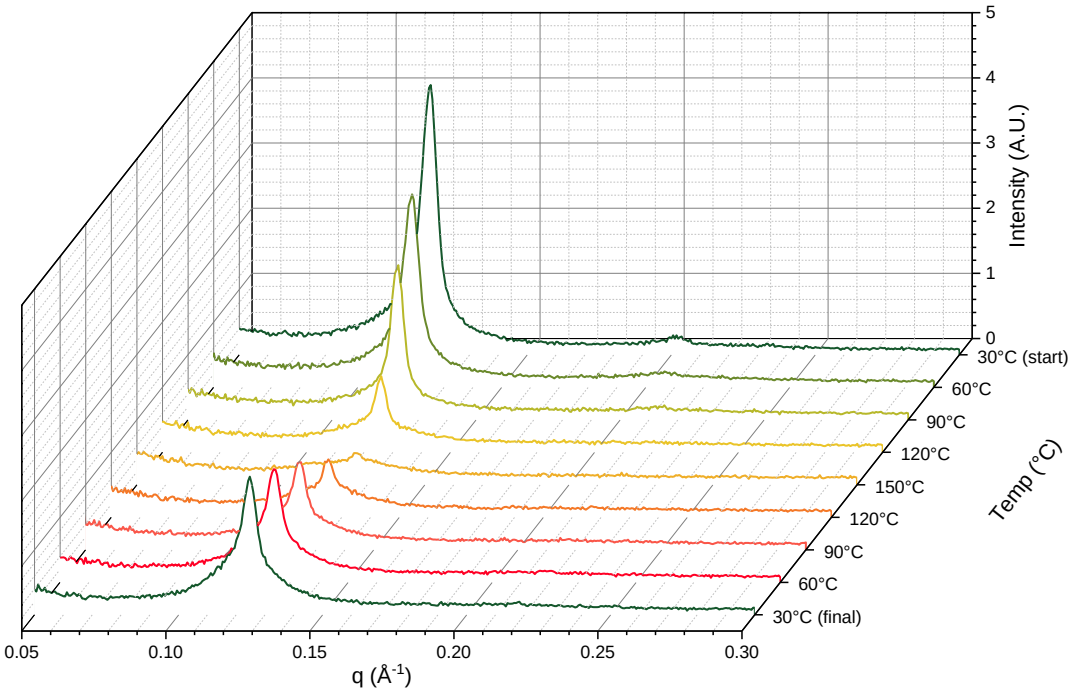

Figure A3-28. Thermal anneal SAXS measurements for F_{17}-PAA_{17}. Sample was heated (30 °C to 150 °C) and cooled (150 °C to 30 °C) at 5 °C/min.

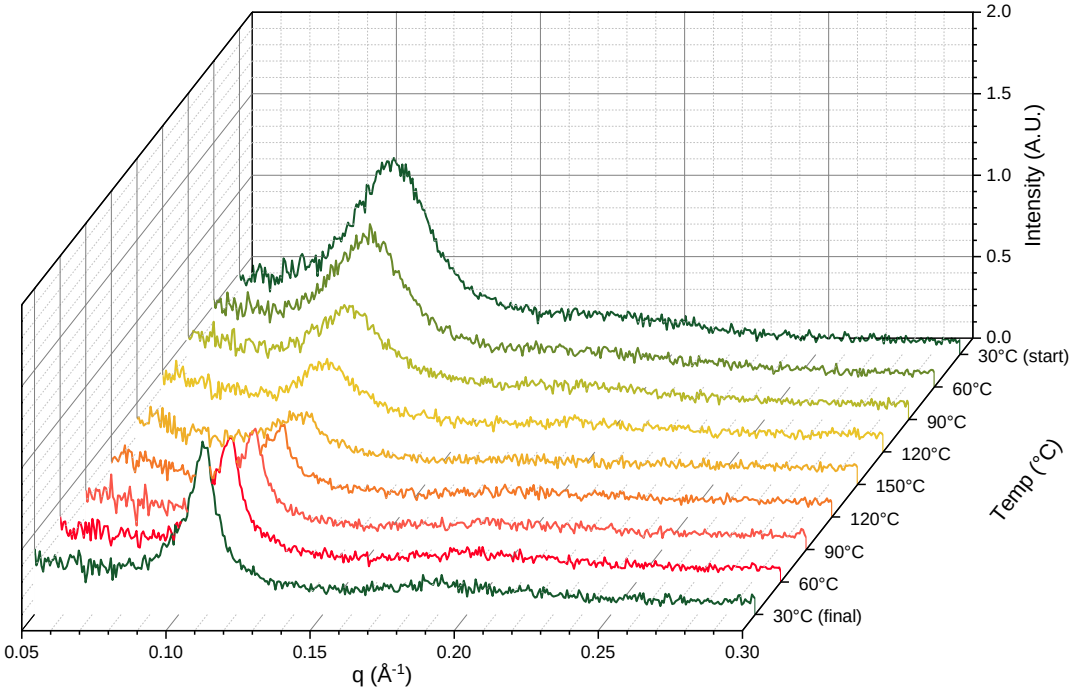

Figure A3-29. Thermal anneal SAXS measurements for F_{17}-PAA_{23}. Sample was heated (30 °C to 150 °C) and cooled (150 °C to 30 °C) at 5 °C/min.

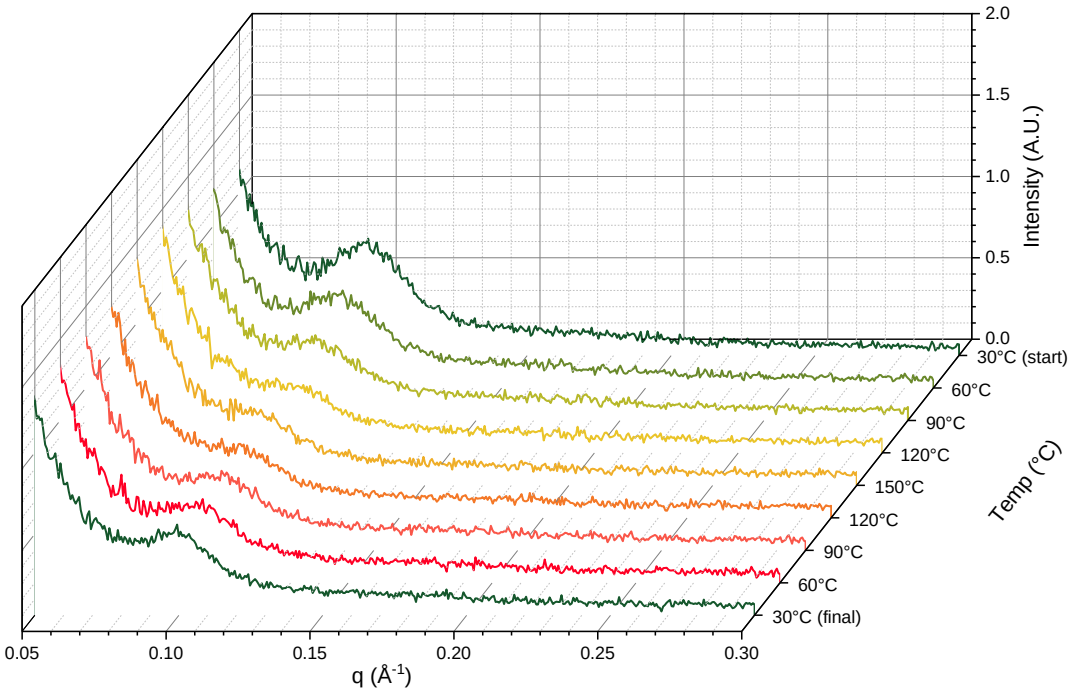

Figure A3-30. Thermal anneal SAXS measurements for F_{17}-PAA_{30}. Sample was heated (30 °C to 150 °C) and cooled (150 °C to 30 °C) at 5 °C/min.

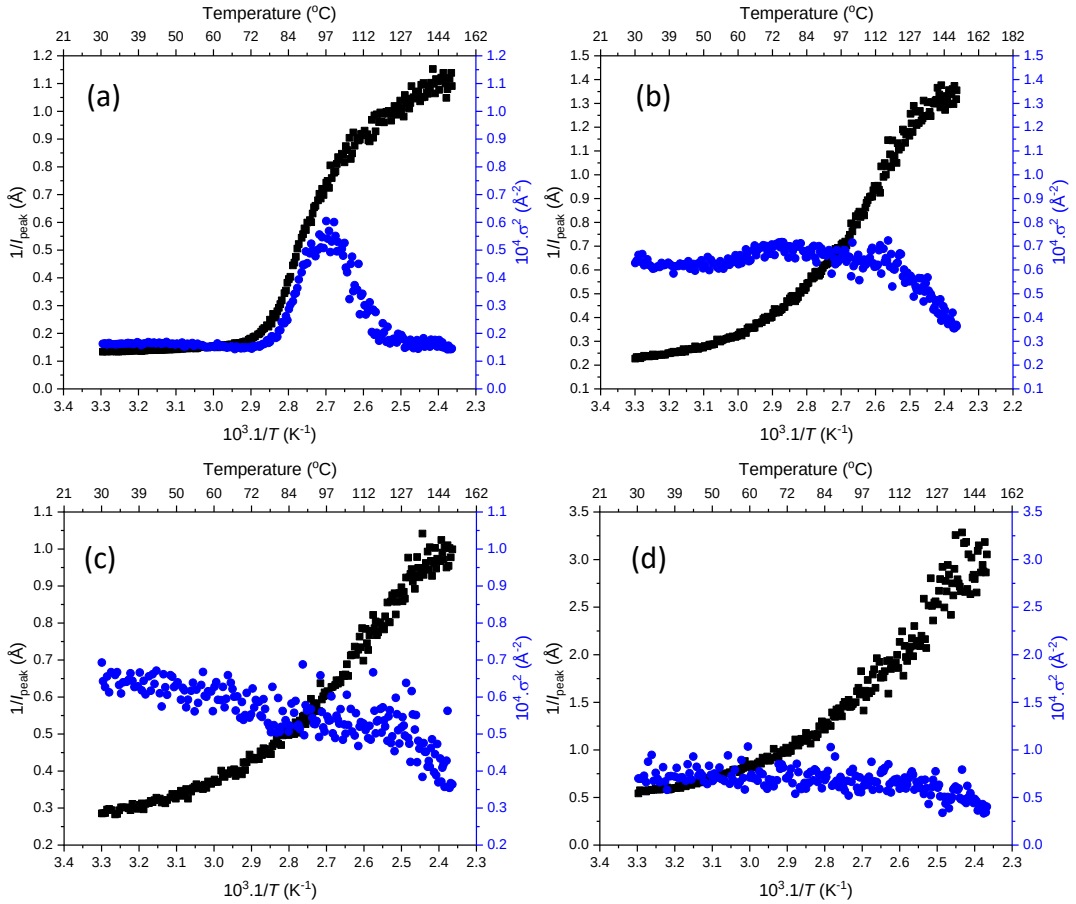

Figure A3-31. 1/peak intensity and FWHM² (σ^2) from time-resolved SAXS heating cycle vs 1/temperature for a) F_{21}-PAA_{10}, T_{OOT} = 72-80 °C. T_{ODT} = 87.4 °C. b) F_{21}-PAA_{16}, T_{ODT} = 102.9 °C. c) F_{21}-PAA_{20}, T_{ODT} = 105.8 °C. d) F_{21}-PAA_{24}, No T_{ODT}.

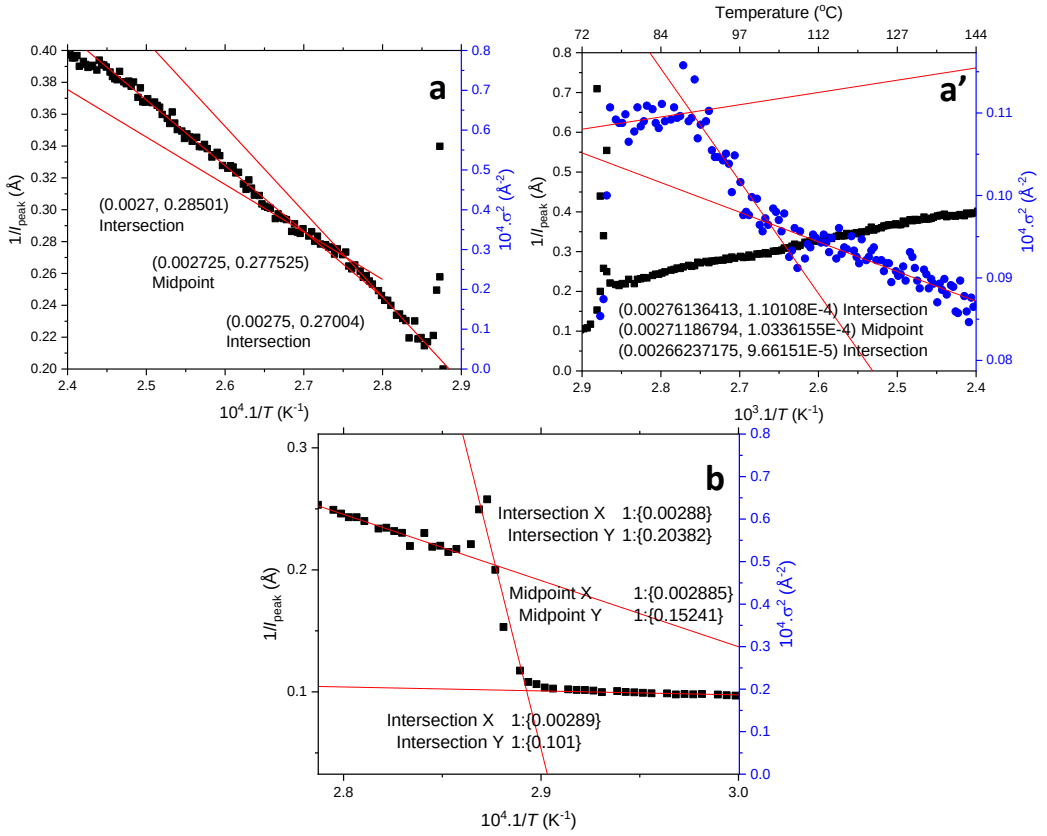

Figure A3-32. Demonstration of calculation of phase transition temperatures (from Figure 3-14). The midpoint of two intersections from linear fits before, during and after the transition gives the transition temperature. a = transition at 94.0 °C, a' = transition at 94.0 °C calculated from FWHM² (σ^2) (95.7 °C), b = transition at 73.6 °C.

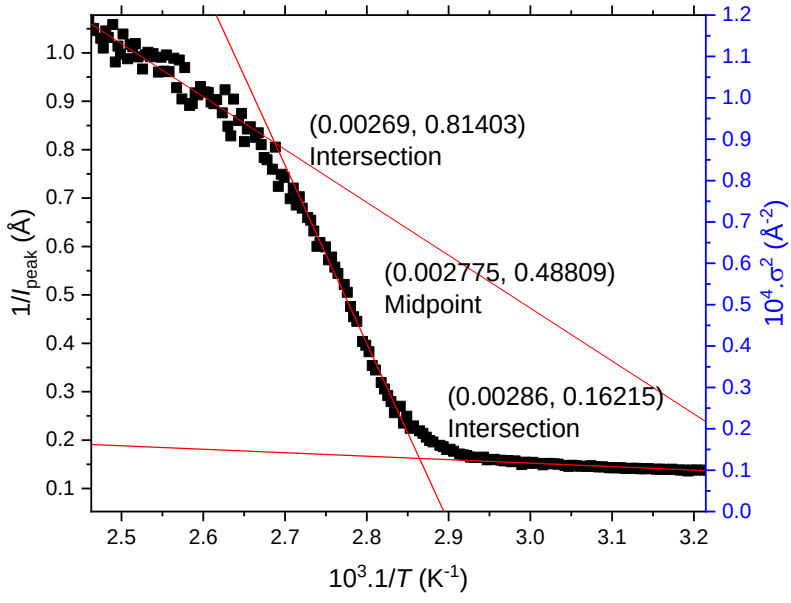

Figure A3-33. Demonstration of calculation of order-disorder phase transition temperature T_{ODT} (from Figure A3-31a). The midpoint of two intersections from linear fits before, during and after the transition gives the transition temperature.

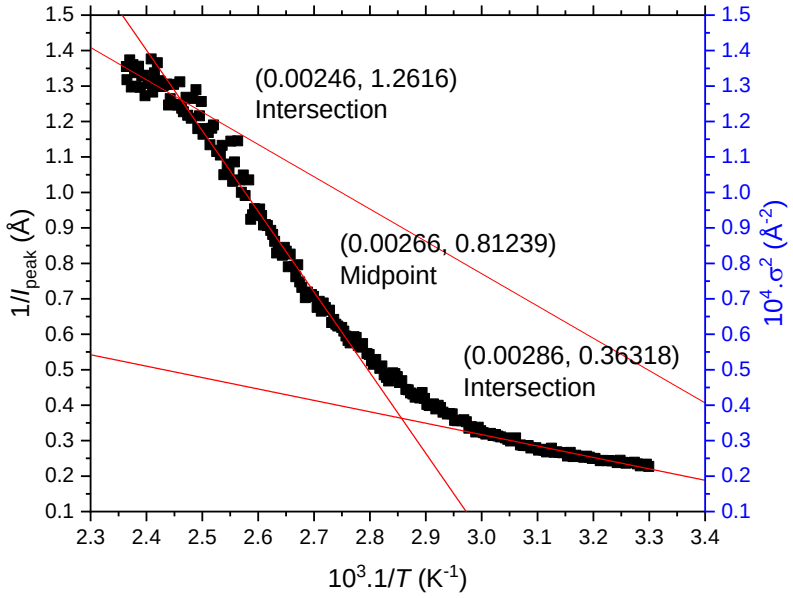

Figure A3-34. Demonstration of calculation of order-disorder phase transition temperature T_{ODT} (from Figure A3-31b). The midpoint of two intersections from linear fits before, during and after the transition gives the transition temperature.

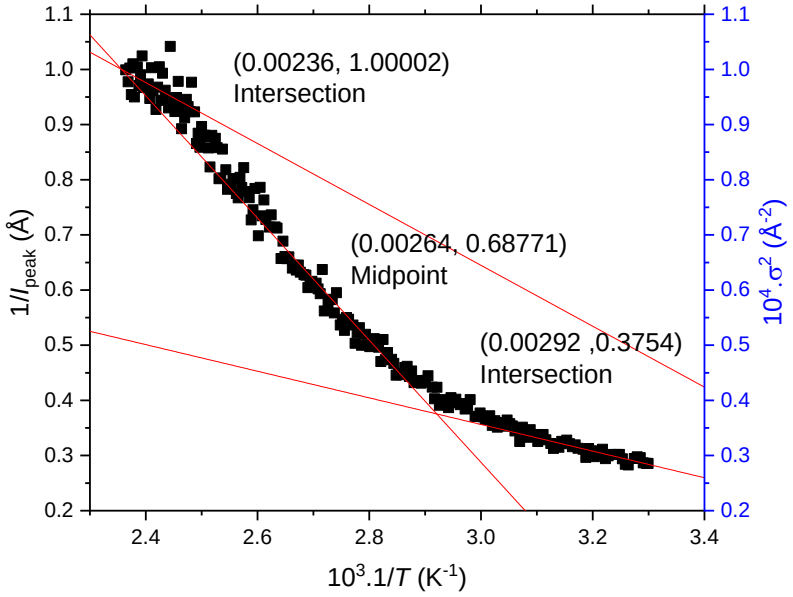

Figure A3-35. Demonstration of calculation of order-disorder phase transition temperature T_{ODT} (from Figure A3-31c). The midpoint of two intersections from linear fits before, during and after the transition gives the transition temperature.

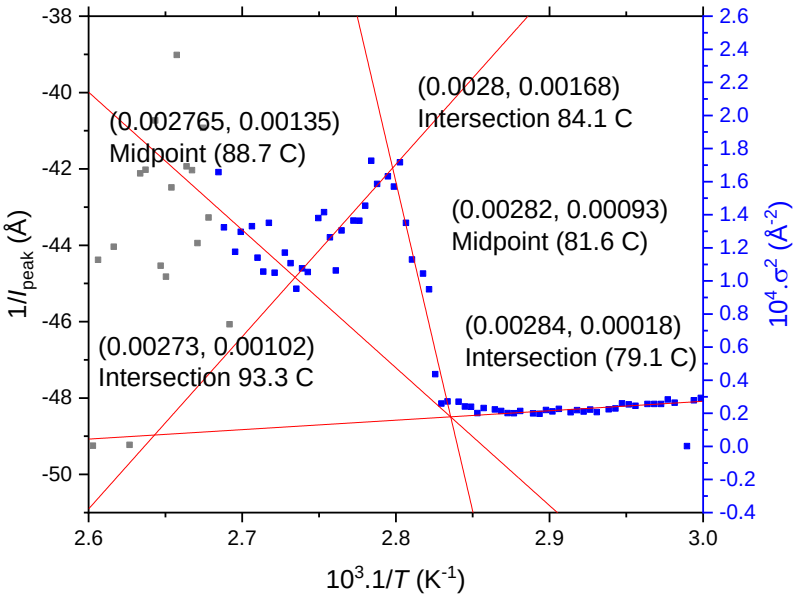

Figure A3-36. Demonstration of calculation of order-order phase transition temperature T_{OOT} from FWHM (from Figure A3-31Figure 3-16). The midpoint of two intersections from linear fits before, during and after the transition gives the transition temperature.

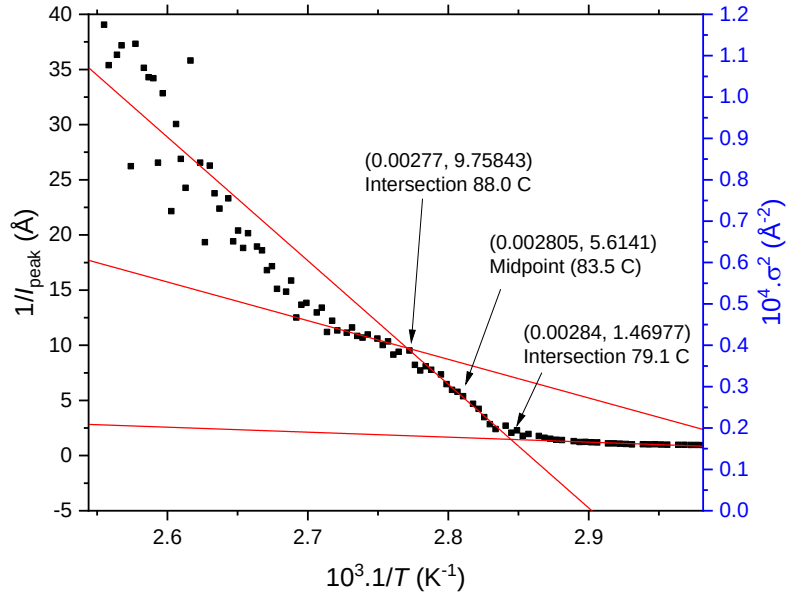

Figure A3-37. Demonstration of calculation of order-order phase transition temperature T_{OOT} from peak intensity (from Figure A3-31Figure 3-16). The midpoint of two intersections from linear fits before, during and after the transition gives the transition temperature.

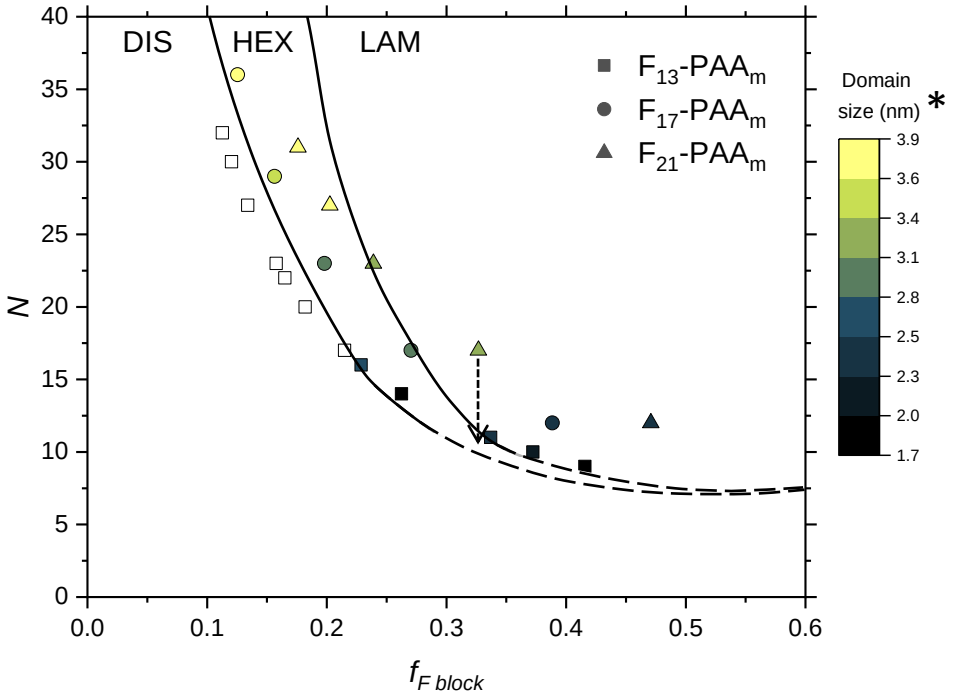

Figure A3-38. Phase diagram for F_n-PAA_m polymers, including data obtained in previous research.[226] Data point at N = 17 (F_{21}-PAA_{10}) showed an order-order transition from LAM (lamellae) to HEX (hexagonally packed cylinders) during time-resolved measurements. Dotted arrow indicates the data point shift across the phase boundary.

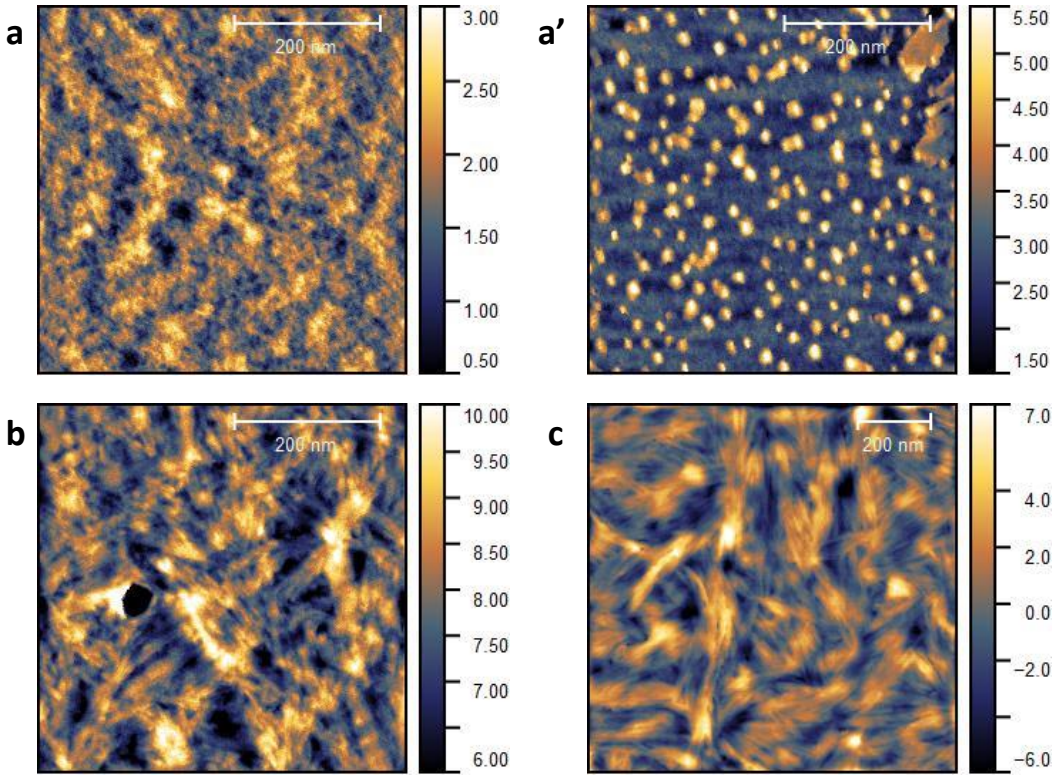

Figure A3-39. Atomic force microscopy topography (Bruker Icon) of F_{21}-PAA_{10} annealed by a/a') no annealing b) H_2O c) MeOH. Solution conditions: 20 µl of 5wt% polymer on a glass slide.

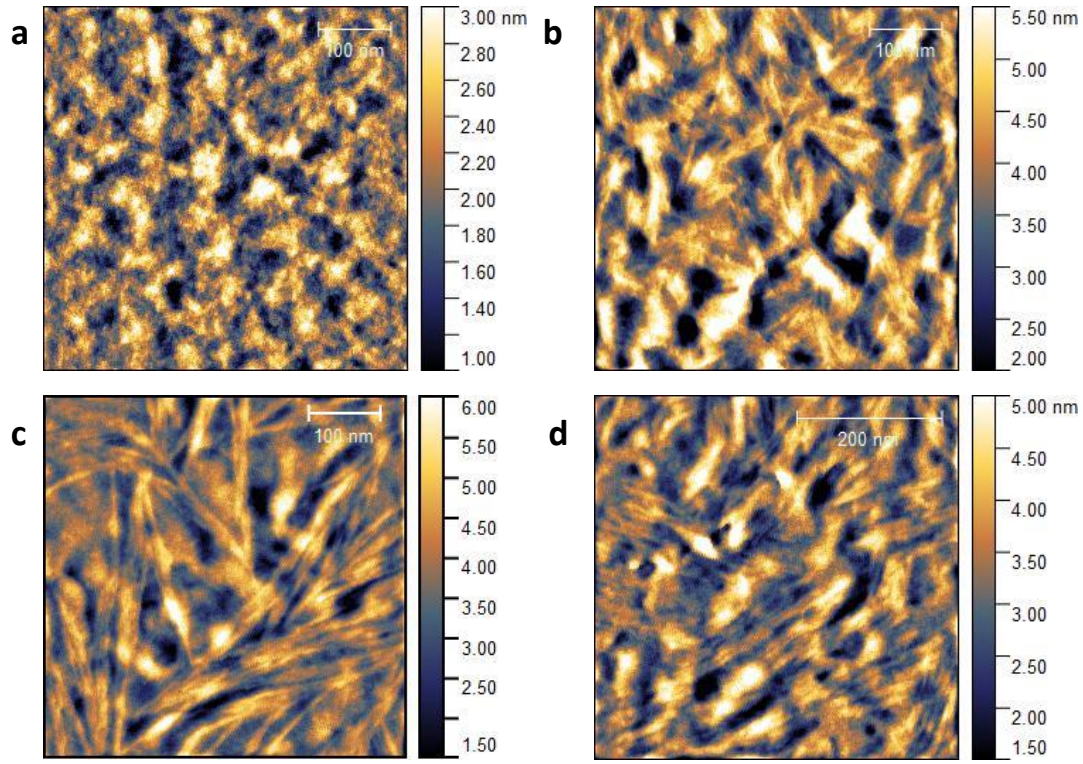

Figure A3-40. Atomic force microscopy topography (Bruker Icon) of F_{21}-PAA_{10} annealed by a) no annealing b) H_2O c) 1:1 vol. H_2O:MeOH. Solution conditions: 40 µl of 2.5 wt% polymer on a glass slide.

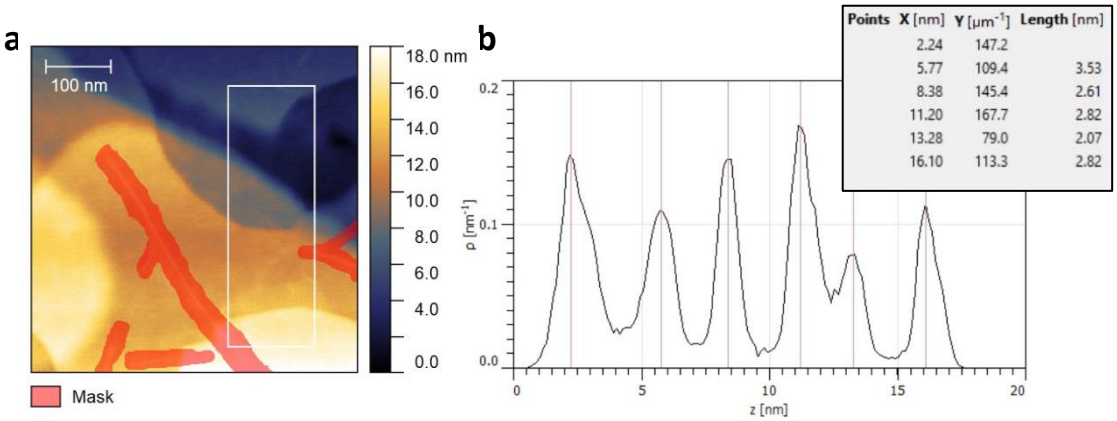

Figure A3-41. a) atomic force microscopy topography (Bruker Icon) of F_{21}-PAA_5 annealed 1:1 vol. H_2O:MeOH. Solution conditions: 40 µl of 2.5 wt% polymer on Mica. The white box shows the area in which height distribution was calculated, masked were excluded. b) height distribution calculated from area in the white box in Figure A41a. Insert table shows x and y data for the vertical intersections, "Length" is the difference between these points *i.e.* layer height.

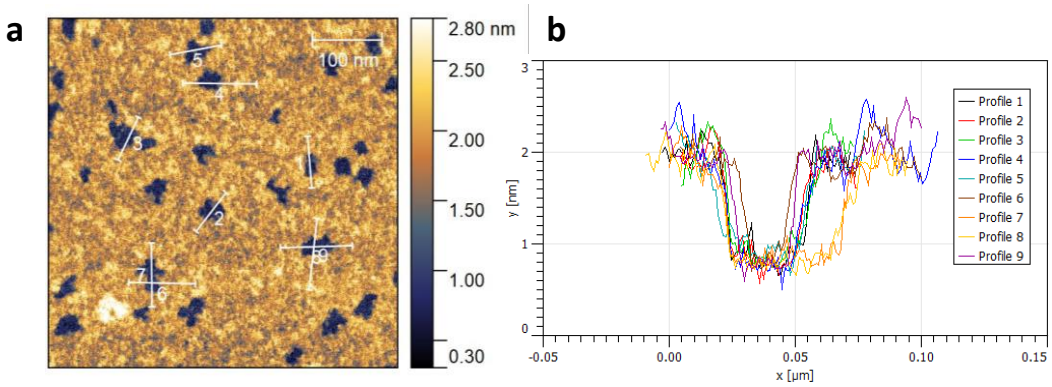

Figure A3-42. a) atomic force microscopy topography (Bruker Icon) of F_{21}-PAA_{10} annealed 1:1 vol. H_2O:MeOH. Solution conditions: 40 µl of 2.5 wt% polymer on Mica. White lines show the cross-section in which height profiles were determined. b) height profiles calculated from the white lines in Figure A42a.

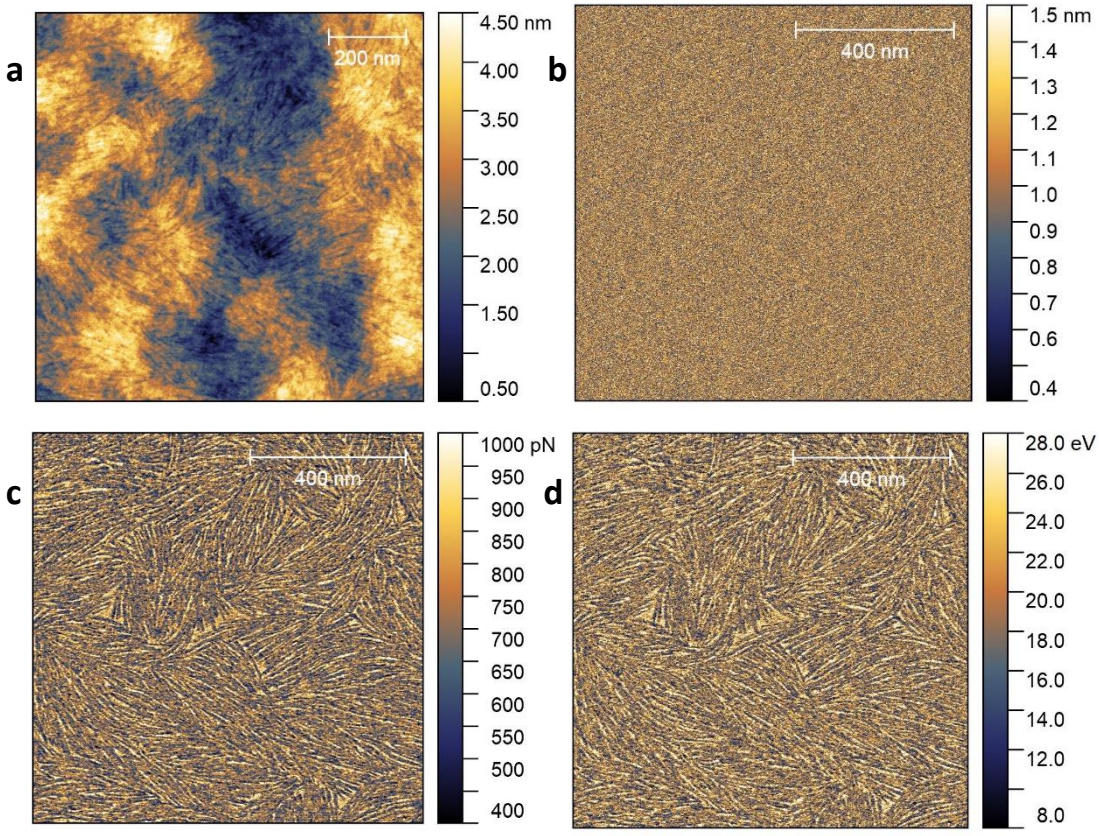

Figure A3-43. Atomic force microscopy mechanical property images (Bruker Icon) of F_{21}-PAA_{20} annealed 1:1 vol. H_2O:MeOH. Solution conditions: 40 µl of 2.5 wt% polymer on Mica. a) topography b) indentation c) adhesion d) dissipation.

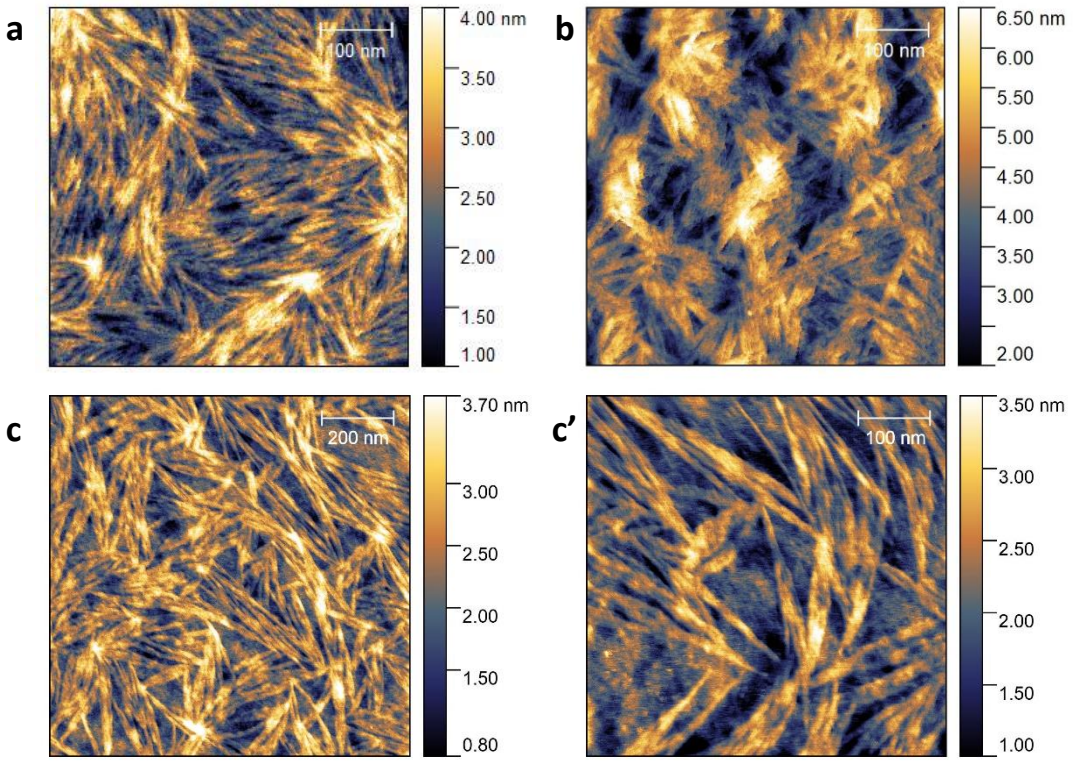

Figure A3-44. Atomic force microscopy topography (Bruker Icon) of a) F_{13}-PAA_{11} (20 µl, 5wt %, Mica) b) F_{21}-PAA_{10} (40 µl, 2.5wt %, Mica) c/c') F_0-PAA_{15} (40 µl, 2.5wt %, Mica), all annealed 1:1 vol. H_2O:MeOH.

Chapter 4: Alternative hydrophobic initiators and hydrophilic monomers for phase separation

Contents

This chapter continues with the premise of using a hydrophobic initiator for polymerisation of a hydrophilic monomer to give low molecular weight polymers which can experience bulk microphase separation. Initiators with different hydrophobic end groups were investigated as alternative possibilities to a fluorocarbon tail, with a focus on the incorporation of additional functionality which would allow microphase separation-induction/alteration properties. Photo-responsive molecules would allow the temporal control of domain sizes or morphology changes. This could also be made reversible depending on the molecule incorporated into the initiator *i.e.* anthracene. Alternative hydrophilic monomers have also been investigated opposed to poly(acrylic acid), including methacrylates. These must be polymerised in their protected form, and so the deprotection conditions were also investigated.

4.1 Hydrophobic initiators

4.1.1 9-Anthracene methanol bromoisobutyrate (AMBiB)

Anthracene was chosen as a potential photo-switching molecule as it was expected to have a dramatic influence on morphology when irradiated. Compared to a monomeric unit, where a change in end group size (or polarity etc) would likely allow a change in domain size only, dimerization of anthracene units would allow, for example, the opening/closing of pores in a hexagonally packed array of cylinders.

Anthracene consists of 3 fused aromatic rings, is strongly hydrophobic, seemed suitable for microphase separation and undergoes a reversible photo dimerisation by [4+4] cycloaddition across its centre ring which is highly cited.[148,227–229]

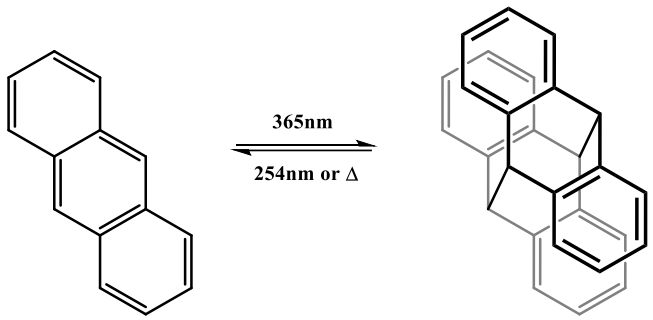

Figure 4-1. Dimerisation of anthracene.

4.1.1.1 Initiator synthesis

An anthracene derivative with an available hydroxy group was needed for the initiator synthesis (to remove additional synthesis steps). Hydroxyanthracenes are a component of aloe extracts and are therefore relatively inexpensive and readily available. While aloe extracts are typically considered beneficial to health (such as improving bowel function)[230], more recent studies have shown that hydroxyanthracenes may contribute towards the formation of cancer cells.[231] 9-Anthracene methanol is one such hydroxyanthracene derivative that is stable at room temperature and pressure and has an available hydroxy group therefore, it was suitable for the synthesis of the hydrophobic initiator 9-Anthracene methanol bromoisobutyrate (AMBiB), Figure 4-2. The stability is due to the single methylene group that acts as a spacer and inhibits tautomerisation. 9-hydroxyanthracene (with no methylene spacer) exists as the ketone tautomer, whereas hydroxyl groups at the 1 or 2 positions exist as the alcohol.[232]

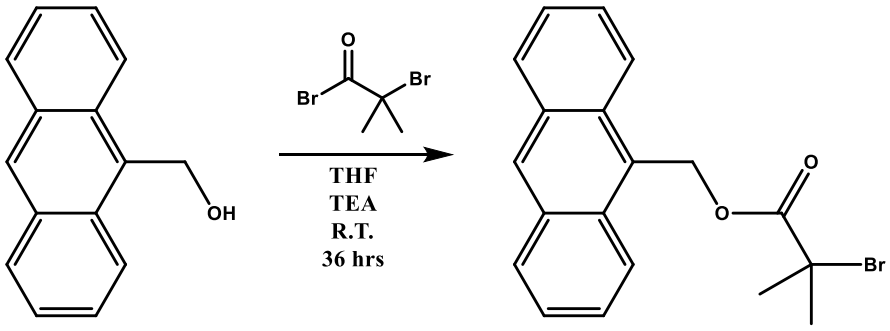

Figure 4-2. Synthesis of 9-Anthracene methanol bromoisobutyrate (AMBiB).

9-Anthracene methanol was used as received (^{1}H NMR, Figure A4-1) and reacted with bromoisobutyryl bromide to synthesise the alkyl bromide initiator, AMBiB was obtained in acceptable yield (64%) and high purity (Figure 4-3, Figure A4-2) after additional purification. Environments (c) and (d) in the ^{1}H spectrum were distinguishable when inspecting the COSY NMR spectrum (Figure A4-3). The ^{13}C spectrum (Figure 4-4) also supported the assignment of high purity and each peak was assigned with support from HSQC (Figure A4-4) and HMBC (Figure A4-5).

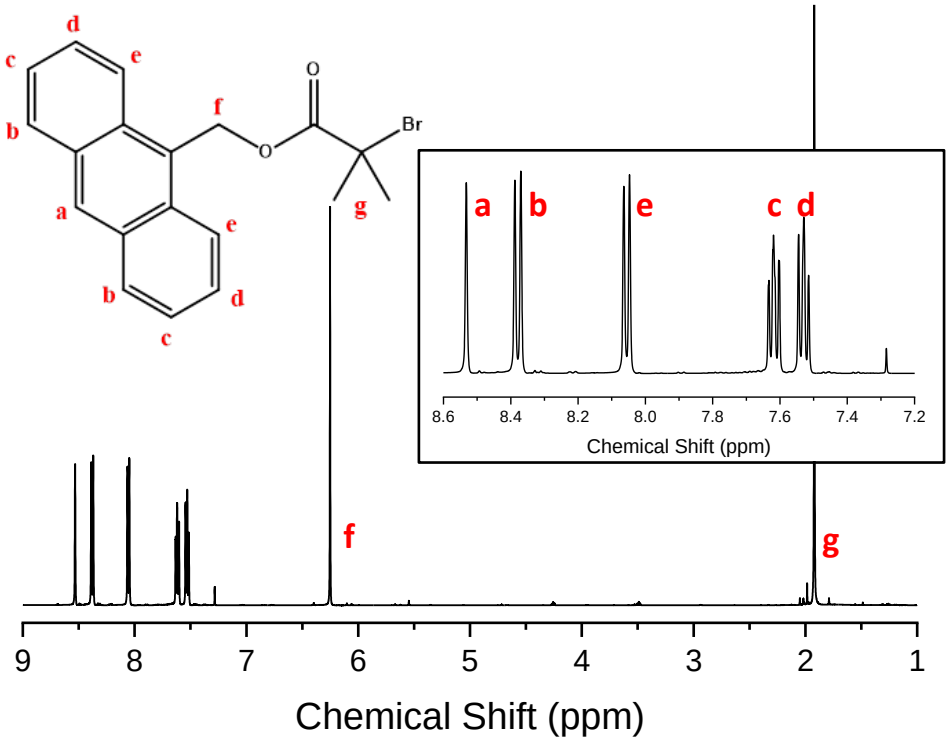

Figure 4-3. ^{1}H NMR (500 MHz, CDCl3) spectrum of 9-Anthracene methanol bromoisobutyrate (AMBiB). Inset shows expansion of chemical shift values 8.6 to 7.2 ppm.

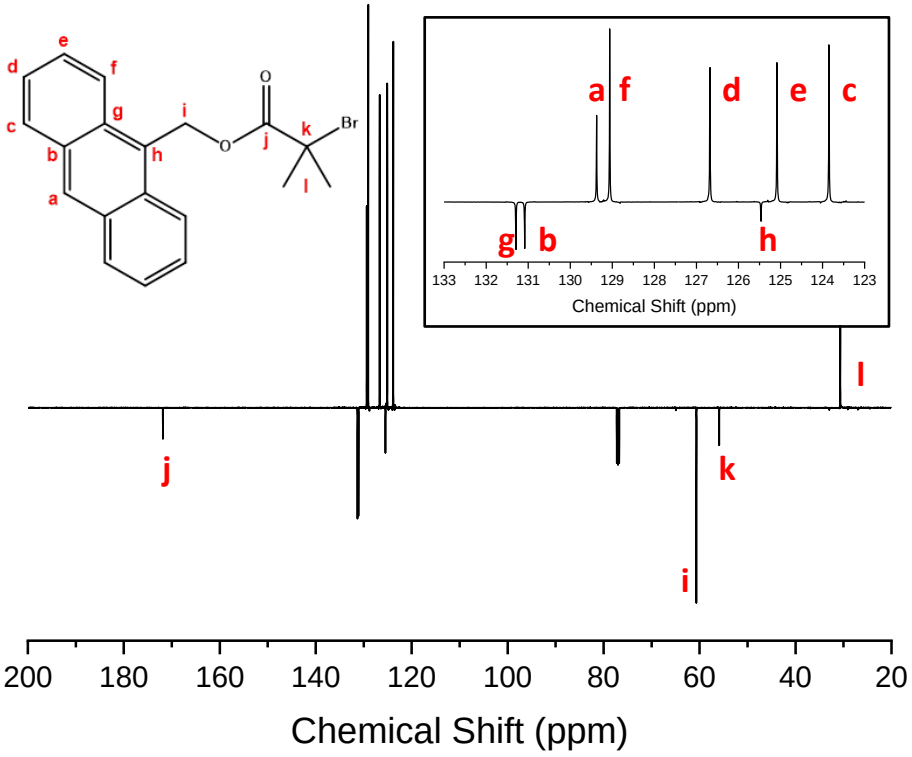

Figure 4-4. ^{13}C NMR (126 MHz, CDCl3) spectrum of 9-Anthracene methanol bromoisobutyrate (AMBiB). Inset shows expansion of chemical shift values 133 to 123 ppm.

4.1.1.2 Dimerisation investigation

A key feature of anthracene, that influenced this initiator design, was the potential for a reversible [4+4] cycloaddition dimerisation reaction, Figure 4-5. The major product is likely to be a head-to-tail or *trans* product due to steric hinderance, however the possibility of head-to-head or *cis* product has not been overlooked, as polarity of the solvent can affect which isomer is formed which has been shown in the literature.[233–235] Dimerisation occurs across the 9, 10- positions preferentially as the thermodynamic product forms the highest number of benzene rings, which have a higher resonance stabilisation per ring than a naphthalene ring.[228] In this section only, reference to monomer means a single unit of AMBiB and dimer refers to the 2-unit dimer of AMBiB.

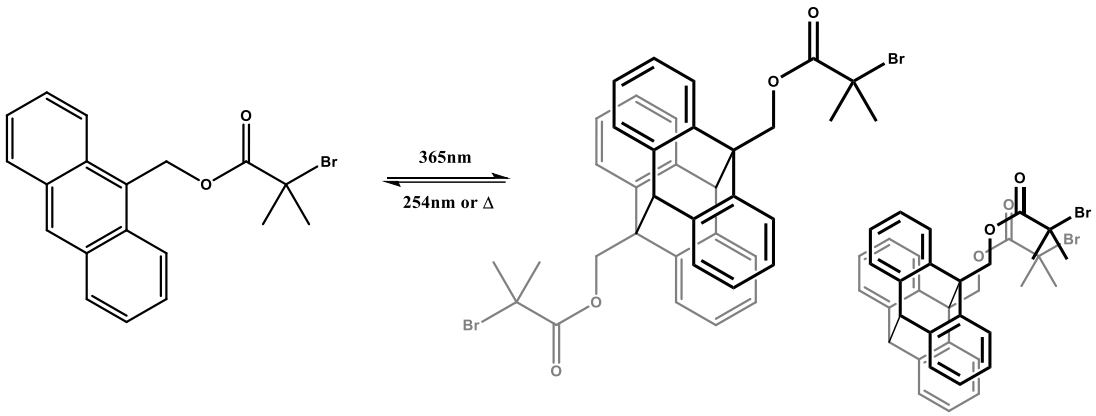

Figure 4-5. Dimerisation of 9-Anthracene methanol initiator (AMBiB).

UV-Vis spectroscopy was used to investigate the dimerisation. A 3.125 x 10^{-3} mg ml^{-1} solution of AMBiB in DMF was irradiated for 1 minute with 320-390 nm light in a vial. The solution was then transferred to a cuvette and UV-Vis absorption was measured, this irradiate/measure process was repeated 10 times (Figure 4-6). The region of 325-400 nm shows a pattern of fingers in the absorption, typical of anthracene and other polycyclic aromatic hydrocarbons.[236] With each interval of exposure to 320-390 nm light, the absorbance decreases in this region. The decrease in absorbance of the "fingers" is associated with the formation of the dimer product (or the loss of the monomer). Simultaneously, there is a slight increase in absorbance at ~275-310 nm.

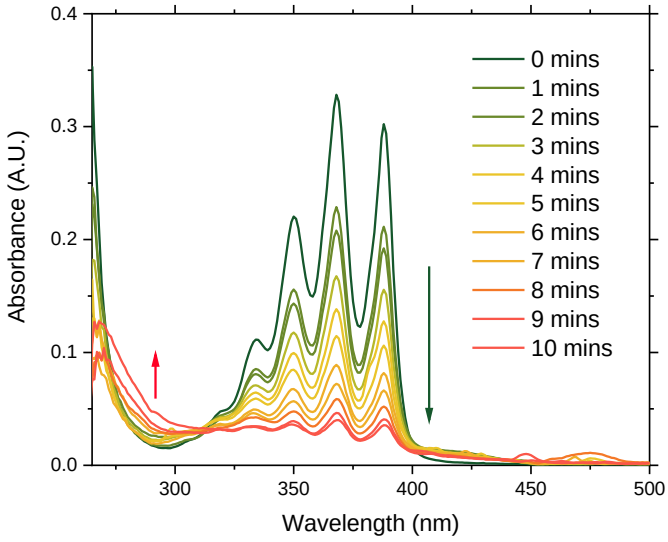

Figure 4-6. UV-Vis absorbance spectrum of AMBiB in DMF (3.125 x10^{-3} mg ml^{-1}) with sequential exposures to 320-390 nm light. Legend indicates total amount of exposure time.

4.1.1.3 Reversibility by exposure to 254 nm light

This sample was then used to investigate the reversion of the dimerisation by exposure to 254 nm light, Figure 4-7. It was expected that an increase in absorbance, so that the spectrum resembles the monomer before irradiation, would be observed. However, despite an increase in absorbance after a total of 15 mins exposure, the height of the peak does not return to its starting value. The sample was left at room temperature/pressure and out of direct sunlight for 14 days and measured a final time. This measurement showed a further increase in absorbance, suggesting that any reversion that occurred throughout the experiment may not have been caused by 254 nm light alone. This was previously thought to be an issue with the type of solvent (which was changed to hexane), however, a more prevalent issue was that the UV cut-off of borosilicate glass (approximately 290-300 nm or lower depending on composition)[237,238] was likely inhibiting the 254 nm light from passing through the vial. Therefore, Figure 4-7 actually shows the stability of the dimer when left in standard temperature/pressure/lighting conditions. There is a slow increase in absorbance, suggesting the gradual reversion to monomer of the AMBiB dimer.

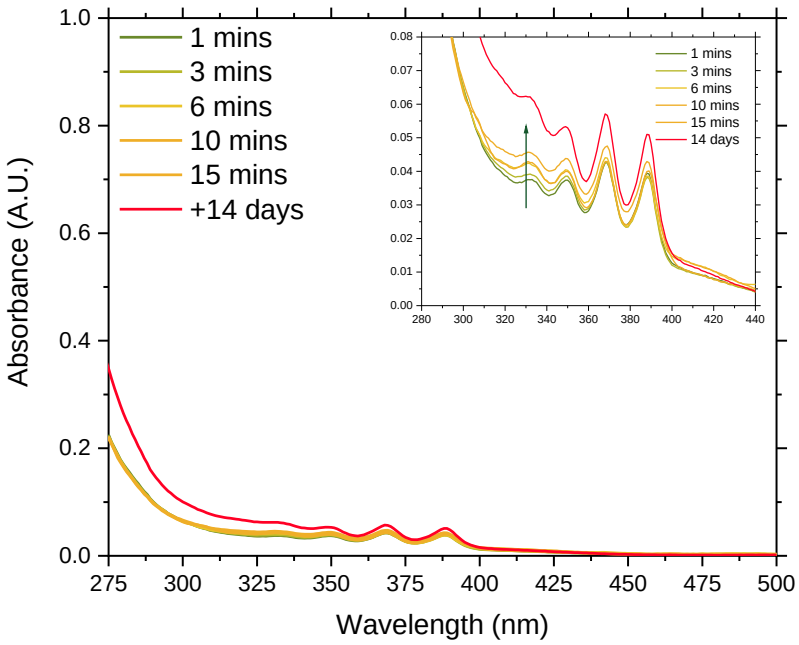

Figure 4-7. UV-Vis absorbance spectrum of AMBiB in DMF (3.125 x10^{-3} mg ml^{-1}) with sequential exposures to 254 nm light. Legend indicates total amount of exposure time.

The experiment was repeated in a quartz cuvette to allow all wavelengths to pass through. The cuvette was irradiated with 320-290 nm light for a total of 20 minutes

with UV-Vis absorption measures taken at intervals, then 254 nm for a total of 30 minutes with interval measurements, Figure 4-8. As expected with exposure to 365 nm, the absorbance drops. With exposure to 254 nm, the absorbance did not increase in the 325-400 nm region and resemble the monomer trace. While there is a small increase in absorbance, the finger pattern did not reappear. Also, the trace in the region of 225 – 270 nm continued to decrease in absorbance when exposed to 254 nm light, a sign that the reversion to monomer was not occurring. It was reasoned that the presence of oxygen in the sample could form a peroxide bridge across the 9 and 10 positions on the anthracene, therefore inhibiting monomer formation (reversion) (Figure 4-9). It is uncertain whether this happens when exposed to 365 nm or 254 nm or both.

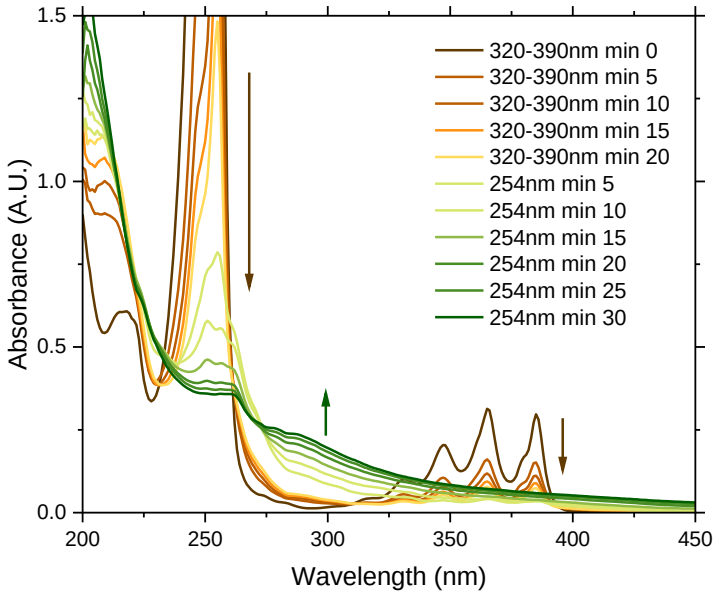

Figure 4-8. UV-Vis absorbance spectrum of AMBiB in hexane (1.25 x10^{-2} mg ml^{-1}) with sequential exposures to 320-290nm light followed by 254 nm light. Legend indicates total exposure time.

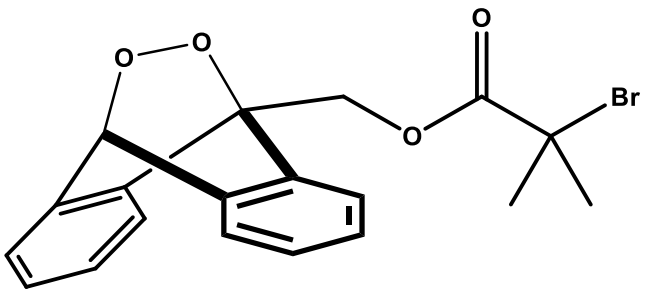

Figure 4-9. Possible peroxide product formed when AMBiB is exposed to either 320-390 nm or 254 nm light in the presence of oxygen.

A similar experiment was then performed, but with a deoxygenated solution of AMBiB in hexane, Figure 4-10. Solid lines show traces recorded after exposure to 365 nm for 5 mins, and dashed show traces recorded after exposure to 254 nm for 5 mins. This was repeated several times, until the solution was exposed to each wavelength for a total of 30 minutes. In the 325-400 nm region, there is initially a large drop in absorbance after the first exposure to 365 nm, followed by a small increase in absorption after the first exposure to 254 nm, suggesting a small amount of reversion to monomer. The steps of 365 nm/254 nm exposure were repeated and showed steady increases/decreases in absorbance, in this region only, suggesting the dimerisation is reversible. An expansion of the 350-400 nm region and a plot of the absorbance (at wavelengths 355, 365, 375, 385 nm) with iterations help clarify this observation, Figure 4-11. The region below 350 nm shows increasing absorbance after exposure to 365 nm and no change after exposure to 254 nm, resulting in an overall increase in absorbance. As the sample was prepared in a cuvette, deoxygenated and sealed with a Suba seal, there may have been some contamination caused by the sealing. This could occur in multiple ways; the seal came in contact with the solution, or the continuous exposure to high energy light caused progressive seal degradation, or solvent vapours dissolved in the AMBiB solution. Either of these points could feasibly result in a non-reversible trend in the absorbance.

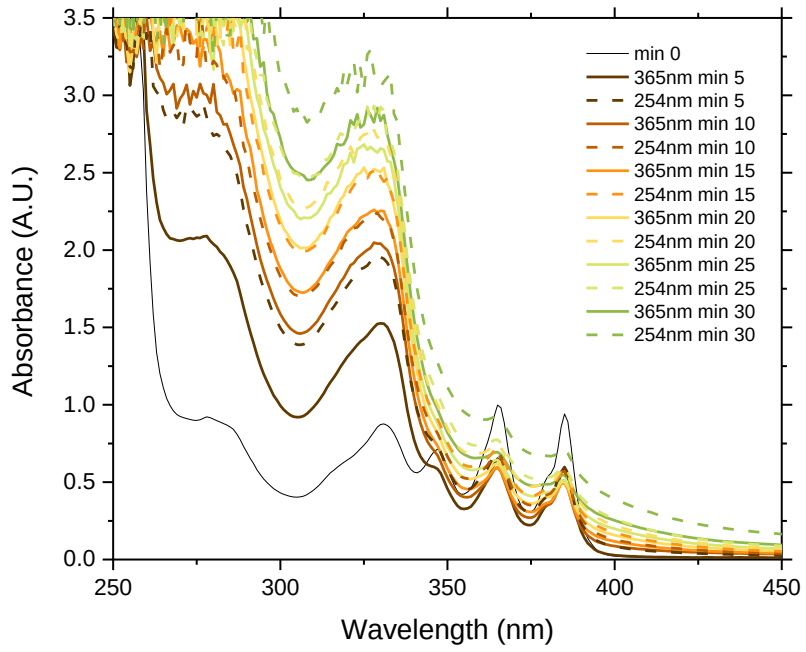

Figure 4-10. UV-Vis absorbance spectrum of AMBiB in hexane (2.5 x10^{-2} mg ml^{-1}) with sequential exposures to 365 nm and 254 nm light. Legend indicates total amount of exposure time for each wavelength.

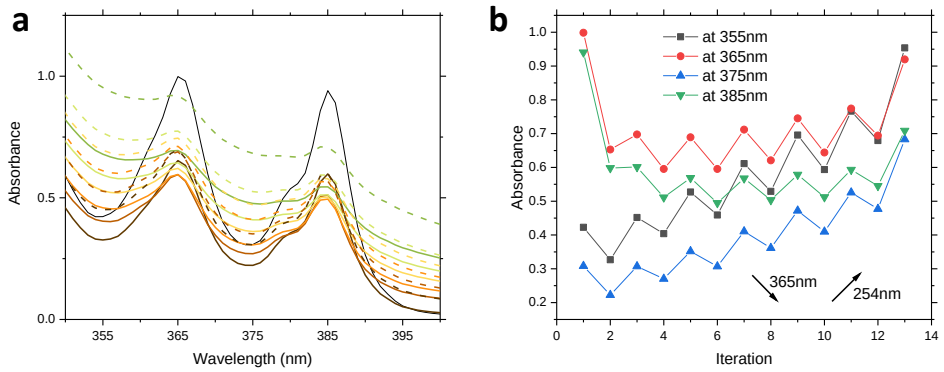

Figure 4-11. UV-Vis absorbance spectrum of AMBiB in hexane (2.5 x10^{-2} mg ml^{-1}) with sequential exposures to 365 nm and 254 nm light. Legend indicates total amount of exposure time for each wavelength. a) Expansion of 350-400 nm region in Figure 4-10. b) Absorbance *versus* light exposure iteration taken at multiple wavelengths.

4.1.1.4 Reversibility by exposure to 40 °C

The dimerisation of anthracene compounds has also been shown to reverse at elevated temperatures.[148,227,229] A preliminary experiment was performed in which a vial of AMBiB in hexane was exposed to 320-290 nm light, producing the dimerisation, then placed in a water bath at 40 °C for a total of 20 minutes (Figure A4-6). The elevated temperature showed some monomer formation by an increase in absorbance and heating for longer than 10 minutes showed no further changes in the spectrum.

An earlier iterative experiment, Figure 4-10, was repeated firstly with 365 nm/40 °C cycles, followed by 254nm/40 °C cycles, Figure 4-12. During the 365 nm/40 °C cycle, 40 °C had little effect on the absorbance, this is more obvious in Figure 4-13. After 8 iterations, there was a gradual increase the absorbance, but this could be due to the overarching increase in absorbance at 300-340 nm, therefore skewing the results. Exposure to 40 °C resulted in an increase in adsorption in the 300-340nm region, rather than the intended increase in the 340-400 nm region. When the same solution was subsequently exposed to 254 nm light, an increase in absorption was observed across the entire experimentally measured wavelength range. All subsequent iterations showed a decrease in absorption in the 300-340 nm region. During the 254 nm/40 °C cycle, the temperature increase *decreased* absorbance rather than increasing (as would be expected), implying it promotes the dimerisation (or another unwanted reaction). Exposure to 254 nm then increases the absorbance, reversing the

reaction caused by heating at 40 °C, *i.e.* 254 nm promotes reversion to monomer. Overall, exposure to 365 nm promotes dimerisation, 254 nm promotes monomer formation and 40 °C somewhat contributes to dimerisation but has no effect on reversion to monomer.

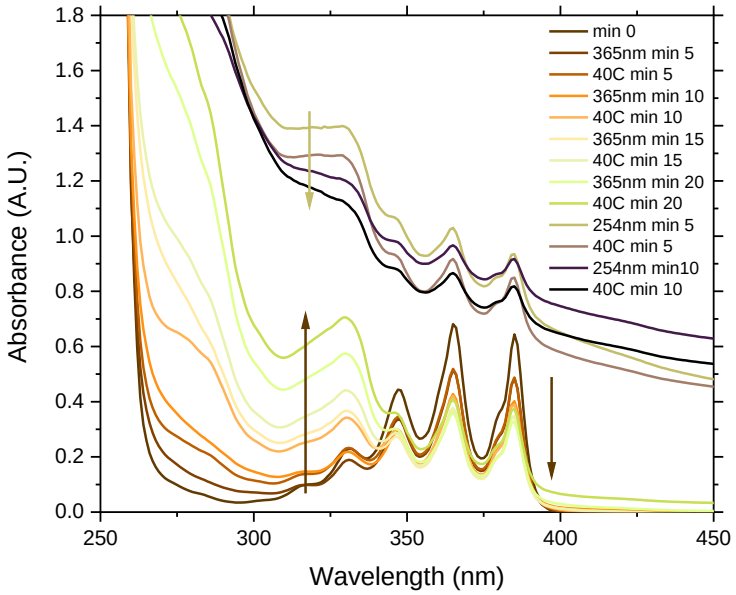

Figure 4-12. UV-Vis absorbance spectrum of AMBiB in hexane (2.5 x10^{-2} mg ml^{-1}) with sequential exposures to 365 nm and 254 nm light. Legend indicates total exposure time for each wavelength.

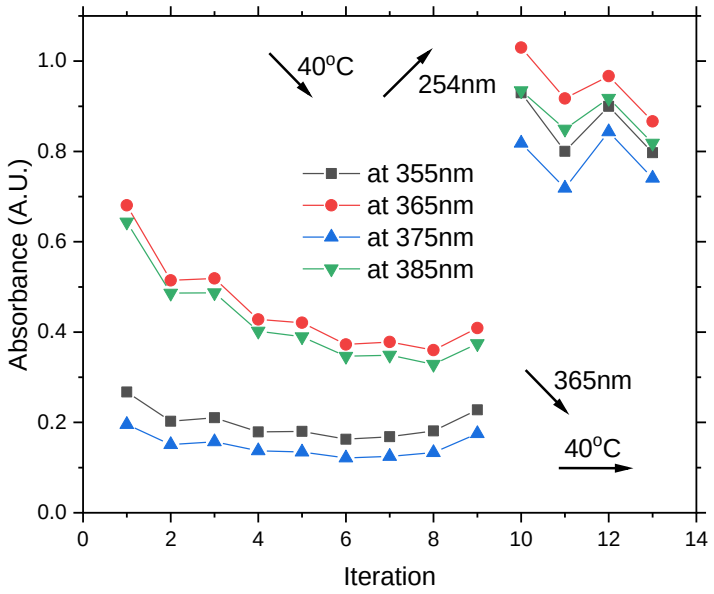

Figure 4-13. Absorbance (taken at different wavelengths) *versus* light or heat exposure iteration. UV-Vis absorbance spectrum of AMBiB in hexane (2.5 x10^{-2} mg ml^{-1}) with sequential exposures to 365 nm and 254 nm light. Legend indicates total exposure time for each wavelength.

4.1.1.5 NMR investigation of the dimerisation reaction

In order to corroborate previous UV-Vis spectroscopy results, ^{1}H NMR was used to monitor the dimerisation of AMBiB. Figure 4-14a shows the spectrum of monomer (AMBiB) in d^{6}-DMSO, which shows no impurities. AMBiB was exposed to 320-390 nm light for 20 minutes in a borosilicate NMR tube, which should not affect the dimerisation but would block 254 nm light to promote the reversion to monomer. New peaks were visible in the spectrum (highlighted in blue) after irradiation, which correspond with chemical shifts expected for the dimerised product, plus some unknown peaks. Peaks highlighted in orange show that some of the AMBiB did not dimerise and the ratio of dimer to monomer is less than ~38%, which is lower than expected. The same NMR tube was then placed in a 40 °C bath for 45 mins and no further change was observed in the spectrum. This agrees with the previous UV-Vis data, despite initial expectations that heating to 40 °C would revert the dimer back to monomer.

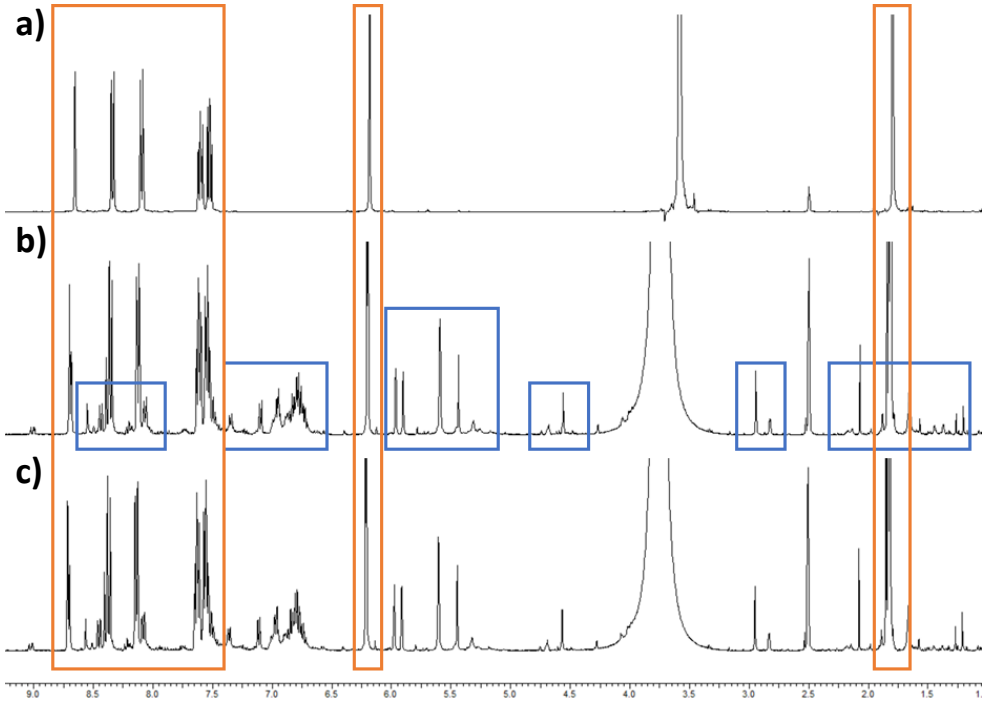

Figure 4-14. ^{1}H NMR spectra of AMBiB in d^{6}-DMSO a) pure b) after 20 mins irradiation of 320-290 nm light c) after subsequent heating at 40 °C for 45 mins.

4.1.1.6

4.1.1.7 Polymer synthesis with AMBiB initiator

As preliminary results from UV-Vis spectroscopy suggested that the dimerisation reaction of AMBiB is reversible, polymers were then synthesised using the AMBiB

initiator. This was done to produce a low molecular weight P*t*BA that can be deprotected to PAA, Figure 4-15. A table of reactions is given in Table 4-1.

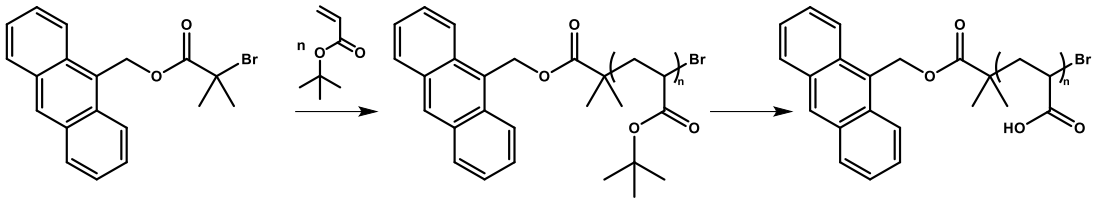

Figure 4-15. Proposed synthesis to poly(acrylic acid) with AMBiB initiator.

Firstly, standard copper-RDRP conditions (copper wire (Cu(0)) and photo-mediated copper (UV)) were used to polymerise *t*BA to later deprotect to poly(acrylic acid). Cu(0) in DMSO resulted in a biphasic reaction mixture with low monomer conversion (32%), which is expected from DMSO and *t*BA polymerisations. The bottom layer was found to be unreacted monomer and the top, polymer-rich layer was used for NMR and GPC analysis (entry 1). IPA also proved to be a poor solvent for this polymerisation, Cu(0) reactions (both DP10 and DP20) did not polymerise (entry 3, 4). UV polymerisation in IPA gave higher conversion (21%) however, this is insufficient for our purposes and the dispersity was poor (entry 4). It is likely that the UV reaction promotes the dimerisation of the initiator during the polymerisation, resulting in poor dispersity. UV initiated reactions were, therefore, no longer used as they did not represent a viable polymerisation technique. Entry 3 was repeated at 40 °C and there was a minimal increase in conversion (entry 5). Due to the inadequate results in entries 1 – 5, an attempt was made to polymerise methyl acrylate in DMSO to check that the polymerisation was possible at all. Entry 6 showed, again, low conversion after 22 hours however, switching the ligand from Me_6TREN to N,N,N′,N′′,N′′-Pentamethyldiethylenetriamine (PMDETA) gave a significant increase in conversion (entry 7) but higher dispersity (the copper wire seemed to be fully oxidised to Cu(II) during the reaction, likely affecting the reaction equilibrium). Higher temperature and PMDETA as ligand were combined (entry 8) in a final optimisation attempt. This gave a higher conversion than entry 5 or 7, however was still inadequate. TFE was also tested as an alternative solvent using Me_6TREN and PMDETA at room temperature but resulted in no observable reaction.

Table 4-1. Polymerisation optimisation (Cu(II)-RDRP) conditions and GPC data for AMBiB initiator.

Entry	Polymer	Conditions	Conversion	GPC	
				M_n (Da)	$Đ$
1	P*t*BA$_{20}$	DMSO, Cu(0)	32% - 20hr	700	1.4
2	P*t*BA$_{20}$	IPA, Cu(0)	3% - 20hr	-	-
3	P*t*BA$_{10}$	IPA, Cu(0)	1% - 20hr	-	-
4	P*t*BA$_{20}$	IPA, UV	21% - 20hr	1500	1.4
5	P*t*BA$_{25}$	IPA, Cu(0), 40 °C	9% - 22hr	-	-
6	PMA$_{25}$	DMSO, Cu(0)	6% - 22hr	-	-
7	PMA$_{25}$	DMSO, Cu(0), PMDETA	30% - 22hr	2600	4.41
8	P*t*BA$_{25}$	IPA, Cu(0), 40 °C PMDETA	13% - 22hr	-	-

Toluene was used as an alternative solvent with better solubility for the anthracene initiator, but increased temperatures are required to increase the rate of reaction, reduce the induction period and quickly form the Cu(I)/Cu(II) equililbrium[36,239] Polymerisation in aromatic hydrocarbon solvents using copper (I)-ATRP is often used when polymerising methacrylates, and was used for these polymerisations, Table 4-2. All entries' conditions using Cu(I) and were polymerised at 90 °C in a Schlenk tube, the initiator was dissolved in a minimal amount of hot solvent before adding to the reaction mixture. Firstly, DP 25 poly(methyl methacrylate) was targeted using toluene and a pyridine imine ligand (entry 1), *N*-propyl-1-pyridin-2-ylmethanimine (*N*-propyl), Figure A4-7. 99% conversion and a dispersity = 1.87 was obtained (due to some unreacted initiator included in the trace, Figure A4-8) suggesting that either using an aromatic hydrocarbon solvent and/or higher reaction temperatures are necessary for efficient polymerisation, however, lower dispersities are required for efficient microphase separation. The solid content was decreased from 50% to 25% (entry 2), showing minimal changes to conversion and dispersity, and 12.5% solids gave lower conversions but lower dispersity (entry 3). These conditions were tested with a DP100 targeted PMMA (entry 4, 5, 6), results were similar to the DP25 and showed that multiple chain lengths could be targeted, and 25% solids is suitable for all targeted DPs. EBiB was used as an initiator (entries 7, 8) to compare the effect of using AMBiB (entries 5, 6). Results obtained were similar, however AMBiB-produced polymers gave better conversion and dispersity due to improved solubility in toluene. The optimised conditions from entry 5 were used to polymerise *t*BA, which resulted in 13% conversion (entry 9). Increasing the solid content to 50% (entry 10) made a

large difference by increasing conversion but also a large dispersity. The ligand was changed to Me_6TREN, a better ligand for acrylates, however, this did not improve the dispersity (entry 11). PMDETA as a ligand gave lower dispersity but also lower conversion and did not react at all when the targeted DP was higher (entries 12 and 13). Finally, using anisole as solvent with different ligands and different weight% did not produce adequate conversion and dispersity (entries 14-16).

Table 4-2. Polymerisation optimisation (Cu(I)-ATRP) conditions and GPC data for AMBiB initiator.

Entry	Polymer	Conditions[a]	Conversion	GPC_{THF}	
				M_n (Da)	$Đ$
1	$PMMA_{25}$	Toluene, N-propyl, 50% solids	99% - 20hr	2200	1.87
2	$PMMA_{25}$	Toluene, N-propyl, 25% solids	98% - 20hr	2900	1.78
3	$PMMA_{25}$	Toluene, N-propyl, 12.5% solids	93% - 20hr	3700	1.38
4	$PMMA_{100}$	Toluene, N-propyl, 12.5% solids	81% - 20hr	10000	1.41
5	$PMMA_{100}$	Toluene, N-propyl, 25% solids	53% - 4hr	7500	1.30 (1.16)[c]
6[b]	$PMMA_{100}$	Toluene, N-propyl, 33% solids	91% - 23hr	12700	1.27
7	EBiB-$PMMA_{100}$	Toluene, N-propyl, 25% solids	59% - 4hr	7400	1.36
8	EBiB-$PMMA_{100}$	Toluene, N-propyl, 33% solids	97% - 20hr	6200	1.38
9	P*t*BA_{25}	Toluene, N-propyl, 25% solids	13% - 7hr	-	-
10	P*t*BA_{25}	Toluene, N-propyl, 50% solids	83% - 20hr	3200	3.05
11	P*t*BA_{25}	Toluene, Me_6TREN 50% solids	82% - 20hr	3800	3.60
12	P*t*BA_{25}	Toluene, PMDETA, 25% solids	48% - 22hr	1900	2.42
13	P*t*BA_{100}	Toluene, PMDETA, 25% solids	3% - 20hr	-	-
14	P*t*BA_{25}	Anisole, PMDETA, 50% solids	72% - 22hr	2500	1.86
15	P*t*BA_{25}	Anisole, PMDETA, 25% solids	77% - 22hr	1900	2.66
16	P*t*BA_{25}	Anisole, N-propyl, 25% solids	89% - 23hr	3400	1.60

a) Performed in a Schlenk tube at 90 °C with [Cu(I)]:[I]:[L] = 1:1:2. Solid weight % being monomer volume percentage (v/v%). b) Most optimal conditions. c) Bracketed dispersity value from GPC in $CHCl_3$.

These reactions showed that methacrylates polymerise more efficiently than acrylates using these conditions, therefore, butyl methacrylate and its isomers (Figure 4-16) were polymerised (Table 4-3) with the optimised conditions from Table 4-2. As bulkiness of the R group increases from *n*-butyl to *t*-butyl methacrylate, the reaction becomes more inhibited which is evident from the decreasing conversion. However, GPC of poly(*n*-butyl methacrylate) showed an M_n = 14000 Da (very close to the theoretical M_n of 14600 Da) despite 56% conversion. All polymers had low dispersity, however, *t*-butyl methacrylate failed to polymerise. This means that *t*-butyl monomers are not polymerisable with AMBiB and alternative monomers that can be deprotected must be used to obtain amphiphilic polymers.

Table 4-3. Polymerisation (Cu(I)-ATRP) conditions and GPC data for AMBiB-PBMA$_{100}$.

Entry	Polymer	Conditions	Conversion	GPC	
				M_n (Da)	$Đ$
1	P*n*BMA$_{100}$	Toluene, N-propyl, 25% solids	56% - 20hr	14000	1.20
2	P*s*BMA$_{100}$	Toluene, N-propyl, 25% solids	44% - 20hr	7800	1.20
3	P*i*BMA$_{100}$	Toluene, N-propyl, 25% solids	27% - 20hr	6200	1.24
4	P*t*BMA$_{100}$	Toluene, N-propyl, 25% solids	2% - 20hr	-	-

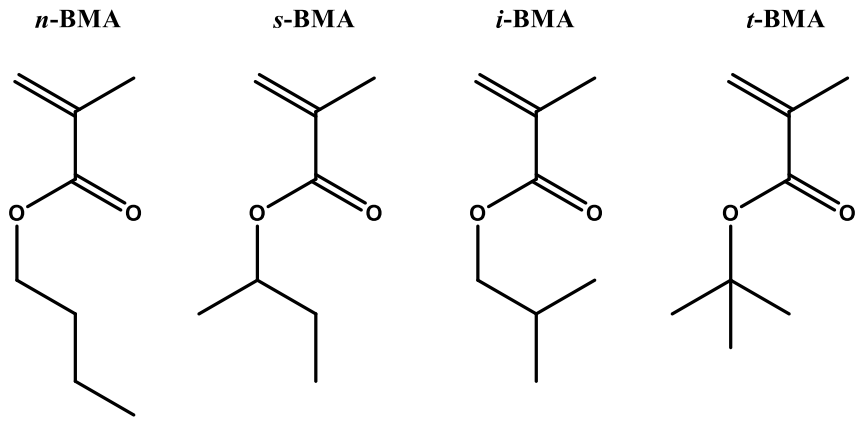

Figure 4-16. Structures of butyl methacrylate isomers. From left to right; *n*-butyl, *sec*-butyl, *iso*-butyl, and *tert*-butyl methacrylate.

4.1.2 Octadecyl bromoisobutyrate (C_{18})

A further hydrophobic alkyl halide initiator was synthesised to have a non-functionalised hydrocarbon tail, which allows comparison to the perfluorinated (F_{13}, F_{17}, F_{21}) and short hydrocarbon (EBiB, F_0) initiators. Naturally, the longer the hydrocarbon tail, the more hydrophobic the initiator, therefore octadecan-1-ol was used as starting material in the synthesis of octadecyl bromoisobutyrate (C_{18}) (Figure 4-17). Product was obtained in 66.3% yield and characterised by ^{1}H (Figure A4-10) and ^{13}C (Figure A4-11) NMR.

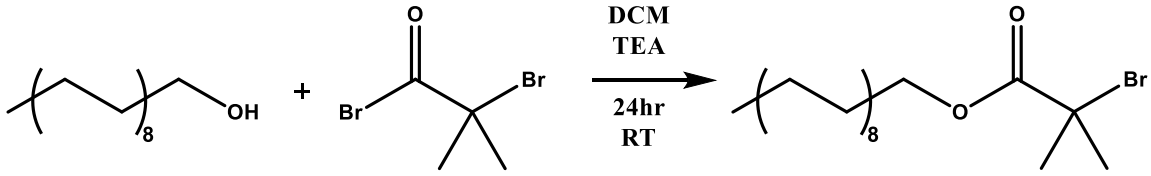

Figure 4-17. Synthesis of octadecyl bromoisobutyrate (C_{18}).

4.1.2.1 Polymer synthesis with C_{18} initiator

Polymerisation conditions were optimised for poly(*tert*-butyl acrylate) for the purpose of deprotecting to poly(acrylic acid) (Table 4-4). Firstly, the general procedure for copper(0) wire polymerisation were tested (entry 1, Figure A4-14), which gave high conversion (94%) and acceptable dispersity (1.31). The theoretical M_n for C_{18}-P*t*BA_{25} is 3600 Da, which was not reflected in the GPC and attempts were made to further decrease dispersity. Reaction solvents IPA, TFE and DMSO were interchanged with ligands Me_6TREN and PMDETA. As expected, DMSO is a poor solvent for polymerisation of P*t*BA and the most optimal conditions were TFE with Me_6TREN, giving 3200 Da and 1.28 dispersity.

The GPC traces for these in THF eluent showed tailing and low molecular weight shoulders (Figure A4-12). Entries 1 and 3 in $CHCl_3$ eluent (entries 1b and 3b) showed monomodal distributions with low dispersity (Figure A4-13) and no tailing or shoulders, due to a different radius of gyration in each solvent. The only significant difference was that polymerising in TFE produces a polymer with higher molecular weight.

Table 4-4. Polymerisation conditions for C_{18}-P*t*BA_{25}.

Entry	Polymer	Conditions[a]	Conversion[d]	GPC	
				M_n (Da)	$Đ$
1	C_{18}-P*t*BA_{25}	IPA, Me_6TREN	94%	2600	1.31
2[b]	C_{18}-P*t*BA_{25}	IPA, PMDETA	74%	3300	1.39
3	C_{18}-P*t*BA_{25}	TFE, Me_6TREN	96%	3200	1.28
4	C_{18}-P*t*BA_{25}	DMSO,Me_6TREN	95%	4100	4.30
-	-	-	-	-	-
1b[c]	C_{18}-P*t*BA_{25}	IPA, Me_6TREN	94%	2600	1.16
3b[c]	C_{18}-P*t*BA_{25}	TFE, Me_6TREN	96%	3400	1.11

[a] Polymerised using general procedure for copper(0) wire polymerisation, reaction time 3 hours. [b] Reaction time 5 hours. [c] Sample 1 and 3 run in $CHCl_3$ GPC eluent. [d] Calculated from ^{1}H NMR.

As the difference in dispersity is minimal between using TFE vs IPA, IPA was chosen as a suitable solvent for the polymerisation of a batch of polymers. The slightly lower molecular weight is beneficial as the aim is to synthesise low molecular weight polymers as final materials. IPA is also considered a safer and 'green' solvent,[240–242] particularly compared to TFE which is toxic and may cause organ damage.

Using the conditions outlined in Table 4-4 entry 1, a set of C_{18}-P*t*BA_n polymers were synthesised with different targeted DPs ranging from 5 to 26. Polymers exhibited good agreement with theoretical values of molecular weight and low dispersity, ideal for microphase separation (Table 4-5). These polymers were all deprotected to poly(acrylic acid) by the general deprotection of P*t*BA procedure, using TFA and DCM.

Table 4-5. Molecular characteristic of C_{18}-PAA_n polymers.

Sample[a]	$M_{n,\ theory}$	$M_{n,\ H\ NMR}$[b]	Conversion[a] (%)	$M_{n,\ GPC}$[b]	$Đ$
C_{18}-P*t*BA_5	1080	1080	98	1000	1.10
C_{18}-P*t*BA_{12}	1700	1960	99	1600	1.12
C_{18}-P*t*BA_{16}	2340	2470	97	2300	1.11
C_{18}-P*t*BA_{19}	3980	2860	93	2800	1.12
C_{18}-P*t*BA_{26}	3620	3750	94	3300	1.12

[a] Calculated from ^{1}H NMR. [b] $CHCl_3$ GPC data against poly(methyl methacrylate) standards.

4.1.2.2 SAXS of C_{18}-PAA_n polymers

C_{18}-PAA_n polymers were annealed in the same manner as F_{13}-PAA_m as described in Chapter 1 (slow evaporation of a methanol polymer solution in a PTFE boat). Small-angle X-ray scattering (SAXS) was measured on solvent annealed and thermal annealed samples (Figure 4-18). Solvent annealed samples show a principal peak, from which a domain spacing can be calculated but has no inherent meaning in disordered morphologies. Thermally annealed samples showed both a principal peak and higher order peaks whereby morphology was determined, Table 4-6. Domain spacing increases with increasing polymer chain length and thermally annealed samples show a change in morphology from LAM to HEX. Unlike the F_n-PAA_m SAXS results, the lower DP samples were less crystalline with higher DP, suggested by less sharp and lower intensity of the higher order peaks. This may be because the initiator tail chain length is much longer in C_{18} than in $F_{13} > F_{17} > F_{21}$, and the volume fraction of the hydrophobic group is > 0.5.

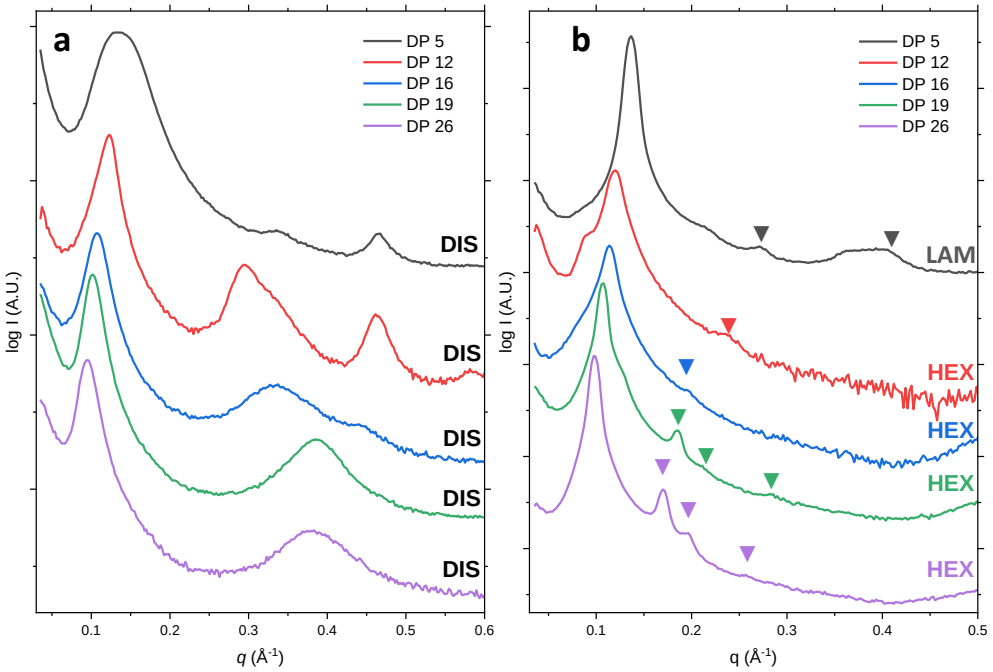

Figure 4-18. SAXS profiles for C_{18}-PAA_n polymers. a) solvent annealed from methanol. b) thermally annealed at 120 °C for 24 hrs.

Table 4-6. Assembly properties of annealing FC_{18}-PAA_n polymers.

Sample	Solvent anneal		Thermal anneal	
	Morphology	***d* (nm)**	**Morphology**	***d* (nm)**
C_{18}-P*t*BA_5	DIS	4.5	LAM	4.6
C_{18}-P*t*BA_{12}	DIS	5.2	HEX	5.3
C_{18}-P*t*BA_{16}	DIS	5.8	HEX	5.6
C_{18}-P*t*BA_{19}	DIS	6.1	HEX	5.9
C_{18}-P*t*BA_{26}	DIS	6.5	HEX	6.4

4.2 Hydrophilic monomers

Alternative hydrophilic monomers were considered for the synthesis of amphiphilic block copolymers, stemming from the failed attempts to polymerise *tert*-butyl acrylate and methacrylate using the AMBiB initiator (4.1.1.7). Examples of hydrophilic monomers that can be polymerised in their protected form include glycidyl (meth)acrylate,[243] 2-(pyridine-2-yl)ethyl (meth)acrylate,[244] and 1-ethoxyethyl (meth)acrylate.[245]

4.2.1 1-Ethoxyethyl methacrylate (EEMA)

1-Ethoxyethyl methacrylate (EEMA) was considered as an alternative route to poly(methacrylic acid), as it can be polymerised in its protected form (similar to *t*BA) then deprotected.[245] EEMA is much less bulky than *tert*-butyl methacrylate, therefore, a suitable monomer for AMBiB to polymerise.

4.2.1.1 Monomer synthesis

EEMA was synthesised according to literature (Figure 4-19)[245], for the polymerisation with AMBiB initiator which was previously shown to have better synergy with methacrylates rather than acrylates. The synthesis required optimisation of the molar equivalents, as an unreacted methacrylic acid was difficult to remove from the product, particularly because the boiling point of methacrylic acid is 163 °C,[246] and EEMA is predicted at 162 °C.[247] Vacuum distillation and alumina filtration steps were taken during purification attempts, which were monitored using gas chromatography (Figure A4-16). It was found that washing the product with hexane and filtering through basic alumina removed any unreacted methacrylic acid,[244] however, the most optimal solution was to increase the molar equivalents of ethyl vinyl ether 2 to 1

during the reaction synthesis. Excess vinyl ether was removed by rotary evaporation and yielded a pure product without the need for distillation (Figure 4-20).

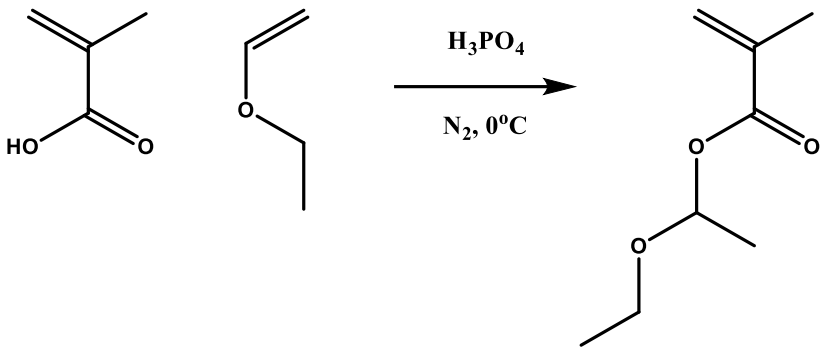

Figure 4-19. Synthesis of monomer 1-Ethoxyethyl methacrylate (EEMA).

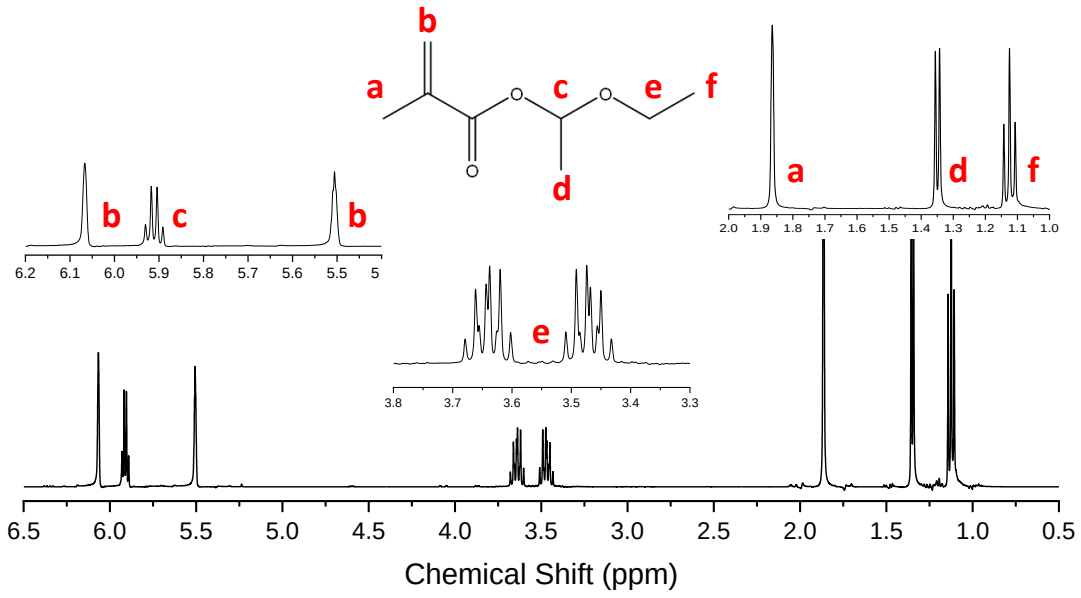

Figure 4-20. ^{1}H NMR Spectrum (400 MHz, CDCl3) of 1-Ethoxyethyl methacrylate (EEMA)
.

4.2.1.2 Polymerisation of EEMA

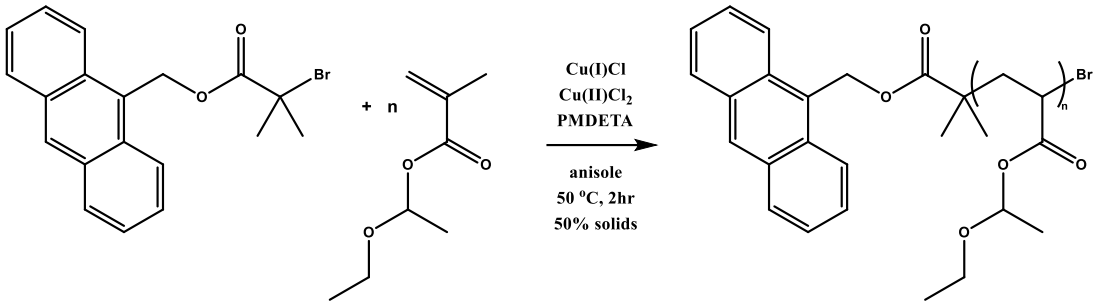

Figure 4-21. Optimum polymerisation conditions for EEMA with AMBiB initiator.

Optimisation of conditions for the polymerisation of EEMA are presented in Table 4-7. Firstly, the general copper(0) wire polymerisation was tested with EBiB as the initiator, this was to determine any adverse effects from polymerising this monomer. The dispersity was found to be higher than expected (at 1.6), however, this was suspected to be the result of an excessive reaction time, or being less effective overall when polymerising methacrylates with EBiB (compared to acrylates).[35] As such, methyl α-bromophenylacetate (MBPA) was tested using the same conditions and showed good conversion but high dispersity. AMBiB was then used with a combination of the previously optimised conditions for the initiator (entry 3) and those from literature,[245] (*i.e.* Cu(I)Br and 50 °C) as the temperature must remain low to prevent thermal deprotection. The polymerisation was successful, however low molecular weight tailing is evident and initiator efficacy may be the underlying cause in these conditions. GPC traces for entries 1, 2 and 3, are presented in Figure A4-17.

Entries 4 and 5 show the same polymerisation conditions carried out by Van Camp *et al.*[245], which showed that the addition of 20 mol % $Cu(II)Cl_2$ (with respect to Cu(I)Cl concentration) gave much better control of the polymer growth and reaction times of 1 hour. Polymerisations with EBiB and AMBiB initiators and targeted DP 50 were tested, they showed 50/73% conversion after 2 hours, and the AMBiB polymer showed better dispersity than when EBiB was used. As a result of these promising results, polymers with lower DPs = 20 and 40 were targeted (entries 6 and 7), showing narrow, monomodal distributions (Figure 4-22).

Table 4-7. Optimisation conditions for the polymerisation of EEMA monomer.

Entry	Polymer	Conditions[c]	Conversion	GPC[a]	
				M_n (Da)	$Đ$[b]
1	EBIB - $PEEMA_{50}$	Cu(0), Me_6TREN, RT, DMSO	51% - 3hr 99% - 72hr	5500- 3hr 8800 – 72hr	1.6 – 3hr 1.6 – 72hr
2	MBPA- $PEEMA_{50}$	Cu(0), Me_6TREN, RT, DMSO	97% - 22hr	7900	2.5
3	AMBiB- $PEEMA_{50}$	Cu(I)Br, PMDETA, 50 °C, toluene, 25% solids	84% - 20hr	4100	3.08
4	EBIB - $PEEMA_{50}$	Cu(I)Cl/Cu(II)Cl_2, 50 °C, anisole, PMDETA, 50% solids	50% - 2hr	6100	1.50
5	AMBIB - $PEEMA_{50}$	Cu(I)Cl/Cu(II)Cl_2, 50 °C, anisole, PMDETA, 50% solids	73% - 2hr	10200	1.22
6	AMBIB - $PEEMA_{20}$	Cu(I)Cl/Cu(II)Cl_2, 50 °C, anisole, PMDETA, 50% solids	75% - 2hr	3700	1.28
7	AMBIB - $PEEMA_{40}$	Cu(I)Cl/Cu(II)Cl_2, 50 °C, anisole, PMDETA, 50% solids	75% - 2.5hr	7000	1.26
8	EBIB - $PEEMA_5$	Cu(I)Cl/Cu(II)Cl_2, 50 °C, anisole, PMDETA, 50% solids	72% – 2hr	1200	1.80
9	EBIB - $PEEMA_{10}$	Cu(I)Cl/Cu(II)Cl_2, 50 °C, anisole, PMDETA, 50% solids	78% - 2hr	2500	1.48

a) $CHCl_3$ GPC data against poly(methyl methacrylate) standards. b) Dispersity. c) 20 mol % Cu(II)Cl_2 *wrt* Cu(I)Cl.

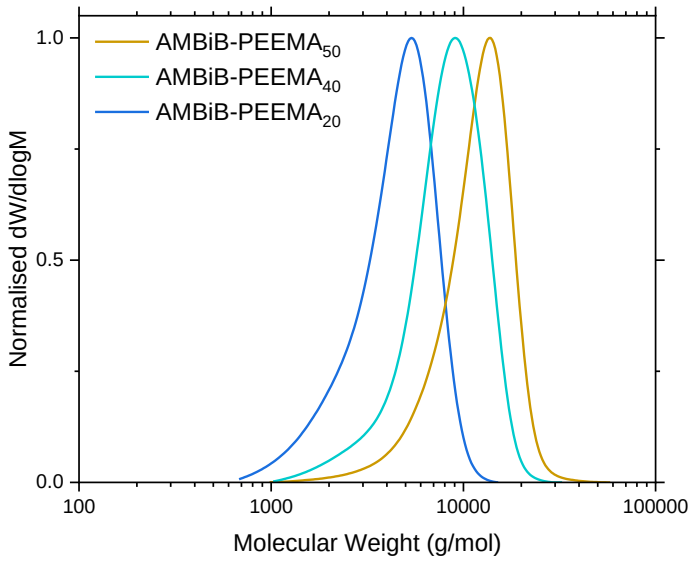

Figure 4-22. GPC traces in $CHCl_3$ eluent of AMBIB-initiated poly(1-Ethoxyethyl methacrylate) (PEEMA) at different targeted molecular weights. (Entries 5, 6, 7 in Table 4-7).

EBiB was then used for preliminary polymerisations at very low targeted DPs = 5 and 10, to prevent unnecessary waste of AMBiB if the polymerisation failed. A polymer with lower DP will have a larger Flory interaction parameter and is expected to show strong microphase separation. Entries 8 and 9 show that good conversion was achieved, however, dispersity increases dramatically at very low DP (Figure 4-23). While EBiB polymerisations have proven harder to control than AMBiB, these results give insight on the polymerisation kinetics at low DP under these conditions. Also, the full GPC traces show unreacted monomer and/or initiator (Figure A4-18) peaks which, for DP5, remained present after purification steps (which is difficult when the polymer length is short as precipitation cannot be used). If initiator efficacy is inhibited at the early stages of polymerisation, the achieved DP is higher than the targeted DP. Ideally, a high degree of growth control and high conversion at low DP is required to remove the necessity of later purification and allow a simple route to amphiphilic polymers.

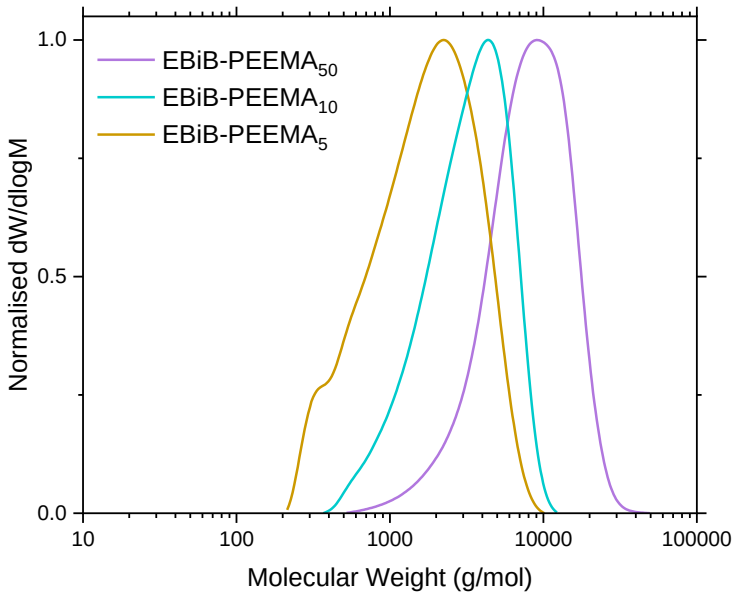

Figure 4-23. GPC traces in $CHCl_3$ eluent of EBIB-initiated poly(1-Ethoxyethyl methacrylate) (PEEMA) at different targeted molecular weights. (Entries 4, 8, 9 in Table 4-7).

4.2.1.3 Deprotection of PEEMA

Three different methods were used to test the deprotection of EEMA to methacrylic acid (Figure 4-24), these include heating, alkaline hydrolysis, and acid hydrolysis.

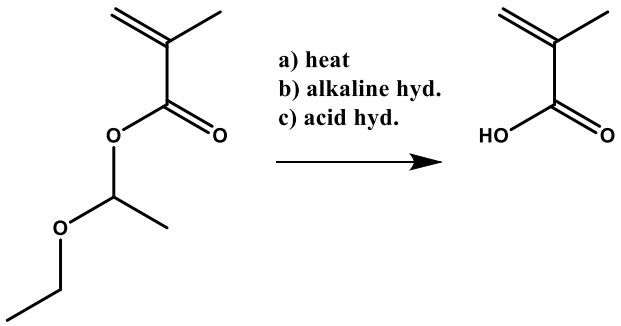

Figure 4-24. Different methods of deprotection of EEMA. a) 160 °C, 30 min. b) NaOD (40% in D_2O). c) DCM/TFA.

Firstly, heating the sample to 160 °C shows a 40% weight loss after 30 minutes, which corresponds to the loss of the ethyl vinyl ether R group.[245] This method was tested on AMBiB-$PEEMA_{20}$ and monitored by ^1H NMR, Figure 4-25. Both red and green labelled peaks correspond with EEMA monomer, but integrals do not imply these groups of peaks are of the same molecule. The vinyl peaks could be due to methacrylic acid (probably unreacted EEMA), and the peak at ~9.8 ppm is due to the carboxylic acid, which is either from methacrylic acid or poly(methacrylic acid). However, there are no broad polymer peaks, meaning the polymer seems to be either fully degraded into small molecules or was insoluble in the NMR solvent.

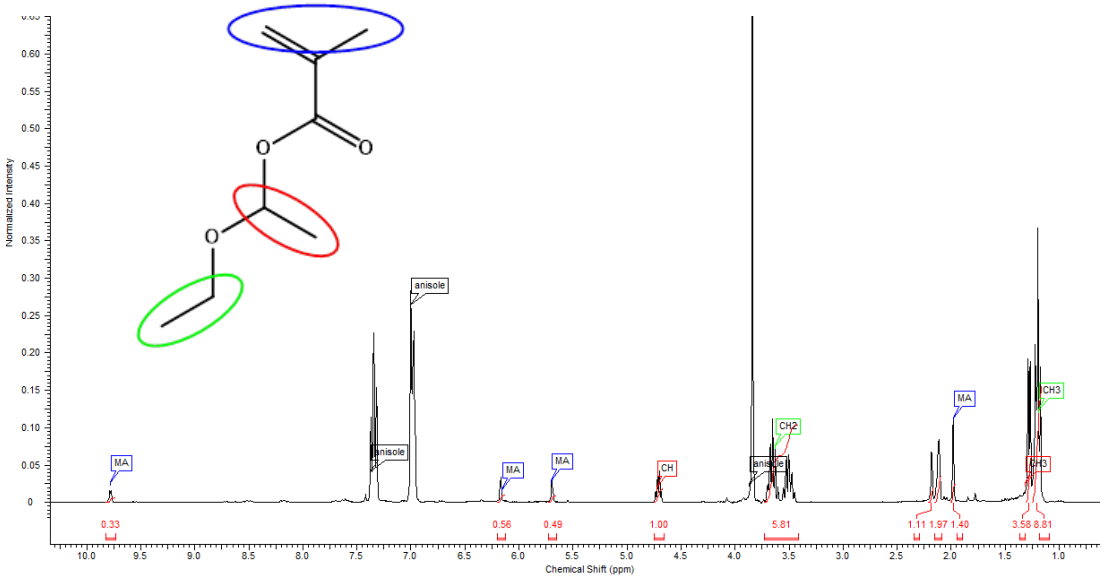

Figure 4-25. ^1H NMR spectrum (400 MHz, CDCl3) of AMBiB-$PEEMA_{20}$ after heating at 160 °C.

Secondly, alkaline conditions were tested for the deprotection.[244] EEMA monomer was reacted with 40% NaOD in D_2O and stirred for 2 hours, the resulting ^1H NMR spectrum shows that EEMA was no longer present, Figure 4-26. The three singlet peaks at 5.60, 5.25 and 1.80 ppm correspond to methacrylate peaks (vinyl and CH_3). The remaining peaks at 3.57 (q) ppm and 1.11 (t) ppm, are typical of an ethyl group. This suggests that the product(s) formed is(are) either ethyl methacrylate or methacrylic acid and ethanol, the singlet peak at 8.40 ppm is likely due to a carboxylic acid and suggests the latter. Volatiles were removed from the sample and the ethyl peaks disappeared, confirming that ethanol and methacrylic acid were produced. Using these alkaline conditions, AMBiB-$PEEMA_{50}$ was subject to hydrolysis, however, the sample concentration was too poor to detect polymer peaks.

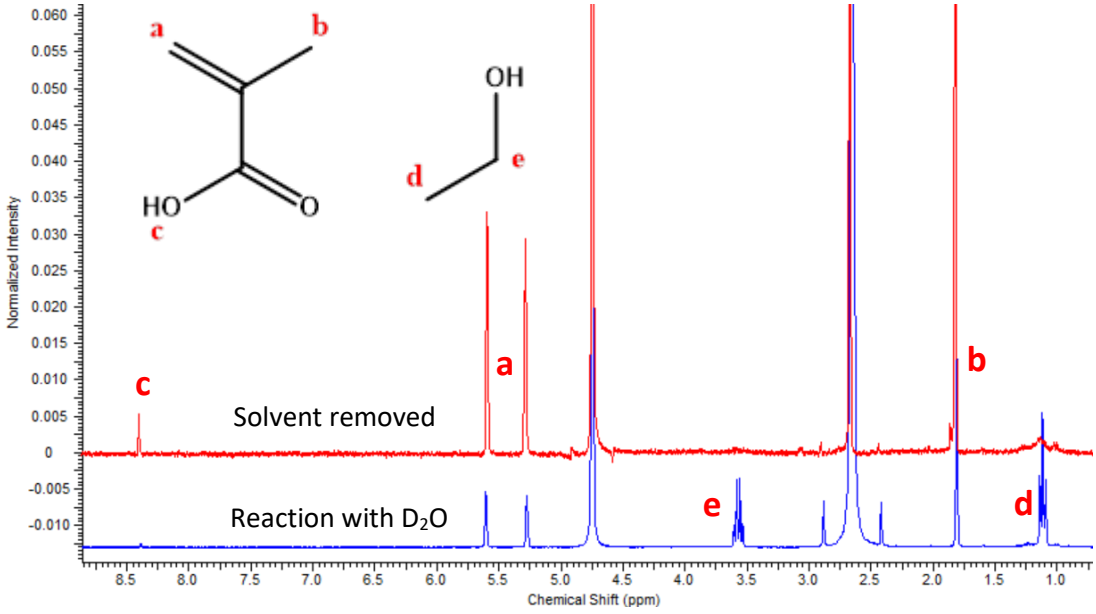

Figure 4-26. ^1H NMR spectrum (400 MHz, in D_2O) of EEMA after alkaline hydrolysis with NaOD (40% in D_2O), and after solvent was removed.

EEMA was also subjected to the acidic conditions used for deprotecting *t*BA - dissolved in DCM and reacted with TFA for 2 hours. ^1H NMR spectra in d_6-DMSO were taken after the reaction and after solvent was removed, Figure 4-27. Like the alkaline hydrolysis case, peaks are present for methacrylic and multiple ethyl groups, the peak at ~12 ppm shows TFA. After solvent was removed, the TFA peak disappears, and some ethyl peaks disappear. This suggests that TFA promotes the esterification of ethanol and methacrylic acid and ethyl methacrylate forms, or that TFA reacts with the ethanol (forming ethyl trifluoroacetate) and is not removed. Regardless, this explains the smaller intensity ethyl peaks at 4.40 (q) and 1.28 ppm (t). Some

methacrylic acid is present in both spectra at 9.64 ppm and shows that hydrolysis occurs but leads to more side products than when alkaline hydrolysis is used.

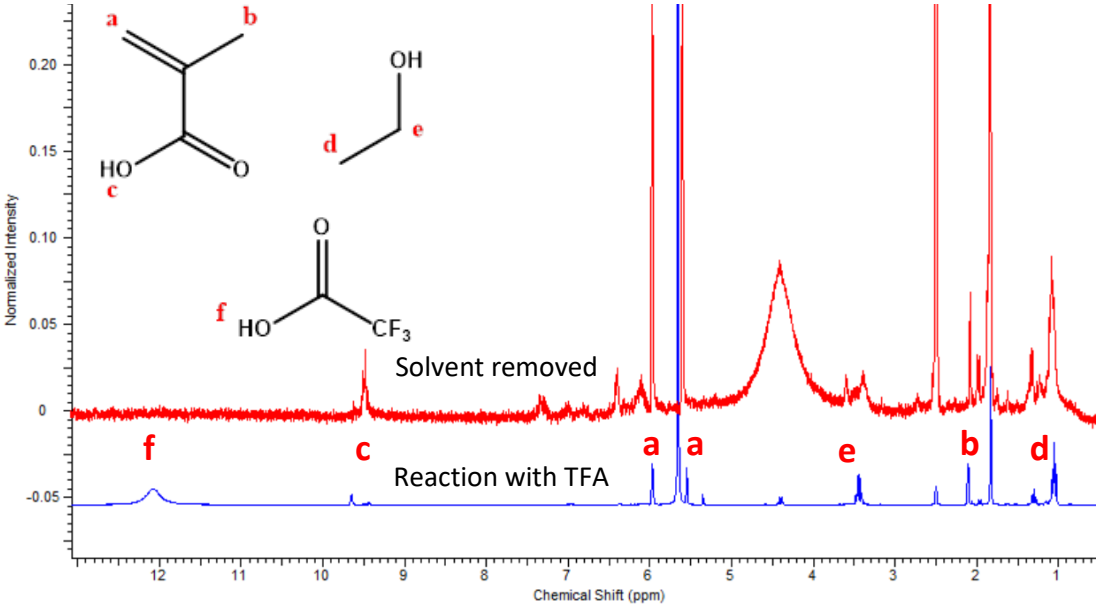

Figure 4-27. ^{1}H NMR spectrum (400 MHz) in d^{6}-DMSO of EEMA after acid hydrolysis with TFA, and after solvent was removed.

4.2.2 Solketal methacrylate (SkMA)

Solketal methacrylate (DL-1,2-Isopropylideneglycerol methacrylate, SkMA) is a protected hydrophilic monomer, which can be deprotected to the more hydrophilic glyceryl monomethacrylate (GMMA). The solketal starting material is made from glycerol (a cheap by-product from biodiesel production) by reaction between glycerol and acetone.[248] While the possible products include one with a 6-membered and one with a 5-membered ring, the 6-membered species is much less stable as the chair conformation has one of the methyl groups in the axial position.[249]

The deprotection of SkMA required less harsh conditions than needed to deprotect *tert*-butyl protecting groups (Figure 4-28, Figure A4-19), as 6M HCl/THF will selectively deprotect SkMA when in the presence of *t*BA.[250] Otherwise, the TFA/DCM conditions for *t*BA deprotection will also deprotect solketal groups. Two hydroxy groups may be less hydrophilic than one carboxylic acid group, which affects the interaction parameter, χ. Despite this, a primary R group in the monomer allows more control during polymerisation and lead to easier synthesis at lower molecular weights.

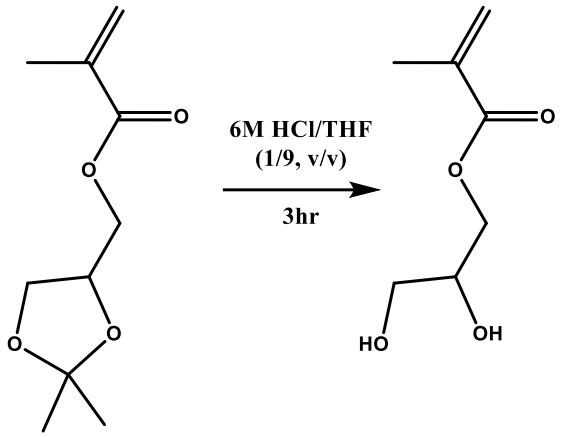

Figure 4-28. Deprotection of solketal methacrylate (SkMA) to glyceryl monomethacrylate (GMMA).

Using the optimised conditions for polymerising AMBiB developed in 4.1.1.7 (Cu(I)Br, 90 °C, toluene, *N*-propyl, 25% solids), four AMBiB-PSkMA polymers were synthesised with targeted DPs of 10, 25, 50 and 100 (Table 4-8). Compared to the polymerisation with EEMA, there is no issue with reaction temperatures at 90 °C as the deprotection required acid catalysis. All polymers exhibited high conversion, and high molecular weight polymers showed low dispersity. As the targeted molecular weight was lowered, the dispersity becomes higher with a very large increase at DP < 25.

Table 4-8. Molecular characteristics of AMBiB-initiated poly(solketal methacrylate) polymers.

Entry	Target DP	Conversion (%)	Target M_n (Da)	GPC_{CHCl_3}	
				M_n (Da)	$Đ$
1	100	94	20400	14100	1.30
2	50	94	10400	6600	1.32
3	25	96	5400	3700	1.39
4	10	98	2400	1500	1.84

The GPC traces are essentially monomodal and show no tailing other than for DP10 (Figure 4-29), which shows unwanted low molecular weight species. As conversion was high, it's likely that this is due to unreacted initiator. This is corroborated by the 360 nm UV trace from GPC (Figure A4-20) which shows an increasing low molecular weight shoulder as polymer length decreases. These GPC traces are from non-purified

polymerisation solution; it is likely that if these were purified, the traces would show more monomodal distributions with reduced dispersity. These samples were not purified due to the issues associated with purifying low molecular weight polymers, as mentioned earlier in this chapter.

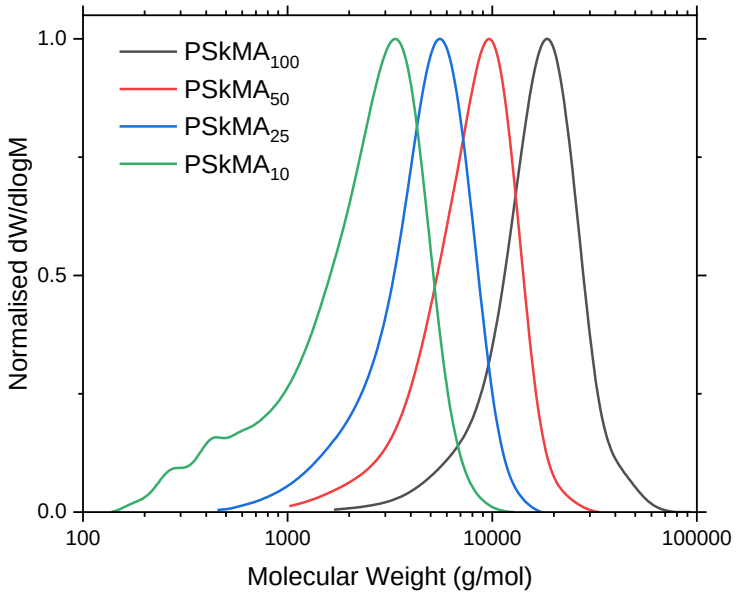

Figure 4-29. GPC traces in $CHCl_3$ eluent of AMBiB-initiated poly(solketal methacrylate) (PSkMA) at different DPs.

4.3 3-[Tris(trimethylsiloxy)silyl]propyl as a hydrophobic group

4.3.1 *N*-[3-[tris(trimethylsiloxy)silyl]propyl] 2-bromoisobutyramide (NtrisBiB)

An alternative to perfluorinated chemicals, siloxanes are highly hydrophobic and have been used in superhydrophobic coatings and materials.[129,251] For this reason, a hydrophobic siloxane initiator was synthesised using an amine starting material; 3-[tris(trimethylsiloxy)silyl]propyl amine, chosen due to product availability (Figure A4-21), and produces a 2-bromoisobutyramide initiator. Isobutyramide initiators are more stable towards degradation in aqueous media,[252] where the isobutyrate ester equivalents are prone to decomposition.[253] The synthesis of the initiator *N*-[3-[tris(trimethylsiloxy)silyl]propyl] 2-bromoisobutyramide (NtrisBiB) was straightforward (Figure 4-30), but required additional column chromatography to purify the product. The full proton NMR spectrum (Figure 4-31, Figure A4-22 with integration values) shows a small peak at ~1.65 ppm which is from the amine starting material, which is not obvious in the ^{13}C NMR spectrum (Figure A4-23). Interestingly, NtrisBiB is a molecule that shows the rare occurrence of non-first order proton coupling. This is clearest when observing environment b in Figure 4-31, which does not show typical splitting, this effect is also evidence in environment c and possibly d, albeit less prominent. Non-first order coupling occurs when two protons are chemically equivalent but magnetically inequivalent when coupled to the same coupling partner. This phenomenon only occurs when the molecule has certain symmetry operators, otherwise the two protons would have separate environments and a different chemical shift. A simulation of the expected ^{1}H NMR spectrum for NtrisBiB agreed with this observation (5.3.4).

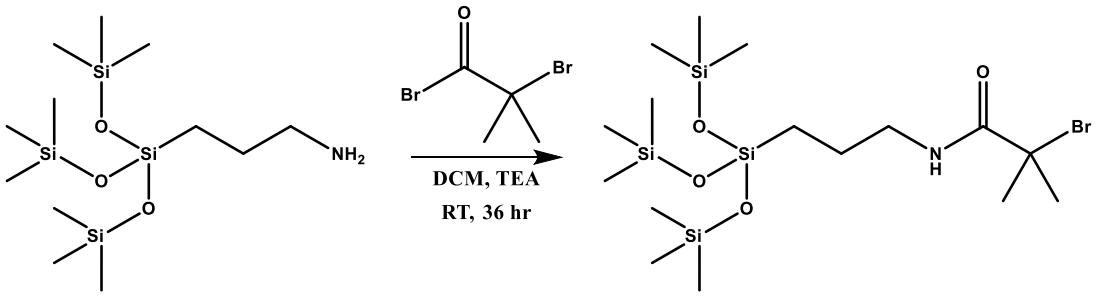

Figure 4-30. Synthesis of 3-[Tris(trimethylsiloxy)silyl]propyl 2-bromoisobutyramide (NtrisBiB).

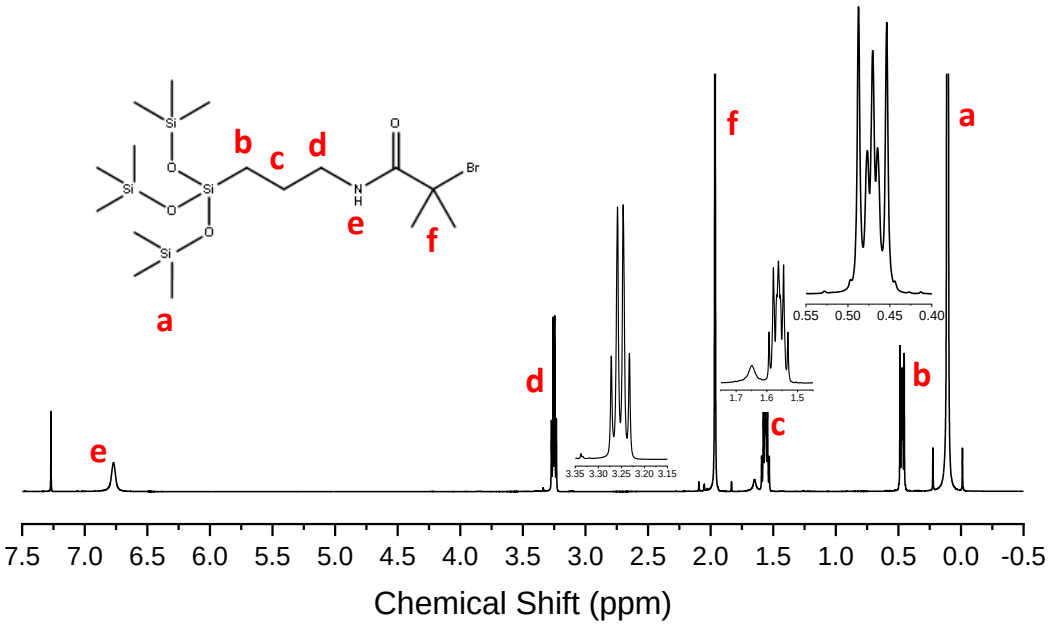

Figure 4-31. ^{1}H NMR spectrum (500 MHz, $CDCl_3$) of 3-[tris(trimethylsiloxy)silyl]propyl 2-bromoisobutyramide (NtrisBiB).

4.3.1.1 Polymer synthesis with NtrisBiB initiator

A series of polymerisations were performed to synthesise P*t*BA, Table 4-9. Firstly, PMA with a target DP50 was polymerised using a Cu(0)-wire polymerisation in DMSO, which worked well in terms of conversion and GPC performance. This was repeated using IPA, which gave lower conversion but still produced a low dispersity polymer. IPA was then used to polymerise *t*BA but produced no reaction when using Cu(0)-wire or Cu(II) UV polymerisations. In the cases that used IPA as solvent, the initiator precipitates and indicates poor solubility and skews the quantitative data from the NMR spectra. The solvent was changed to DMF and Cu(0)-wire for P*t*BA_{50}, which gave high conversion and better dispersity but still higher molecular weight than was targeted. As these conditions were the best available, they were used to target DP25 and DP10. DP25 gave a higher molecular weight than DP50 suggesting that either the concentration of initiator added was incorrect (human error) or there is an issue with the polymerisation. The latter is corroborated by the result from DP10, which shows a very broad GPC trace (Figure 4-32). As the siloxane group is large, it is possible that the initiator molecules struggle to approach the copper catalyst and proceed with the polymerisation, which may also be influenced by the high hydrophobicity. The result is a very large energy barrier to initiation, which is more significant when targeting low DP polymers. The insolubility of the initiator is only evident at the end of the reaction, therefore it's possible that when NtrisBiB interacts

with the copper it dimerises or promotes the loss of the R group from the amide and/or leads to crosslinking. The GPC traces for DP10 and DP25 show a peak at ~1200 Da, suggesting dimerised/aggregated initiator. This also explains the similar molecular weight obtained for DP50 and DP25, both of which were not close to the theoretical molecular weight. Irrespective of the initial concentration of initiator added to the reaction, the solubility per ml of DMF is the same and a similar concentration of initiator leads to polymerisation and would produce polymers of a similar M_n.

Table 4-9. Molecular characteristics of NtrisBiB-initiated polymers.

Entry	Target Polymer	Conditions[a]	Conversion	Target M_n (Da)	GPC_{DMF}	
					M_n (Da)	$Đ$
1	PMA_{50}	DMSO	99% – 21.5hr	4800	14100	1.22
2[b]	PMA_{50}	IPA	59% - 19.5hr	4800	9600	1.25
3[b]	P*t*BA_{20}	IPA	0% - 16.5hr	3100	-	-
4[b]	P*t*BA_{20}	IPA, UV[c]	0% - 16.5hr	3100	-	-
5	P*t*BA_{50}	DMF	98% - 16.5hr	6900	12100	1.27
6	P*t*BA_{25}	DMF	99% - 16hr	3700	13500	1.17
7	P*t*BA_{10}	DMF	~90% - 16hr*	1800	3000	1.56

a) All samples polymerised using Cu(0)-wire polymerisation with Me_6TREN and NtrisBiB initator, excluding entry 4. b) Initiator sedimented in IPA. c) General photo-mediated Cu(II) polymerisation. *issue with NMR measurement.

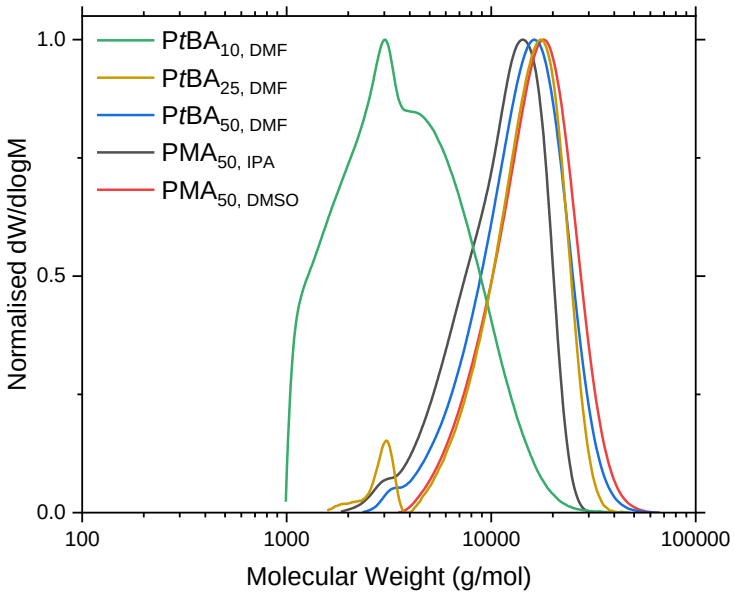

Figure 4-32. GPC traces in DMF eluent of NtrisBiB-initiated polymers (specified in legend).

4.3.2 3-[Tris(trimethylsiloxy)silyl]propyl methacrylate (TRIS)

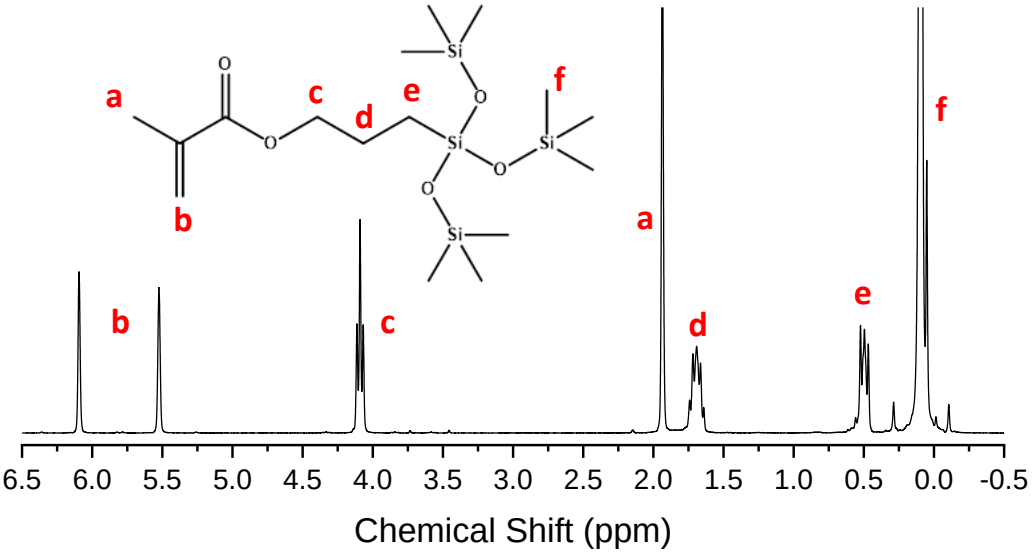

Figure 4-33. ^{1}H NMR spectrum (400 MHz, $CDCl_3$) of 3-[tris(trimethylsiloxy)silyl]propyl methacrylate (TRIS).

Following on from the attempt to use the siloxane moiety incorporated in an initiator, synthesis of a short block copolymer in which the hydrophobic block contained the siloxane moiety was attempted. In order to do this, the readily available 3-

[tris(trimethylsiloxy)silyl]propyl methacrylate (TRIS) monomer was used (Figure 4-33). The proposed route to an amphiphilic block copolymer was to synthesise a short chain PTRIS and chain extend this with *t*BA (Figure 4-34), which can be deprotected to give PTRIS-*b*-PAA. As the hydrophobic siloxane group is one of the blocks, less consideration is given to the choice of initiator. Overall, a hydrophilic initiator should be avoided when the hydrophobic block is polymerised first.

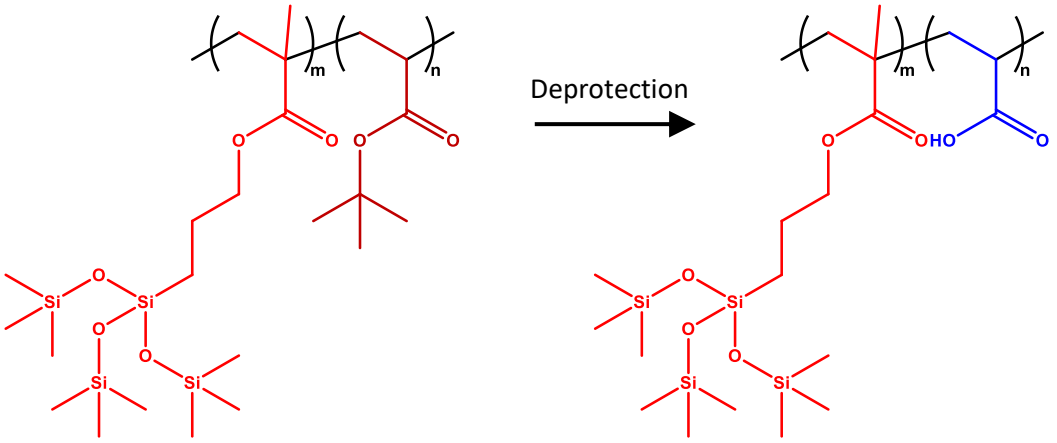

Figure 4-34. Proposed synthesis of an amphiphilic block copolymer using TRIS monomer (PTRIS-*b*-PAA).

Firstly, optimisation of the first block was necessary, as chain extension requires the first block to have very high conversion (>95%) and a low dispersity so that all polymers are comparable in composition. DP10 was targeted using TFE and IPA as solvents and testing both the Cu(0)-wire and Cu(II) UV polymerisations (Table 4-10, Figure 4-35). Samples were taken after 3 hours and 22 hours, showing high conversion after 22 hours except for TFE/Cu(0). Despite the lower conversion after 3 hours, the dispersity was good for all conditions after 3 hours and higher after 22 hours, implying that a more suitable reaction time was approximates 9-12 hours. The UV polymerisation showed higher conversion than the Cu(0) reaction in the same solvent, and IPA gave a lower dispersity than TFE for the UV polymerisations. The IPA/UV polymerisation was chosen for further optimisation.

Table 4-10. Polymerisation conditions and molecular weight details for $PTRIS_{10}$.

Entry	Target Polymer	Conditions	Conversion	Target M_n (Da)	GPC_{CHCl_3}	
					M_n (Da)	$Đ$
1	$PTRIS_{10}$	TFE, Cu(II) UV	96% – 22hr	4400	11100	1.53
2	$PTRIS_{10}$	TFE, Cu(0)	20% - 3hr 25% - 24hr	4400	3900 4000	1.12 1.17
3	$PTRIS_{10}$	IPA, Cu(II) UV	50% - 3hr 99% - 22hr	4400	5400 7800	1.20 1.37
4	$PTRIS_{10}$	IPA, Cu(0)	43% - 3hr 81% - 23hr	4400	5600 7700	1.19 1.41

a) all polymers synthesised using EBiB/Me_6TREN.

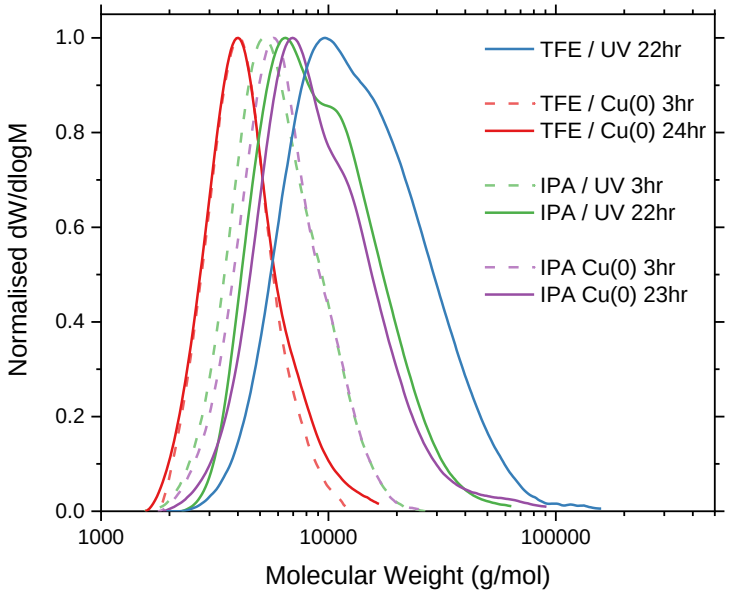

Figure 4-35. GPC traces at 3 hrs and ~22hrs of $PTRIS_{10}$ synthesised using different polymerisation conditions from Table 4-10.

$PTRIS_{10}$ was synthesised with varying concentrations of $Cu(II)Br_2$ and Me_6TREN with the suggestion of altering the optimum reaction time. Polymerisations with [Cu(II)] : [Me_6TREN] molar ratios = [0.02]:[0.12], [0.04]:[0.12] and [0.04]:[0.24] were tested and showed minimal differences. In all cases, conversions and molecular weight data were similar and changing these quantities was, therefore, not worthwhile (Table 4-11. Polymerisation conditions and molecular weight details for $PTRIS_{10}$ cont.Table 4-11). The GPC traces showed a high molecular weight shoulder, which was consistent in all IPA/UV polymerisations and did not change intensity with Cu(II)/Me_6TREN

concentration, Figure 4-36. This implies an issue with the monomer/initiator or polymer-polymer termination occurs due to long reaction times.

Table 4-11. Polymerisation conditions and molecular weight details for $PTRIS_{10}$ cont.

Entry	Target Polymer	Conditions[a]	Conversion	Target M_n (Da)	GPC_{CHCl_3}	
					M_n (Da)	$Đ$
1	$PTRIS_{10}$	0.02 *eq*.Cu(II) 0.12 *eq*. Me_6TREN	50% - 3hr 99% - 22hr	4400	5400 7800	1.20 1.37
2	$PTRIS_{10}$	0.04 *eq*.Cu(II) 0.12 *eq*. Me_6TREN	44% - 3hr 99% - 22hr	4400	4900 8100	1.17 1.49
3	$PTRIS_{10}$	0.04 *eq*.Cu(II) 0.24 *eq*. Me_6TREN	45% - 3hr 99% - 22hr	4400	4900 7900	1.18 1.34

a) all polymers synthesised using EBiB/IPA and photo-induced polymerisation but with different equivalents of Cu(II) and Me_6TREN ligand with respect to initiator.

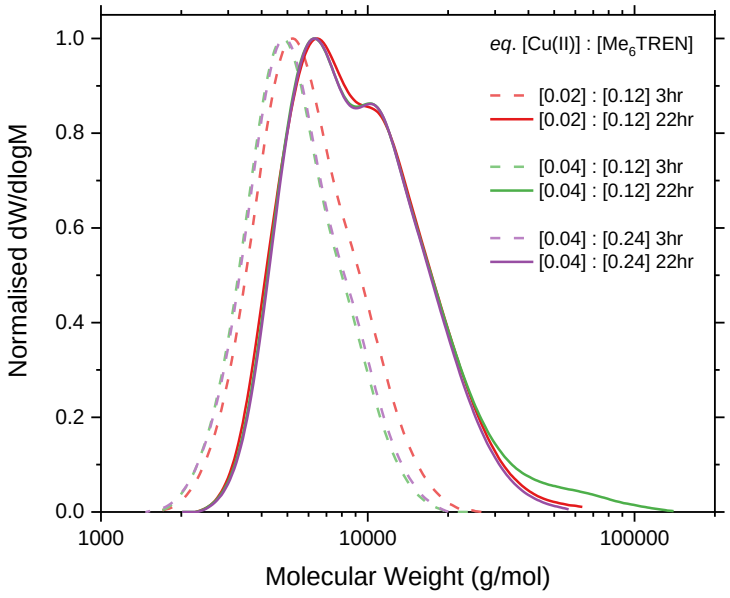

Figure 4-36. GPC traces at 3 hrs and 22hrs of $PTRIS_{10}$ synthesised using different molar ratios of $Cu(II)Br_2$: Me_6TREN in a photo-induced IPA/EBiB system - Table 4-11.

The "*universal conditions*" for controlled Cu(0)-RDRP polymerisations were then referred to.[43] Here, MBPA was used as an initiator for the polymerisation of methacrylates, with PMDETA as the ligand. These conditions were used to polymerise $PTRIS_{10}$ (Table 4-12), where the molar ratio of ligand was changed in the UV polymerisation, and temperature was increased in the Cu(0)-wire system. The

difference in reaction time was only noticeable from the 3hr sample, of which the PMDETA reactions were slower as they only reach ~10% conversion after 3hrs, but all were >98% after 22hrs. When MBPA and PMDETA were used instead of EBiB and Me_6TREN, the Cu(0)-wire polymerisation was successful, although increasing the reaction temperature to 40 °C did not improve the reaction. The final molecular weight of these samples agreed with the theoretical mass. Dispersity was too high for use in microphase separation due to the persistent high molecular weight shoulder in the GPC traces (Figure 4-37).

Table 4-12. Polymerisation conditions and molecular weight details for $PTRIS_{10}$ cont.

Entry	Target Polymer	Conditions[a]	Conversion	Target M_n (Da)	GPC_{CHCl_3}	
					M_n (Da)	$Đ$
1	$PTRIS_{10}$	UV, Cu(II) (0.02 *eq.*), L (0.12 *eq.*)	11% - 3hr 98% - 22hr	4400	4400	1.45
2	$PTRIS_{10}$	UV, Cu(II) (0.02 *eq.*), L (0.24 *eq.*)	9% - 3hr 99% - 22hr	4400	4700	1.39
3	$PTRIS_{10}$	Cu(0), Cu(II) (0.05 *eq.*), L (0.36 *eq.*)	10% - 3hr 99% - 22hr	4400	5300	1.43
4	$PTRIS_{10}$	Cu(0), Cu(II) (0.05 *eq.*), L (0.36 *eq.*), 40°C	2% - 3hr 98% - 22hr	4400	4800	1.44

a) all polymers synthesised in IPA using PMDETA as the ligand. Reacted at room temperature unless stated otherwise and GPC data used from 22 hr sample.

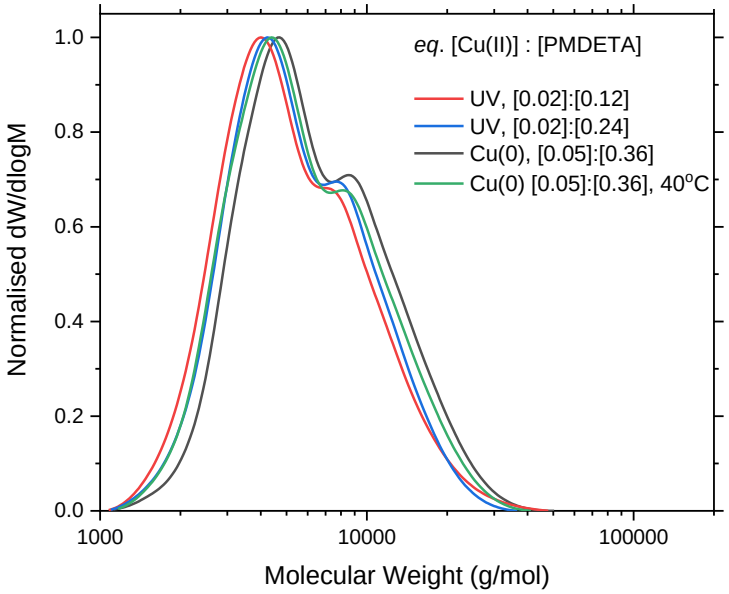

Figure 4-37. GPC traces at 22hrs of $PTRIS_{10}$ synthesised using different molar ratios of $Cu(II)Br_2$: PMDETA with universal conditions - Table 4-12.

Figure 4-35 and Figure 4-36 show that the high molecular weight shoulder becomes apparent after 3hrs of reaction time. Therefore, the decision was made to synthesise the P*t*BA block (which later becomes the hydrophilic block) first, then chain extend this with a block of PTRIS and purposefully end the reaction after 3hrs, before the shoulder forms, Figure 4-38.

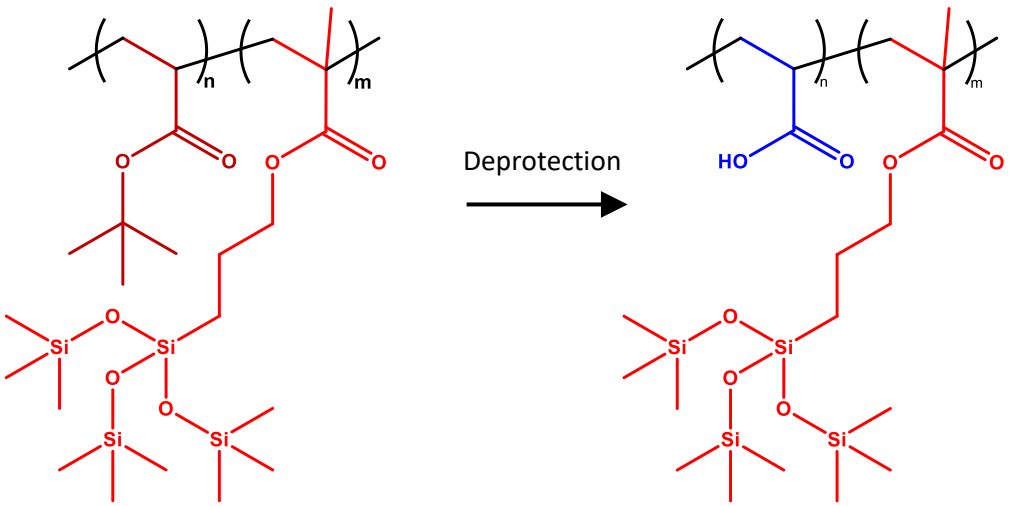

Figure 4-38. Proposed synthesis of an amphiphilic block copolymer using TRIS monomer (PAA-*b*-PTRIS).

The polymerisation of *t*BA with EBiB is straightforward and has previously been demonstrated in Chapter 1. As such the polymerisation of the first P*t*BA block was simple and successful, it was polymerised using the general photoinduced Cu(II)-RDRP system in IPA, Table 4-13. This was then chain extended with a DP 10 block of PTRIS and samples were taken at 3, 5 and 24 hours to monitor the reaction. GPC traces in $CHCl_3$ showed that the polymer does chain extend (Figure 4-39a) and ^1H NMR showed 98% conversion after 24hrs. The full GPC trace also shows that a large proportion of the P*t*BA_{10} does not chain extend (Figure 4-39b). This explains the high M_n, as the concentration of initiating species is effectively lower.

Table 4-13. Polymerisation conditions and molecular weight details for P*t*BA-*b*-TRIS.

Entry	Target Polymer[a]	Data concerns	Conversion	Target M_n (Da)	GPC_{CHCl_3}[a]	
					M_n (Da)	$Đ$
1	P*t*BA$_{10}$	Block 1	>99% - 19hr	1500	1200	1.16
2	P*t*BA$_{10}$-*b*-PTRIS$_{10}$	Block 2	41% - 3hr	5700	12200	1.18
3	P*t*BA$_{10}$-*b*-PTRIS$_{10}$	Block 2	77% - 5hr	5700	15300	1.37
4	P*t*BA$_{10}$-*b*-PTRIS$_{10}$	Block 2	98% - 24hr	5700	17300	1.60

a) all polymers synthesised by photo-induced Cu(II)-RDRP in IPA/Me_6TREN with EBiB initiator at RT. b) Data shown for the chain extended peak and disregards the non-extended polymer peak.

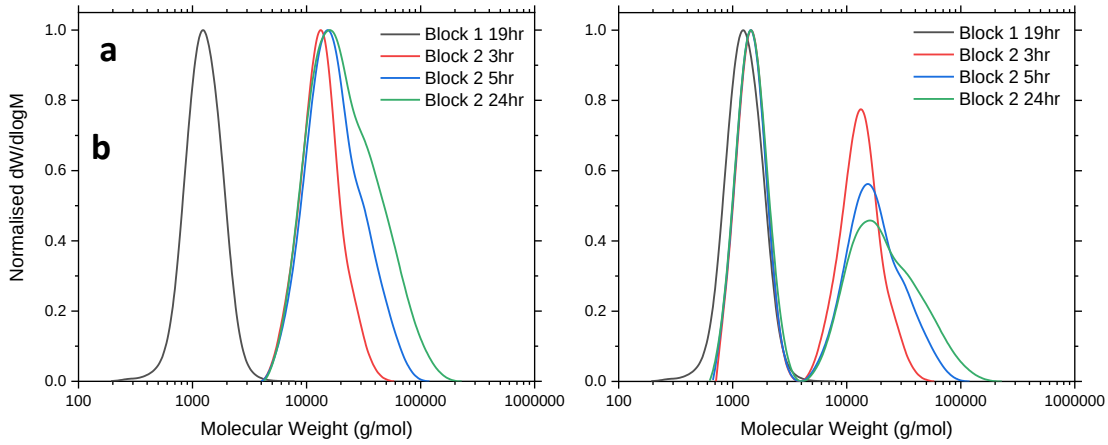

Figure 4-39. GPC traces in $CHCl_3$ eluent of P*t*BA$_{10}$-*b*-PTRIS$_{10}$. a) Traces show chain extended polymer only. b) Traces include non-extended P*t*BA$_{10}$.

GPC measurements of the 24hr sample were taken in THF and $CHCl_3$ eluents, and the ratio of peak heights changes dramatically. This suggests that the two peaks correspond to different chemical species and purification by dialysis was used to remove the non-extended P*t*BA$_{10}$ block. Dialysis was performed in MeOH using a 3000 Da MWCO membrane, Figure 4-40. This had almost no effect on the GPC traces and therefore did not contribute to the purification. As dialysis tubing is designed to work most effectively in water, it was expected that extra dialysis steps would be needed but would show some decrease in the relative concentration of the P*t*BA block. The purpose of this step was to show that there was potential to separate the two species (rather than fully purify the product), however, this result cast doubt upon that.

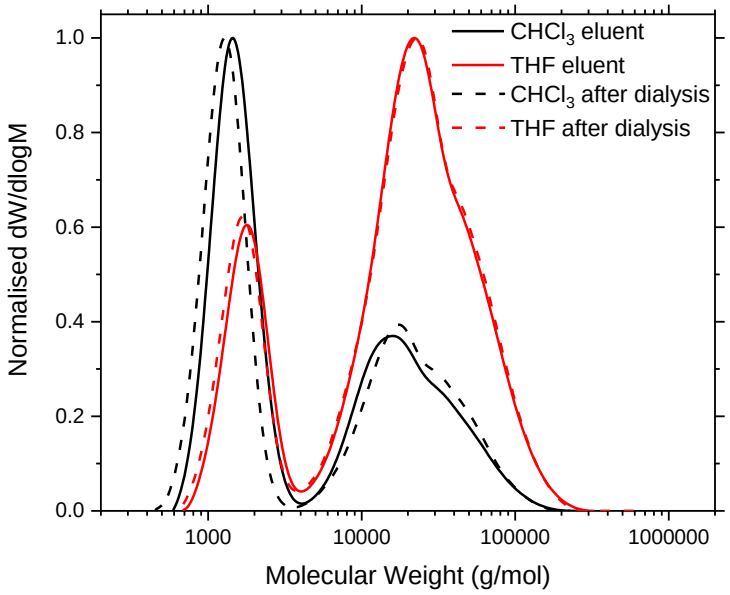

Figure 4-40. GPC traces in THF and $CHCl_3$ eluent of P*t*BA$_{10}$-*b*-pTRIS$_{10}$ after 24 hours reaction time.

4.3.2.1 Deprotection of P*t*BA$_{10}$-*b*-PTRIS$_{10}$

The polymer was deprotected to investigate whether the higher molecular weight peak (Figure 4-40) is a homopolymer of PTRIS or the desired block copolymer. If it is a homopolymer, it should not change molecular weight after exposure to deprotection conditions. If, however, it is a result of chain extension it will decrease in molecular weight with the loss of the *tert*-butyl groups.

TRIS monomer was first exposed to the deprotection conditions for *tert*-butyl groups. TRIS was dissolved in DCM/TFA and left for a total of 71 hrs and samples were taken periodically for ^{1}H NMR, Figure 4-41. The CH_2 groups next to the Si and O are of interest as these are groups that are vulnerable to possible attack of TFA, therefore expansions of these peaks are given in Figure 4-41. Up to 3 hours reaction time there is minimal change in the spectra, however after 5 hours there was more noticeable broadening of peaks and by 71 hrs, these were very broad and possibly polymeric. These observations suggest that a reaction does occur with TFA, and it has been reported in the literature that attack at the ester is possible with trimethylsilyl ethyl groups and results in the formation of a carboxylic acid.[254] TFA has also been shown to react with silane groups,[255] either of these pathways would allow crosslinking routes and explain the formation of polymeric species.

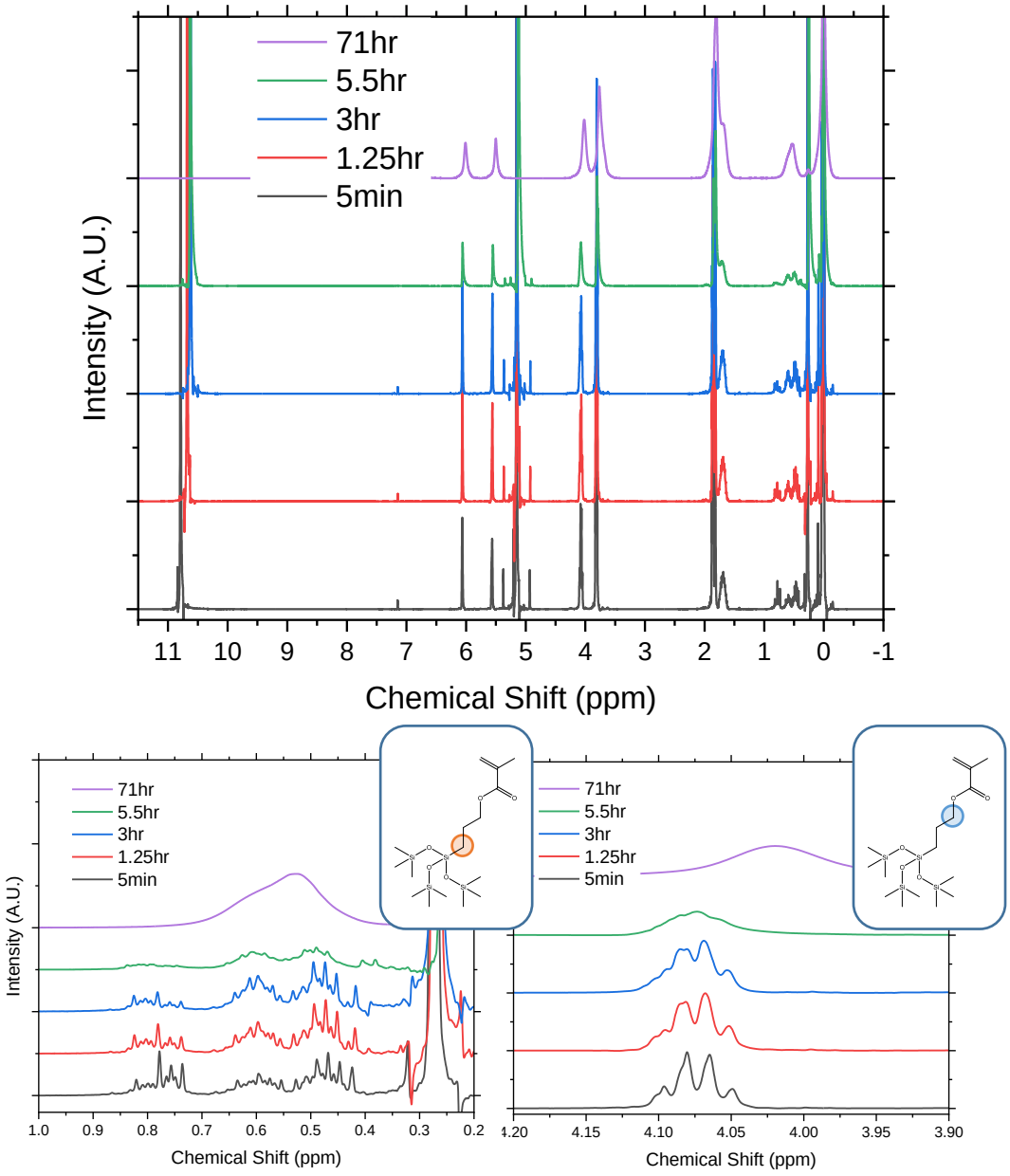

Figure 4-41. ^{1}H NMR (400 MHz, $CDCl_3$) spectra of TRIS monomer over time when exposed to TFA/DCM (deprotection conditions for *t*BA). Top image shows full spectrum. Bottom images show expansions of the peaks caused by the labelled proton environments.

What was of more concern is that when comparing the spectra of unreacted TRIS to the 5-minute exposure spectrum, most of the changes occur within the first 5 minutes of the reaction (Figure 4-42). The relative integrals of the peaks completely change and new peaks form in the 0.9-0.2 ppm region. It is unclear which side products are being formed but any reaction here is unwanted. Ultimately, these findings reveal that TRIS cannot used as a hydrophobic moiety in an amphiphilic block copolymer, or that it cannot be used with *t*BA as the second block, because any deprotection conditions used to deprotect *t*BA will also influence TRIS.

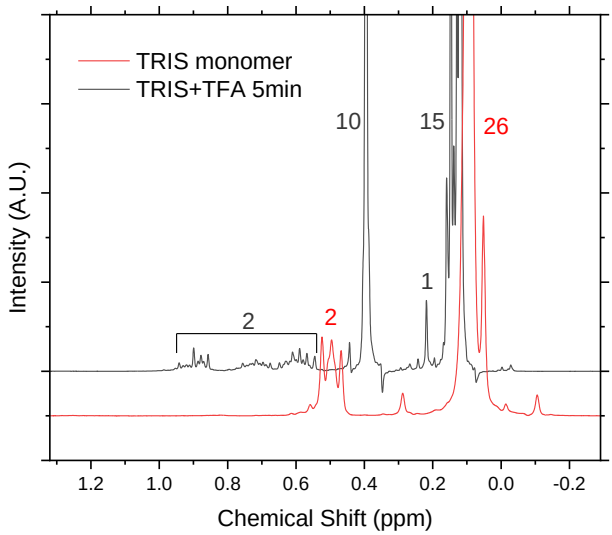

Figure 4-42. ^{1}H NMR spectra in $CDCl_3$ of TRIS monomer before exposure and after exposure to TFA/DCM for 5 mins. Numbers indicate the relative integral values when referenced to one of the vinyl peaks.

Finally this side reaction was also confirmed using GPC, in which TRIS at time=o and TRIS a time = 5 minutes of reaction time with TFA, Figure 4-43, were compared. There was a clear increase in molecular weight after the reaction with TFA, suggesting some degree of crosslinking or dimerisation. There was also a small high molecular weight shoulder in the TRIS monomer trace, which may be dimer or an impurity from the chemical synthesis. If this impurity includes a hydroxysilyl group (which is likely due to common reaction syntheses), it would be a source of many unwanted reactions.

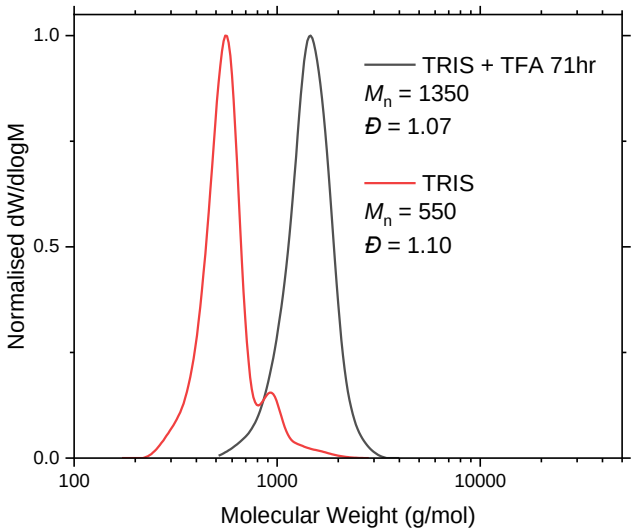

Figure 4-43. GPC traces in THF eluent of TRIS monomer and TRIS after 5 min reaction with TFA.

4.4 Conclusions

Different hydrophobic initiators and hydrophilic monomers were investigated for the purpose of microphase separation, following the notion of using discrete hydrophobic "pseudo" block in the synthesis of low molecular weight polymers with a high χ parameter.

Anthracene was chosen as a suitable hydrophobic group which also exhibits photo-reversible dimerisation, allowing the possibility of photo-induced microphase separation or morphology modification. This was monitored by UV-Vis spectroscopy and was found to dimerise and revert to monomer successfully and repeatably. A hydrocarbon initiator (18 carbons) was synthesised, used to polymerise poly(acrylic acid) and directly compared to poly(acrylic acid) synthesised with a fluorocarbon initiator. SAXS results showed that the HEX phase was more crystalline than with the fluoro-initiators, but domain sizes were similar, and both showed a trend from LAM to HEX morphology with increasing chain length.

Hydrophilic monomers EEMA and SkMA were synthesised for the polymerisation with AMBiB, which requires a methacrylate with low steric hinderance. Both polymerised well and deprotections were straightforward. Higher dispersities were obtained for low DP polymers however, this was attributed to non-purified samples that contain either unreacted monomer or initiator.

Siloxane was also investigated as a hydrophobic group in an initiator (NtrisBiB) and monomer (TRIS). Overall, the high hydrophobicity led to poor solvability in most solvents, for both the initiator and the monomer. NtrisBiB was unable to target low molecular weight polymers and the polymerisation of TRIS showed a high molecular weight shoulder after 3 hours. This was overcome by polymerising the hydrophilic block first and end the reaction of the second block (PTRIS) at 3 hours, however, the efficacy of chain extension was poor and purification of the homopolymer from block copolymer was unsuccessful.

4.5 Appendix

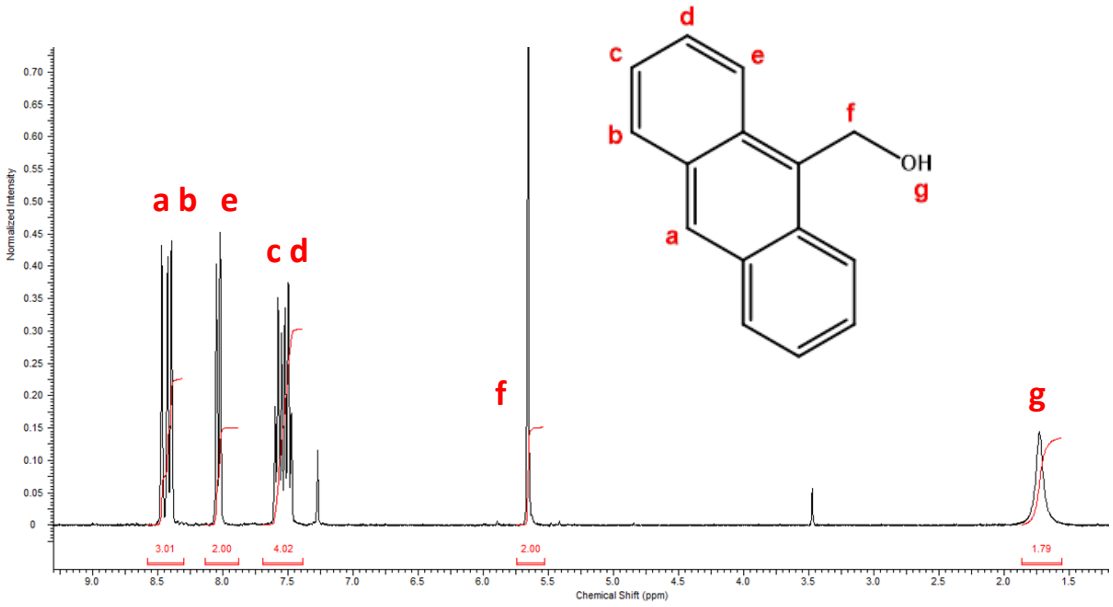

Figure A4-1. ^{1}H NMR (500 MHz, $CDCl_3$) spectrum of 9-Anthracene methanol.

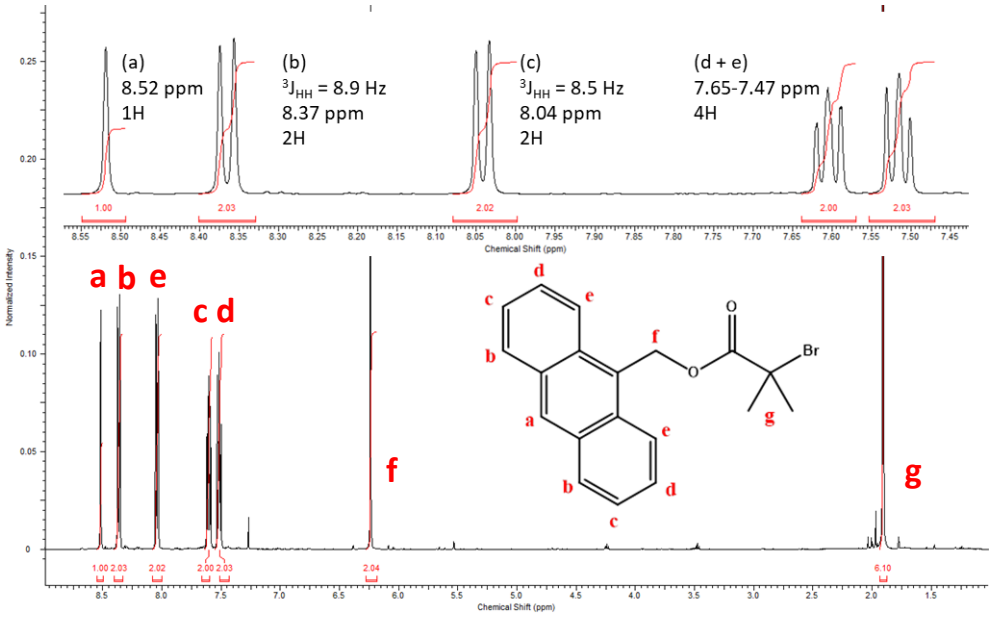

Figure A4-2. ^{1}H NMR (500 MHz, $CDCl_3$) spectrum of 9-Anthracene methanol bromoisobutyrate (AMBiB).

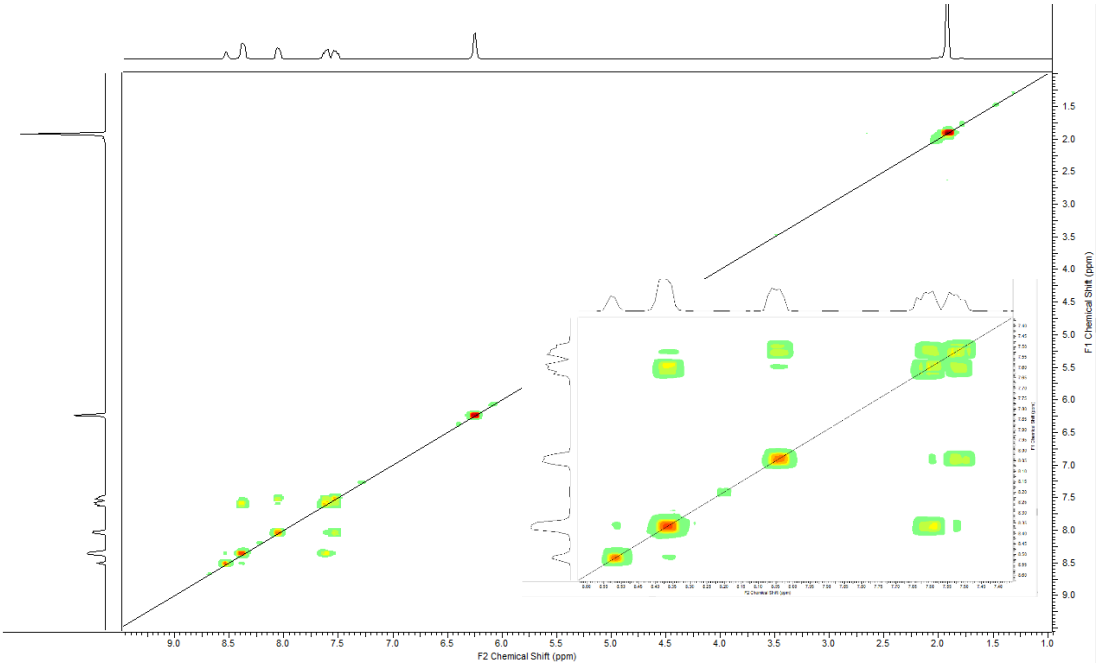

Figure A4-3. COSY NMR (500 MHz, $CDCl_3$) spectrum of 9-Anthracene methanol bromoisobutyrate (AMBiB). Inset shows expansion of chemical shift values 8.6 to 7.4 ppm.

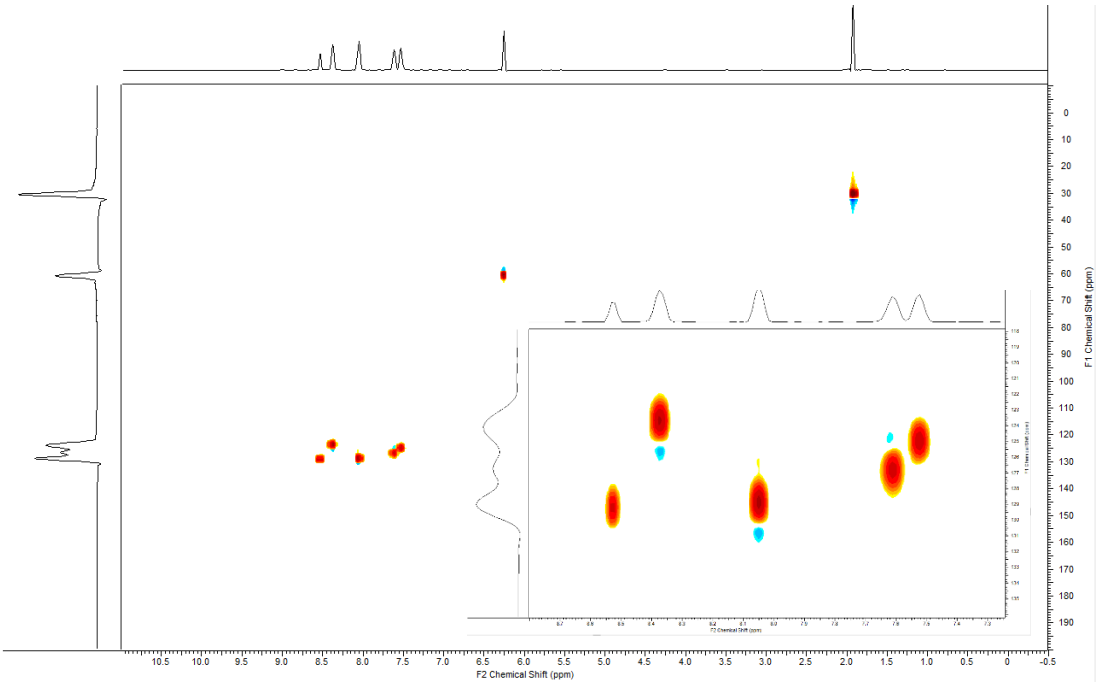

Figure A4-4. HSQC NMR (500 MHz, $CDCl_3$) spectrum of 9-Anthracene methanol bromoisobutyrate (AMBiB). Inset shows expansion of chemical shift values 8.7 to 7.3 ppm (^1H) x 136 to 118 ppm (^{13}C).

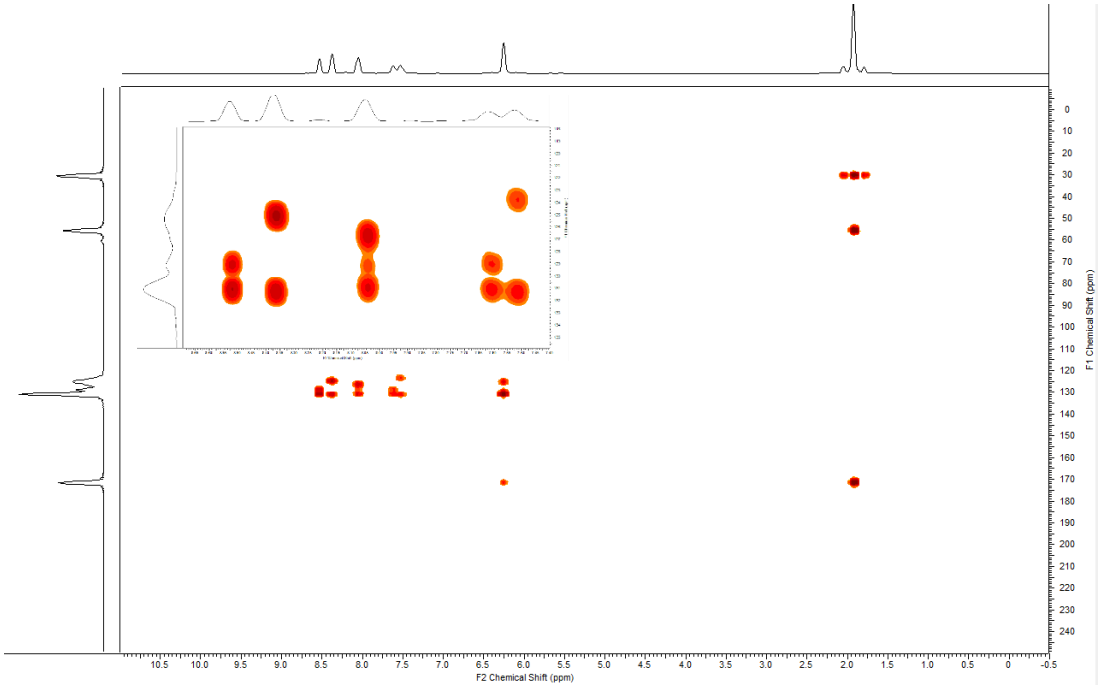

Figure A4-5. HMBC NMR (500 MHz, $CDCl_3$) spectrum of 9-Anthracene methanol bromoisobutyrate (AMBiB). Inset shows expansion of chemical shift values 8.7 to 7.4 ppm (^1H) x 136 to 118 ppm (^{13}C).

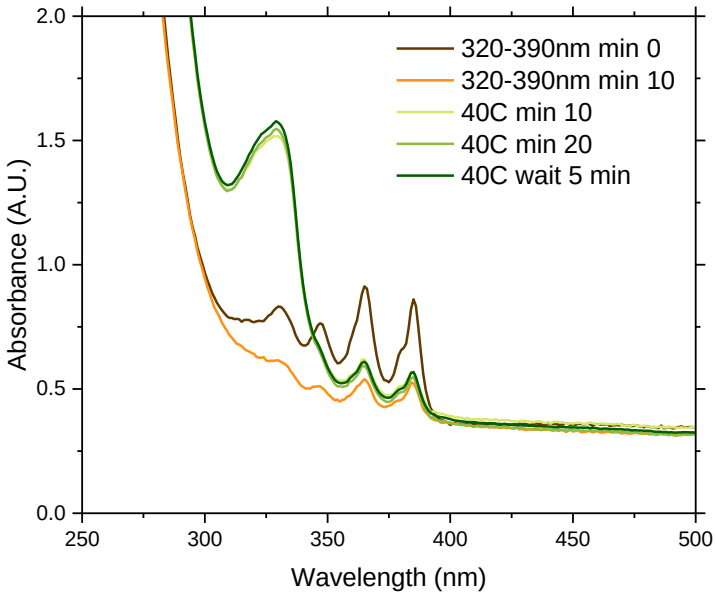

Figure A4-6. UV-Vis absorbance spectrum of AMBiB in hexane (1.25 x10^{-2} mg ml^{-1}) after exposure to 320-390 nm light followed by submersion in a 40 °C water bath. Legend indicates total amount of exposure for each condition.

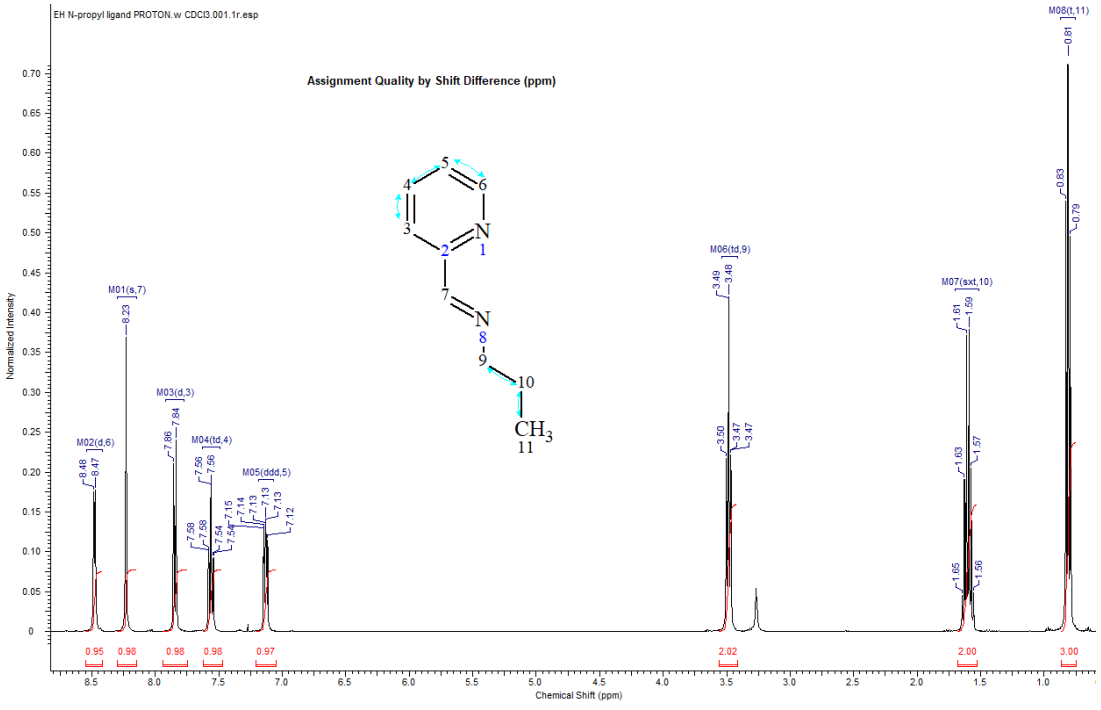

Figure A4-7. ^{1}H NMR spectrum (400 MHz, $CDCl_3$) of *N*-propyl-1-pyridin-2-ylmethanimine .

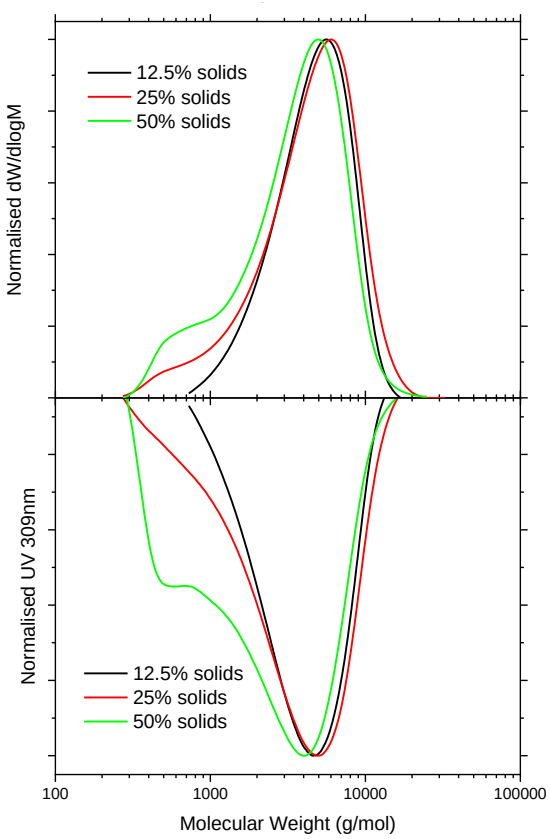

Figure A4-8. GPC traces in THF eluent of AMBiB-PMMA$_{25}$ polymerised at 50%, 25% and 12.5% solid weight content. Top shows RI, bottom shows UV (308 nm).

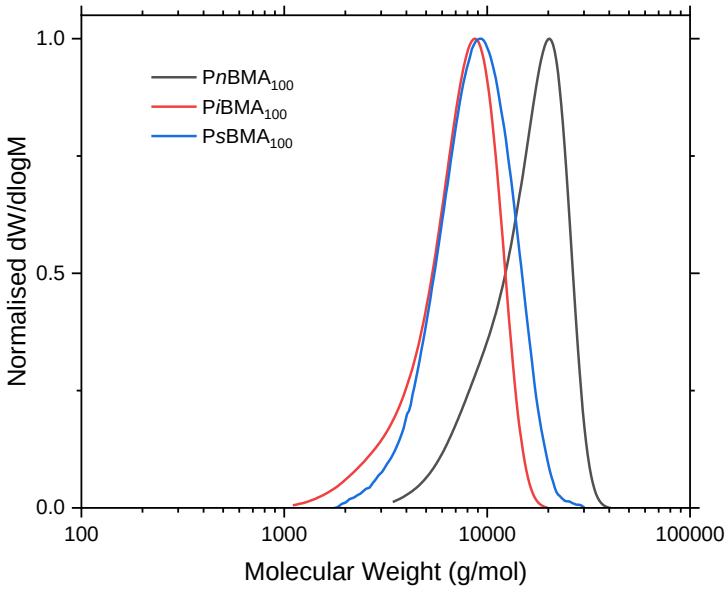

Figure A4-9. GPC traces in $CHCl_3$ eluent of AMBIB-initiated polymer of butyl methacrylate isomers.

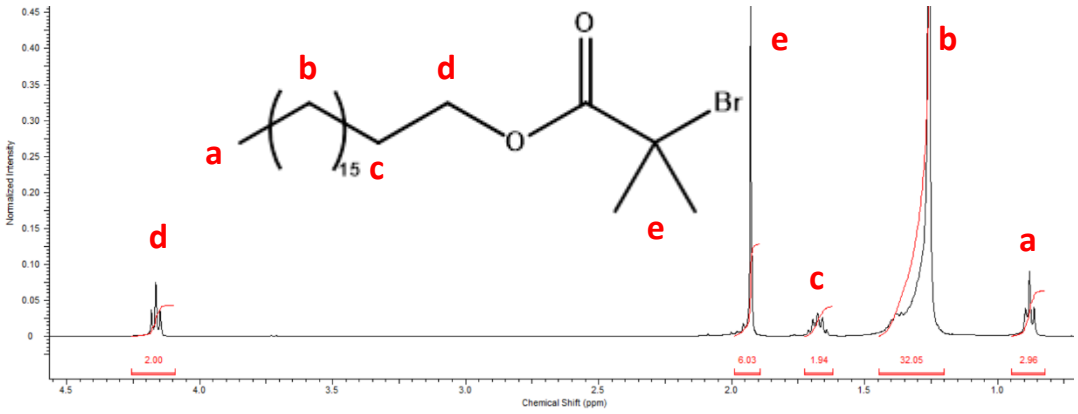

Figure A4-10. ^{1}H NMR (400 MHz, $CDCl_3$) spectrum of octadecyl bromoisobutyrate (ODBiB).

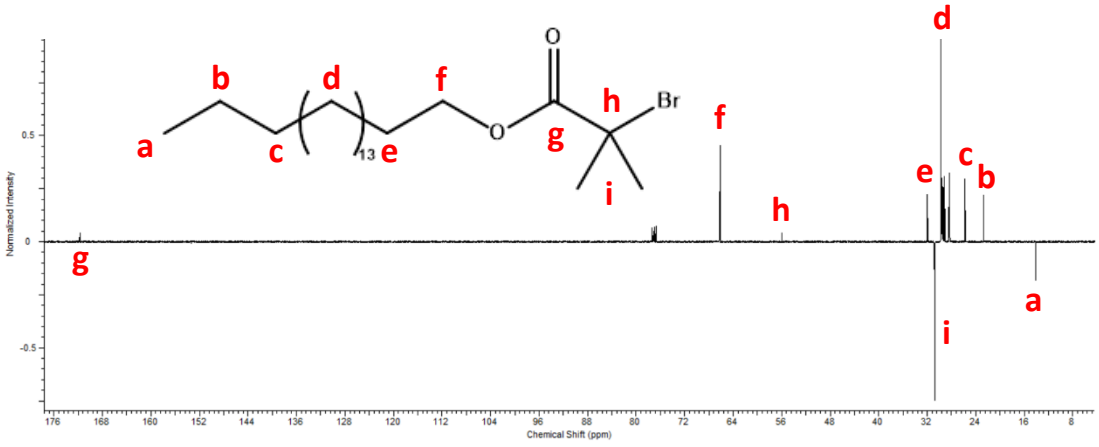

Figure A4-11. ^{13}C NMR (APT) (100 MHz, $CDCl_3$) spectrum of octadecyl bromoisobutyrate (ODBiB).

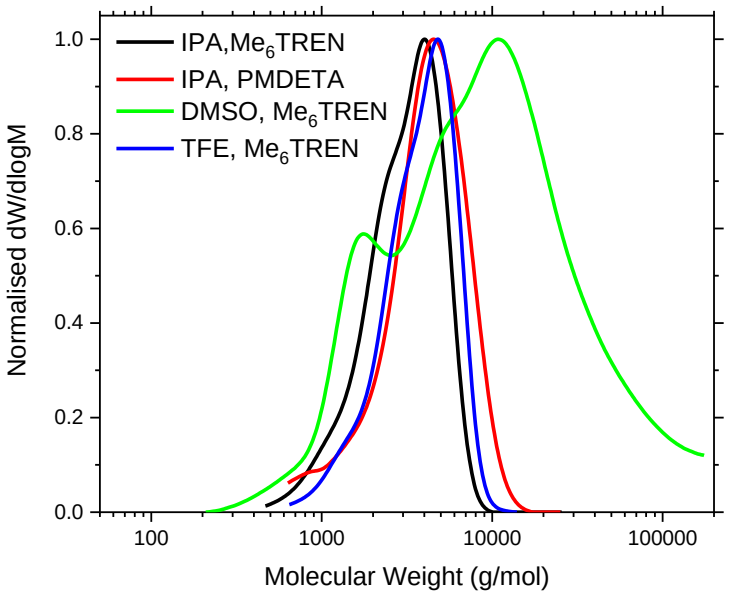

Figure A4-12. GPC traces of ODBiB-P*t*BA$_{25}$ synthesised by Cu(0)-RDRP with different solvent and ligands, in THF eluent.

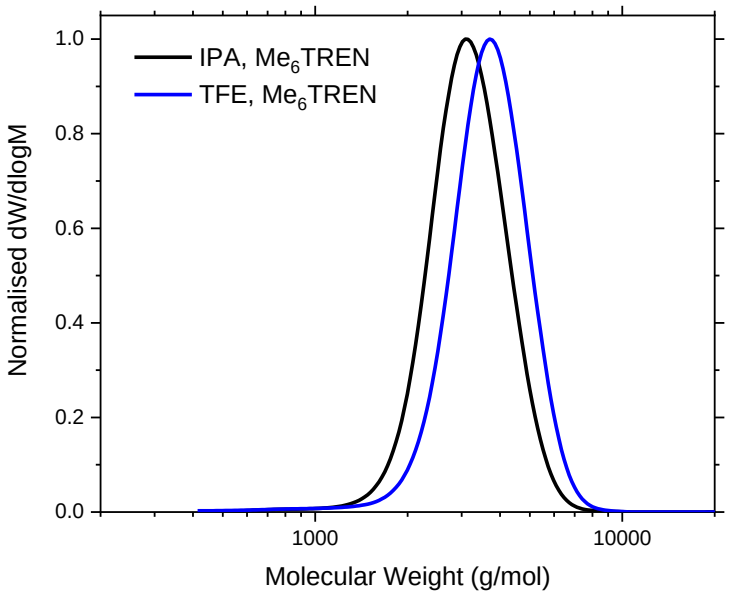

Figure A4-13. GPC traces of ODBiB-P*t*BA$_{25}$ synthesised by Cu(0)-RDRP with different solvent and ligands, in $CHCl_3$ eluent.

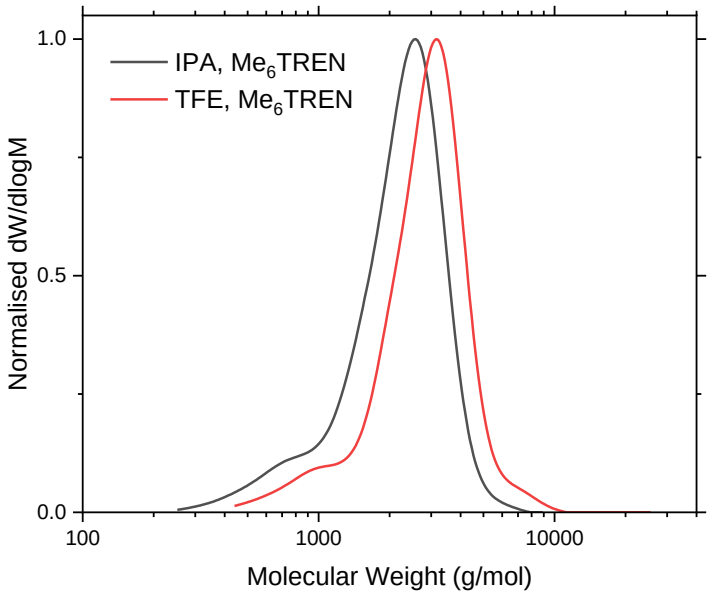

Figure A4-14. GPC traces of ODBiB-PMA$_{25}$ synthesised by Cu(0)-RDRP with different solvent and ligands, in $CHCl_3$ eluent.

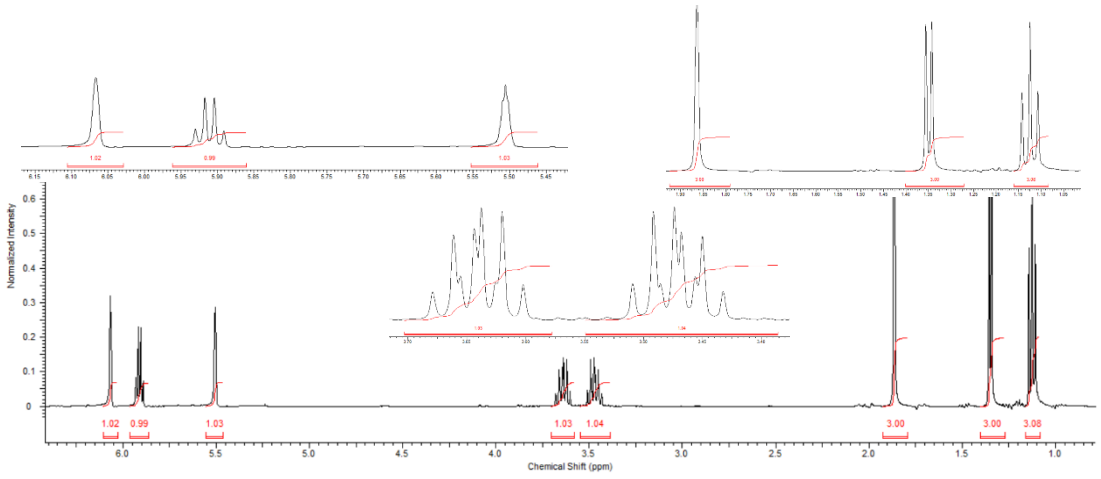

Figure A4-15. ^{1}H NMR (400 MHz, $CDCl_3$) spectrum of 1-Ethoxyethyl methacrylate (EEMA).

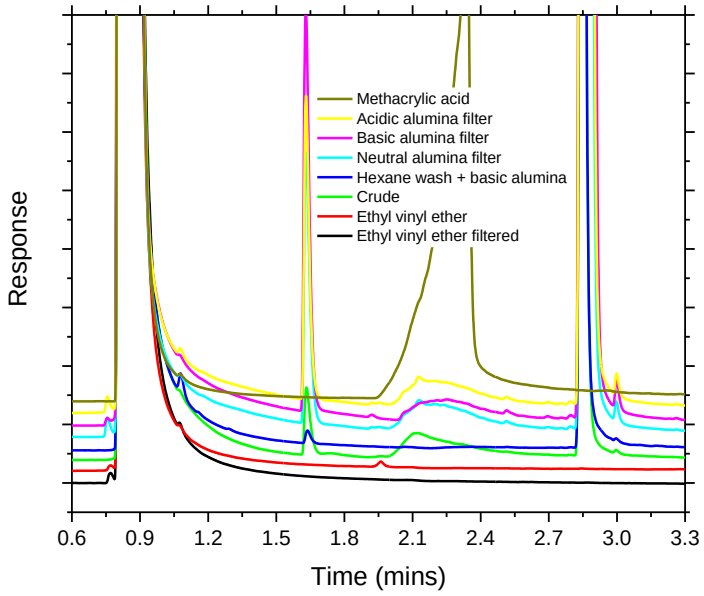

Figure A4-16. Gas chromatograms (GC) of various steps taken to improve purity during the synthesis of EEMA monomer.

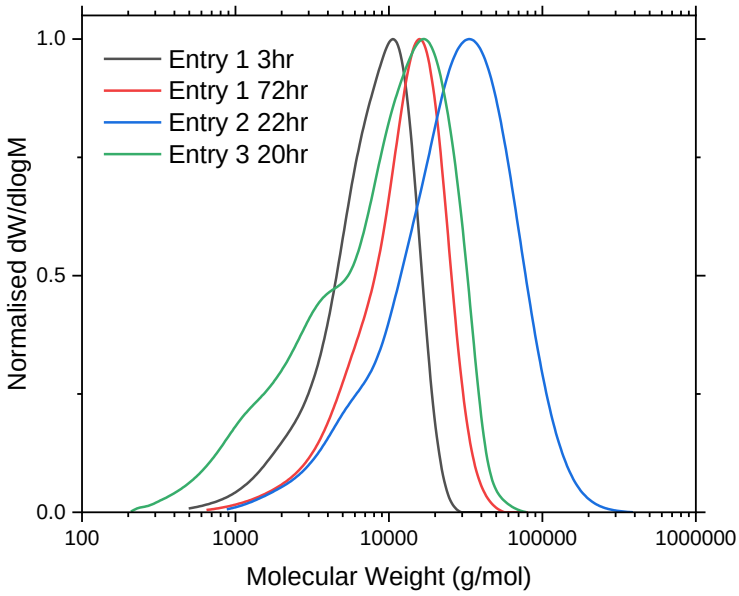

Figure A4-17. GPC traces in $CHCl_3$ eluent of poly(1-Ethoxyethyl methacrylate) (PEEMA) polymers listed in Table 4-7.

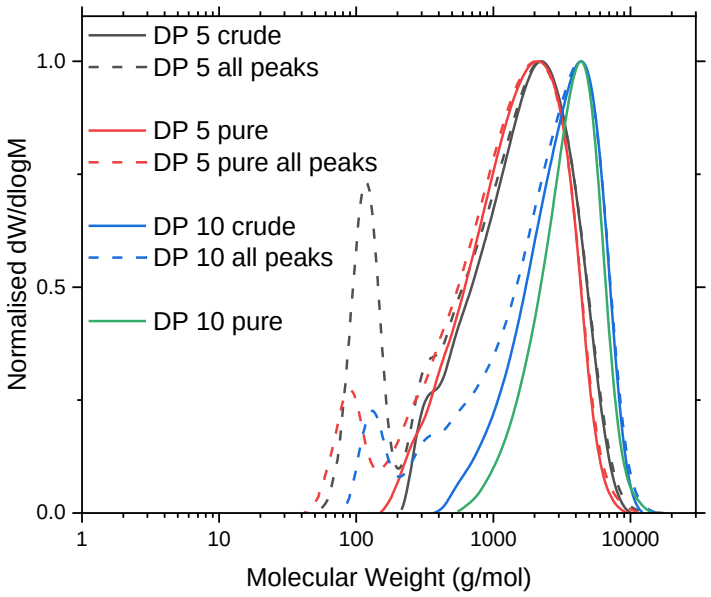

Figure A4-18. GPC traces in $CHCl_3$ eluent of EBiB-initiated poly(1-Ethoxyethyl methacrylate) (PEEMA) DP 5 and DP 10. "all peaks" shows the full trace including unreacted monomer/initiator peak.

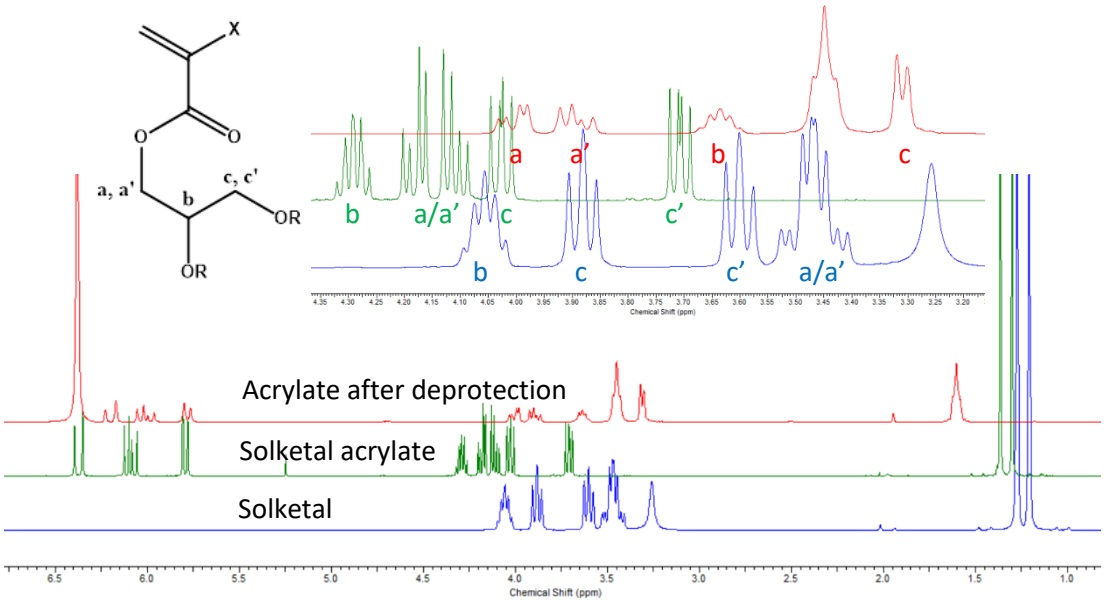

Figure A4-19. ^1H NMR (400 MHz, $CDCl_3$) spectrum of solketal (bottom, blue), solketal acrylate (middle, green) and solketal acrylate after acid hydrolysis (top, red).

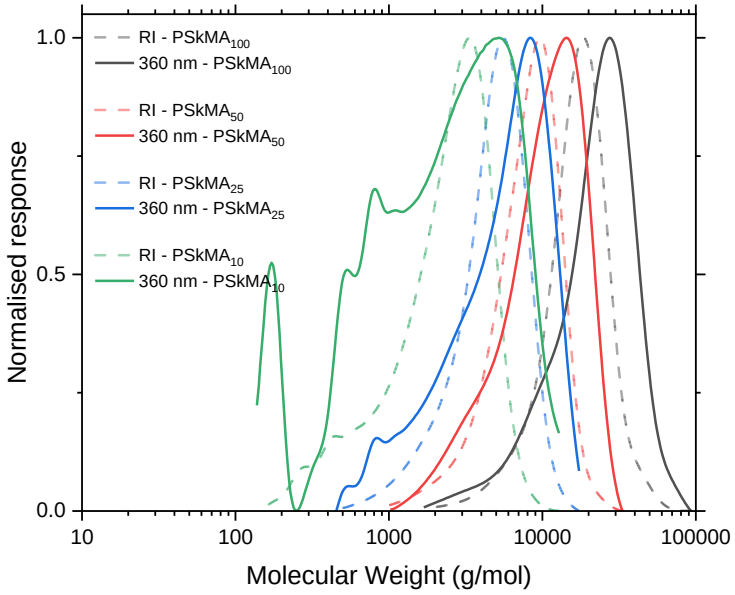

Figure A4-20. GPC traces in $CHCl_3$ eluent (RI and 360 nm detection) of AMBiB-PSkMA polymers.

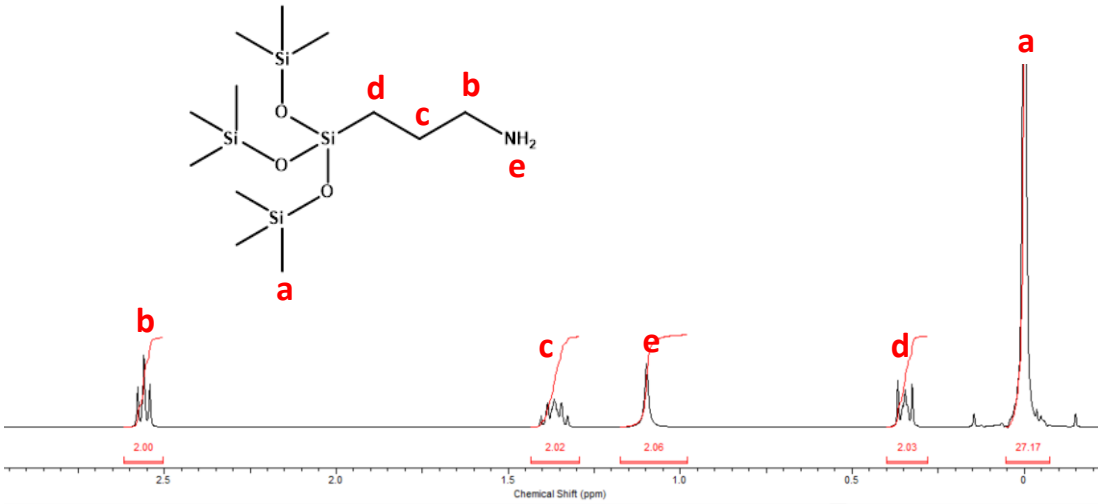

Figure A4-21. ^1H NMR spectrum (400 MHz, $CDCl_3$) of 3-[Tris(trimethylsiloxy)silyl]propyl amine.

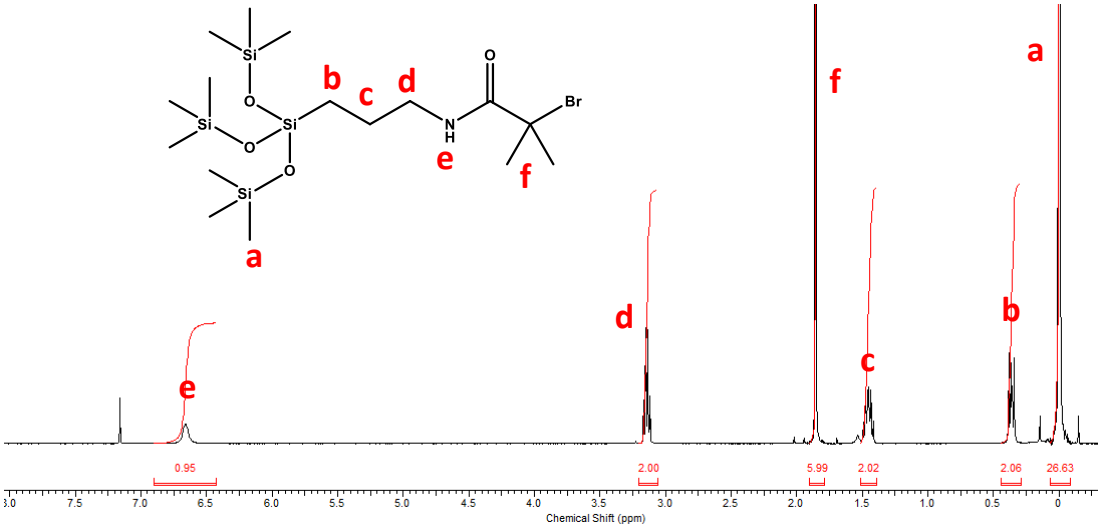

Figure A4-22. ^{1}H NMR spectrum (400 MHz, $CDCl_3$) of 3-[Tris(trimethylsiloxy)silyl]propyl 2-bromoisobutyramide (NtrisBiB).

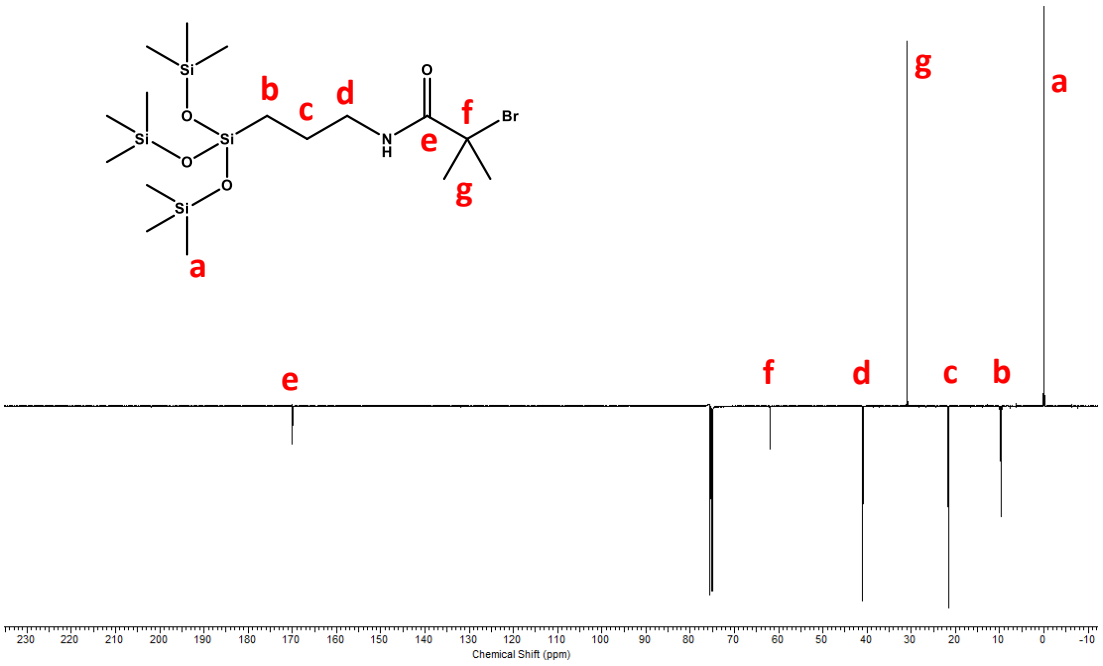

Figure A4-23. ^{13}C NMR spectrum (126 MHz, $CDCl_3$) of 3-[tris(trimethylsiloxy)silyl]propyl 2-bromoisobutyramide (NtrisBiB).

Chapter 5: Experimental, Methods & Calculations

Contents

5.1 Experimental

5.1.1 Synthesis of fluorinated initiators

Perfluorooctyl bromoisobutyrate, F_{13}. Synthesis was adapted from literature.[181] DCM (60 ml), triethylamine (6.46 x 10^{-2} mol, 6.54 g) and 1H,1H,2H,2H-perfluorooctanol (5.36 x 10^{-2} mol, 19.52 g) were added to a 250 ml 3-necked round bottom flask (RBF) equipped with a constant pressure drop funnel. The RBF was purged with nitrogen and cooled in an ice-water bath containing NaCl and acetone. DCM (10 ml) containing α-bromoisobutyryl bromide (8.06 x 10^{-2} mol, 18.53 g) was placed in the constant pressure drop funnel and added dropwise to the reaction flask. The reaction was kept for 2 hrs in the ice-water bath followed by 36 hrs at 25 °C. The resulting solution was extracted (x4) in saturated aqueous $NaHCO_3$ solution and 1M NaOH solution, drying over anhydrous magnesium sulfate and filtering. Rotary evaporation of the solution resulted in a yellow liquid, which was further purified by flash column chromatography using DCM as the mobile phase and basic alumina as the stationary phase, followed by solvent evaporation under reduced pressure. The resulting yellow liquid was dried in a vacuum oven at 25 °C overnight. Yield 78.4%, ^{1}H NMR (500 MHz, $CDCl_3$): δ (ppm) 4.49 (t, 2H, CO_2CH_2, J 6 Hz), 2.53 (tt. 2H, $CO_2CH_2CH_2$, J 6, 18 Hz), 1.94 (s, 6H, $CO_2C(CH_3)_2$); ^{13}C NMR (125.8 MHz, $CDCl_3$): δ (ppm) 171.5 (s, 1C, CO), 117.6 (tt, 1C, CF_2CH_2, J 32, 256 Hz), 117.4 (qt, 1C, CF_3, J 33, 288 Hz), 113.7-105.7 (m, 4C, $CF_3(CF_2)_4$), 58.0 (t, 1C, CH_2O, J 4 Hz), 55.1 (s, 1C, CBr), 30.7 (s, 2C, $CH(CH_3)_2$), 30.5 (t, 1C, CH_2CH_2O, J 22 Hz); ^{19}F NMR (376.5 MHz, $CDCl_3$) δ (ppm) -81.2 (t, 1F, CF_3, J 10 Hz), -113.6--113.9 (m, 1F, CF_3CF_2), -121.9--122.3 (m, 1F, $CF_3CF_2CF_2$), -122.9--123.3 (m, 1F, $CF_3(CF_2)_2CF_2$), -123.7--123.9 (m, 1F, $CF_3(CF_2)_3CF_2$), -126.3--126.6 (m, 1F, $CF_3(CF_2)_4CF_2$).

Perfluorodecyl bromoisobutyrate, F_{17}. Synthesis followed the same procedure as for F_{13}, using 1H,1H,2H,2H-perfluorodecan-1-ol as starting material. Yield = 75.7%.

Perfluorododecyl bromoisobutyrate, F_{21}. Synthesis followed the same procedure as for F_{13}, using 1H,1H,2H,2H-perfluorododecan-1-ol as starting material but with CHCl3 as a solvent in place of DCM. Yield = 50.5%.

5.1.2 Synthesis of anthracene initiator

9-anthracene methanol bromoisobutyryl bromide (AMBiB). Synthesis was adapted from literature.[256] Anhydrous THF (60 ml), triethylamine (5.3 x 10^{-2} mol, 5.34 g) and 9-anthracene methanol (4.8 x 10^{-2} mol, 10 g) were added to a nitrogen-

purged 250 ml 3-necked round bottom flask (RBF) equipped with a constant pressure drop funnel. The RBF was cooled in an ice-water bath containing NaCl and acetone. Anydrous THF (10 ml) containing α-bromoisobutyryl bromide (5.8 x 10^{-2} mol, 13.24 g) was placed in the constant pressure drop funnel and added dropwise to the reaction flask. The reaction was kept for 2 hrs in the ice-water bath followed by 36 hrs at 25 °C. Solids were removed and the solvent removed. The crude product was dissolved in DCM and washed (x4) with H2O, dried over anhydrous magnesium sulfate and filtered. Rotary evaporation resulted in a yellow solid which was dried in a vacuum oven at 25 °C overnight. Yield 87%, ^{1}H NMR (500 MHz, d^{6}-DMSO): δ_H (ppm) 8.52 (s, 1H), 8.37 (d, 2H, CCHCC*H*, J 9 Hz), 8.04 (d, 2H, CCC*H*, J 8.5 Hz), 7.64-7.49 (m, 4H, CCHC*H*), 6.24 (s, 2H, CH_2), 1.91 (s, 6H, (CH_3)$_2$); ^{13}C NMR (125.8 MHz, $CDCl_3$): δ_C (ppm) 171.86 (1C, CO), 131.3 (2C, CH_2CC), 131.0 (2C, CH_2CCC), 129.4 (1C, *C*HCCHCH), 129.0 (2C, CH_2CCCH), 126.7 (2C, CHCCH*C*H), 125.5 (1C, CH_2C), 125.1 (2C, CH_2CCCHCH), 123.9 (2C, CHC*C*HCH), 60.7 (1C, *C*H$_2$), 55.9 (1C, *C*Br), 30.7 (2C, $(CH_3)_2$).

5.1.3 Synthesis of hydrocarbon initiator

Octadecyl bromoisobutyrate (ODBiB). Synthesis was adapted from literature.[181] DCM (75 ml), triethylamine (8 x 10^{-2} mol, 11.25 ml) and octadecane-1-ol (67 x 10^{-2} mol, 18.13 g) were added to a nitrogen-purged 250 ml 3-necked round bottom flask (RBF) equipped with a constant pressure drop funnel. The RBF was cooled in an ice-water bath containing NaCl and acetone. Anydrous DCM (25 ml) containing α-bromoisobutyryl bromide (10 x 10^{-2} mol, 12.45 ml) was placed in the constant pressure drop funnel and added dropwise to the reaction flask. The reaction was kept for 2 hrs in the ice-water bath followed by 36 hrs at 25 °C. Solids were removed and the solvent removed. The crude product was dissolved in DCM and washed (x4) with H2O, dried over anhydrous magnesium sulfate and filtered. Rotary evaporation resulted in a yellow solid which was dried in a vacuum oven at 25 °C overnight. Yield 66.3%, ^{1}H NMR (400 MHz, CDCl3) δ_H (ppm): 4.09 (2H, t, J8.0, CH_2O), 1.86 (6H, s, $C(CH_3)_2$), 1.61 (2H, q, J8.0, CH_2CH_2O), 1.19 (30H, m, $(CH_2)_{15}CH_3$), 0.81 (3H, t, J8.0, CH_2CH_3). ^{13}C NMR (400 MHz, $CDCl_3$)) δ_C (ppm): 171.7 (C=O), 66.1 (CH_2O), 55.9 (CBr), 31.9 (CH_2CH_2O), 30.8 ($C(CH_3)_2$)), 29.7 (($CH_2)_{12}CH_2$), 29.5 ($CH_3CH_2CH_2$), 25.8 ($OCH_2CH_2CH_2$), 22.7 (CH_3CH_2), 14.1 (CH_3CH_2).

5.1.4 Synthesis of *N*-[3-[tris(trimethylsiloxy)silyl]propyl] 2-bromoisobutyramide initiator (NtrisBiB)

Synthesis was adapted from literature.[256] Anhydrous DCM (60 ml), triethylamine (1.1 *eq*., 6.21 x 10^{-2} mol, 6.29 g) and 3-[Tris(trimethylsiloxy)silyl]propyl amine (1 *eq*., 5.65 x 10^{-2} mol, 20 g) were added to a nitrogen-purged 250 ml 3-necked round bottom flask (RBF) equipped with a constant pressure drop funnel. The RBF was cooled in an ice-water bath containing NaCl and acetone. Anydrous DCM (10 ml) containing α-bromoisobutyryl bromide (1.2 *eq*., 6.78 x 10^{-2} mol, 15.59 g) was placed in the constant pressure drop funnel and added dropwise to the reaction flask. The reaction was kept for 2 hrs in the ice-water bath followed by 36 hrs at 25 °C. Solids were filtered, and the solvent removed. Product was purified by column chromatography with 4:1 pet ether:diethyl ether. Rotary evaporation resulted in a white solid which was dried in a vacuum oven at 25 °C overnight. Yield 18.3%, ^{1}H NMR (400 MHz, d^{1}-$CDCl_3$): δ_H (ppm) 6.77 (s, 1H, NH), 3.28-3.20 (m, 2H, $NHCH_2$), 1.97 (s, 6H, $(CH_3)_2$), 1.59-1.51 (m, 2H, $NHCH_2CH_2$), 0.49-0.43 (m, 2H, $SiCH_2$), 0.11 (s, 27H, $(Si(CH_3)_3)_3$); ^{13}C NMR (125.8 MHz, $CDCl_3$): δ_C (ppm) 171.8 (1C, CO), 63.7 (1C, CBr), 42.7 (NHCH), 32.7 (2C, $(CH_3)_2$), 23.3 ($NHCH_2CH_2$), 11.5 (1C, $SiCH_2$), 1.7 $(Si(CH_3)_3)_3$). See section 5.3.4 for ^{1}H NMR spectrum simulation.

5.1.5 General procedure for photoinduced Cu(II) polymerisation

Example target F_{13}-P*t*BA_{25}. $CuBr_2$ (2.45 mg, 0.02 eq.) was dissolved in IPA (2 ml) by sonication, followed by addition of Me_6TREN (17.6 µl, 0.12 eq.). *t*BA (2 ml, 25 eq.) was filtered through basic alumina (to remove inhibitor) prior to addition to the reaction mixture. The mixture was degassed with nitrogen for 10 min before adding F_{13} initiator (159 µl, 1 eq.) and further degassed for 5 min. The reaction was left under a Mylee Nailcare ultraviolet lamp overnight. The resulting polymer was dissolved in the smallest practical volume of acetone and precipitated in 50:50 deionised H2O:MeOH. Product was dissolved in acetone and passed through neutral alumina, solvent removed and dried in a vacuum oven at 25 °C overnight. ^{1}H NMR (300 MHz, $CDCl_3$): δ_H (ppm) 4.40-4.30 (m, 2H, CO_2CH_2), 2.39-1.51 (m, $(CH_2CH)_n$), 1.45 (s, $((CH_3)_3)_n$), 1.23 (s, 2H, $COCH_2CH_2$), 1.15 (s, 6H, $(CH_3)_2$). 99% conversion obtained by ^{1}H NMR. $Đ_{GPC(THF)}$ = 1.13, $M_{n,GPC}$ = 4300 g mol^{-1} .

5.1.6 General procedure for Copper(0) wire polymerisation

Example target F_{13}-P*t*BA_{25}. 5 cm of copper wire was wrapped around a stirrer bar and cleaned in concentrated HCl for 10 min, then rinsed in water and acetone. $CuBr_2$

(6.13 mg, 0.05 eq.) was dissolved in DMSO (2 ml) by sonication. Me_6TREN (26.4 µl, 0.18 eq.) and *t*BA (2 ml, 25 eq.) were added to the reaction mixture with the wire-wrapped stirrer bar. The mixture was degassed with nitrogen for 10 min before addition of the F_{13} initiator (159 µl, 1 eq.) and further degassed for 5 min. The reaction was then left overnight. The resulting polymer was dissolved in minimum acetone and precipitated in 50:50 deionised H_2O:MeOH. Product was dissolved in acetone and passed through neutral alumina, solvent removed and dried in a vacuum oven at 25 °C overnight. 99% conversion obtained by ^{1}H NMR. $Đ_{GPC(THF)}$ = 4.39, $M_{n,GPC}$ = 7800 g mol^{-1}.

5.1.7 Synthesis of P*t*BA$_{10}$-*b*-TRIS$_{10}$ (polymer chain extension)

$CuBr_2$ (3 mg, 0.02 eq.) was dissolved in IPA (1 ml) by sonication, followed by addition of Me_6TREN (22 µl, 0.12 eq.). *t*BA (1 ml, 10 eq.) was filtered through basic alumina (to remove inhibitor) prior to addition to the reaction mixture. The mixture was degassed with nitrogen for 10 min before adding EBiB initiator (101 µl, 1 eq.) and further degassed for 5 min. The reaction was left under a Mylee Nailcare ultraviolet lamp for 19 hrs and a sample was taken with a degassed syringe for ^{1}H NMR analysis. A mixture of TRIS (3.16 ml, 10 eq.) and IPA (3.16 ml) was degassed with nitrogen, added to the reaction mixture, and left for 24 hrs. A sample was taken for ^{1}H NMR and GPC analysis.

5.1.8 General procedure for Cu(I)-ATRP

Example target AMBiB-PMMA$_{25}$.

Cu(I)Br (1 *eq*., 6.7 mg, 4.67 x10^{-4} mol) was added to a Schlenk tube and purged with nitrogen prior to deoxygenated toluene (33.3% solids, 10 ml) being added at room temperature. *N*-propyl-1-pyridin-2-ylmethanimine ligand (2 *eq*., 137 µl, 13.9 x10^{-2} mol) was added and the Schlenk tube was immersed in an oil bath at 90 °C. Once the reaction temperature was reached (monitored with a thermostat), AMBIB (1 *eq*., 166 mg, 4.67 x10^{-4} mol) was added via a degassed syringe, the reaction was then stirred for 20 hours. The resulting polymer mixture was dissolved in minimum acetone and precipitated in 50:50 deionised H_2O:MeOH, redissolved in acetone and filtered through a column of basic alumina to remove residual catalyst.

5.1.9 General deprotection of P*t*BA$_n$

Example target F$_{13}$-PAA$_{25}$. 100 mg of F_{13}-PtBA$_{25}$ was dissolved in 1 ml DCM. 1 ml TFA was added slowly and stirred at ambient temperature overnight. TFA was

removed using by rotary evaporation and residual TFA was removed with the addition of acetone to form an azeotrope (x3). This caused the polymer to simultaneously precipitate and swell with the acetone. Acetone was added to dissolve a yellow impurity and removed by decanting (x3), the product was then dried under vacuum at 25°C overnight. Methanol was found as a good solvent for both segments and 1H NMR was carried out in either CD_3OD or d^6 -DMSO. Integration of backbone peaks approximately agreed with the values obtained from the F_n-P*t*BA_m spectra. ^{1}H NMR (400 MHz, [d_1]$CDCl_3$): δ (ppm) 4.52-4.47 (m, 1H; C*H*Br), 4.40-4.28 (m, 2H; CO_2CH_2), 2.75-1.41 (m; $((CH_3)_3)_n$), 1.32 (s, 2H; $COCH_2CH_2$), 1.20 (d, 6H; $(CH_3)_2$). 99% conversion obtained by ^{1}H NMR. $M_{n,MALDI}$ = 2097 g mol^{-1} .

5.1.10 Synthesis of poly(sodium acrylate) salt (F_{13}-$PNaA_{25}$)

F_{13}-PAA_{25} (0.0457 g, 1 eq.) and NaOH (0.0205 g, 30 eq.) were separately dissolved in a minimum amount of Milli-Q water. The polymer solution was stirred and $NaOH_{(aq)}$ was added dropwise, then covered and left for 30 mins at 25 °C. Universal Indicator paper showed a pH change of the polymer solution from 2 to 7. The resulting polymer solution was dialysed twice with deionised water over 24 hrs, then freeze-dried to give a white solid. IR: (cm^{-1}) 1560 (s, C=O stretch), 1437 (C-H bend $(CH_3)_2$).

5.1.11 Synthesis of 1-ethoxyethyl methacrylate monomer (EEMA)

Synthesis was adapted from literature.[245] Methacrylic acid (1 *eq*., 14.8 ml, 0.174 mol) was added dropwise to a mixture ethyl vinyl ether (1.2 *eq*., 20 ml, 0.208 mol) and phosphoric acid (0.002 *eq*., 0.002 ml, 3.48 x10^{-4} mol) under nitrogen atmosphere at 0 °C. The reaction was stirred for 48 hrs at room temperature. Ethyl vinyl ether was removed under reduced pressure, then the reaction mixture was dissolved in DCM and filtered through basic alumina to remove catalyst and unreacted methacrylic acid. The product was distilled under reduced pressure: the boiling point of EEMA is 32 °C (at 6 mbar). Yields ~ 90%. ^{1}H NMR (400 MHz, [d_1]$CDCl_3$): δ_H (ppm): 6.04 (s, 1H, C*H*HC), 5.89 (q, 1H, J 5.5, C*H*CH_3), 5.48 (m, 1H, CH*H*C), 3.62 (dq, 1H, J 9.5, 7.0, C*H*HCH_3), 3.45 (dq, 1H, J 9.5, 7.0, CH*H*CH_3), 1.84 (s, 3H, CH_3C), 1.33 (d, 3H, J 5.5, CHC*H*$_3$), 1.10 (t, 3H, J7.0, CH_2CH_3).

5.1.12 Deprotection of 1-ethoxyethyl methacrylate (EEMA)

5.1.12.1 Alkaline hydrolysis

0.12 g (120 μl) of EEMA was dissolved in 0.8 ml of d_6-DMSO. 240 μl of NaOD (40% in D_2O) was added to the solution and stirred for 2 hrs. The resulting polymer precipitate was dissolved in D_2O for analysis using ^{1}H NMR spectroscopy.

5.1.12.2 Acid hydrolysis

0.12 g (120 μl) of EEMA was dissolved in 0.8 ml of d_6-DMSO. 240 μl of TFA was added to the solutions and stirred for 2 hrs. The resulting polymer precipitate was dissolved in d_6-DMSO for analysis using ^{1}H NMR spectroscopy.

5.1.13 Synthesis of solketal (meth)acrylate (SkMA/SkA)

DL-1,2-Isopropylideneglycerol (39.9 g, 301.3 mmol) and triethylamine (33.6 g, 331.7 mmol) were dissolved in dry DCM (200 mL) and the solution was cooled in an ice bath under N_2 for 15 min. DCM solution (100 mL) of (meth)acryloyl chloride (27.85 g, 307.5 mmol) was added dropwise to the previous solution over a period of 2 hr. After stirring for 1 hr at 0 °C, the mixture was then allowed to warm up to room temperature and stirred further for 8 hr. The white precipitated by-product was filtered off and the clear product solution was washed with water (3 x 100 mL), and brine (2 x 50 mL), dried over anhydrous Na_2SO_4, filtered, passed through neutral alumina and evaporated under reduced pressure to afford SkA as a yellow oil (47.75g, 85%).

5.1.14 Deprotection of solketal (meth)acrylate

Deprotection procedure was adapted from literature.[250] Solketal (meth)acrylate was dissolved in 6M HCl/THF (1/9, v/v) and stirred at room temperature for 2 hours. Product was purified by dialysis and solvent removed to obtain glycerol mono(meth)acrylate.

5.1.15 Film preparation/Annealing

3 ml of a saturated solution of F_n-PAA_m in methanol was placed in a PTFE boat. This boat and a separate vial of methanol were placed under a beaker and left to evaporate for 48 hours; a thick polymer film remained in the PTFE boat. These films were then thermally annealed at a static temperature of 120 °C for 24 hours.

5.1.16 Spin-coating

5.1.16.1 Sample preparation

Unless otherwise stated, all polymer samples were dissolved in methanol (either at 2.5 or 5 wt%) then spin-coated on a cleaned surface at 1000 rpm with acceleration rate of 200 rpm s^{-1} for 1 minute. Solutions were spin-coated on either Mica sheets (cleaved immediately prior to spin-coating using tape) or glass slides (cleaned prior to spin-coating by sonication in acetone then IPA).

5.1.16.2 Solvent annealing spin-coated samples

Spin-coated samples were placed in a sealed jar with a solvent vapour, obtained by placing the annealing solvent in smaller vials (8 x 1.75 ml vial) inside a 100 ml jar. The sample was placed on a raised platform (28 ml vial) inside the jar and left for 24 hours unless otherwise specified, then removed for analysis.

5.1.17 Sample preparation for UV-Vis Absorption Spectroscopy

AMBiB was dissolved in DMF (3.125 x10^{-3} mgml^{-1}) in a vial, cuvette or NMR tube and irradiated with a light source. UV-Vis absorption was then measured at different intervals. Light sources used include:

320-390 nm – Excelitas OmniCure Series S2000 with 320-390 nm lightguide filter

254 nm – Analytik Jena CL-1000 UVP Crosslinker, energy = 3000 x 100 uJ/cm^2

365 nm - Analytik Jena CL-1000L UVP Crosslinker, energy = 3000 x 100 uJ/cm^2

5.1.18 Sample preparation of F_{21}-PAA_m (with NaOH) in water for AFM

1 mg of F_{21}-PAA_{10} was dissolved in 1 ml of THF (a good solvent) prior to additions of 0.1 M NaOH solution in 3 μl portions until the correct volume was added. A total of 5 ml of deionised water was then added to all solutions in sequential portions, ramping aliquot volume from 3 μl up to 250 μl. This allowed the slow exchange of solvent from THF to water, a solvent in which self-assembly should occur as it is a bad solvent for the fluorinated segment. AFM samples were prepared by pipetting the solution on to Mica (immediately and after 24 hours) and blotting the excess with filter paper. These were left open to air for a minimum of 1 hour before AFM measurements.

5.2 Methods

5.2.1 Small-angle X-ray scattering (SAXS)

5.2.1.1 Single data acquisition measurements.

SAXS measurements were made using a Xenocs Xeuss 2.0 equipped with a micro-focus Cu Kα source collimated with Scatterless slits. Scattering was measured using a Pilatus 300k detector with a pixel size of 0.172 mm x 0.172 mm. The detector was translated vertically and the images combined to form a virtual detector with double the number of pixels. The distance between the detector and the sample was calibrated using silver behenate ($AgC_{22}H_{43}O_2$), giving a value of 0.339(5) m. The magnitude of the scattering vector (q) is given by $q = 4\pi\sin\theta/\lambda$, where 2θ is the angle between the incident and scattered X-rays and λ is the wavelength of the incident X-rays. This gave a q range for the detector of 0.035 Å^{-1} to 1.66 Å^{-1}. A Pilatus 100k was also used to measure the wider-angle scattering response. This detector was static at an angle of 36° to the beam direction and at a distance of 0.162(2) m. This gave a q range for the detector of 1.31 Å^{-1} to 3.27 Å^{-1}. The samples were mounted between two windows of Kapton, coated with an adhesive film. A radial integration (as function of q) was performed on the 2D scattering profile and the resulting data was corrected for the absorption and background from the sample holder. The wider-angle data were rescaled to match the scale of the SAXS measurements taken using the same experimental geometry.

5.2.1.2 Time-resolved SAXS during thermal annealing measurements

These experiments were carried out in a similar way to the single data acquisition measurements, with a Linkam HFSX 350 being used to control the temperature of samples mounted between Kapton sheets. Samples were heated and cooled at a rate of 0.5 °C/min while making 1 min data collections. After every 5 measurements the transmitted intensity was measured for making corrections.

5.2.2 Thermal Analysis

5.2.2.1 Differential Scanning Calorimetry (DSC)

Data for F_{13}-PAA_m polymers were obtained using a Mettler-Toledo DSC1 with autosampler under nitrogen, samples were heated and cooled between 25-180 °C at 10 °C per minute (heating cycles were repeated 3 times). Data for F_{17}-PAA_m and F_{21}-PAA_m polymers were obtained using a PEDSC6000 with intracooler, samples were

heated and cooled between 0-200 °C at 10 °C per minute. Heating cycles were repeated 3 times.

5.2.2.2 Thermogravimetric analysis

Data for F_{13}-PAA_m polymers were obtained using a Mettler-Toledo TGA with autosampler under nitrogen, samples were heated from 30-550 °C at a rate of 10°C per minute.

5.2.3 Atomic Force Microscopy (AFM)

Bruker Dimension Icon:

AFM images were taken using PeakForce Tapping mode with ScanAsyst with NanoScope V software. ScanAsyst-Air Silicon Nitride probes (115 μm x 25 μm x 2 nm).

PeakForce QNM (quantitative nanomechanical mapping) mode was used to obtain adhesion (stickiness), indentation (squishiness), dissipation (hard/spongey) images.

Bruker Innova:

AFM images were taken using an Innova AFM (Bruker) using NanoDrive v8.05 software. Tips were Antimony doped Silicon (225 μm x 35 μm x 3 μm.) Images were taken in tapping mode at 73 kHz.

All images were processed in Gwyddion.[257]

5.2.4 UV-Vis Absorption Spectroscopy

Spectra were measured using an Agilent Technologies Cary 60 UV-Vis Spectrometer. Blank spectrum was subtracted prior to plotting.

5.2.5 Gel Permeation Chromatography (GPC)

Agilent Infinity II MDS instrument equipped with differential refractive index (DRI), viscometry (VS), dual angle light scatter (LS) and multiple wavelength UV detectors. The system was equipped with 2 x PLgel Mixed C columns (300 x 7.5 mm) and a PLgel 5 μm guard column. The eluents were either THF with 2 % TEA (triethylamine) and 0.01 % BHT (butylated hydroxytoluene, or DMF with 5 mmol NH_4BF_4 as additives. Samples were run at 1ml/min at 30'C. Poly(methyl methacrylate) and polystyrene standards (Agilent EasyVials) were used for calibration. Analyte samples were filtered through a GVHP membrane with 0.22 μm pore size before injection. Respectively,

experimental molar mass ($M_{n,GPC}$) and dispersity ($Đ$) values of synthesized polymers were determined by conventional calibration using Agilent GPC/SEC software.

5.2.6 Matrix-Assisted Laser Desorption/Ionisation Time-of-Flight Mass Spectroscopy (MALDI-ToF-MS)

Samples for MALDI ToF analysis were dissolved at 10 mg/ml in THF with 1 mg/ml of sodium iodide. 10 µl of this sample mixture was then mixed with 10 µl matrix solution of 40 mg/ml trans-2-[3-(4-tert-Butylphenyl)-2-methyl-2-propenylidene]malononitrile (DCTB) in THF and 1mg/ml of sodium iodide. 0.5 µl of the resulting solution was then spotted on a 384 ground steel multi target plate, using a dried droplet methodology. The dried crystal structure was then analysed using a Bruker autoflex, equipped with a 337 nm N2 laser, operating in reflectron positive mode with an ion source voltage of 19 kV. Data analysis was then carried out on Bruker fleXanalysis and mMass.

5.3 Calculations

5.3.1 Calculation of *N* (total degree of polymerisation) and volume fraction (f_F/f_{PAA})

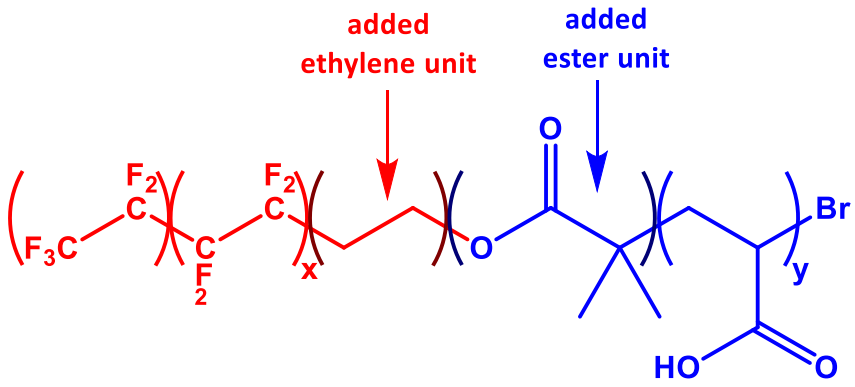

Figure above shows the chemical structure compartmentalisation of the F_n-PAA_m polymers, where the colours indicate the chemical groups attributed to the separate segments (fluorinated segment in red and PAA segment in blue).

The volume fractions and total degree of polymerisation ($N = N_F + N_{PAA}$) of each segment were calculated to account for the bridging unit between the fluorinated segment and PAA segment. The degree of polymerisation of the fluorinated segment (N_F) was counted as number of tetrafluoroethylene (TFE) repeat units ("x" units) in the fluorinated initiator, plus the terminal unit which contains a CF_3. An additional unit was added to account for the adjacent ethylene unit which is approximated to have the same volume as a TFE repeat unit. Example F_{13}-PAA_m – 2 "x" units, 1 terminal unit, 1 ethylene unit, $N_F = 4$.

The degree of polymerisation of the PAA segment (N_{PAA}) differed in each polymer. The number of "y" units was calculated from ^{1}H NMR, and 1 repeat unit was added to account for the adjacent ester unit and approximated to have the same volume as 1 AA unit. Example F_n-PAA_{12} – 12 "y" units, 1 ester unit, $N_{PAA} = 13$.

Example F_{13}-PAA_{12} – 4 (N_F) + 13 (N_{PAA}) = 17 (N).

The volume fractions were calculated using the following equations:

$$f_{PAA} = \frac{(N_{PAA} \times Mr_{AA})/\rho_{PAA}}{((N_{PAA} \times Mr_{AA})/\rho_{PAA}) + ((N_F \times Mr_{TFE})/\rho_{PTFE})} \qquad f_F = 1 - f_{PAA}$$

$M_{r,AA}$ is the molar mass of acrylic acid (72.06 g mol^{-1}) and $M_{r,TFE}$ is the molar mass of tetrafluoroethene (100.02 g/mol). ρ_{PAA} and ρ_{PTFE} are the densities of PAA and PTFE which are taken as 1.41 and 2.2 g/mL, respectively.

5.3.2 Determination of morphology from SAXS data

SAXS data were fit with a gaussian function. The x value at peak maximum was taken as q from the principal peak and any higher order peaks that could be be fitted. Values were added to excel spreadsheet for calculations ("q1", "q2" etc.), Figure 5-1.

Morphology calculation (LAM/HEX/DIS): The theoretical position of higher order peaks from the experimental principal peak q position is calculated . This value is then compared with the experimental higher order peak q values. A percentage difference is calculated and the lowest (and most reasonable) was labelled as the morphology. Domain spacing calculated using principal peak q with equation $d = 2\pi/q$.

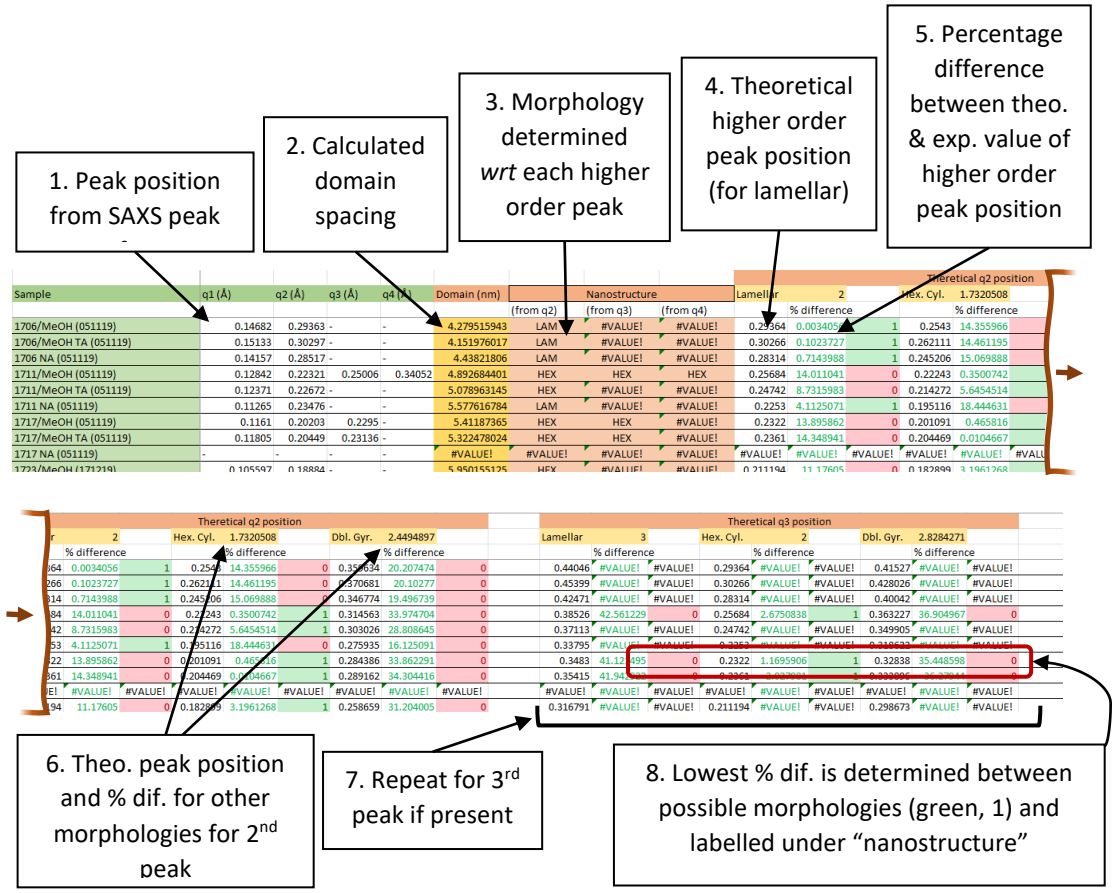

Figure 5-1. Explanation of morphology determination and domain spacing calculation using excel spreadsheet.

5.3.3 Calculation of centre-to-centre domain distance for hexagonally packed cylinders (HEX) morphology

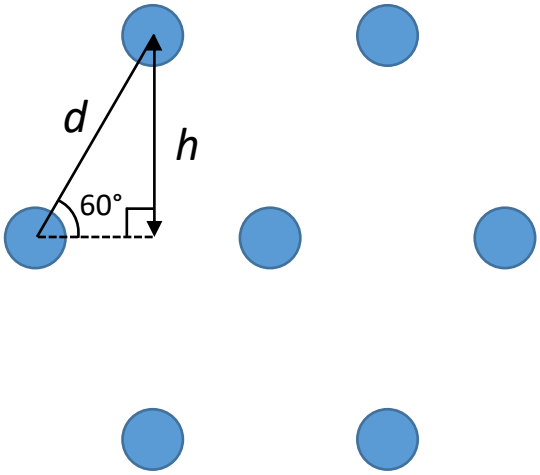

In the diagram above, *h* is the interplane spacing (taken directly from SAXS data) and *d* is the calculated distance between domain centres for hexagonally packed cylinders (domain spacings at full pitch).

	q^* (Å^{-1})	$h = 2\pi/q^*$ (nm)	$d = h/\sin 60$ (nm)	$d^* = d/2$ (nm)
F_{13}-PAA_9	0.15114	4.16	4.80	2.4
F_{13}-PAA_{11}	0.14079	4.46	5.15	2.6
F_{17}-PAA_{11}	0.12371	5.08	5.87	2.9
F_{17}-PAA_{17}	0.11805	5.32	6.14	3.1
F_{17}-PAA_{23}	0.10691	5.88	6.79	3.4
F_{17}-PAA_{30}	0.09996	6.29	7.26	3.6
F_{21}-PAA_{20}	0.09503	6.61	7.63	3.8
F_{21}-PAA_{24}	0.09381	6.70	7.74	3.9

5.3.4 ^{1}H NMR spectrum simulation for NtrisBiB

Here we assume that there is no coupling to the methyl groups, and so they have not been included in the simulation. The coupling between the NH and the NCH_2 is not observed in the NH signal.

The NCH_2 is simulated to be coupling via first order coupling to both the NH and the adjacent, middle, CH_2. The coupling between the $SiCH_2$ and the middle CH_2 is simulated as second order coupling.

Simulated spectrum (top) and measured spectrum (bottom).

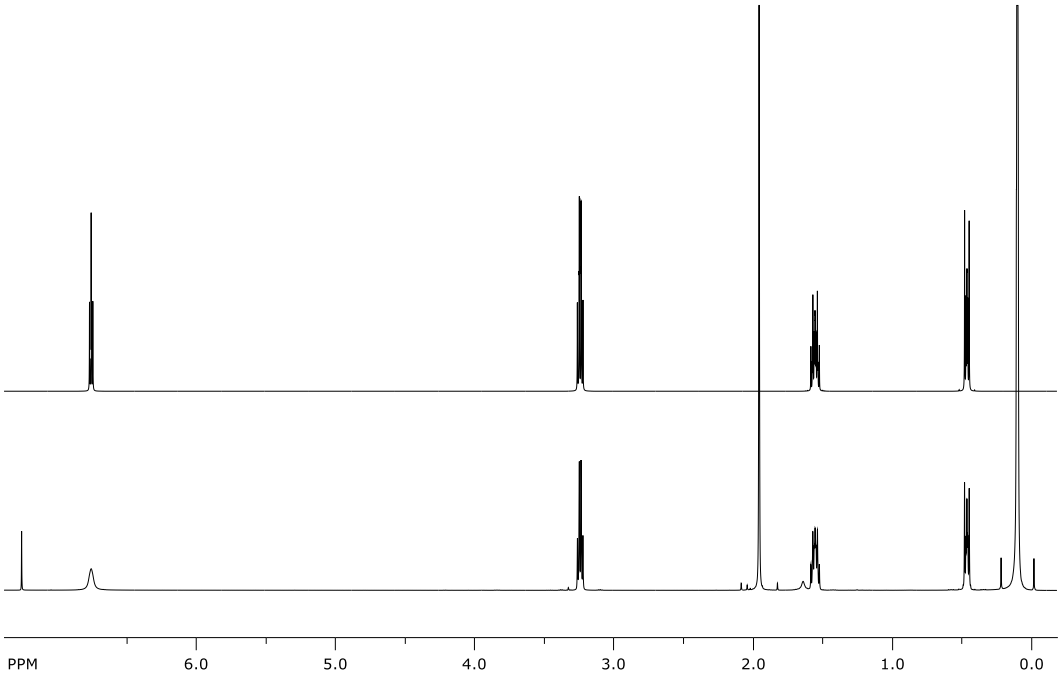

The 4 peaks are shown below. In each case the top spectrum is simulated, and the bottom spectrum is the measured spectrum. The peaks have been shown with the following fitted J-values (rounded to the nearest 0.1 Hz). All other J-values were fixed at zero.

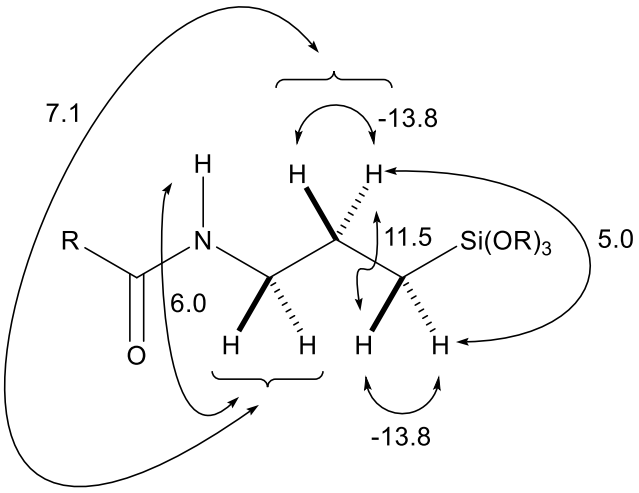

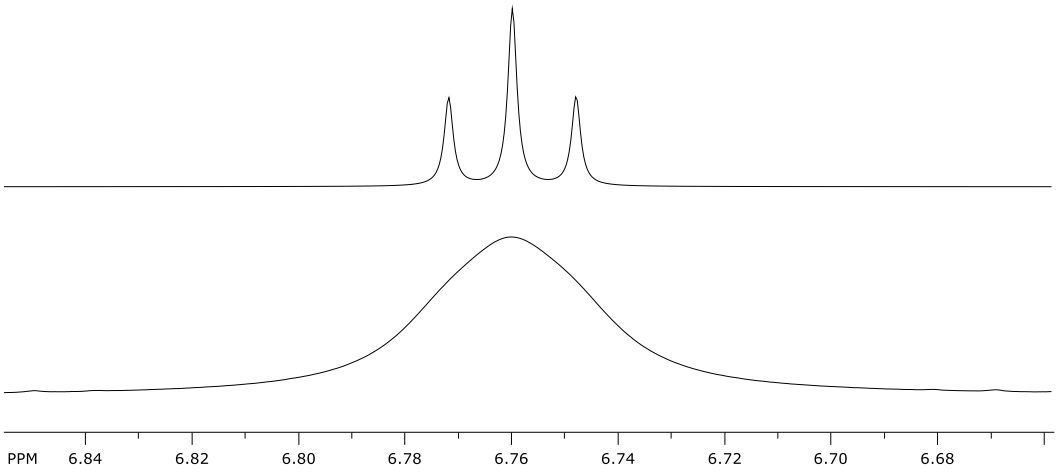
PPM
6.84
6.82
6.80
6.78
6.76
6.74
6.72
6.70
6.68

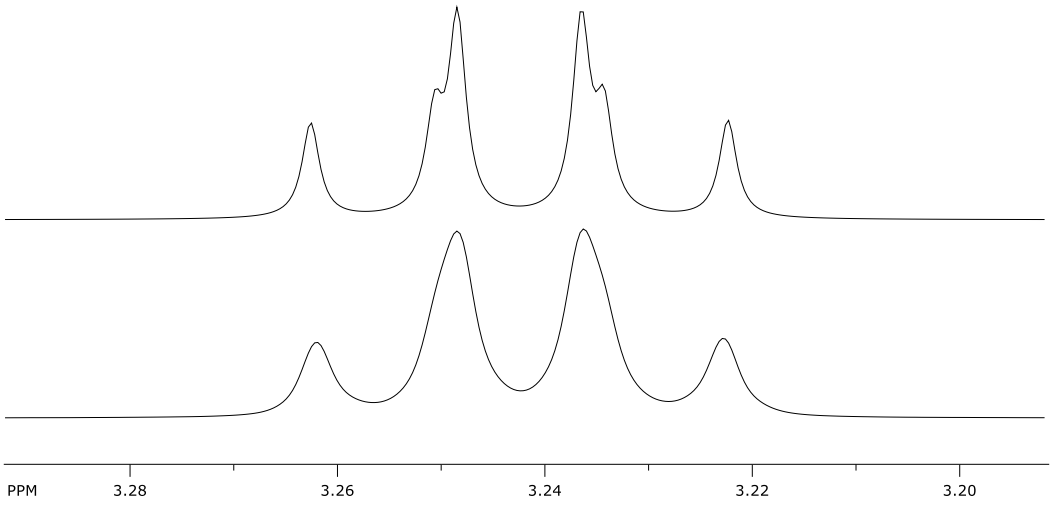
PPM
3.28
3.26
3.24
3.22
3.20

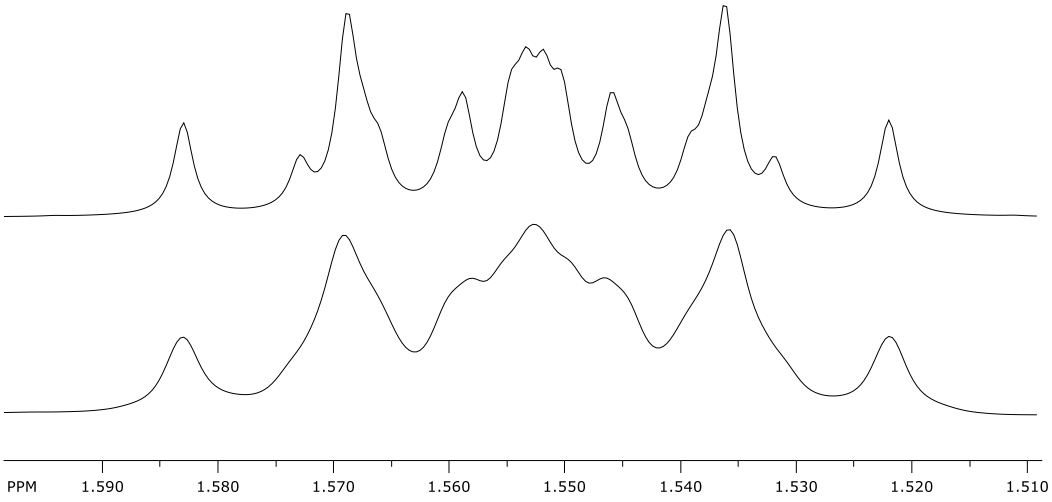
PPM
1.590
1.580
1.570
1.560
1.550
1.540
1.530
1.520
1.510

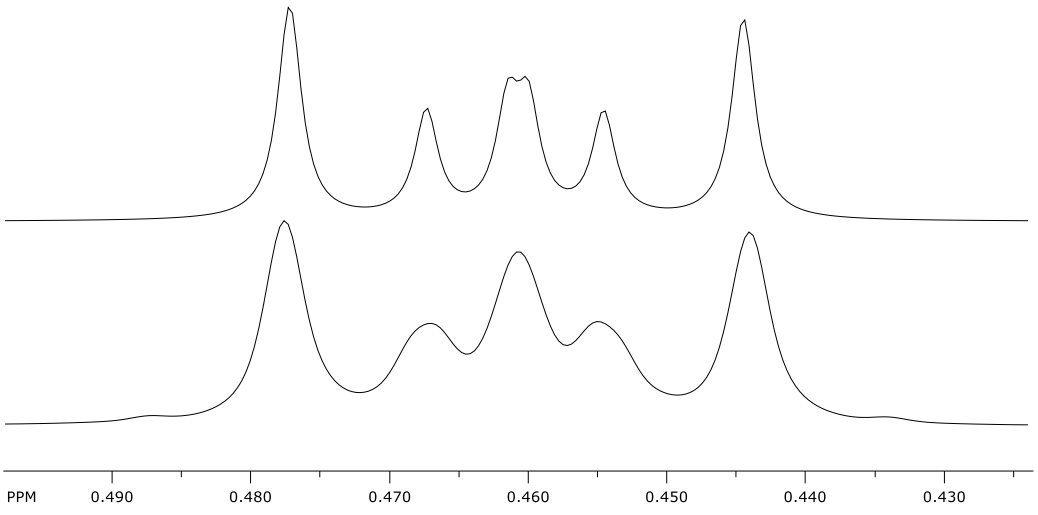
PPM
0.490
0.480
0.470
0.460
0.450
0.440
0.430

Chapter 6: Conclusions and Future work

6.1 Conclusions

A fluorinated alkyl halide initiator was synthesised for use as a hydrophobic, discrete "pseudo" block in the synthesis of low molecular weight, heterotelechelic, amphiphilic polymers. The optimum conditions for polymerising poly(acrylic acid), a hydrophilic segment, were investigated using copper-mediated RDRP and the fluorinated initiator did not hinder the polymerisation. Poly(*tert*-butyl acrylate) polymers were synthesised with low molecular weight (M_n 1400 – 4300 g mol^{-1}) and low dispersity (1.06 - 1.13), and deprotected to poly(acrylic acid). The most suitable characterisation methods and conditions were investigated (including selection of solvents for NMR and GPC, and MALDI-ToF-MS for structure analysis), considering the solubility issues that accompany amphiphilic polymers. Microphase separation of F_n-PAA_m polymers was investigated using both solvent and thermal annealing methods, of which thermal annealing was found to have the fewest associated variables. SAXS measurements revealed a change in morphology from lamellar to hexagonally packed cylinders and an increase in domain spacing from 3.38 – 5.80 nm with increasing poly(acrylic acid) chain length.

Fluoro-acrylic acid polymers with higher fluorine content were synthesised to modify the Flory-Huggins interaction parameter, by using alkyl halide initiators with longer fluorinated tail groups. A library of polymers was synthesised with differing ratios of block A to block B using photo-mediated copper-RDRP. Two types of SAXS measurements were performed: single acquisition after thermal annealing and time-resolved measurements. Theoretical modelling gave insight into the phase behaviour of F_n-PAA_m polymers, and a rod-coil model was found to be most representative in both the strong and weak segregation regime. Time-resolved SAXS measurements were used to obtain thermal transition temperatures (order-order and order-disorder) and monitor changes in morphology with thermal annealing. An experimental phase diagram was constructed from single acquisition data, which provides the synthesis parameters for targeted morphologies. AFM images were obtained from F_n-PAA_m samples annealed in different solvent vapour environments. These showed fine features (sub-5 nm) which were similar in size to the morphological features determined from SAXS and showed annealing solvent dependent morphologies. The small domains sizes that these polymers can achieve may potentially lead to unexplored research areas or prevail over current technologies

in industrial applications such as microelectronics, biomedical applications, nanocomposites, and nanoparticles, which were previously limited by feature size.

A series of hydrophobic initiators were synthesised and investigated for use in the synthesis of low molecular weight polymers with low dispersity. Anthracene was chosen as a suitable hydrophobic moiety and incorporated in an alkyl halide initiator (AMBiB), which was shown to dimerise with 365 nm light and at 40 °C (unexpectedly) and revert to monomer with 254 nm light. This was a highly repeatable process but required the absence of oxygen and was affected by impurities. The polymerisation of methacrylates with AMBiB was optimised, although steric considerations of *t*BMA prevented polymerisation. A hydrocarbon initiator, C_{18}, was used for the synthesis of poly(acrylic acid) polymers which were compared to those polymerised with a fluorocarbon initiator. These proved to show more crystalline nature (HEX symmetry) than with the fluoro-initiators.

Alternative protected hydrophilic monomers, EEMA and SkMA, were investigated for the use with AMBiB. EEMA polymerised well with AMBiB but there was uncertainty in the initiator efficacy at early stages in the polymerisation. SkMA also polymerised well, although high dispersities were found for low DP polymers. This was, most probably, due to unreacted monomer being present in a non-purified sample.

Finally, siloxanes were investigated as both a hydrophobic initiator (NtrisBiB) and as a hydrophobic monomer (TRIS). Due to poor solubility, NtrisBiB was found to be a poor initiator when targeting low molecular weight polymers. TRIS was also found to have polymerisation issues due to solubility, despite multiple stages of optimisation being attempted. A high molecular weight shoulder consistently appeared after 3 hours reaction time. This led to an attempt to polymerise the hydrophilic block first and stop the second block after 3 hours, which was successful. The deprotection was attempted, followed by GPC, which showed that the efficacy of chain extension was poor, and purification was unsuccessful. ^{1}H NMR revealed that the deprotection conditions for *t*BA cause additional, unwanted, reactions with TRIS which occur within the first 5 minutes.

6.2 Future work

This work has demonstrated that the F_n-PAA_m polymers are capable of microphase separation on an ultra-small scale (sub-3 nm). However, the assembly of these polymers is susceptible to defect formation in polymer films (as proven in AFM images) and further investigation is needed to better control the polymer assembly. Utilising directed self-assembly (DSA) methods would facilitate a significant step towards reducing the defect density. By using a pre-treated surface, with either a coating that allows preferential orientation of one of the polymer segments or a surface with an engraved pattern, the polymer would be forced to microphase separate in a more controlled manner. Integrated circuits (IC) possess highly intricated features and are layered upon each other, which is simply not feasible to achieve with block copolymer self-assembly alone. Following any DSA, metal deposition could be investigated along with conductivity measurements, which would be of importance in IC manufacture.

In chapter 3, significant progress was made using an anthracene initiator (AMBiB) to polymerise protected hydrophilic monomers. This was achieved successfully with PEEMA and SkMA, though some further optimisation may be needed for the creation of polymers with very low molecular weight. Future steps would be to synthesise these polymers at a range of chain lengths (including low molecular weight), deprotect them (using the previously determined conditions), study the dimerisation of AMBiB-polymers via UV-Vis spectroscopy, and anneal polymers as films and investigate their morphology/domain spacing with SAXS measurements. Hopefully, these would successfully microphase separate in a similar fashion to F_n-PAA_m polymers, due to their inherent high χ/low N nature. These polymers would also possess the electron dense, photo-responsive anthracene moiety, which would allow easier TEM imaging. Previous attempts at imaging of this kind were unsuccessful due to a lack of electron density in F_n-PAA_m polymers. Secondly, the photo-responsive nature of the AMBiB polymers could be investigated in solution and in solid state: solution would allow more polymer mobility and possibly a full change in morphology. In the solid state, a change in domain spacing rather than a full change in morphology is likely, which would be interesting as it opens an avenue towards the photo-controlled opening/closing of pores in membranes.

References

1 G. Odian, *Principles of Polymerization*, 2004.

2 M. Szwarc, *Nature*, 1956, **178**, 1168–1169.

3 M. Szwarc, M. Levy and R. Milkovich, *J. Am. Chem. Soc.*, 1956, **78**, 2656–2657.

4 A. D. Jenkins, R. G. Jones and G. Moad, *Pure Appl. Chem*, 2010, **82**, 483–491.

5 T. Otsu, *J. Polym. Sci.*, 1956, **21**, 559–561.

6 T. Otsu, *J. Polym. Sci.*, 1957, **26**, 236–239.

7 T. Otsu and M. Yoshida, *Die Makromol. Chemie, Rapid Commun.*, 1982, **3**, 127–132.

8 G. Moad and D. H. Solomon, *The Chemistry of Radical Polymerization*, Elsevier, 2006.

9 E. Rizzardo and D. H. Solomon, *Polym. Bull.*, 1979, **1**, 529–534.

10 G. Moad and E. Rizzardo, in *RSC Polymer Chemistry Series*, 2016, vol. 2016-Janua, pp. 1–44.

11 1984, 581.

12 A. D. Jenkins, R. G. Jones and G. Moad, *Pure Appl. Chem.*, 2010, **82**, 483–491.

13 C. J. Hawker, A. W. Bosman and E. Harth, *Chem. Rev.*, 2001, **101**, 3661–3688.

14 C. J. Hawker, G. G. Barclay, A. Orellana, J. Dao and W. Devonport, *Macromolecules*, 1996, **29**, 5245–5254.

15 J. Chiefari, Y. K. Chong, F. Ercole, J. Krstina, J. Jeffery, T. P. T. Le, R. T. A. Mayadunne, G. F. Meijs, C. L. Moad, G. Moad, E. Rizzardo and S. H. Thang, *Macromolecules*, 1998, **31**, 5559–5562.

16 S.-H. Qin, D.-Q. Qin and K.-Y. Qiu, *New J. Chem.*, 2001, **25**, 893–895.

17 H. Fischer, *Chem. Rev.*, 2001, **101**, 3581–3610.

18 S. Perrier, *Macromolecules*, 2017, **50**, 7433–7447.

19 G. Moad, E. Rizzardo and S. H. Thang, *Aust. J. Chem.*, 2012, **65**, 985–1076.

20 M. Kato, M. Kamigaito, M. Sawamoto and T. Higashimura, *Macromolecules*, 1995, **28**, 1721–1723.

21 J. S. Wang and K. Matyjaszewski, *J. Am. Chem. Soc.*, 1995, **117**, 5614–5615.

22 Z. Guan and B. Smart, *Macromolecules*, 2000, **33**, 6904–6906.

23 T. Ando, M. Kamigaito and M. Sawamoto, *Macromolecules*, 2000, **33**, 5825–5829.

24 K. Ibrahim, B. Löfgren and J. Seppälä, *Eur. Polym. J.*, 2003, **39**, 2005–2010.

25 H. Uegaki, Y. Kotani, M. Kamigaito and M. Sawamoto, *Macromolecules*, 1997, **30**, 2249–2253.

26 P. Lecomte, I. Drapier, P. Dubois, P. Teyssié and R. Jérôme, *Macromolecules*, 1997, **30**, 7631–7633.

27 F. Stoffelbach, D. M. Haddleton and R. Poli, *Eur. Polym. J.*, 2003, **39**, 2099–2105.

28 K. Matyjaszewski, *Macromolecules*, 2012, **45**, 4015–4039.

29 K. Matyjaszewski and J. Xia, *Chem. Rev.*, 2001, **101**, 2921–2990.

30 M. Ouchi, T. Terashima and M. Sawamoto, *Chem. Rev.*, 2009, **109**, 4963–5050.

31 K. Matyjaszewski, D. A. Shipp, G. P. McMurtry, S. G. Gaynor and T. Pakula, *J. Polym. Sci. Part A Polym. Chem.*, 2000, **38**, 2023–2031.

32 T. Grimaud and K. Matyjaszewski, *Macromolecules*, 1997, **30**, 2216–2218.

33 K. Matyjaszewski, S. Mu Jo, H. Paik and S. G. Gaynor, *Macromolecules*, 1997,

30, 6398–6400.

34 V. Percec, B. Barboiu, T. K. Bera, M. Van Der Sluis, R. B. Grubbs and J. M. J. Fréchet, *J. Polym. Sci. Part A Polym. Chem.*, 2000, **38**, 4776–4791.

35 G. R. Jones, R. Whitfield, A. Anastasaki, N. Risangud, A. Simula, D. J. Keddie and D. M. Haddleton, *Polym. Chem.*, 2018, **9**, 2382–2388.

36 A. G. West, B. Hornby, J. Tom, V. Ladmiral, S. Harrisson and S. Perrier, *Macromolecules*, 2011, **44**, 8034–8041.

37 K. Matyjaszewski, T. E. Patten and J. Xia, *J. Am. Chem. Soc.*, 1997, **119**, 674–680.

38 K. A. Davis, H. J. Paik and K. Matyjaszewski, *Macromolecules*, 1999, **32**, 1767–1776.

39 K. Matyjaszewski, S. M. Jo, H. J. Paik and D. A. Shipp, *Macromolecules*, 1999, **32**, 6431–6438.

40 W. Tang, Y. Kwak, W. Braunecker, N. V. Tsarevsky, M. L. Coote and K. Matyjaszewski, *J. Am. Chem. Soc.*, 2008, **130**, 10702–10713.

41 T. Ando, M. Kamigaito and M. Sawamoto, *Tetrahedron*, 1997, **53**, 15445–15457.

42 A. Anastasaki, V. Nikolaou, G. Nurumbetov, P. Wilson, K. Kempe, J. F. Quinn, T. P. Davis, M. R. Whittaker and D. M. Haddleton, *Chem. Rev.*, 2016, 116, 835–877.

43 R. Whitfield, A. Anastasaki, V. Nikolaou, G. R. Jones, N. G. Engelis, E. H. Discekici, C. Fleischmann, J. Willenbacher, C. J. Hawker and D. M. Haddleton, *J. Am. Chem. Soc.*, 2017, **139**, 1003–1010.

44 A. Anastasaki, C. Waldron, P. Wilson, R. McHale and D. M. Haddleton, *Polym. Chem.*, 2013, **4**, 2672.

45 D. Konkolewicz, Y. Wang, P. Krys, M. Zhong, A. A. Isse, A. Gennaro and K. Matyjaszewski, *Polym. Chem.*, 2014, **5**, 4396–4417.

46 D. Konkolewicz, Y. Wang, M. Zhong, P. Krys, A. A. Isse, A. Gennaro and K.

Matyjaszewski, *Macromolecules*, 2013, **46**, 8749–8772.

47 K. Matyjaszewski, S. Coca, S. G. Gaynor, M. Wei and B. E. Woodworth, *Macromolecules*, 1997, **30**, 7348–7350.

48 V. Percec, T. Guliashvili, J. S. Ladislaw, A. Wistrand, A. Stjerndahl, M. J. Sienkowska, M. J. Monteiro and S. Sahoo, *J. Am. Chem. Soc.*, 2006, **128**, 14156–14165.

49 G. R. Jones, Z. Li, A. Anastasaki, D. J. Lloyd, P. Wilson, Q. Zhang and D. M. Haddleton, *Macromolecules*, 2016, **49**, 483–489.

50 Q. Zhang, P. Wilson, Z. Li, R. McHale, J. Godfrey, A. Anastasaki, C. Waldron and D. M. Haddleton, *J. Am. Chem. Soc.*, 2013, **135**, 7355–7363.

51 Y. Zhang, Y. Wang, C. H. Peng, M. Zhong, W. Zhu, D. Konkolewicz and K. Matyjaszewski, *Macromolecules*, 2012, **45**, 78–86.

52 F. Alsubaie, A. Anastasaki, V. Nikolaou, A. Simula, G. Nurumbetov, P. Wilson, K. Kempe and D. M. Haddleton, *Macromolecules*, 2015, **48**, 5517–5525.

53 F. Alsubaie, A. Anastasaki, V. Nikolaou, A. Simula, G. Nurumbetov, P. Wilson, K. Kempe and D. M. Haddleton, *Macromolecules*, 2015, **48**, 6421–6432.

54 B. P. Fors, J. E. Poelma, M. S. Menyo, M. J. Robb, D. M. Spokoyny, J. W. Kramer, J. H. Waite and C. J. Hawker, *J. Am. Chem. Soc.*, 2013, **135**, 14106–14109.

55 M. Tanabe, G. W. M. Vandermeulen, W. Y. Chan, P. W. Cyr, L. Vanderark, D. A. Rider and I. Manners, *Nat. Mater.*, 2006, **5**, 467–470.

56 N. Bortolamei, A. A. Isse, A. J. D. Magenau, A. Gennaro and K. Matyjaszewski, *Angew. Chemie*, 2011, **123**, 11593–11596.

57 A. J. D. Magenau, N. C. Strandwitz, A. Gennaro and K. Matyjaszewski, *Science (80-.).*, 2011, **332**, 81–84.

58 N. D. Dolinski, Z. A. Page, E. H. Discekici, D. Meis, I.-H. Lee, G. R. Jones, R. Whitfield, X. Pan, B. G. McCarthy, S. Shanmugam, V. Kottisch, B. P. Fors, C. Boyer, G. M. Miyake, K. Matyjaszewski, D. M. Haddleton, J. R. de Alaniz, A. Anastasaki and C. J. Hawker, *J. Polym. Sci. Part A Polym. Chem.*, 2018, **57**,

268–273.

59 E. H. Discekici, A. Anastasaki, R. Kaminker, J. Willenbacher, N. P. Truong, C. Fleischmann, B. Oschmann, D. J. Lunn, J. Read De Alaniz, T. P. Davis, C. M. Bates and C. J. Hawker, *J. Am. Chem. Soc.*, 2017, **139**, 5939–5945.

60 G. R. Jones, R. Whitfield, A. Anastasaki and D. M. Haddleton, *J. Am. Chem. Soc.*, 2016, **138**, 7346–7352.

61 S.-H. Qin, D. Qin and K. Qiu, *Chin. J. Polym. Sci.*, 2001, **19**, 441–445.

62 M. Chen, M. Zhong and J. A. Johnson, *Chem. Rev.*, 2016, **116**, 10167–10211.

63 D. Konkolewicz, K. Schröder, J. Buback, S. Bernhard and K. Matyjaszewski, *ACS Macro Lett.*, 2012, **1**, 1219–1223.

64 Q. Zhang, P. Wilson, Z. Li, R. McHale, J. Godfrey, A. Anastasaki, C. Waldron and D. M. Haddleton, *J. Am. Chem. Soc.*, 2013, **135**, 7355–7363.

65 A. Anastasaki, V. Nikolaou, Q. Zhang, J. Burns, S. R. Samanta, C. Waldron, A. J. Haddleton, R. McHale, D. Fox, V. Percec, P. Wilson and D. M. Haddleton, *J. Am. Chem. Soc.*, 2014, **136**, 1141–1149.

66 N. A. Lynd and M. A. Hillmyer, *Macromolecules*, 2005, **38**, 8803–8810.

67 A. S. Dunn, B. D. Stead and H. W. Melville, *Trans. Faraday Soc.*, 1954, **50**, 279.

68 A. Mühlebach, S. G. Gaynor and K. Matyjaszewski, *Macromolecules*, 1998, **31**, 6046–6052.

69 P. Alexandridis and T. Alan Hatton, *Colloids Surfaces A Physicochem. Eng. Asp.*, 1995, **96**, 1–46.

70 S. Y. Yang, J. A. Yang, E. S. Kim, G. Jeon, E. J. Oh, K. Y. Choi, S. K. Hahn and J. K. Kim, *ACS Nano*, 2010, **4**, 3817–3822.

71 S. Kumar, J. F. Allard, D. Morris, Y. L. Dory, M. Lepage and Y. Zhao, *J. Mater. Chem.*, 2012, **22**, 7252–7257.

72 S. Zhai, Y. Ma, Y. Chen, D. Li, J. Cao, Y. Liu, M. Cai, X. Xie, Y. Chen and X.

Luo, *Polym. Chem.*, 2014, **5**, 1285–1297.

73 J. Wu, X. Li, Y. Wu, G. Liao, P. Johnston, P. D. Topham and L. Wang, *Appl. Surf. Sci.*, 2017, **422**, 769–777.

74 S. Desbief, B. Grignard, C. Detrembleur, R. Rioboo, A. Vaillant, D. Seveno, M. Voué, J. De Coninck, A. M. Jonas, C. Jérôme, P. Damman and R. Lazzaroni, *Langmuir*, 2010, **26**, 2057–2067.

75 J. T. Han, X. Xu and K. Cho, *Langmuir*, 2005, **21**, 6662–6665.

76 J. M. DeSimone, G. A. York, J. E. McGrath, A. S. Gozdz and M. J. Bowden, *Macromolecules*, 1991, **24**, 5330–5339.

77 K. Brassat, D. Kool, J. Bürger and J. K. N. Lindner, *Nanoscale*, 2018, **10**, 10005–10017.

78 A. Nunns, J. Gwyther and I. Manners, *Polymer (Guildf).*, 2013, **54**, 1269–1284.

79 H. Yu, *Prog. Polym. Sci.*, 2014, **39**, 781–815.

80 J. M. G. Swann and P. D. Topham, *Polymers (Basel).*, 2010, 2, 454–469.

81 O. Kim, S. J. Kim and M. J. Park, *Chem. Commun.*, 2018, 54, 4895–4904.

82 P. D. Topham, J. R. Howse, C. M. Fernyhough and A. J. Ryan, *Soft Matter*, 2007, **3**, 1506–1512.

83 O. Kim, S. Y. Kim, B. Park, W. Hwang and M. J. Park, *Macromolecules*, 2014, **47**, 4357–4368.

84 E. A. Jackson and M. A. Hillmyer, *ACS Nano*, 2010, **4**, 3548–3553.

85 P. Antony, J. E. Puskas and M. Kontopoulou, *Polym. Eng. Sci.*, 2003, **43**, 243–253.

86 G. L. Gregory, G. S. Sulley, L. P. Carrodeguas, T. T. D. Chen, A. Santmarti, N. J. Terrill, K. Y. Lee and C. K. Williams, *Chem. Sci.*, 2020, **11**, 6567–6581.

87 H. Schmalz, V. Abetz and R. Lange, *Compos. Sci. Technol.*, 2003, **63**, 1179–1186.

88 S. B. Darling, *Prog. Polym. Sci.*, 2007, **32**, 1152–1204.

89 A. M. Rumyantsev, A. A. Gavrilov and E. Y. Kramarenko, *Macromolecules*, 2019, **52**, 7167–7174.

90 P. J. Flory, *J. Chem. Phys.*, 1942, **10**, 51–61.

91 K. Aissou, I. Otsuka, C. Rochas, S. Fort, S. Halila and R. Borsali, *Langmuir*, 2011, **27**, 4098–4103.

92 J. G. Kennemur, L. Yao, F. S. Bates and M. A. Hillmyer, *Macromolecules*, 2014, **47**, 1411–1418.

93 C. Sinturel, F. S. Bates and M. A. Hillmyer, *ACS Macro Lett.*, 2015, **4**, 1044–1050.

94 M. E. Arnold, K. Nagai, R. J. Spontak, B. D. Freeman, D. Leroux, D. E. Betts, J. M. DeSimone, F. A. DiGiano, C. K. Stebbins and R. W. Linton, *Macromolecules*, 2002, **35**, 3697–3707.

95 J. Shen, V. A. Piunova, S. Nutt and T. E. Hogen-Esch, *Polym. (United Kingdom)*, 2013, **54**, 5790–5800.

96 Y. Mai and A. Eisenberg, *Chem. Soc. Rev.*, 2012, **41**, 5969–5985.

97 L. Leibler, *Macromolecules*, 1980, **13**, 1602–1617.

98 A. Blanazs, S. P. Armes and A. J. Ryan, *Macromol. Rapid Commun.*, 2009, 30, 267–277.

99 N. J. Warren and S. P. Armes, *J. Am. Chem. Soc.*, 2014, **136**, 10174–10185.

100 J. N. Israelachvili, *Intermolecular and surface forces*, Academic Press, 2011.

101 R. Nagarajan, *Langmuir*, 2002, **18**, 31–38.

102 S. W. Sides and G. H. Fredrickson, *J. Chem. Phys.*, 2004, **121**, 4974–4986.

103 S. Harrisson, *Polym. Chem.*, 2018, 9, 1366–1370.

104 N. A. Lynd and M. A. Hillmyer, *Macromolecules*, 2005, **38**, 8803–8810.

105 B. Oschmann, J. Lawrence, M. W. Schulze, J. M. Ren, A. Anastasaki, Y. Luo, M. D. Nothling, C. W. Pester, K. T. Delaney, L. A. Connal, A. J. McGrath, P. G. Clark, C. M. Bates and C. J. Hawker, *ACS Macro Lett.*, 2017, **6**, 668–673.

106 G. E. Moore, *Electronics*, 1965, **38**, 114.

107 D. Bratton, D. Yang, J. Dai and C. K. Ober, *Polym. Adv. Technol.*, 2006, 17, 94–103.

108 L. R. Harriott, *Proc. IEEE*, 2001, **89**, 366–374.

109 S. Wang, L. Li, C. K. Ober, E. P. Giannelis, X. Liu and S. Pal, *Chem. Soc. Rev.*, 2017, **46**, 4855–4866.

110 X. Gu, I. Gunkel, A. Hexemer, W. Gu and T. P. Russell, *Adv. Mater.*, 2014, **26**, 273–281.

111 C. Jin, B. C. Olsen, E. J. Luber and J. M. Buriak, *Chem. Mater.*, 2017, 29, 176–188.

112 A. Selkirk, N. Prochukhan, R. Lundy, C. Cummins, R. Gatensby, R. Kilbride, A. Parnell, J. Baez Vasquez, M. Morris and P. Mokarian-Tabari, *Macromolecules*, 2021, **54**, 1203–1215.

113 C. Jin, J. N. Murphy, K. D. Harris and J. M. Buriak, *ACS Nano*, 2014, **8**, 3979–3991.

114 S. W. Kim, E. Kim, H. Lee, B. C. Berry, H. C. Kim and D. Y. Ryu, *Polymer (Guildf).*, 2015, **74**, 63–69.

115 L. D. Williamson, R. N. Seidel, X. Chen, H. S. Suh, P. Rincon Delgadillo, R. Gronheid and P. F. Nealey, *ACS Appl. Mater. Interfaces*, 2016, **8**, 2704–2712.

116 D. Borah, M. T. Shaw, J. D. Holmes and M. A. Morris, *ACS Appl. Mater. Interfaces*, 2013, **5**, 2004–2012.

117 C. Cummins, P. Mokarian-Tabari, P. Andreazza, C. Sinturel and M. A. Morris, *ACS Appl. Mater. Interfaces*, 2016, **8**, 8295–8304.

118 A. A. Leniart, P. Pula, A. Sitkiewicz and P. W. Majewski, *ACS Nano*, 2020, **14**, 4805–4815.

119 P. W. Majewski and K. G. Yager, *ACS Nano*, 2015, **9**, 3896–3906.

120 M. Luo, D. M. Scott and T. H. Epps, *ACS Macro Lett.*, 2015, **4**, 516–520.

121 S. Jo, S. Jeon, H. Kim, C. Y. Ryu, S. Lee and D. Y. Ryu, *Chem. Mater.*, 2020, **32**, 9633–9641.

122 G. Ginige, Y. Song, B. C. Olsen, E. J. Luber, C. T. Yavuz and J. M. Buriak, *ACS Appl. Mater. Interfaces*, 2021, **13**, 28639–28649.

123 H. S. Suh, D. H. Kim, P. Moni, S. Xiong, L. E. Ocola, N. J. Zaluzec, K. K. Gleason and P. F. Nealey, *Nat. Nanotechnol.*, 2017, **12**, 575–581.

124 C. K. Ober, *Nat. Nanotechnol.*, 2017, 12, 507–508.

125 J. Y. Kim, P. Liu, M. J. Maher, D. H. Callan, C. M. Bates, M. C. Carlson, Y. Asano, G. Blachut, C. T. Rettner, J. Y. Cheng, D. F. Sunday, R. J. Kline, D. P. Sanders, N. A. Lynd, C. J. Ellison, C. G. Willson and C. R. Baiz, *ACS Appl. Mater. Interfaces*, 2020, **12**, 23399–23409.

126 J. Arias-Zapata, S. Böhme, J. Garnier, C. Girardot, A. Legrain and M. Zelsmann, *Adv. Funct. Mater.*, 2016, **26**, 5690–5700.

127 M. A. Morris, *Microelectron. Eng.*, 2015, **132**, 207–217.

128 H. Jung, S. Woo, S. Park, S. Lee, M. Kang, Y. Choe, J. G. Son, D. Y. Ryu, J. Huh and J. Bang, *Soft Matter*, 2015, **11**, 4242–4250.

129 X. M. Li, D. Reinhoudt and M. Crego-Calama, *Chem. Soc. Rev.*, 2007, **36**, 1350–1368.

130 K. R. Gadelrab, Y. Ding, R. Pablo-Pedro, H. Chen, K. W. Gotrik, D. G. Tempel, C. A. Ross and A. Alexander-Katz, *Nano Lett.*, 2018, **18**, 3766–3772.

131 M. R. Hammond, E. Cochran, G. H. Fredrickson and E. J. Kramer, *Macromolecules*, 2005, **38**, 6575–6585.

132 J. Bang, S. H. Kim, E. Drockenmuller, M. J. Misner, T. P. Russell and C. J. Hawker, *J. Am. Chem. Soc.*, 2006, **128**, 7622–7629.

133 I. Otsuka, S. Tallegas, Y. Sakai, C. Rochas, S. Halila, S. Fort, A. Bsiesy, T.

Baron and R. Borsali, *Nanoscale*, 2013, **5**, 2637.

134 C. W. Chang, M. H. Cheng, H. W. Ko, C. W. Chu, Y. H. Tu and J. T. Chen, *Soft Matter*, 2017, **14**, 35–41.

135 X. Zhang, K. D. Harris, N. L. Y. Wu, J. N. Murphy and J. M. Buriak, *ACS Nano*, 2010, **4**, 7021–7029.

136 C. Liang, K. Hong, G. A. Guiochon, J. W. Mays and S. Dai, *Angew. Chemie - Int. Ed.*, 2004, **43**, 5785–5789.

137 S. H. Kim, M. J. Misner, T. Xu, M. Kimura and T. P. Russell, *Adv. Mater.*, 2004, **16**, 226–231.

138 P. D. Topham, J. R. Howse, C. M. Fernyhough and A. J. Ryan, *Soft Matter*, 2007, **3**, 1506–1512.

139 H. Il Lee, W. Wu, J. K. Oh, L. Mueller, G. Sherwood, L. Peteanu, T. Kowalewski and K. Matyjaszewski, *Angew. Chemie - Int. Ed.*, 2007, **46**, 2453–2457.

140 F. Ercole, T. P. Davis and R. A. Evans, *Polym. Chem.*, 2010, **1**, 37–54.

141 T. Sendai, S. Biswas and T. Aida, *J. Am. Chem. Soc.*, 2013, **135**, 11509–11512.

142 N. Katsonis, T. Kudernac, M. Walko, S. J. Van Der Molen, B. J. Van Wees and B. L. Feringa, *Adv. Mater.*, 2006, **18**, 1397–1400.

143 T. Seki, *Polym. J.*, 2014, **46**, 751–768.

144 H. Yu, T. Iyoda and T. Ikeda, *J. Am. Chem. Soc.*, 2006, **128**, 11010–11011.

145 Y. Morikawa, S. Nagano, K. Watanabe, K. Kamata, T. Iyoda and T. Seki, *Adv. Mater.*, 2006, **18**, 883–886.

146 Y. Zhao, X. Tong and Y. Zhao, *Macromol. Rapid Commun.*, 2010, **31**, 986–990.

147 Y. Morikawa, T. Kondo, S. Nagano and T. Seki, *Chem. Mater.*, 2007, **19**, 1540–1542.

148 A. Lennartson, A. Roffey and K. Moth-Poulsen, *Tetrahedron Lett.*, 2015, **56**,

1457–1465.

149 N. Wagner and P. Theato, *Polymer (Guildf).*, 2014, **55**, 3436–3453.

150 N. Katsonis, M. Lubomska, M. M. Pollard, B. L. Feringa and P. Rudolf, *Prog. Surf. Sci.*, 2007, **82**, 407–434.

151 Y. Zheng, M. Micic, S. V. Mello, M. Mabrouki, F. M. Andreopoulos, V. Konka, S. M. Pham and R. M. Leblanc, *Macromolecules*, 2002, **35**, 5228–5234.

152 S. Helmy, F. A. Leibfarth, S. Oh, J. E. Poelma, C. J. Hawker and J. R. De Alaniz, *J. Am. Chem. Soc.*, 2014, **136**, 8169–8172.

153 S. Jia, A. Tan, A. Hawley, B. Graham and B. J. Boyd, *J. Colloid Interface Sci.*, 2019, **548**, 151–159.

154 S. Helmy, S. Oh, F. A. Leibfarth, C. J. Hawker and J. Read De Alaniz, *J. Org. Chem.*, 2014, **79**, 11316–11329.

155 K. Beppu, Y. Nagashima, M. Hara, S. Nagano and T. Seki, *Macromol. Rapid Commun.*, , DOI:10.1002/marc.201600659.

156 M. C. Spiridon, N. Demazy, C. Brochon, E. Cloutet, G. Hadziioannou, K. Aissou and G. Fleury, *Macromolecules*, 2020, **53**, 68–77.

157 S. Sun, S. Liang, W. C. Xu, G. Xu and S. Wu, *Polym. Chem.*, 2019, **10**, 4389–4401.

158 W. C. Xu, S. Sun and S. Wu, *Angew. Chemie - Int. Ed.*, 2019, **58**, 9712–9740.

159 G. Mantovani, V. Ladmiral, L. Tao and D. M. Haddleton, *Chem. Commun.*, 2005, 2089–2091.

160 X.-M. Peng, G. L.V. Damu and C.- He Zhou, *Curr. Pharm. Des.*, 2013, **19**, 3884–3930.

161 B. Zhang, C. Ge, J. Yao, Y. Liu, H. Xie and J. Fang, *J. Am. Chem. Soc.*, 2015, **137**, 757–769.

162 C. M. Liu, R. Bao, J. J. Qiu, F. Hu, Y. Xu, C. Zhao and Y. Zhou, *Polym. Bull.*, 2006, **57**, 139–149.

163 L. Yang, H. Tang and H. Sun, , DOI:10.20944/PREPRINTS201805.0430.V1.

164 J. Van Damme, O. Van Den Berg, J. Brancart, L. Vlaminck, C. Huyck, G. Van Assche, B. Van Mele and F. Du Prez, *Macromolecules*, 2017, **50**, 1930–1938.

165 H. Durmaz, B. Colakoglu, U. Tunca and G. Hizal, *J. Polym. Sci. Part A Polym. Chem.*, 2006, **44**, 1667–1675.

166 S. Bringmann, R. Brodbeck, R. Hartmann, C. Schäfer and J. Mattay, *Org. Biomol. Chem.*, 2011, **9**, 7491–7499.

167 D. A. M. Egbe, S. Türk, S. Rathgeber, F. Kühnlenz, R. Jadhav, A. Wild, E. Birckner, G. Adam, A. Pivrikas, V. Cimrova, G. Knör, N. S. Sariciftci and H. Hoppe, *Macromolecules*, 2010, **43**, 1261–1269.

168 C. J. Hawker and T. P. Russell, *MRS Bull.*, 2005, **30**, 952–966.

169 A. Blanazs, S. P. Armes and A. J. Ryan, *Macromol. Rapid Commun.*, 2009, **30**, 267–277.

170 T. Smart, H. Lomas, M. Massignani, M. V. Flores-Merino, L. R. Perez and G. Battaglia, *Nano Today*, 2008, **3**, 38–46.

171 C. Cummins, R. Lundy, J. J. Walsh, V. Ponsinet, G. Fleury and M. A. Morris, *Nano Today*, , DOI:10.1016/j.nantod.2020.100936.

172 J. E. Poelma, K. Ono, D. Miyajima, T. Aida, K. Satoh and C. J. Hawker, *ACS Nano*, 2012, 121129132529008.

173 P. D. Topham, *X-ray scattering in polymer science*, 2017.

174 S. Y. Chen, A. Maksimchuk and D. Umstadter, *Nature*, 1998, **396**, 653–655.

175 H. Schnablegger and Y. Singh, *The SAXS Guide*, Anton Paar GmbH, 3rd edn., 2013.

176 J. Lyklema, *Fundamentals of Interface and Colloid Science: Particulate Colloids, Volume IV*, Elsevier Academic Press, 1st edn., 2005.

177 L. Wang, P. D. Topham, O. O. Mykhaylyk, H. Yu, A. J. Ryan, J. P. A. Fairclough and W. Bras, *Macromol. Rapid Commun.*, 2015, **36**, 1437–1443.

178 K. J. Hanley, T. P. Lodge and C. I. Huang, *Macromolecules*, 2000, **33**, 5918–5931.

179 M. K. Khan, Q. Y. Wang and M. E. Fitzpatrick, in *Materials Characterization Using Nondestructive Evaluation (NDE) Methods*, Elsevier Inc., 2016, pp. 1–16.

180 B. Ameduri, *Chem. Rev.*, 2009, **109**, 6632–6686.

181 L. W. Zhu, B. H. Wu, L. S. Wan and Z. K. Xu, *Polym. Chem.*, 2014, **5**, 4311–4320.

182 D. A. L. Otte, D. E. Borchmann, C. Lin, M. Weck and K. A. Woerpel, *Org. Lett.*, 2014, **16**, 1566–1569.

183 A. Gryff-Keller and P. Szczeciński, *RSC Adv.*, 2016, **6**, 82783–82792.

184 E. W. Della, E. Cotsaris and P. T. Hine, *J. Am. Chem. Soc.*, 1981, **103**, 4131–4135.

185 A. Foris, *Magn. Reson. Chem.*, 2001, **39**, 386–398.

186 R. Martino, V. Gilard, F. Desmoulin and M. Malet-Martino, *J. Pharm. Biomed. Anal.*, 2005, **38**, 871–891.

187 H. A. Naqi, T. J. Woodman, S. M. Husbands and I. S. Blagbrough, *Anal. Methods*, 2019, **11**, 3090–3100.

188 D. D. Elleman, L. C. Brown and D. Williams, *J. Mol. Spectrosc.*, 1961, **7**, 393–398.

189 A. A. Ribeiro, *Magn. Reson. Chem.*, 1997, **35**, 215–221.

190 B. F. Lundt, N. L. Johansen, A. Vølund and J. Markussen, *Int. J. Pept. Protein Res.*, 1978, **12**, 258–268.

191 M. Zhang, T. Breiner, H. Mori and A. H. E. Müller, *Polymer (Guildf).*, 2003, **44**, 1449–1458.

192 O. Colombani, M. Ruppel, F. Schubert, H. Zettl, D. V Pergushov and A. H. E. Müller, *Macromolecules*, 2007, **40**, 4338–4350.

193 A. J. Ryan, C. J. Crook, J. R. Howse, P. Topham, R. A. L. Jones, M. Geoghegan, A. J. Parnell, L. Ruiz-Pérez, S. J. Martin, A. Cadby, A. Menelle, J. R. P. Webster, A. J. Gleeson and W. Bras, *Faraday Discuss.*, 2005, **128**, 55–74.

194 M. Fantin, A. A. Isse, A. Venzo, A. Gennaro and K. Matyjaszewski, *J. Am. Chem. Soc.*, 2016, **138**, 7216–7219.

195 C. Boyer, A. Atme, C. Waldron, A. Anastasaki, P. Wilson, P. B. Zetterlund, D. Haddleton and M. R. Whittaker, *Polym. Chem.*, 2013, **4**, 106–112.

196 R. H. French, J. M. Rodriguez-Parada, M. K. Yang, R. A. Derryberry, M. F. Lemon, M. J. Brown, C. R. Haeger, S. L. Samuels, E. C. Romano and R. E. Richardson, in *Conference Record of the IEEE Photovoltaic Specialists Conference*, 2009, pp. 000394–000399.

197 W. M. Haynes, D. R. Lide and T. J. Bruno, *CRC Handbook of Chemistry and Physics*, 2014, vol. 95.

198 T. Tamura, S. Kawauchi, M. Satoh and J. Komiyama, *Polymer (Guildf).*, 1997, **38**, 2093–2098.

199 C. E. Kassis, J. M. DeSimone, R. W. Linton, E. E. Remsen, G. W. Lange and R. M. Friedman, *Rapid Commun. Mass Spectrom.*, 1997, **11**, 1134–1138.

200 T. G. Fox Jr and P. J. Flory, *J. Appl. Phys.*, 1950, **21**, 581–591.

201 S. Dubinsky, G. S. Grader, G. E. Shter and M. S. Silverstein, *Polym. Degrad. Stab.*, 2004, **86**, 171–178.

202 I. C. McNeill and S. M. T. Sadeghi, *Polym. Degrad. Stab.*, 1990, **29**, 233–246.

203 I. C. McNeill and S. M. T. Sadeghi, *Polym. Degrad. Stab.*, 1990, **30**, 267–282.

204 M. A. Meyers and K. K. Chawla, *Mechanical behavior of materials*, Cambridge University Press, 2nd edn., 2008.

205 R. J. Young and P. A. Lovell, *Introduction to polymers*, Boca Raton : CRC Press, 3rd edn., 2011.

206 F. S. Bates, *Macromolecules*, 1984, **17**, 2607–2613.

207 L. J. T. Hughes and D. B. Fordyce, *J. Polym. Sci.*, 1956, **22**, 509–526.

208 E. J. Ashford, V. Naldi, R. O'Dell, N. C. Billingham and S. P. Armes, *Chem. Commun.*, 1999, **0**, 1285–1286.

209 X. S. Wang, R. A. Jackson and S. P. Armes, *Macromolecules*, 2000, **33**, 255–257.

210 D. H. Williams and I. Fleming, *Spectroscopic Methods in Organic Chemistry*, McGraw-Hill Education, 6th edn., 2007.

211 R. A. Brown, A. J. Masters, C. Price and X. F. Yuan, in *Comprehensive Polymer Science and Supplements*, Elsevier, 1989, pp. 155–198.

212 S. Ham, C. Shin, E. Kim, D. Y. Ryu, U. Jeong, T. P. Russell and C. J. Hawker, *Macromolecules*, 2008, **41**, 6431–6437.

213 S. Jo, S. Jeon, T. Jun, C. Park and D. Y. Ryu, *Macromolecules*, 2018, **51**, 7152–7159.

214 G. F. Pauli, B. U. Jaki and D. C. Lankin, *J. Nat. Prod.*, 2005, **68**, 133–149.

215 F. Bates, *Annu. Rev. Phys. Chem.*, 1990, **41**, 525–557.

216 K. M. Salerno and N. Bernstein, *J. Chem. Theory Comput.*, 2018, **14**, 2219–2229.

217 S. W. Cranford and M. J. Buehler, *Macromolecules*, 2012, **45**, 8067–8082.

218 H. Li, B. Liu, X. Zhang, C. Gao, J. Shen and G. Zou, *Langmuir*, 1999, **15**, 2120–2124.

219 M. Müller and M. Schick, *Macromolecules*, 1996, **29**, 8900–8903.

220 S. M. Mai, J. P. A. Fairclough, I. W. Hamley, M. W. Matsen, R. C. Denny, B. X. Liao, C. Booth and A. J. Ryan, *Macromolecules*, 1996, **29**, 6212–6221.

221 T. Ohta and K. Kawasaki, *Macromolecules*, 1986, **19**, 2621–2632.

222 K. Y. Suh and H. H. Lee, *Macromolecules*, 1998, **31**, 3136–3138.

223 R. Holyst and M. Schick, *J. Chem. Phys.*, 1992, **96**, 730–739.

224 E. Hancox, D. Haddleton, P. D. Topham, L. Al-Shok, S. Huband, J. S. Town, M. Greenall and M. J. Derry, *Chem. Sci.*, 2022, **13**, 4019–4028.

225 D. J. Adams and P. D. Topham, in *Supramolecular Chemistry*, 2012.

226 E. Hancox, E. Liarou, J. S. Town, G. R. Jones, S. A. Layton, S. Huband, M. J. Greenall, P. D. Topham and D. M. Haddleton, *Polym. Chem.*, 2019, **10**, 6254–6259.

227 J. Van Damme, L. Vlaminck, G. Van Assche, B. Van Mele, O. van den Berg and F. Du Prez, *Tetrahedron*, 2016, **72**, 4303–4311.

228 G. W. Breton and X. Vang, *J. Chem. Educ.*, 1998, **75**, 81–82.

229 H. Bouas-Laurent, A. Castellan, J. P. Desvergne and R. Lapouyade, *Chem. Soc. Rev.*, 2000, **29**, 43–55.

230 C. Agostoni, R. Berni Canani, S. Fairweather-Tait, M. Heinonen, H. Korhonen, S. La Vieille, R. Marchelli, A. Martin, A. Naska, M. Neuhäuser-Berthold, G. Nowicka, Y. Sanz, A. Siani, A. Sjödin, M. Stern, S. Strain, I. Tetens, D. Tomé, D. Turck, J.-L. Bresson, H. Przyrembel, H. Van Loveren, H. Verhagen and P. Willatts, *EFSA J.*, 2013, **11**, 3412.

231 M. Younes, P. Aggett, F. Aguilar, R. Crebelli, M. Filipič, M. J. Frutos, P. Galtier, D. Gott, U. Gundert-Remy, G. G. Kuhnle, C. Lambré, J. C. Leblanc, I. T. Lillegaard, P. Moldeus, A. Mortensen, A. Oskarsson, I. Stankovic, I. Waalkens-Berendsen, R. A. Woutersen, R. J. Andrade, C. Fortes, P. Mosesso, P. Restani, F. Pizzo, C. Smeraldi, A. Papaioannou and M. Wright, *EFSA J.*, 2018, 16.

232 B. Ośmiałowski, E. D. Raczyńska and T. M. Krygowski, *J. Org. Chem.*, 2006, **71**, 3727–3736.

233 P. Niermeier, K. A. M. Maibom, J. H. Lamm, B. Neumann, H. G. Stammler and N. W. Mitzel, *Chem. Sci.*, 2021, **12**, 7943–7952.

234 J. Brancart, J. Van Damme, F. Du Prez and G. Van Assche, *Phys. Chem. Chem. Phys.*, 2021, **23**, 2252–2263.

235 J. Van Damme, L. Vlaminck, G. Van Assche, B. Van Mele, O. van den Berg

and F. Du Prez, *Tetrahedron*, 2016, **72**, 4303–4311.

236 J. Pina, D. Pinheiro, B. Nascimento, M. Piñeiro and J. S. Seixas de Melo, *Phys. Chem. Chem. Phys.*, 2014, **16**, 18319–18326.

237 SchottAG, *Technical Glasses, Physical and Technical Properties*, 2014.

238 S. Peng, Z. Ke, X. Cao, C. Shan, F. Zhao, M. Guan, L. Shi, Y. Sun, Y. Yang and L. Ma, *J. Non. Cryst. Solids*, , DOI:10.1016/j.jnoncrysol.2019.119735.

239 A. Limer and D. M. Haddleton, *Eur. Polym. J.*, 2006, **42**, 61–68.

240 Z. Wang, B. Huai, G. Yang, M. Wu and J. Yu, *J. Lumin.*, 2018, **204**, 110–115.

241 E. Yilgor, G. E. Atilla, A. Ekin, P. Kurt and I. Yilgor, *Polymer (Guildf).*, 2003, **44**, 7787–7793.

242 H. Pawar and A. Lali, *RSC Adv.*, 2014, **4**, 26714–26720.

243 Y. Yoshimura, A. Chandra, Y. Nabae and T. Hayakawa, *Soft Matter*, 2019, **15**, 3463–3632.

244 M. Elladiou and C. S. Patrickios, *Polym. Chem.*, 2012, **3**, 3228–3231.

245 W. Van Camp, F. E. Du Prez and S. A. F. Bon, *Macromolecules*, 2004, **37**, 6673–6675.

246 Methacrylic acid 99% | Sigma-Aldrich, https://www.sigmaaldrich.com/GB/en/product/aldrich/395374, (accessed 3 May 2022).

247 Sigma-Aldrich, Pressure-Temperature Nomograph Interactive Tool, https://www.sigmaaldrich.com/GB/en/support/calculators-and-apps/pressure-temperature-nomograph-interactive-tool, (accessed 3 May 2022).

248 M. R. Nanda, Y. Zhang, Z. Yuan, W. Qin, H. S. Ghaziaskar and C. Xu, *Renew. Sustain. Energy Rev.*, 2016, **56**, 1022–1031.

249 A. B. Foster, M. H. Randall and J. M. Webber, *J. Am. Soc.*, 1965, 3388–3394.

250 Y. Zhen, S. Wan, Y. Liu, H. Yan, R. Shi and C. Wang, *Macromol. Chem. Phys.*,

2005, **206**, 607–612.

251 L. Li, B. Li, J. Dong and J. Zhang, *J. Mater. Chem. A*, 2016, **4**, 13677–13725.

252 J. Zhang, E. Liarou, J. Town, Y. Li, A. M. Wemyss and D. M. Haddleton, *Polym. Chem.*, 2020, **11**, 5534–5541.

253 G. R. Jones, A. Anastasaki, R. Whitfield, N. Engelis, E. Liarou and D. M. Haddleton, *Angew. Chemie - Int. Ed.*, 2018, **57**, 10468–10482.

254 K. Jansson, T. Frejd, J. Eihlberg and G. Magnusson, *Tetrahedron Lett.*, 1988, **1**, 361–362.

255 K. G. Andrews, R. Faizova and R. M. Denton, *Nat. Commun.*, 2017, **8**, 1–6.

256 J. A. Syrett, G. Mantovani, W. R. S. Barton, D. Price and D. M. Haddleton, *Polym. Chem.*, 2010, **1**, 102–106.

257 D. Nečas and P. Klapetek, *Cent. Eur. J. Phys.*, 2012, **10**, 181–188.